



NTNU – Trondheim
Norwegian University of
Science and Technology

Application of mechanistic models for flow distribution and heat transfer in finned tube bundles

Astrid Øygarden Eikill

Master of Energy and Environmental Engineering

Submission date: June 2013

Supervisor: Erling Næss, EPT

Co-supervisor: Anna Holfeld, EPT

Norwegian University of Science and Technology
Department of Energy and Process Engineering

EPT-M-2013-34

MASTER THESIS

for

Stud.techn. Astrid Eikill

Spring 2013

Application of mechanistic models for flow distribution and heat transfer in finned tube bundles

*Anvendelse av mekanistiske modeller for strømningsfordeling og varmeovergang i finnedede rørsatser***Background and objective**

Exhaust gas from a gas turbine contains a large amount of heat that can be utilized for process purposes or for power generation. On offshore platforms, it is necessary to make heat recovery units as compact and light-weight as possible. The Department, in cooperation with SINTEF Energy Research and international oil companies are engaged in a work which seeks to develop compact heat exchanger solutions for such applications. In the present incarnation, finned tubes shall be used. Existing models and experimental data for flow distribution and heat transfer in finned tube bundles shall be applied, aiming to develop improved prediction models and design methods. A test rig for measurements on heat transfer and pressure drop on finned tube bundles is available in the laboratory of NTNU.

The following tasks are to be considered:

1. Carry out a literature survey on mechanistic models and CFD models for flow distribution and heat transfer and pressure drop on finned tubes and tube bundles.
2. Apply and compare the available models with the available experimental data on finned tube bundles (both serrated and solid-fin tubes). Based on the comparisons, model improvements shall be proposed and tested to improve the prediction performance. Additional experiments necessary for further improvement shall be proposed.
3. Participate in experiments on heat transfer and pressure drop of one or more fin-tube geometries, selected in cooperation with the Department. A complete data analysis including uncertainty analysis shall be performed, and the results shall be discussed and presented.
4. Suggestions for further work shall be made.

- " --

Within 14 days of receiving the written text on the master thesis, the candidate shall submit a research plan for his project to the department.

When the thesis is evaluated, emphasis is put on processing of the results, and that they are presented in tabular and/or graphic form in a clear manner, and that they are analyzed carefully.

The thesis should be formulated as a research report with summary both in English and Norwegian, conclusion, literature references, table of contents etc. During the preparation of the text, the candidate should make an effort to produce a well-structured and easily readable report. In order to ease the evaluation of the thesis, it is important that the cross-references are correct. In the making of the report, strong emphasis should be placed on both a thorough discussion of the results and an orderly presentation.

The candidate is requested to initiate and keep close contact with his/her academic supervisor(s) throughout the working period. The candidate must follow the rules and regulations of NTNU as well as passive directions given by the Department of Energy and Process Engineering.

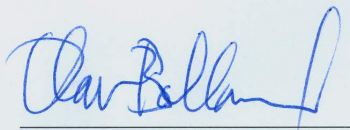
Risk assessment of the candidate's work shall be carried out according to the department's procedures. The risk assessment must be documented and included as part of the final report. Events related to the candidate's work adversely affecting the health, safety or security, must be documented and included as part of the final report. If the documentation on risk assessment represents a large number of pages, the full version is to be submitted electronically to the supervisor and an excerpt is included in the report.

Pursuant to "Regulations concerning the supplementary provisions to the technology study program/Master of Science" at NTNU §20, the Department reserves the permission to utilize all the results and data for teaching and research purposes as well as in future publications.

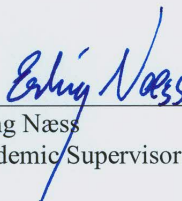
The final report is to be submitted digitally in DAIM. An executive summary of the thesis including title, student's name, supervisor's name, year, department name, and NTNU's logo and name, shall be submitted to the department as a separate pdf file. Based on an agreement with the supervisor, the final report and other material and documents may be given to the supervisor in digital format.

- Work to be done in lab (Water power lab, Fluids engineering lab, Thermal engineering lab)
 Field work

Department of Energy and Process Engineering, 14. January 2013



Olav Bolland
Department Head



Erling Næss
Academic Supervisor

Research Advisor: PhD student Anna Holfeld, NTNU

Preface

The work presented in this thesis was carried out by me, Stud. Techn. Astrid Øy garden Eikill, at the Department of Energy and Process Engineering at NTNU, in the spring of 2013.

I would like to thank my head supervisor, Erling Næss, for taking me on as his MSc candidate and for his guidance and encouragement. I would also like to thank my co-supervisor Anna Holfeld, for letting me participate in her experimental research and making this a part of my thesis, and for her feedback on my writing.

Lastly, I would like to thank my family and my boyfriend Åsmund, for their love and support throughout my studies.

Trondheim, 24.06.2013

Abstract

The focus of this thesis was heat transfer and pressure drop in staggered tube bundles with solid and serrated fins. The first part of the work dealt with five prediction models, namely PFR's model (1976), Nir's model (1991), Ralston et al.'s HTFS1 model (1997), Chu and Ralston's HTFS2 model (1998) and McIlwain's HTFS3 model (2003). The models all had correlations for prediction of heat transfer and pressure drop, but only PFR and Nir had specific correlations for serrated fins. The correlations were tested for a multitude of tube bundle geometries - both solid finned and serrated finned - and Reynold's numbers, taken from a database containing hundreds of experiments by several investigators. The predicted results were compared to the measured values for heat transfer and pressure drop from the database. The comparison revealed that none of the models could accurately predict both heat transfer and pressure drop, for both solid fin and serrated fin tube bundles. Overall, the most accurate model was PFR, while the least accurate model was HTFS1. An attempt to improve the prediction accuracy of the models' correlations, by introducing corrections based on different geometric parameters, was carried out. This improvement succeeded for some correlations, but failed for others. The correlations that were ultimately found to have the best prediction accuracy were:

- For heat transfer, solid fins: Modified Nir, with 76.2 % of data predicted within ± 20 % and 47.4 % of data predicted within ± 10 % AND modified HTFS2, with 79.8 % of data predicted within ± 20 % and 42.4 % of data predicted within ± 10 %.
- For heat transfer, serrated fins: Modified HTFS3, with 74.1 % of data predicted within ± 20 % and 51.4 % of data predicted within ± 10 %.
- For pressure drop, solid fins: Modified PFR, with 92.3 % of data predicted within ± 30 % and 67.0 % of data predicted within ± 15 % AND modified Nir, with 89.6 % of data predicted within ± 30 % and 71.2 % of data predicted within ± 15 %.
- For pressure drop, serrated fins: Original PFR, with 64.6 % of data predicted within ± 30 % and 40.2 % of data predicted within ± 15 %.

The second part of the work was participation in pressure drop and heat transfer testing of one tube bundle geometry. The bundle consisted of 8 longitudinal tubes and 4 transversal tubes in a staggered layout, with a layout angle of 30° . The tubes had an outer diameter of 31.75 mm. The fins were of the I-foot serrated type, with a total fin height of 18 mm, fin thickness 1 mm and fin pitch 3.62 mm. The pressure drop tests were done in the flow range $3.4 \times 10^3 \leq Re \leq 4.1 \times 10^4$. The heat transfer tests were done in the flow range $6.4 \times 10^3 \leq Re \leq 3.4 \times 10^4$ with inlet air temperature around 120-130°C. The results of the testing showed pressure drop and heat transfer values in a plausible range, but with very high

pressure drop uncertainty for low Re. The experimental values were compared to values calculated with the five prediction models. The measured pressure drop and heat transfer were found to best agree with the predictions of Nir and PFR, respectively.

Sammendrag

Fokuset i denne masteroppgaven var på varmeovergang og trykktap i forsatte rørbunter med heltrukne og serraterter finner. Den første delen av arbeidet dreide seg om fem prediksjonsmodeller: PFRs modell (1976), Nirs modell (1991), Ralston et al.s HTFS1-modell (1997), Chu og Ralstons HTFS2-modell (1998) og McIlwains HTFS3-modell (2003). Alle modellene hadde korrelasjoner for prediksjon av varmeovergang og trykktap, men kun PFR og Nir hadde spesifikke korrelasjoner for serraterter finner. Korrelasjonene ble testet for en mengde rørbuntsgeometrier - både med heltrukne og serraterter finner - og Reynoldstall, tatt fra en database som inneholder hundrevis av eksperimenter av flere utredere. De predikerte resultatene ble sammenlignet med målte verdier for varmeovergang og trykktap fra databasen. Sammenligningen avslørte at ingen av modellene kunne forutse nøyaktig både varmeovergang og trykktap, for både heltrukne og serraterter finnerørbunter. Totalt sett var PFR var den mest nøyaktige modellen, mens HTFS1 var den minst nøyaktige. Et forsøk på å forbedre prediksjonsnøyaktigheten til modellenes korrelasjoner, ved å innføre korreksjoner basert på ulike geometriparametre, ble utført. Denne forbedringen lyktes for noen av korrelasjonene, men mislyktes for andre. Korrelasjonene som til slutt ble funnet å ha best prediksjonsnøyaktighet var:

- Varmeovergang, heltrukne finner: Modifisert Nir, med 76.2 % av dataene predikert innenfor ± 20 % og 47.4 % av dataene predikert innenfor ± 10 % OG modifisert HTFS2, med 79.8 % av dataene predikert innenfor ± 20 % og 42.4 % av dataene predikert innenfor ± 10 %.
- Varmeovergang, serraterter finner: Modifisert HTFS3, med 74.1 % av dataene predikert innenfor ± 20 % og 51.4 % av dataene predikert innenfor ± 10 %.
- Trykktap, heltrukne finner: Modifisert PFR, med 92.3 % av dataene predikert innenfor ± 30 % og 67.0 % av dataene predikert innenfor ± 15 % OG modifisert Nir, med 89.6 % av dataene predikert innenfor ± 30 % og 71.2 % av dataene predikert innenfor ± 15 %.
- Trykktap, serraterter finner: Original PFR, med 64.6 % av dataene predikert innenfor ± 30 % og 40.2 % av dataene predikert innenfor ± 15 %.

Den andre delen av arbeidet var deltagelse i trykktaps- og varmeovergangsforsøk på én rørbuntsgeometri. Buntene bestod av 8 longitudinale og 4 transversale rør i forsatt arrangement, med en arrangementsvinkel på 30° . Rørene hadde ytre diameter 31.75 mm. Finnene var av I-fot serraterter type, med total finnehøyde 18 mm, finnetykkelse 1 mm og finneavstand 3.62 mm. Trykktapsforsøkene ble gjort i strømningsområdet $3.4 \times 10^3 \leq Re \leq 4.1 \times 10^4$. Varmeovergangsforsøkene ble gjort i strømningsområdet $6.4 \times 10^3 \leq Re \leq 3.4 \times 10^4$ med innløps lufttemperatur rundt $120\text{-}130^\circ\text{C}$. Forsøksresultatene

viste trykktaps- og varmeovergangsverdier i et plausibelt område, men med svært høy usikkerhet for trykktap for lave Re . De eksperimentelle verdiene ble sammenlignet med verdier beregnet med de fem prediksjonsmodellene. Det målte trykktapet og den målte varmeovergangen ble funnet til å stemme best overens med beregningene fra henholdsvis Nir og PFR.

Contents

Nomenclature	12
1 Introduction	16
2 Background theory on finned tube bundles	17
2.1 Tube and fin geometry	18
2.2 Bundle geometry	21
2.3 Flow in finned tube bundles	22
2.4 Heat transfer and pressure drop in finned tube bundles	24
3 Literature on mechanistic models for heat transfer and pressure drop in staggered tube bundles with fins	26
3.1 PFR Report, 1976: Heat transfer and pressure drop characteristics of dry tower extended surfaces	26
3.2 A. Nir, 1991: Heat transfer and friction factor correlations for crossflow over staggered tube banks	28
3.3 J. A. R. Henry, 1994: Effect of fin frequency and tube pitch on bundle pressure loss	32
3.4 Ralston et. al, 1997: HTFS models for heat transfer and pressure drop applied to staggered arrangements of tubes with plain helical fins	35
3.5 Chu and Ralston, 1998: HTFS2: Improved models for heat transfer and pressure drop applied to staggered arrangements of tubes with plain helical fins	38
3.6 S. R. McIlwain, 2003: Improved prediction methods for finned tube bundle heat exchangers in crossflow	39
3.7 Discussion	43
4 Model application and improvement	44
4.1 Presentation of database	44
4.2 Assumptions and limitations	44
4.3 Model performance: Comparison of measured and predicted values	45
4.3.1 Heat transfer	46

4.3.2	Pressure drop	49
4.4	Geometry dependency	54
4.5	Model improvements and modified model performance	57
4.5.1	Heat transfer	57
4.5.2	Pressure drop	60
4.6	Discussion	63
5	Experimental setup	65
5.1	Rig design	65
5.2	Test geometry	67
5.3	Data reduction	68
6	Test results and analysis	72
6.1	Pressure drop	72
6.1.1	Comparison with measured values for similar geometry . .	73
6.1.2	Comparison with predicted values	73
6.2	Heat transfer	74
6.2.1	Comparison with measured values for similar geometry . .	75
6.2.2	Comparison with predicted values	75
6.3	Discussion	76
7	Conclusion	77
	References	79
	List of figures	81
	List of tables	88
A	Model performance	89
A.1	PFR	89
A.2	Nir	91
A.3	HTFS1	93

A.4	HTFS2	95
A.5	HTFS3	97
B	Geometry dependency	99
B.1	PFR	99
B.2	Nir	109
B.3	HTFS1	119
B.4	HTFS2	129
B.5	HTFS3	139
C	Modified model performance	149
C.1	PFR	149
C.2	Nir	151
C.3	HTFS1	153
C.4	HTFS2	155
C.5	HTFS3	157
D	Experimental uncertainty	159
D.1	Pressure drop test	159
D.2	Heat transfer test	160
E	Sintef 10 geometry	163

Nomenclature

Symbol	Units	Description
Greek symbols		
α	W/(m ² K)	Convective heat transfer coefficient
α_g	W/(m ² K)	Gas side convective heat transfer coefficient
α_i	W/(m ² K)	Tube side convective heat transfer coefficient
β	–	Parameter for fin tip clearance
Γ	–	Correction factor for crossflow LMTD
η_f	–	Actual fin efficiency
η_{th}	–	Theoretical fin efficiency
$\eta_{l,th}$	–	Theoretical fin efficiency for rectangular fin
$\eta_{p,th}$	–	Theoretical fin efficiency for solid part of fin
$\eta_{s,th}$	–	Theoretical fin efficiency for serrated part of fin
ρ	kg/m ³	Fluid density
θ	rad	Layout angle
κ	–	Bypass parameter (Henry)
μ	kg/(ms)	Dynamic viscosity
ν	m ² /s	Kinematic viscosity
σ	–	Ratio of approach area to minimum flow area (Henry)
ϕ	–	Ratio of fin area to bundle approach area (Henry)
χ	–	Fin efficiency correction factor
Latin symbols		
A_0	m ² /m	Superficial flow area, per tube length
$A_{0,d}$	m ² /m	Diagonal flow area at tube face per tube length for any tube bundle (Nir)
$A_{0,f}$	m ² /m	Frontal free flow area at tube face per tube length for any tube bundle (Nir)
$A_{0,t}$	m ² /m	Frontal free flow area at tube face per tube length for a tube bundle with no fin gap (Nir)
A_{fin}	m ² /m	Fin area, per tube length
$A_{fin,serr}$	m ² /m	Area of segmented part of I-foot serrated fin, per tube length
$A_{fin,sol}$	m ² /m	Area of solid part of I-foot serrated fin, per tube length
$A_{ht} = A_t$	m ² /m	Total heat transfer area, per tube length
A_i	m ² /m	Inner tube surface area, per tube length
$A_{min} = A_c$	m ² /m	Minimum flow area, per tube length
A_r	–	Ratio of heat transfer area to base tube area
$A_{t,0}$	m ² /m	Exposed tube surface area, per tube length
A_{tube}	m ² /m	Base tube area, per tube length

Symbol	Units	Description
B	m	Blockage per unit length
c_f	–	Fanning friction factor
c_p	J/(kgK)	Specific heat
d	m	Outer base tube diameter
d_h	m	Hydraulic diameter
D	m	Fin diameter
F_P	–	Form drag friction factor (Henry)
F_F	–	Skin drag friction factor (Henry)
G_A	m	Diagonal gap correction term (McIlwain)
G_D	m	Diagonal gap (McIlwain)
G_T	m	Transversal gap (McIlwain)
GR_{eff}	–	Effective gap ratio (McIlwain)
h	m	Effective fin height for rectangular fin
h_e	m	Equivalent fin height for round fin
h_f	m	Total fin height
h_s	m	Segment height
H_B	(m/s) ²	Overall bundle pressure head (Henry)
H_P	(m/s) ²	Form drag contribution to overall pressure head (Henry)
H_F	(m/s) ²	Skin drag contribution to overall pressure head (Henry)
k	W/(mK)	Thermal conductivity
K_B	–	Bundle loss coefficient (Ralston)
K_{fins}	–	Fin loss coefficient (Ralston)
K_{gap}	–	Gap loss coefficient (Ralston)
K_{tube}	–	Tube loss coefficient (Ralston)
$K_{z,h}$	–	Heat transfer correction factor (Nir)
$K_{z,p}$	–	Pressure drop correction factor (Nir)
l_t	m	Tube length
L	m)	Characteristic legth scale
$LMTD$	K	Logarithmic mean temperature difference
\dot{m}	kg/s)	Mass flow rate
n_f	m ⁻¹	Fin frequency, number of fins per tube length
N_g	–	Number of tube gaps in the longitudinal direction
N_r	–	Number of tube rows in the longitudinal direction
N_t	–	Number of tubes per row
p	Pa	Pressure
p_f	m	Fin pitch

Symbol	Units	Description
P_D	m	Diagonal tube pitch
P_T	m	Transversal tube pitch
P_L	m	Longitudinal tube pitch
R_b	–	Ratio of frontal free flow area for any tube bundle to frontal free flow area for a tube bundle with no fin gap (Nir)
R_d	–	Ratio of diagonal flow area for any tube bundle frontal free flow area for any tube bundle (Nir)
R_f	–	Ratio of frontal free flow area for any tube bundle to face area of any tube bundle (Nir)
R_t	–	Ratio of frontal free flow area for a tube bundle with no fin gap to face area for a tube bundle with no fin gap (Nir)
Re_0	–	Reynolds number based on superficial flow area and velocity
Re_D	–	Reynolds number based on fin diameter
Re_f	–	Reynolds number based on fin flow area and velocity
Re_h	–	Reynolds number based on hydraulic diameter
$Re_{max} = Re_d$	–	Reynolds number based on minimum flow area/tube diameter
s_f	m	Fin spacing
S_0	m ²	Superficial flow area
S_{min}	m ²	Minimum flow area
t_f	m	Fin thickness
T	K	Temperature
u	m/s	Fluid velocity
u_0	m/s	Superficial flow velocity
u_f	m/s	Fin flow velocity
u_g	m/s	Gap flow velocity
U	W/(m ² K)	Overall heat transfer coefficient
w_s	m	Segment width
W	–	Ratio of heat transfer area to free flow area (Nir)
x	m	General length scale

Dimensionless groups

$$Eu = \frac{\Delta p}{\frac{1}{2}\rho u^2} \quad \text{Euler number}$$

$$Nu = \frac{\alpha x}{k} \quad \text{Nusselt number}$$

$$Pr = \frac{\mu c_p}{k} \quad \text{Prandtl number}$$

$$Re = \frac{\rho u x}{\mu} \quad \text{Reynolds number}$$

NOTE: In the diagrams and tables presented, $NuPr^{-1/3}$ is denoted simply as $NuPr$. Period marks the decimal, except in table 9 and 10, where comma is the decimal sign.

1 Introduction

The heat contained in waste gas streams from industrial processes is a valuable source of energy. This waste heat can, when recovered, be used for heating purposes or electricity generation by use of thermal power cycles (Næss, 2007). Waste heat recovery units in the form of finned tube bundles represent the current technology. The optimal dimensioning of these units is crucial for maximum energy recovery. On offshore oil platforms for instance, where one source of waste heat is the exhaust from gas turbines, it is important that the waste heat recovery units are light and compact, while recovering as much heat as possible.

The amount of energy recovered in a waste heat recovery unit depends on the heat transfer performance of the finned tubes. The better the heat transfer effectiveness of the finned surface, the more heat is transferred from the waste gas to the heat recovery fluid inside the tubes. The pressure drop over the tube bundle affects the efficiency of the whole system. These factors are influenced by the geometric parameters of the fins, tubes and bundle. Fin height, density and thickness, tube diameter and bundle layout all contribute to determining the flow distribution and therefore pressure drop and heat transfer across the bundle.

To assist the design of waste heat recovery units, models have been developed to predict the heat transfer and pressure drop dependent on geometry and flow conditions. In this thesis, the prediction accuracy of five such models is tested against experimental heat transfer and pressure drop data from a database covering hundreds of tests by a handful of investigators. On the basis of this comparison, suggestions on how to possibly improve the models will be made, and the most accurate heat transfer and pressure drop correlations will be announced.

In addition, the results of heat transfer and pressure drop tests done on one new geometry will be presented and compared with predicted values. The experimental work was supervised by PhD candidate Anna Holfeld. Due to several delays in the delivery of the tubes and completion of the test rig and some equipment malfunction, the tests were finished less than one week before the thesis deadline. The processing and analysis of the experimental results is therefore not as comprehensive as first intended.

2 Background theory on finned tube bundles

The focus of this thesis is on finned tube bundles used in crossflow heat exchangers for heat recovery applications. Hot gas flowing across the bundle heats up fluid flowing inside the tubes, which goes on to be used for further heating purposes or electricity generation. The so-called fins are extended surfaces that increase the overall heat transfer area of the tubes and thus the heat transfer effectiveness.

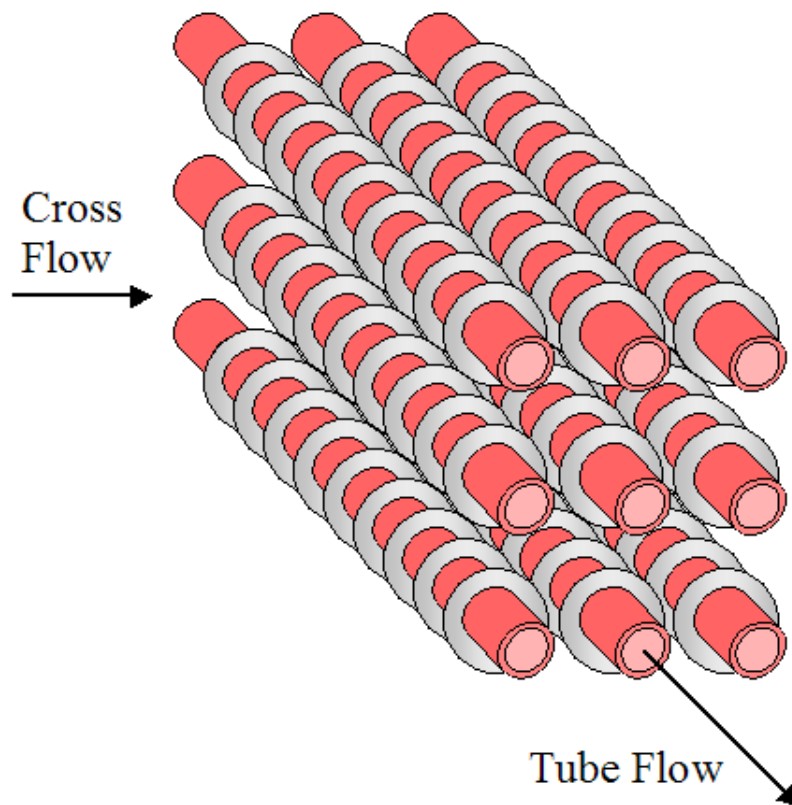


Figure 1: Crossflow finned tube bundle heat exchanger (Source: Real World Physics Problems website)

2.1 Tube and fin geometry

Finned tubes come in many varieties. The shape of the tube itself can vary from round, to elliptical or drop-shaped. The fins can be annular, helical, studded, square or form a continuous plate over the bundle. The finned tubes studied in this thesis are round, with annular or helically wound fins. See figure 2.

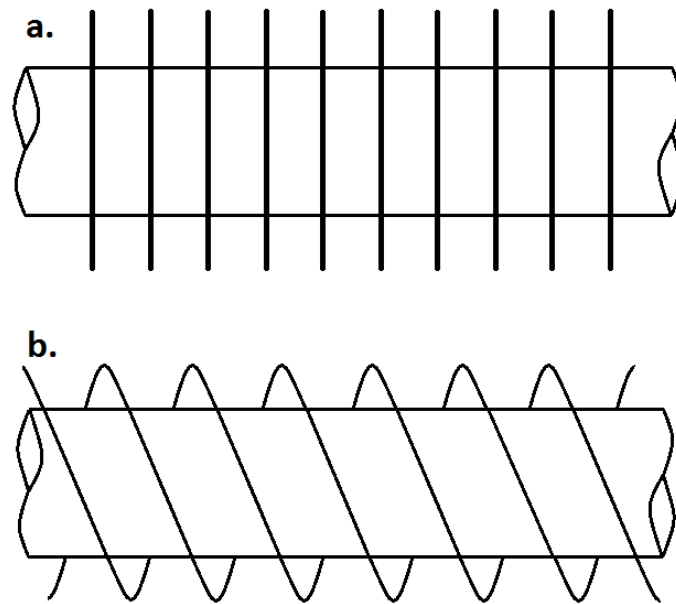


Figure 2: a. Individual annular fins; b. Helically wound fins (according to PFR, 1976)

In addition, segmentation or serration of the fins alter their geometric characteristics. Serration will enhance heat transfer by breaking up the flow boundary layers (Næss, 2007). See figure 3.

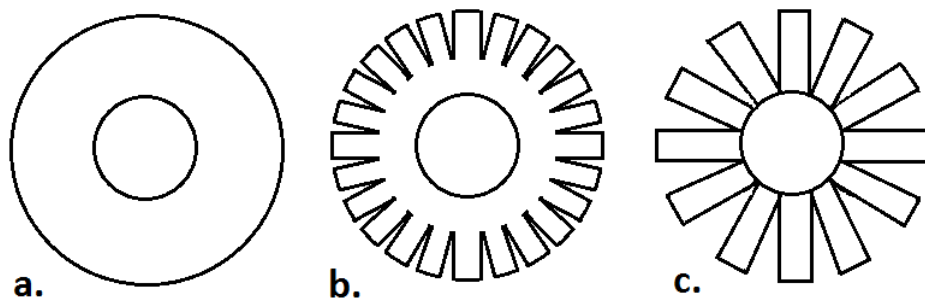


Figure 3: Types of round fins: a. Plain/solid fin; b. I-foot serrated fin; c. L-foot serrated fin (according to PFR, 1976)

Fin attachments can be of the I-foot or L-foot type. Serrated I-foot fins are plain fins that have segments created by partially cutting into the fin. Serrated L-foot fins have individual segments welded to the base tube. See figure 4.

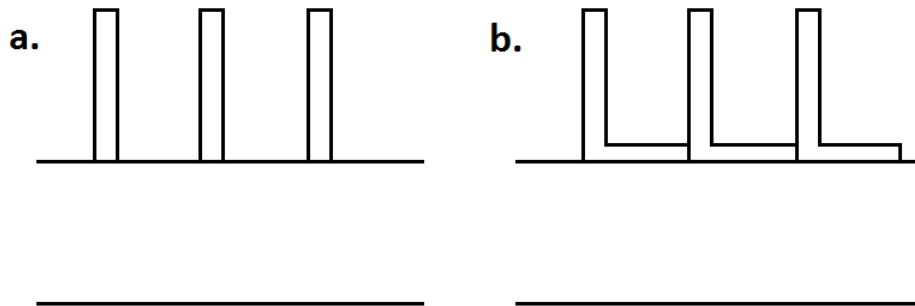


Figure 4: Attachment methods for serrated fins: a. I-foot fins; b. L-foot fins

All in all, there are several geometric characteristics to take into account when calculating flow over finned tubes. Figure 5 shows the important geometric parameters of a finned tube: the base tube diameter d , the fin height h_f , the fin diameter $D = 2h_f + d$, the fin thickness t_f , the fin spacing (the distance between the edges of two fins) s_f , the fin pitch p_f (the distance between the center of two fins) and for serrated fins the segment width w_s and segment height h_s (which for L-foot fins is equal to h_f). See figure 5.

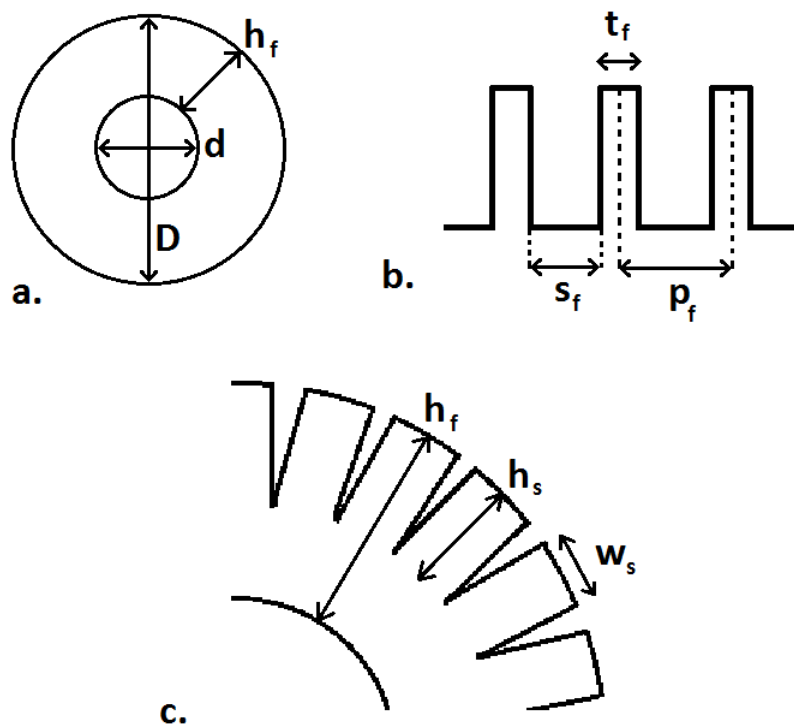


Figure 5: Tube and fin parameters: a. Tube and fin diameters; b. Fin thickness and spacing; c. Segment height and width

From these single parameters, several useful areas can be calculated. Per tube length, the area of a round base tube is expressed as

$$A_{tube} = \pi d \quad (1)$$

The exposed part of the tube - i.e. the part of the tube surface that is not attached to fins and is open to heat transfer - has an area, per length of tube, of

$$A_{t,0} = A_{tube} - n_f \pi d t_f \quad (2)$$

where $n_f = 1/p_f$ is the number of fins per tube length. The extended area - the area of the fins - depends on the fin type. For plain round fins the fin area per tube length is

$$A_{fin} = n_f \left(2 \frac{\pi}{4} (D^2 - d^2) + \pi D t_f \right) \quad (3)$$

For L-foot type serrated fins the fin area per tube length is

$$A_{fin} = n_f (2h_f w_s + 2h_f t_f + w_s t_f) \frac{\pi d}{w_s} \quad (4)$$

For I-foot type serrated fins the fin area consists of a solid part and a segmented part. The areas are, per tube length,

$$A_{fin,sol} = n_f \left(2 \frac{\pi}{4} ((d + 2(h_f - h_s))^2 - d^2) \right) \quad (5)$$

$$A_{fin,ser} = n_f (2h_s w_s + 2h_s t_f + w_s t_f) \frac{\pi (d + 2(h_f - h_s))}{w_s} \quad (6)$$

The area that comes into contact with the heat transfer medium - the total heat transfer area - is then, per tube length,

$$A_{ht} = A_{t,0} + A_{fin} \quad (7)$$

The area ratio A_r is used as a non-dimensional geometric parameter in pressure drop and heat transfer correlations. It is the ratio of total heat transfer area to base tube area, given by

$$A_r = \frac{A_{ht}}{A_{tube}} \quad (8)$$

2.2 Bundle geometry

The tubes in a crossflow heat exchanger can be arranged in two principal ways: inline and staggered bundles. For inline bundles, the tube rows are directly in line with one another. For staggered bundles, every other tube row is displaced so that every tube is in line with the gap between two tubes in the other row. See figure 6.

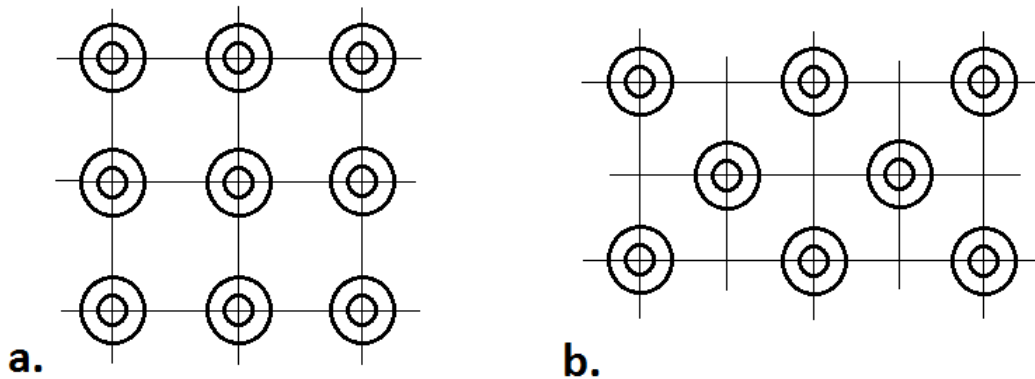


Figure 6: Bundle arrangements: a. Inline bundle; b. Staggered bundle (according to PFR, 1976)

Staggered bundles are generally preferred because they have better heat transfer performance due to the flow pattern over the bundle, and can be made more compact than inline bundles. Inline bundles have the advantage of being easier to clean. In this work, the focus is on staggered tube bundles. The parameters characterizing the bundle layout are the transversal pitch P_T , the longitudinal pitch P_L , the diagonal pitch P_D and the layout angle θ . See figure 7.

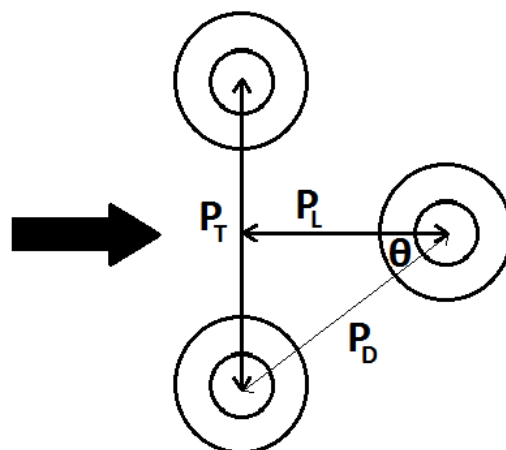


Figure 7: Staggered layout parameters

2.3 Flow in finned tube bundles

The heat transfer medium, be it air or exhaust gases, will flow over the tube bundle, penetrating the spaces between the fins. Some flow goes right through the gap between the fin tips of adjacent tubes. This is called bypass. See figure 8. Henry (1994) formulates a simple bypass flow model as such:

$$u_0 P_T = u_f D + u_g (P_T - D) \quad (9)$$

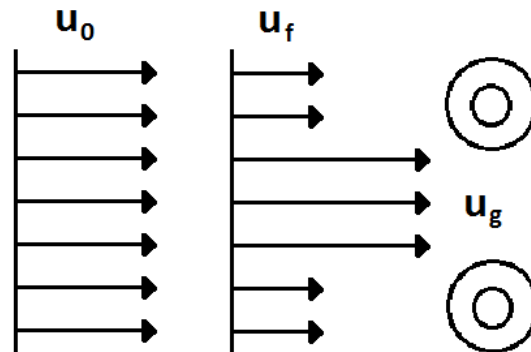


Figure 8: Bypass flow model (according to Henry, 1994)

The model states that the approach flow, having a superficial velocity u_0 , can be broken up into two components, one passing between the fin spaces with velocity u_f and one through the bypass path, i.e. between the fin tips, with velocity u_g . The flow area per tube length corresponding to the superficial velocity is equal to the transversal pitch:

$$A_0 = P_T \quad (10)$$

The total fin and gap flow area is also called the minimum flow area. See the white part of figure 9.

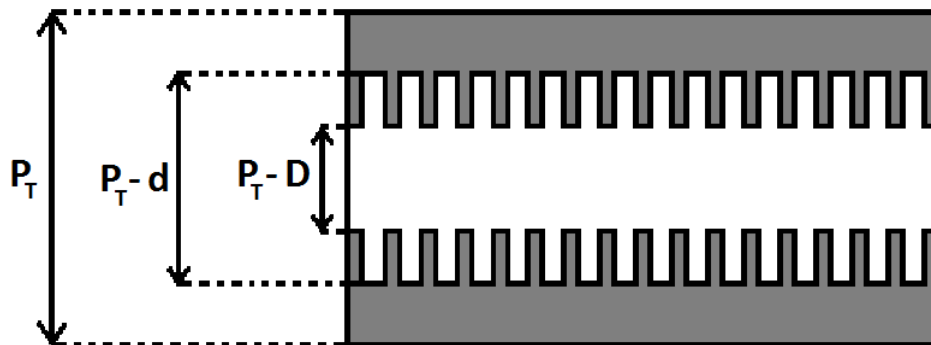


Figure 9: Flow area between two adjacent tubes

This area (per tube length) is expressed as

$$A_{min} = (P_T - d) - n_f t_f (D - d) \quad (11)$$

The Reynolds number is an important dimensionless flow descriptor. It represents the ratio of inertia to viscous forces in the flow (Incropera et al., 2007) and is defined as

$$Re = \frac{\rho u x}{\mu} \quad (12)$$

where ρ is the density of the fluid, u is the fluid velocity and x is the characteristic length scale.

Different Reynolds numbers are associated with the different velocities in the flow over the bundle: the superficial Reynolds number Re_0 , the maximum Reynolds number Re_{max} and the fin Reynolds number Re_f . Like the velocities, these numbers relate to each other by areas,

$$\frac{Re_0}{A_0} = \frac{Re_{max}}{A_{min}} = \frac{Re_f}{A_f} \quad (13)$$

If for instance the maximum Reynolds number is given, the superficial Reynolds number can be calculated thus

$$Re_0 = \frac{A_0}{A_{min}} Re_{max} = \frac{P_T}{(P_T - d) - n_f t_f (D - d)} Re_{max} \quad (14)$$

2.4 Heat transfer and pressure drop in finned tube bundles

Heat is transferred between the gas flowing over the tube bundle and the fluid flowing inside the tubes via the fin and tube surfaces. This occurs by convection between the gas and the outer surface, conduction through the extended surface and tube wall and convection between the inner tube surface and the fluid. This heat transfer is described by the dimensionless Nusselt number. For a tube with outer diameter d

$$Nu = \frac{\alpha d}{k} \quad (15)$$

which represents the ratio of convective and conductive heat transfer. Here α is the convective heat transfer coefficient and k is the thermal conductivity of the fluid. The Nusselt number thus represents the temperature gradient at the tube surface (Incropera et al., 2007). The Nusselt number is a function of two similarity parameters: the Prandtl number and the Reynolds number. To describe the gas flowing over the bundle, the dimensionless Prandtl number is used. The Prandtl number represents the ratio of momentum diffusivity to thermal diffusivity and is defined as:

$$Pr = \frac{c_p \mu}{k} \quad (16)$$

where c_p is the specific heat and μ is the dynamic viscosity of the fluid. In the literature, many investigators use the Chilton-Colburn j-factor to represent heat transfer:

$$j = \frac{\alpha}{c_p \rho u} Pr^{2/3} = St Pr^{2/3} \quad (17)$$

where $St = \frac{\alpha}{c_p \rho u} = \frac{Nu}{Re Pr}$ is the Stanton number. The Stanton number is a modified version of the Nusselt number and represents the ratio of heat transferred to the thermal capacity of the fluid (Incropera et al., 2007). The j-factor includes the Prandtl number, making it independent on the gas used (Kaspersen, 1995). The measure for heat transfer in experiments done by previous investigators is the dimensionless group $Nu Pr^{-1/3}$. This relates to the j-factor thus:

$$Nu Pr^{-1/3} = j Re \quad (18)$$

The pressure drop occurring in the flow over the tube bundle is caused by two drag force components: friction drag due to boundary layer surface shear stress and pressure drag due to a pressure differential in the flow direction, resulting from turbulent wake formation (Incropera et al., 2007). See figure 10.

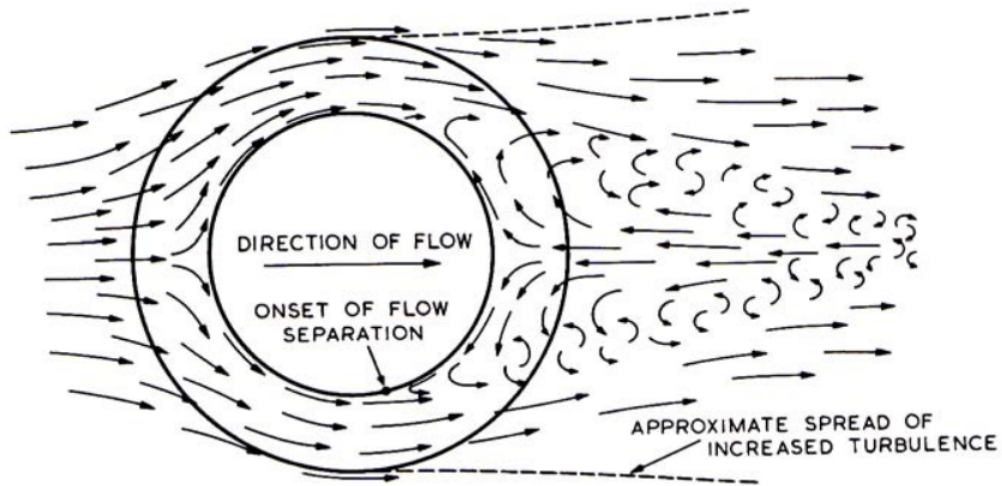


Figure 10: Flow pattern over a finned tube (Neal & Hitchcock, 1966)

With regards to finned tubes, serration of the fins leads to a breakup of the boundary layer and therefore both an increase in heat transfer and pressure drop (Næss, 2007). The dimensionless pressure coefficient, the Euler number, is used to describe the pressure drop in the tube bundle. It is defined as

$$Eu = \frac{\Delta p}{\frac{1}{2}\rho u^2} \quad (19)$$

where Δp is the pressure difference in the gas, ρ is the density of the gas and u is the gas velocity.

3 Literature on mechanistic models for heat transfer and pressure drop in staggered tube bundles with fins

Developing correlations for the heat transfer and pressure drop performance of tube banks has been an area of special interest since the middle of the last century (Nir, 1991). Grimison (1937) established one of the first correlations for banks of bare tubes in 1937. The geometry of tube bundle arrangement and the addition of fins have since been taken into account by many researchers. Prediction models for heat transfer and pressure drop in staggered, finned tube bundles based on experimental data is the focus of the work presented in this literature review.

3.1 PFR Report, 1976: Heat transfer and pressure drop characteristics of dry tower extended surfaces

In 1976, PFR Engineering Systems, Inc. released their report on heat transfer and pressure drop in extended surface heat exchangers. The report is a compilation and analysis of data from collected literature on finned tube, crossflow heat exchangers. The data was analysed to determine the effects of geometric configurations on the heat transfer and pressure drop characteristics of finned tube bundles. From this analysis, correlations for heat transfer and pressure drop were developed.

Experimental data for three basic configurations of extended surfaces was analyzed:

- (a) Round tube, helical round smooth fins
- (b) Round tube, helical round serrated fins
- (c) Round tube, continuous plate smooth fins

The data used was from tests by several investigators, where tube and fin geometries had been varied. The variables taken into consideration were among others tube and fin diameters, fin height and number of fins per unit length. Differences in fin attachment method was not considered. This was found to not have a significant impact on the results. Some of the reported data on heat transfer came in the form of an apparent heat transfer coefficient, which included the fin conduction resistance. This was converted to a consistent convective heat transfer coefficient, by application of the fin effectiveness concept.

Fin variables such as fin height, spacing and thickness determine the surface area of the finned tubes and flow behaviour in the bundle, and influence the heat transfer and pressure drop. The analyses of Briggs and Young (1963) and

Kuntysh and Iokhvedov (1971) found that the ratio of fin height to fin pitch, $\frac{h_f}{p_f}$ is a dominant variable affecting both heat transfer and pressure drop. The influence of the bundle layout on heat transfer and pressure drop was also studied, and the conclusion was that the tube pitch has no evident influence on heat transfer, but a strong effect on pressure drop.

Ultimately the geometric variables found to affect the performance were lumped in dimensionless form and regression analysis of the data was performed to produce correlations. For staggered tube bundles with helically finned round tubes, the heat transfer was found to be best expressed using the area ratio, A_r . A_r contains the most important fin variables: fin height, fin frequency, fin thickness, and for serrated fins, segment width and height (see section 2.1 for definition of A_r). The general correlation form for heat transfer used was

$$j = CRe^{-m}A_r^{-n} \quad (20)$$

where C is a constant. Regression analysis yielded values for the constant and the exponents. For plain fins, the heat transfer j -factor correlation is

$$j = 0.29Re^{-0.367}A_r^{-0.17} \quad (21)$$

The correlation was found to predict 80 % of the data within ± 10 % and 95 % of the data within ± 18 %. For serrated fins, the same correlation was found to be

$$j = 0.195Re^{-0.3}A_r^{-0.17} \quad (22)$$

This predicted 80 % of the data within ± 15 % and 95 % of the data within ± 20 %.

The correlation for pressure drop in staggered tube bundles with helically finned round tubes was best described as a function of both tube pitch and fin and tube variables. The pressure drop was found to have a less simple dependency on Re than the heat transfer. Furthermore, it was determined that the hydraulic diameter was a more suitable length scale than the base tube diameter. The friction factor $F = Eu$ for plain fins is given by

$$F = (150Re_h^{-1} + 1.8Re_h^{-0.2})\left(\frac{P_L}{d_h}\right)^{0.35} \quad (23)$$

for $\frac{P_L}{d_h} > 4.0$ and

$$F = 13.6Re_h^{-0.3}\left(\frac{P_L}{d_h}\right)^{-0.42} \quad (24)$$

for $\frac{P_L}{d_h} \leq 4.0$

Here, Re_h is based on the hydraulic diameter d_h , given by

$$d_h = 4((N_r - 1)P_L + D) \frac{A_c}{A_t} \quad (25)$$

where N_r is the number of tube rows, P_L is the longitudinal tube pitch, D is the fin diameter, $A_c = A_{min}$ is the minimum flow area and $A_t = A_{ht}$ is the total surface (heat transfer area). See section 2.1 for definitions of A_{min} and A_{ht} . For serrated fins, the pressure drop correlation is simply the correlation for plain fins multiplied with a factor of 1.4.

3.2 A. Nir, 1991: Heat transfer and friction factor correlations for crossflow over staggered tube banks

In his 1991 paper, Nir presents the theoretical background to the description of flow across finned tube bundles, and establishes a flow model on the basis of similarity with heat transfer in channels. Kays and London (1955) described pressure drop and heat transfer in channels as functions of characteristic length and hydraulic diameter as such

$$StPr^{2/3} = f_1(Re_h, \frac{L}{d_h}) \quad (26)$$

$$f = f_2(Re_h, \frac{L}{d_h}) \quad (27)$$

where L is the characteristic length and the hydraulic diameter is defined

$$d_h = \frac{4L}{W} \quad (28)$$

W is here the ratio of heat transfer area of a row of tubes to free flow area:

$$W = \frac{A_t}{A_{0,t}} = \frac{4L}{d_h} \quad (29)$$

for all fin and tube geometries. The friction factor f equals the Euler number divided by the ratio W , so that $Eu = Wf$.

When analysing the flow distribution across a bundle of tubes, three major factors influencing the pressure drop and heat transfer performance were identified:

1. Flow passing through the space between the fins. The length of the flow path is proportional to the fin diameter. The equivalent hydraulic diameter, assuming $L = D$ is then given by

$$d_h = \frac{4D}{W} \quad (30)$$

2. Flow bypassing the tubes through the gap between the fin tips. See figure 11 for illustration of tube pitch ranges.

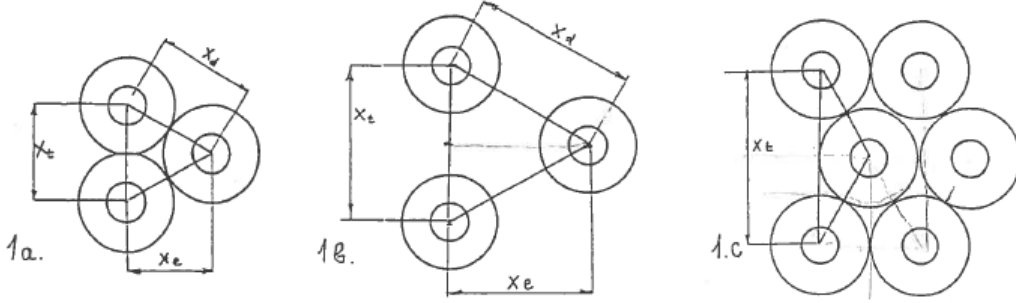


Figure 11: Tube layout in staggered tube banks: a. $X_t/D = 1, R_b = 1, R_d = 2$; b. $X_t/D > 1, R_b > 1, R_d = 2$; c. $X_t/D = 0.5, R_b < 1$ (Nir, 1991)

Here, $X_t = P_T$, $X_l = P_L$ and $X_d = P_D$ are the transversal, longitudinal and diagonal tube pitch, respectively. The parameter describing the effect of flow bypass on the heat transfer process is the ratio

$$R_b = \frac{A_{0,f}}{A_{0,t}} \quad (31)$$

The larger the ratio R_b is, the less influence the tubes have on each other. A large R_b means the tube bundle will behave more like individual finned tubes in crossflow. Here, $A_{0,t}$ is the free flow area at the face of the tube per unit length for a tube bundle where $X_t/D = 1$, meaning no clearance between the fin tips. It is defined as

$$A_{0,t} = (D - d)(1 - t_f n_f) \quad (32)$$

where t_f is the fin thickness, d is the tube diameter and n_f is number of fins per unit length. The ratio of free flow area at the face to the face area for this bundle arrangement is

$$R_t = \frac{A_{0,t}}{D} = \left(1 - \frac{d}{D}\right)(1 - t_f n_f) \quad (33)$$

$A_{0,f}$ is the frontal free flow area of one tube per unit length for any tube bundle where $X_t/D > 1$:

$$A_{0,f} = X_t - D + A_{0,t} \quad (34)$$

The ratio of free flow at the face area to face area is then

$$R_f = \frac{A_{0,f}}{X_t} = 1 - \left(\frac{D}{X_t}\right)(1 - R_t) \quad (35)$$

3. Irregular velocity and temperature fields when flow passes a tube row. The ratio of the diagonal and frontal free flow areas is given by

$$R_d = \frac{A_{0,d}}{A_{0,f}} = \frac{2(X_d - D + A_{0,t})}{(X_t - D + A_{0,t})} \quad (36)$$

where the diagonal tube pitch is defined as

$$X_d = \sqrt{0,25X_t^2 + X_l^2} \quad (37)$$

The dimensionless form of R_d is

$$R_d = \frac{2(\sqrt{0,25(X_t/D)^2 - (X_l/D)^2} - 1 + R_t)}{X_t/D - 1 + R_t} \quad (38)$$

For equilateral triangular pitch tube bundles, $R_d = 2$. Increasing R_d decreases the influence of the tube rows on each other, and a multirow tube bank will behave more like a series of one-row tube banks.

Using these dimensionless groups, Nir formulated the heat transfer and friction factor correlations:

$$StPr^{2/3} = ARe_h^{n1}W^{n2}R_b^{n3}R_d^{n4} \quad (39)$$

$$f = BRe_h^{m1}W^{m2}R_b^{m3}R_d^{m4} \quad (40)$$

where, A and B are constants, and, for individually finned tubes,

$$W = \frac{A_t}{X_t R_f} = \frac{A_t}{A_{0,f}} \quad (41)$$

To find the constant A and the exponents, a databank consisting of data from 16 published sources was analysed. A heat transfer correlation was produced, found to be valid for $Re_h = 300 - 10000$, $W = 10 - 60$, $R_t = 1.0 - 3.0$ and $R_f = 1.0 - 4.6$ for bundles with more than one tube row:

$$StPr^{2/3} = 1.745Re_h^{-0.4}W^{-2/3}R_b^{-0.4}K_{z,h} \quad (42)$$

where $K_{z,h}$ is a correction factor for tube banks with less than four tube rows. Its value was found to be 0.95 for bundles with three tube rows and 0.90 for bundles with two tube rows.

When it comes to the pressure drop, the existing data was insufficient in order to estimate the value of the Reynolds number exponent m_1 . An average value

of -0.25 was found to be a good compromise for most data in the range $300 < Re_h < 10000$. The friction factor dependency on W was found to be represented by an exponent value of -0.8 . It is not dependent on R_b , and only dependent on R_d when this ratio has a value equal to or less than 1.3:

$$f = 3.0Re_h^{-0.25}W^{-0.8}K_{z,p} \quad (43)$$

where the correction factor $K_{z,p}$ represents the dependency on the tube spacing. For $R_d > 1.3$ its value is 1. For values between 1 and 1.3, it can be estimated by

$$K_{z,p} = 2.08 - 0.83R_d \quad (44)$$

For tubes with serrated fins, the friction factor correlation is

$$f = 1.75Re_h^{-0.25}W^{-0.57}K_{z,p} \quad (45)$$

The correlations can be rewritten using the fin diameter D as the characteristic length. The heat transfer of tube bundles with plain and segmented fins is then

$$StPr^{2/3} = 1.0Re_D^{-0.4}W^{-0.266}Re_b^{-0.4}K_{z,h} \quad (46)$$

The friction factor becomes

$$f = 2.12Re_D^{-0.25}W^{-0.55}K_{z,p} \quad (47)$$

or

$$f = 1.24Re_D^{-0.25}W^{-0.32}K_{z,p} \quad (48)$$

for plain and segmented fins, respectively.

The same correlations using the tube diameter d as the characteristic length are

$$StPr^{2/3} = 1.0Re_d^{-0.4}W^{-0.266}R_b^{-0.4}\left(\frac{D}{d}\right)^{-0.4}K_{z,h} \quad (49)$$

(where $Re_d = Re_{max}$) for the heat transfer and

$$f = 2.12Re_d^{-0.25}W^{-0.55}\left(\frac{D}{d}\right)^{-0.25}K_{z,p} \quad (50)$$

or

$$f = 1.24Re_d^{-0.25}W^{-0.32}\left(\frac{D}{d}\right)^{-0.25}K_{z,p} \quad (51)$$

for the pressure drop for plain and segmented fins, respectively.

3.3 J. A. R. Henry, 1994: Effect of fin frequency and tube pitch on bundle pressure loss

Up until this point, few of the studies on pressure drop and heat transfer characteristics of bundles have involved systematic variation of the bundle geometry. In his 1994 paper, Henry presents data on the testing of pressure loss on staggered tube bundles with helically wound solid fins with the goal of providing insight into the interactions between the geometry parameters. Interdependencies were examined by changing one parameter of the bundle's geometry at a time. The results make up the basis of a pressure loss prediction model. The test section consisted of six longitudinal by two transversal rows of staggered tubes. See figure 12

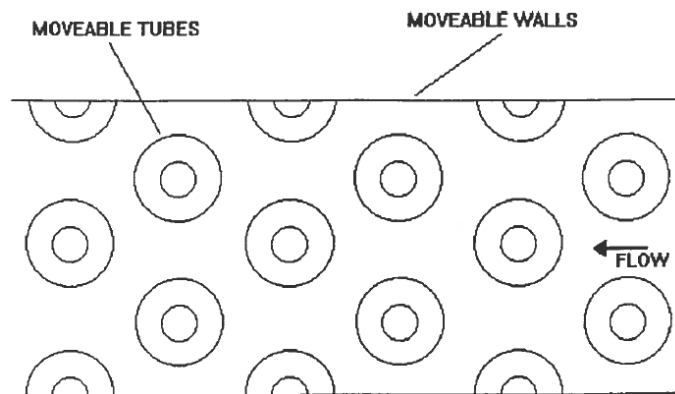


Figure 12: Test section (Henry, 1994)

The transverse pitch of the bundle, P_T was varied, while the longitudinal pitch, P_L , was held constant. See figure 13. As a limiting case, the most closely packed arrangement, where the fin tips are touching, represents the maximum possible pressure loss.

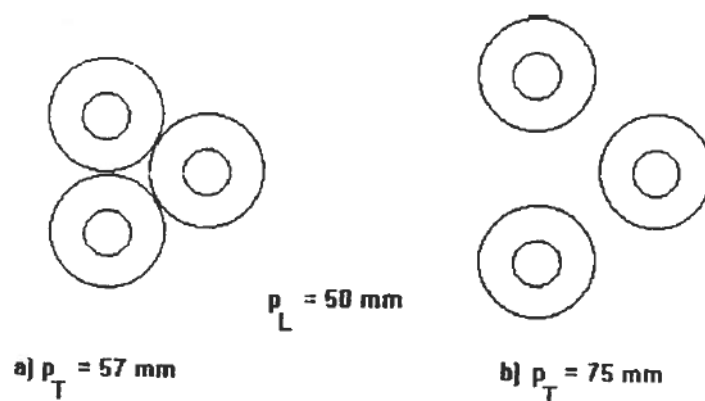


Figure 13: Range of pitches (Henry, 1994)

The results showed that for the closely packed arrangement, pressure head is proportional to the face velocity raised to the power of 1.7. Increasing the transverse pitch decreases the pressure loss across the bundle, because the pressure loss between the fins is reduced when the gap between the fins, $G_T = P_T - D$ is increased. This reduction in pressure loss is much greater for the bundle with higher fin frequency. See figure 14.

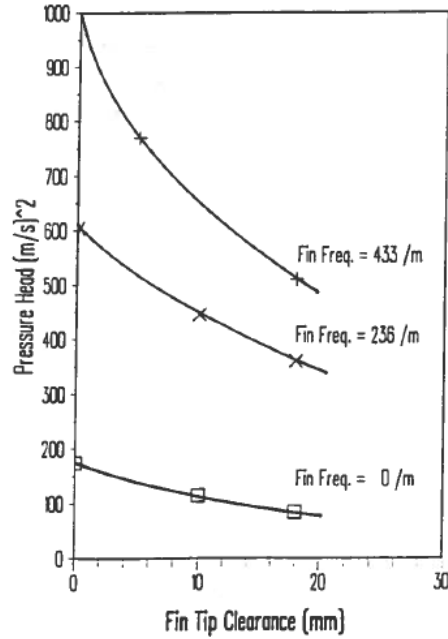


Figure 14: Effect of transverse pitch on pressure drop (Henry, 1994)

From the test results, a prediction model was formulated. The measured pressure loss over finned tube bundles was found to extrapolate approximately linearly back to values for unfinned tube bundles calculated using HTFS Handbook Sheet SM3. This would suggest that, for the limiting case of zero gap between fin tips, the overall pressure loss can be regarded as the sum of form drag of the base tube and skin drag of the fins. The bundle head loss can thus be expressed as

$$H_B = H_P + H_F \quad (52)$$

where H_P is the form drag contribution and H_F is the fin skin drag contribution. The calculation method for H_P is given in Handbook Sheet SM3. H_F was found to have the correlation

$$H_F = \frac{1.126}{Re_0^{0.3}} \phi \sigma^{0.5} \frac{u_0^2}{2} \quad (53)$$

where the Reynolds number is

$$Re_0 = \frac{\rho u_0 d}{\mu} \quad (54)$$

The parameter ϕ is the ratio of total fin surface area per unit approach area, and is given by

$$\phi = \frac{\pi(D^2 - d^2)n_f N_r}{2D} \quad (55)$$

where d is the base tube diameter, D is the fin diameter, n_f is the fin frequency and N_r is the number of rows in flow direction. The parameter σ is the flow area ratio, and is given by

$$\sigma = \frac{S_0}{S_{min}} = \frac{D}{D - B} \quad (56)$$

where $S_0 = A_0 l_t$ is the face area of the tube bundle and $S_{min} = A_{min} l_t$ is the minimum flow area. See section 2.3 for definitions of A_0 and A_{min} . B is the blockage per unit length, given by

$$B = d + n_f t_f (D - d) \quad (57)$$

As mentioned in section 2.3, when there is bypass flow - flow passing through the gap between the fin tips - the velocity of the approach air stream, u_0 , can be expressed as having two components: the velocity of air passing over/around/between the fins, u_F , and the velocity of air passing through the bypass path, u_G . See figure 15. These velocities can be related by the equation

$$u_0 P_T = u_F D + u_G (P_T - D) \quad (58)$$

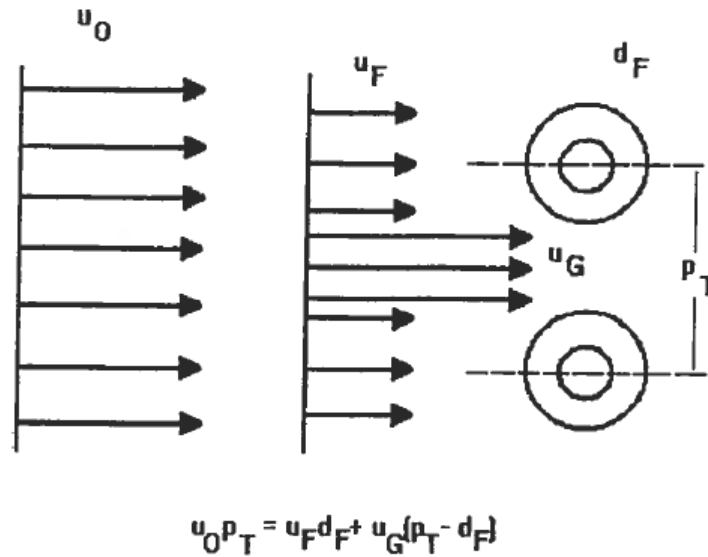


Figure 15: Velocities in bypass flow model (Henry, 1994)

The effect of bypass manifests itself as a reduction in pressure drop (compared to no bypass). This reduced pressure drop can be interpreted in terms of a reduced face velocity. Examination of the data showed that the relation between u_F and u_0 can be expressed as

$$u_F = \frac{P_T}{D - R(P_T - D)} u_0 = \kappa u_0 \quad (59)$$

where R is a function of the fin frequency. When there is no gap between the fin tips, $u_f = u_0$. The overall pressure loss for the bundle can now be calculated from

$$H_B = (F_P + F_F) \frac{u_0^2}{2} \quad (60)$$

Here, F_P is the friction factor for the base tube form drag, given by

$$F_P = C \frac{l_P}{d} \quad (61)$$

where l_P is the overall bundle length and the calculation method for C is found in the HTFS Handbook. F_F is the friction factor for the fin skin drag, given by

$$F_F = \frac{1.126}{Re^{0.3}} \phi \sigma^{0.5} \kappa^{1.7} \quad (62)$$

In this model, the parameter ϕ allows for the skin drag of the fins, σ allows for the blockage caused by the fins and base tube and κ allows for bypass.

The prediction model was shown to be in good agreement with the measured data. Henry proposed further work to extend the model to other geometries and to use a similar approach to model heat transfer.

3.4 Ralston et. al, 1997: HTFS models for heat transfer and pressure drop applied to staggered arrangements of tubes with plain helical fins

Ralston et al. build on the work of Henry to develop mechanistic models for predicting pressure drop and heat transfer performance of staggered tube bundles with plain helical fins. Using the HTFS databank for finned tubes, empirical correlations were derived, and the models refined.

The model for pressure drop was based on Henry's model and the data in the HTFS databank. The pressure head loss for a staggered bundle of tubes with plain helical fins is here calculated by

$$\frac{\Delta p}{\rho} = 1.3K_B u_0^{1.7} \quad (63)$$

where K_B is the bundle loss coefficient for a bundle with bypass between fin tips, given by

$$K_B = \frac{K_{ft}}{\left(\frac{D}{P_T} + \left(\frac{K_{ft}}{K_{gap}}\right)^{\frac{1}{1.7}} \left(1 - \frac{D}{P_T}\right)\right)^{1.7}} \quad (64)$$

The bundle loss consists of base tube, fin and gap contributions. For the special case of zero bypass between fin tips (fin tips touching) the bundle loss is the sum of a bare tube and a fin contribution as follows:

$$K_B = K_{ft} = K_{tube} + K_{fins} \quad (65)$$

The bare tube bundle loss coefficient is calculated from the standard HTFS method in Handbook Sheet SM3:

$$K_{tube} = \frac{4.75}{\left(\frac{P_T}{d} - 1\right)^{1.86}} \frac{N_r P_L}{d^{1.3}} \left(\frac{\mu}{\rho}\right)^{0.3} \quad (66)$$

The fin loss coefficient is given by

$$K_{fins} = 0.0265\phi\sigma^{1.7} \quad (67)$$

where

$$\phi = \frac{\pi(D^2 - d^2)n_f N_r}{2D} \quad (68)$$

$$\sigma = \frac{D}{D - B} \quad (69)$$

and

$$B = d + n_{ft} f_f (D - d) \quad (70)$$

An empirical equation for gap loss coefficient, dependent on fin tip clearance, was found from the data:

$$K_{gap} = (N_r - 1)(1 - 0.65 \tanh(28(P_T - D))) \quad (71)$$

When it comes to prediction of heat transfer, a purely empirical approach was taken to produce a model. Out of the two flow paths postulated by the HTFS pressure drop model (fin flow and bypass flow), only the flow over the fin and tube surface is assumed to be associated with heat transfer. The bypass flow is neglected, and the heat transfer process is characterized by the fin velocity. The model starts out by balancing pressure loss over a bundle as follows:

$$K_B u_0^{1.7} = K_{ft} u_f^{1.7} = K_{gap} u_g^{1.7} \quad (72)$$

The fin velocity can then be explicitly expressed as

$$u_f = \left(\frac{K_B}{K_{ft}} \right)^{\frac{1}{1.7}} u_0 \quad (73)$$

The Reynolds number based on fin velocity and diameter of base tube is then given by

$$Re_f = \frac{\rho u_f d}{\eta} \quad (74)$$

The HTFS j-factor correlation for plain fins derived from the benchmark data is found to be

$$j_p = 0.215 Re_f^{-0.405} A_r^{-0.088} \quad (75)$$

where A_r is the ratio of the total extended surface to the area of the base tube, calculated by

$$A_r = 1 + 2n_f h_f \left(1 + \frac{h_f + t_f}{d} \right) \quad (76)$$

for a solid finned tube. Here h_f is the fin height, given by

$$h_f = 0.5(D - d) \quad (77)$$

When testing the prediction models against HTFS finned tube databank, it was found that Ralston et al.'s pressure drop model performed better than the previous model (Henry, 1994), while the heat transfer model performed marginally worse. The recommendation was to use the new pressure drop model in the HTFS computer programs and Handbook, while further developing the heat transfer model.

3.5 Chu and Ralston, 1998: HTFS2: Improved models for heat transfer and pressure drop applied to staggered arrangements of tubes with plain helical fins

Two main shortcomings in Ralston et al.'s HTFS methods were identified: The pressure drop model needed improvement for larger diameter tubes used for heat recovery applications and the heat transfer model proved less effective than current empirical correlations. The work to improve the HTFS methods resulted in new model formulations designated HTFS2. The modified equations from Ralston et al. are as follows:

Pressure head loss for a staggered bundle of helically finned tubes is calculated from

$$\frac{\Delta p}{\rho} = 0.024 K_{ft} u_0^{1.7} \quad (78)$$

where K_{ft} is the sum of the base tube and fin contribution as in Ralston et al. The fin loss coefficient is here given by

$$K_{fins} = 21.87 \phi^{(0.44+1.41\beta)} \sigma^{1.7} \quad (79)$$

where the exponent β allows for the influence of fin tip clearance on pressure loss and is defined as follows:

$$\beta = \frac{(P_T - D) l_t N_t}{S_{min}} = \frac{(P_T - D) N_t}{A_{min}} \quad (80)$$

where N_t is the number of tubes per row, l_t is the tube length and S_{min} is the minimum flow area. The gap loss coefficient was found to have the non-dimensional formulation

$$K_{gap} = (N_r - 1) (1 - 9.72 \tanh(-0.79\beta)) \left(\frac{\phi}{N_r}\right)^{0.31} \quad (81)$$

As for the heat transfer, the updated correlation is now defined as

$$j = 0.22 Re_f^{0.04} Re_{max}^{-0.368} A_r^{-0.15} \quad (82)$$

where Re_{max} is the Reynolds number based on the minimum flow area. One significant change in the methods from Ralston et al. lies in the reduced influence of Re_f . Both the pressure drop model and the heat transfer model were found to be superior to the available correlations at the time and the HTFS2 methods were recommended for inclusion in the HTFS computer programs and Handbook.

3.6 S. R. McIlwain, 2003: Improved prediction methods for finned tube bundle heat exchangers in crossflow

The HTFS2 models were found, according to McIlwain, to underpredict pressure drop for deep bundles - bundles with a large number of tube rows. He conducted a parametric study to compare the predictions of the HTFS1 method (Ralston et al., 1997), the HTFS2 method (Chu & Ralston, 1998) and the PFR method for a typical air-cooler bundle. Figures 16, 17 and 18 show the characteristics of pressure drop for increasing fin gap, for the three methods.

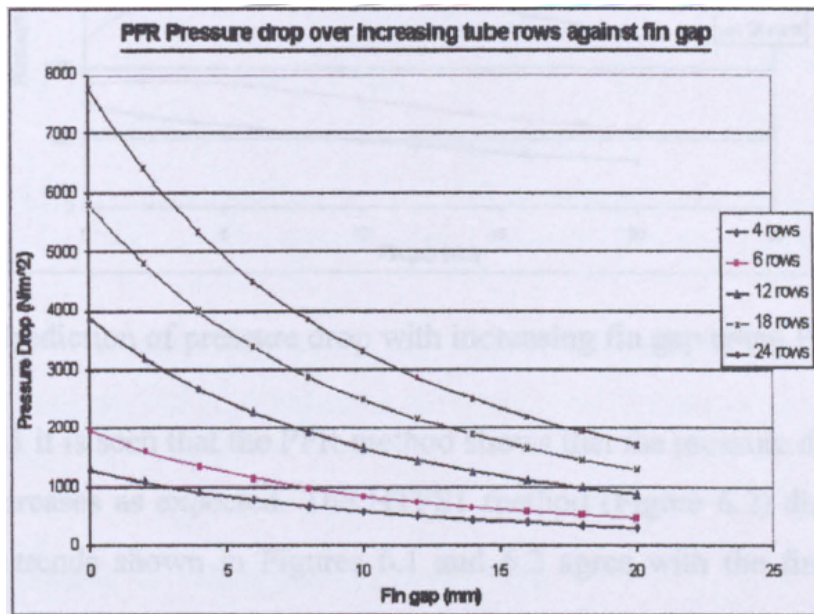


Figure 16: Pressure drop, PFR (McIlwain, 2003)

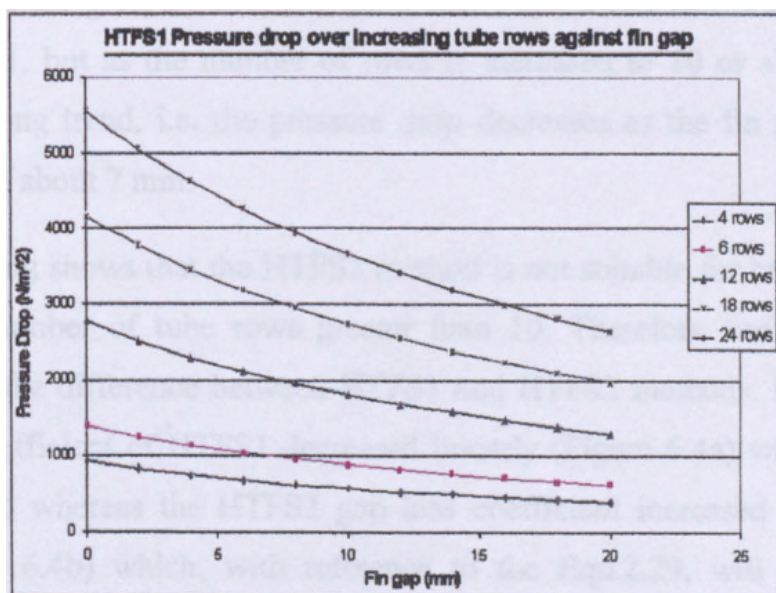


Figure 17: Pressure drop, HTFS1 (McIlwain, 2003)

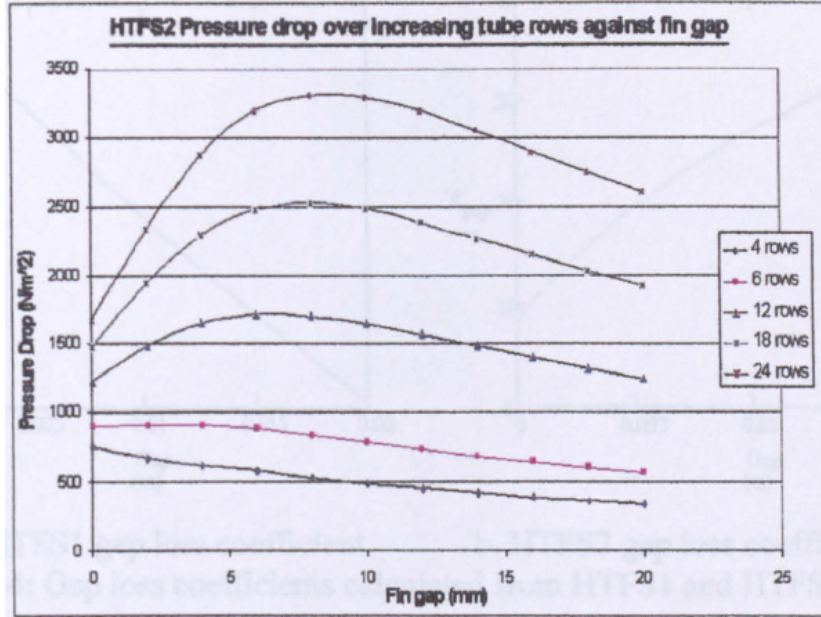


Figure 18: Pressure drop, HTFS2 (McIlwain, 2003)

The results show that while the PFR and HTFS1 methods predict increased pressure drop for decreased fin gaps all around, the HTFS2 method predicts a pressure drop *decrease* as the fin gap is reduced below about 7 mm for bundles of 10 tube rows or more. This trend is not plausible, and the HTFS2 method was therefore deemed unsuitable for bundles with small fin gaps and large number of tube rows. The culprit behind this behavior was found to be the gap loss coefficient, which in HTFS1s case decreases linearly with increasing gap while it increases logarithmically in the HTFS2 method.

McIlwain carried out a CFD analysis of staggered bundles that proved the previous method basis to be inaccurate. Instead of the premise of the flow splitting into two distinct regions; flow through the gaps between fins and flow over/around/between the fins, he found that there is a boundary layer around the fin surface and top of tube, and a higher speed "core" flow between the fins. The new model is thus based on the newly identified regions; extended gap and fin flow. See figure 19.

McIlwain decided on using the pressure drop coefficients for the bare tube and fins as those used in Ralston et al.'s HTFS1 model:

$$K_{tube} = \frac{4.75}{\left(\frac{P_T}{d} - 1\right)^{1.86}} \frac{N_r P_L}{d^{1.3}} \left(\frac{\mu}{\rho}\right)^{0.3} \quad (83)$$

$$K_{fins} = 0.0265 \phi \sigma^{1.7} \quad (84)$$

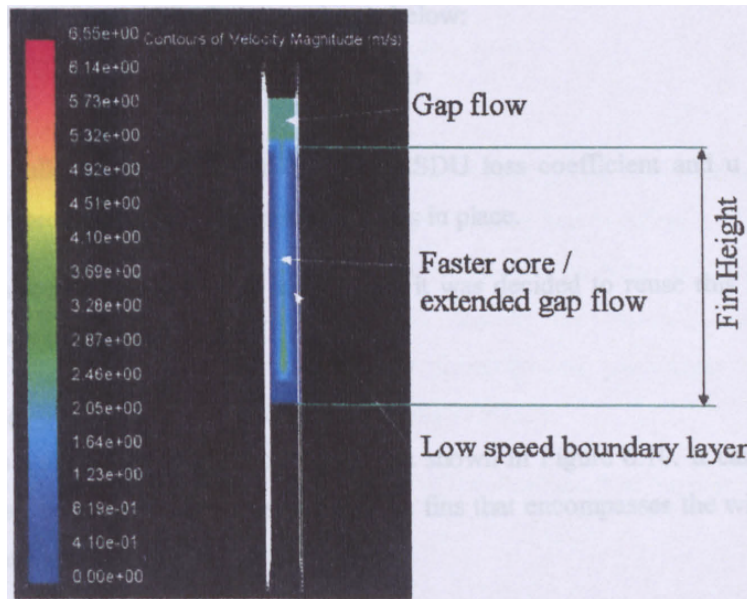


Figure 19: Velocity contours (McIlwain, 2003)

For the gap loss, on the other hand, McIlwain developed a new coefficient based on three parameters of influence:

1. Number of gaps in between tube rows
2. Ratio of effective diagonal gap to transverse gap
3. Pitch angle between tube centres in adjacent rows

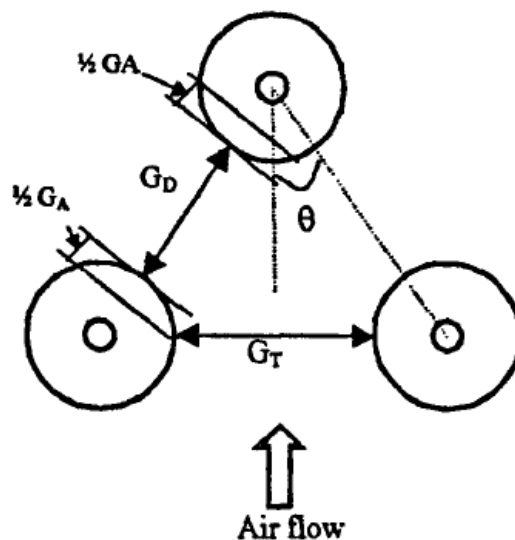


Figure 20: Geometric parameters (McIlwain, 2003)

The number of tube gaps is given by

$$N_g = (N_r - 1) \quad (85)$$

where N_r is the number of tube rows. The effective gap ratio is expressed by three terms; the diagonal gap G_D , the transverse gap G_T and a diagonal gap correction term G_A :

$$GR_{eff} = \frac{G_D + G_A}{G_T} \quad (86)$$

where

$$G_D = \sqrt{P_L^2 + (0.5P_T)^2} - D \quad (87)$$

$$G_T = P_T - D \quad (88)$$

and

$$G_A = 0.5(D - d) \quad (89)$$

The pitch angle θ is given by Henry (1993) as

$$\theta = \tan^{-1}\left(\frac{0.5P_T}{P_L}\right) \frac{\pi}{180} \quad (90)$$

Altogether, the new gap loss coefficient is expressed as

$$K_{gap} = N_g \theta \cdot GR_{eff} \quad (91)$$

The overall bundle loss coefficient retains the formulation of HTFS1:

$$K_B = \frac{K_{ft}}{\left(\frac{D}{P_T} + \left(\frac{K_{ft}}{K_{gap}}\right)^{\frac{1}{1.7}} \left(1 - \frac{D}{P_T}\right)\right)^{1.7}} \quad (92)$$

Comparing the model components against the data, McIlwain came up with the pressure drop correlation

$$\frac{\Delta p}{\rho} = 1.081 K_B u_0^{1.7} \quad (93)$$

This model gives a constant pressure drop per tube row, and can thus be used reliably for deep bundles.

For the heat transfer, McIlwain based his model on Henry's (1994) definition of fin velocity and Ralston et al.'s (1997) definition of fin Reynolds number. Using multivariate regression on HTFS test data, the following j-factor correlation was produced:

$$j = 0.205 Re_f^{0.04} Re_{max}^{-0.368} A_r^{-0.15} \quad (94)$$

The new method was found to present a generally improved prediction and was released by the HTFS as the HTFS3 method and implemented in the HTFS computer programs.

3.7 Discussion

The reviewed models differ in their use of flow models as basis for prediction correlations for pressure drop and heat transfer. PFR is the simplest model, with a heat transfer correlation based only on Reynolds number and the heat transfer area. The PFR pressure drop correlation takes the flow area into consideration as it is included in the hydraulic diameter. Nir's model considers bypass and irregular velocity fields by including the flow area ratios R_b and R_d in both the heat transfer and pressure drop correlation. Ralston et. al's HTFS1 model and the improved HTFS2 model by Chu and Ralston introduce pressure loss coefficients for tube surface, fin and gap flow based on Henry's flow velocity model to the pressure drop correlation, while their heat transfer correlation only includes Re and A_r . McIlwain developed a new gap loss coefficient based on layout parameters for his HTFS3 model. The HTFS1, HTFS2 and HTFS3 correlations include the kinematic viscosity of the gas, and are therefore dependent on temperature. Only PFR and Nir have specified correlations for serrated fin tubes. The prediction models are also based on varying, and, to some extent, insufficient experimental data. Applying the five models to the same set of geometries and flow conditions, and comparing the calculated values with measured values, will help uncover their strengths and weaknesses.

4 Model application and improvement

4.1 Presentation of database

The data used for the application of the prediction models comes from two databases - one for solid finned tube bundles and one for serrated finned tube bundles. The serrated fin database was first built by Stud. Techn. Terje Kaspersen in 1995 as a part of his thesis (Kaspersen, 1995). He gathered published experimental data for heat transfer and pressure drop in serrated finned tube bundles and developed the structure of the database. Since then, the serrated fin database has been updated to include recent findings, and a similar database for solid fins has been developed.

The databases have columns detailing geometric parameters for the tubes and bundles, flow parameters (Re) and measured values for heat transfer ($NuPr^{-1/3}$) and pressure drop (Eu) pertaining to experiments done by several investigators. The geometric parameters of the tested tube bundles as well as the Reynolds number are fed into the five prediction models to produce calculated values for heat transfer and pressure drop. From the solid fin database, 382 measured values for $NuPr^{-1/3}$ and 518 values for Eu are taken into consideration. From the serrated fin database, the same numbers are 465 (455 for HTFS3) and 525 (515 for HTFS3) respectively.

4.2 Assumptions and limitations

Several limitations apply to the use of the measured heat transfer and pressure drop values from the database. First of all, only measurements where $Re < 50000$ are used, since this represents the limit for fully turbulent flow. As a consequence, geometries with no or only one point of measurement for $Re < 50000$ are not considered at all. This includes, for solid fins, Stasiulevicius and Skrinska 1, 2, 3, 4 and 7, and for serrated fins, Worley and Ross 2, 5, 10 and 14.

Some geometries are excluded due to uncertain quality of the measured data. This applies to Brauer 5, 7 and 9 and all of Gianolio and Cuti's geometries. In addition, Schryber 1 and Vampola 1 are not considered for calculation with HTFS3, as these represent cased with no gap between the fin tips of adjacent tubes, i.e. $G_T = 0$.

There is some uncertainty attached to the heat transfer data in that the investigators may have used different correlations for the fin efficiency, some taking uneven heat transfer distribution into account while others not. See section 5.3.

For the three HTFS models, a few assumptions are made. Firstly, seeing as temperature and pressure data for the tests are not available in the database, the kinematic viscosity ν is chosen to have a value of $1.7 \times 10^{-5} \text{ m}^2/\text{s}$ for all geometries and Reynolds numbers. This is an estimation for an average air

temperature of 40°C, and atmospheric pressure. The doubling or halving of this value was found to have negligible effect on $NuPr^{-1/3}$ and respectively give a decrease or increase in Eu of about 17 %. Secondly, the HTFS correlations use a fin Reynolds number Re_f . The fin velocity u_f is defined as $u_f = (\frac{K_B}{K_{ft}})^{1/7} u_0$. This allows for the fin Reynolds number to be calculated as

$$Re_f = \left(\frac{K_B}{K_{ft}}\right)^{1/7} Re_0 \quad (95)$$

The HTFS pressure drop equations are of the form $\frac{\Delta p}{\rho} = AK_B u_0^{1.7}$, where A is a constant. The Euler number correlations are then of the form

$$Eu = \frac{\Delta p}{\frac{1}{2}\rho u_0^2} = \frac{AK_B u_0^{1.7}}{\frac{1}{2}u_0^2} \quad (96)$$

The superficial velocity u_0 is unknown, but can be expressed by the superficial Reynolds number:

$$Re_0 = \frac{u_0 d \rho}{\mu} \implies u_0 = \frac{Re_0 \mu}{d \rho} \quad (97)$$

Introducing this into the equation for Eu :

$$Eu = 2AK_B u_0^{-0.3} = 2AK_B \nu^{-0.3} Re_0^{-0.3} d^{0.3} \quad (98)$$

When it comes to the geometries in the serrated fin database, only Ma's geometries are of the I-foot type, the rest are L-foot, and the fin areas are calculated accordingly. For Kawaguchi, values for segment width w_s are missing. The fin area is here estimated as $A_{fins} = \pi(2dh_f + dt_f)$.

It's also worth mentioning that none of the geometries in the database fulfill the PFR limit value $\frac{P_L}{d_h} > 4$. This means that, in effect, only the PFR friction factor for $\frac{P_L}{d_h} \leq 4$ is tested.

4.3 Model performance: Comparison of measured and predicted values

Comparing the values of $NuPr^{-1/3}$ and Eu taken from the database with the values calculated with the different models gives an indication of which of the correlations are best suited to predict heat transfer and pressure drop in finned tube bundles of different types.

4.3.1 Heat transfer

The comparison of experimental and predicted values for heat transfer shows that the models mostly underpredict $NuPr^{-1/3}$. See figures 21 and 22.

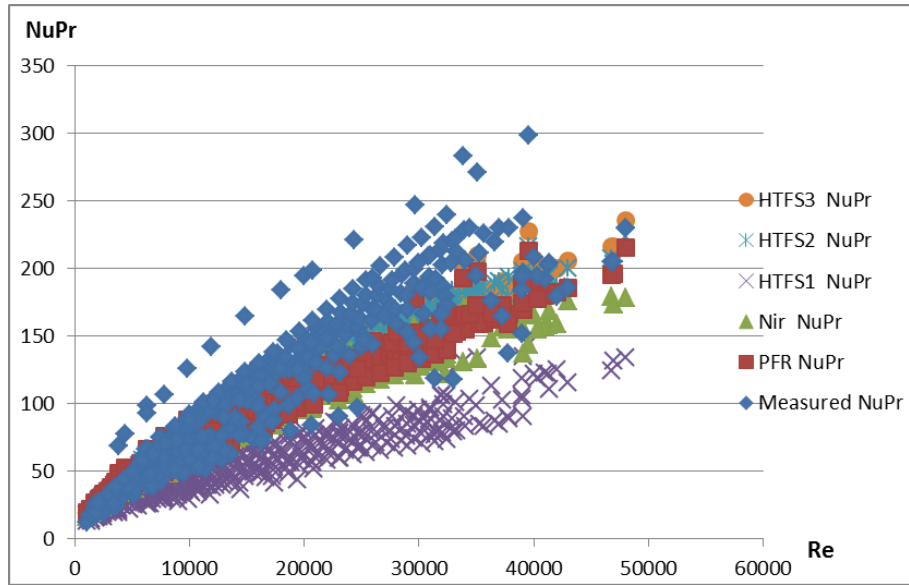


Figure 21: Experimental and predicted values for $NuPr^{-1/3}$ plotted against Reynolds number, solid fins

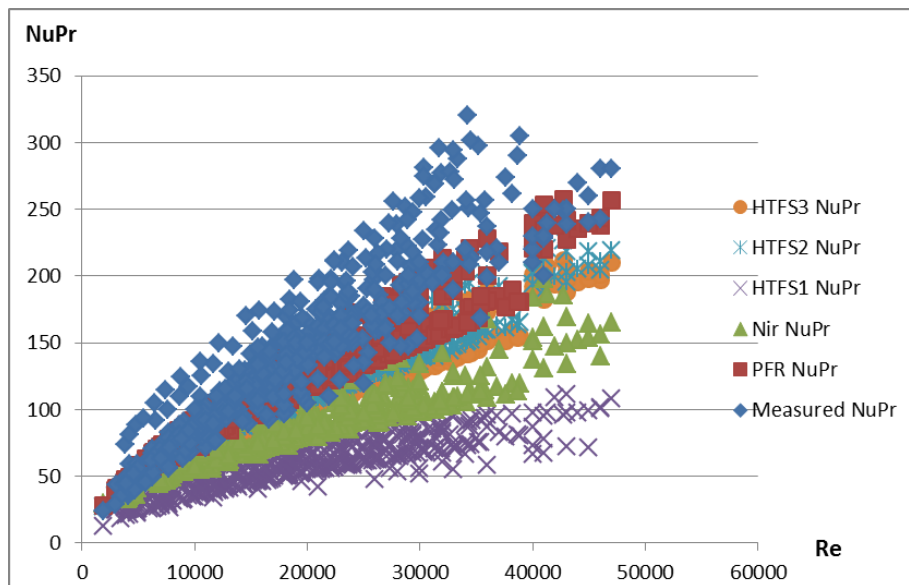


Figure 22: Experimental and predicted values for $NuPr^{-1/3}$ plotted against Reynolds number, serrated fins

A statistic analysis of the values shows that the prediction accuracies for the different models vary significantly. The results are as follows:

For solid fins:

- PFR predicts 61.5 % of the data within ± 20 %, and 27.7 % within ± 10 %. 95 % of the data is predicted within the range -35 % to +40 %
- Nir predicts 69.1 % of the data within ± 20 %, and 27.7 % within ± 10 %. 95 % of the data is predicted within the range -51 % to +30 %
- HTFS1 predicts 7.3 % of the data within ± 20 %, and 4.2 % within ± 10 %. 95 % of the data is predicted within the range -64 % to -5 %
- HTFS2 predicts 68.2 % of the data within ± 20 %, and 36.4 % within ± 10 %. 95 % of the data is predicted within the range -31 % to +43 %
- HTFS3 predicts 69.4 % of the data within ± 20 %, and 35.9 % within ± 10 %. 95 % of the data is predicted within the range -30 % to +45 %

Table 1: Heat transfer prediction accuracy of the five models, solid fins

	Within ± 20 %	Within ± 10 %	95 % of data
PFR	61.5 %	27.7 %	-35 % to +40 %
Nir	69.1 %	27.7 %	-51 % to +30 %
HTFS1	7.3 %	4.2 %	-64 % to -5 %
HTFS2	68.2 %	36.4 %	-31 % to +43 %
HTFS3	69.4 %	35.9 %	-30 % to +45 %

For serrated fins:

- PFR predicts 61.9 % of the data within ± 20 %, and 44.9 % within ± 10 %. 95 % of the data is predicted within the range -43 % to +32 %
- Nir predicts 17.0 % of the data within ± 20 %, and 5.3 % within ± 10 %. 95 % of the data is predicted within the range -62 % to +3 %
- HTFS1 predicts 0.4 % of the data within ± 20 %, and 0 % within ± 10 %. 95 % of the data is predicted within the range -74 % to -30 %
- HTFS2 predicts 52.0 % of the data within ± 20 %, and 17.6 % within ± 10 %. 95 % of the data is predicted within the range -48 % to +14 %
- HTFS3 predicts 42.0 % of the data within ± 20 %, and 11.4 % within ± 10 %. 95 % of the data is predicted within the range -51 % to +11 %

Table 2: Heat transfer prediction accuracy of the five models, serrated fins

	Within $\pm 20\%$	Within $\pm 10\%$	95 % of data
PFR	61.9 %	44.9 %	-43 % to +32 %
Nir	17.0 %	5.3 %	-62 % to +3 %
HTFS1	0.4 %	0 %	-74 % to -30 %
HTFS2	52.0 %	17.6 %	-48 % to +14 %
HTFS3	42.0 %	11.4 %	-51 % to +11 %

The correlations with the best prediction accuracy for heat transfer are HTFS3/HTFS2 and PFR, for solid and serrated fins, respectively. The plots in figures 23 and 24 show the heat transfer prediction accuracy of HTFS3 and PFR. The red line in the plot represents $NuPr_{Pred}^{-1/3} = NuPr_{Exp}^{-1/3}$, and the dashed lines show the $\pm 20\%$ range.

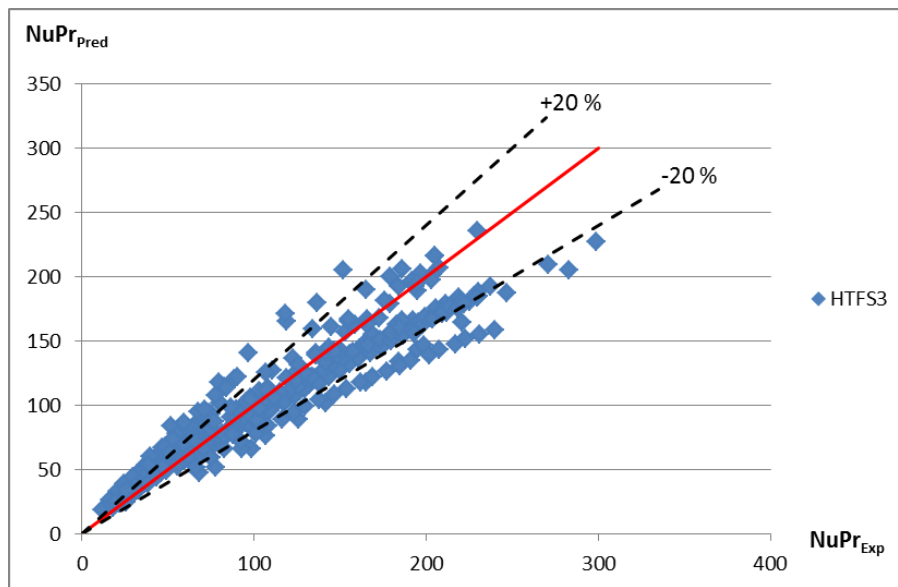


Figure 23: Heat transfer prediction accuracy of HTFS3, solid fins

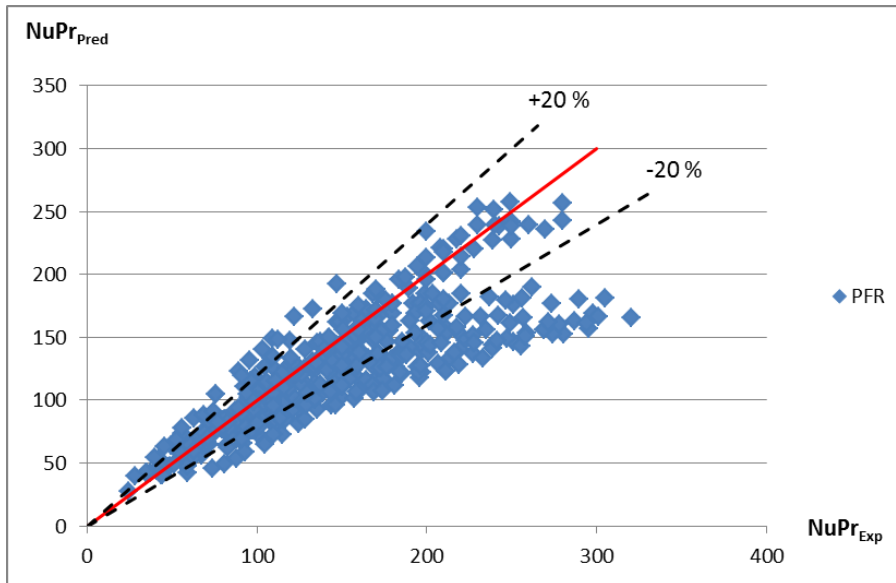


Figure 24: Heat transfer prediction accuracy of PFR, serrated fins

4.3.2 Pressure drop

The comparison of experimental and predicted values for pressure drop shows that the values calculated from HTFS1, HTFS2 and HTFS3 are much more scattered than the measured values, while PFR is less scattered. HTFS1 and HTFS3 severely overpredict Eu , at most giving values 6 times higher than the experimental values for solid fins and 16 times higher for serrated fins. See figures 25, 26, 27 and 28.

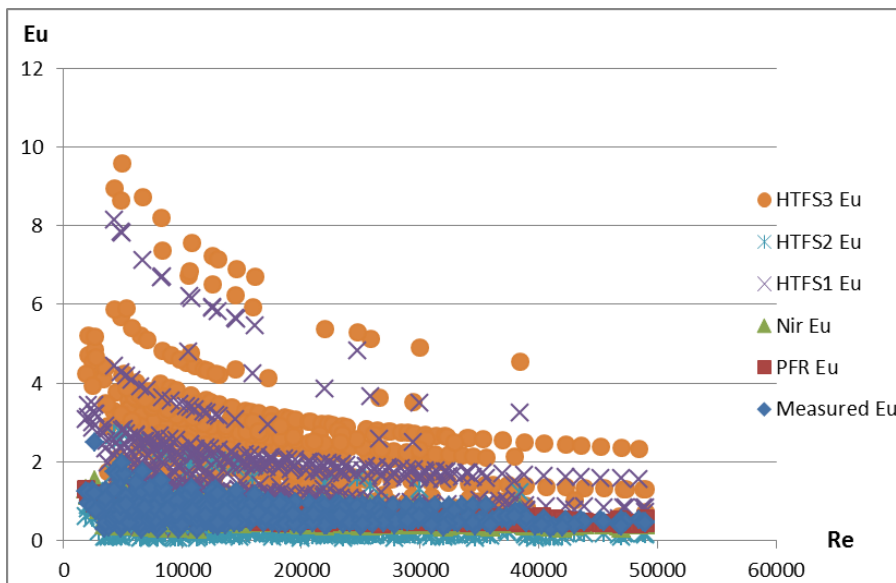


Figure 25: Experimental and predicted values (all models) for Eu plotted against Reynolds number, solid fins

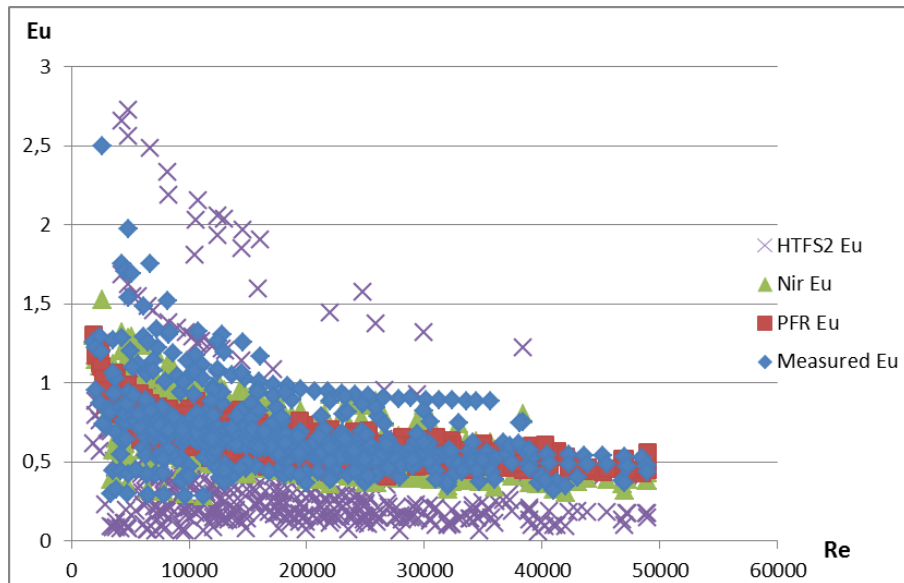


Figure 26: Experimental and predicted values (PFR, Nir and HTFS2) for Eu plotted against Reynolds number, solid fins

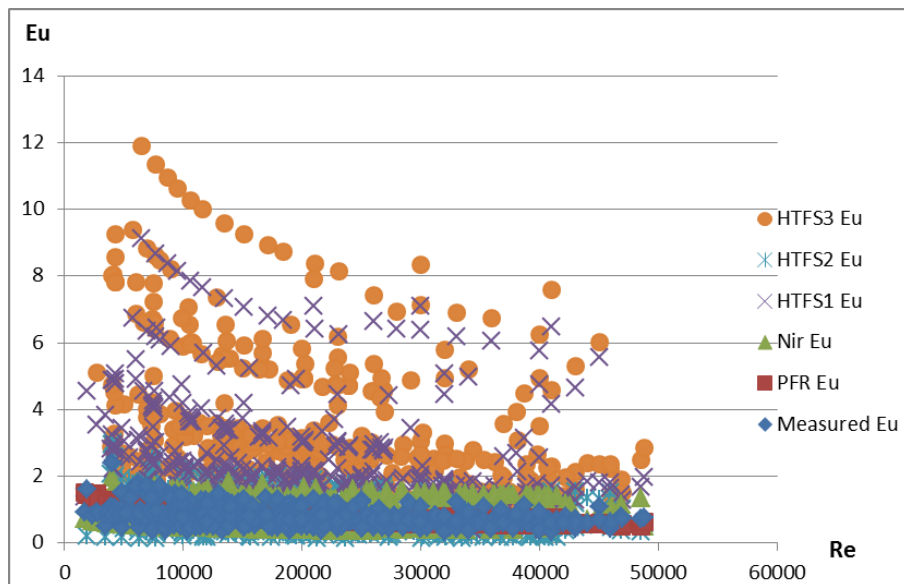


Figure 27: Experimental and predicted values (all models) for Eu plotted against Reynolds number, serrated fins

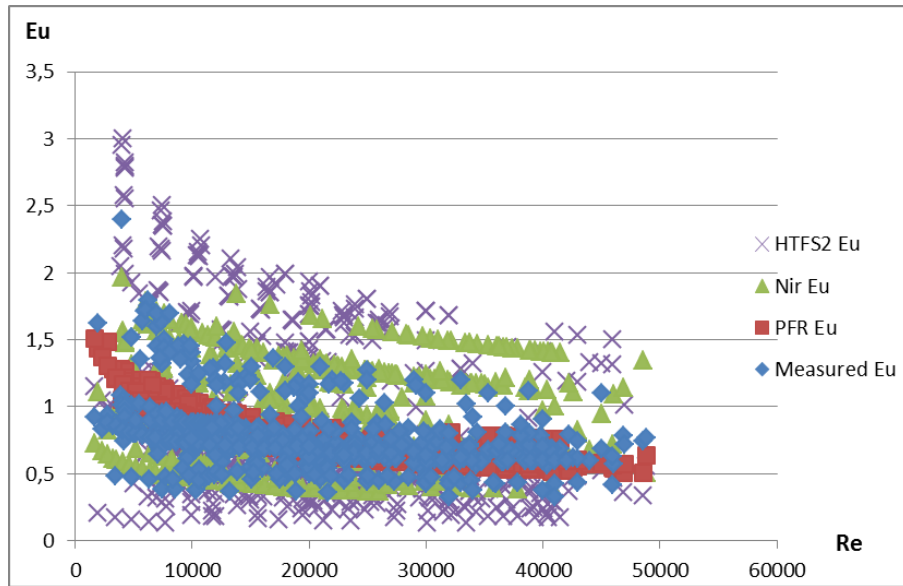


Figure 28: Experimental and predicted values (PFR, Nir and HTFS2) for Eu plotted against Reynolds number, serrated fins

For solid fins:

- PFR predicts 70.5 % of the data within ± 30 %, and 44.8 % within ± 15 %. 95 % of the data is predicted within the range -48 % to +82 %
- Nir predicts 92.7 % of the data within ± 30 %, and 58.5 % within ± 15 %. 95 % of the data is predicted within the range -29 % to +36 %
- HTFS1 predicts 14.7 % of the data within ± 30 %, and 3.9 % within ± 15 %. 95 % of the data is predicted within the range +9 % to +356 %
- HTFS2 predicts 30.7 % of the data within ± 30 %, and 14.1 % within ± 15 %. 95 % of the data is predicted within the range -82 % to +68 %
- HTFS3 predicts 4.4 % of the data within ± 30 %, and 1.9 % within ± 15 %. 95 % of the data is predicted within the range +19 % to +501 %

Table 3: Pressure drop prediction accuracy of the five models, solid fins

	Within ± 30 %	Within ± 15 %	95 % of data
PFR	70.5 %	44.8 %	-48 % to +82
Nir	92.7 %	58.5 %	-29 % to +36 %
HTFS1	14.7 %	3.9 %	+9 % to +356 %
HTFS2	30.7 %	14.1 %	-82 % to +68 %
HTFS3	4.4 %	1.9 %	+19 % to +501 %

For serrated fins:

- PFR predicts 64.6 % of the data within ± 30 %, and 40.2 % within ± 15 %. 95 % of the data is predicted within the range -46 % to +84 %
- Nir predicts 38.7 % of the data within ± 30 %, and 21.1 % within ± 15 %. 95 % of the data is predicted within the range -43 % to +114 %
- HTFS1 predicts 27.8 % of the data within ± 30 %, and 16.6 % within ± 15 %. 95 % of the data is predicted within the range -22 % to +1003 %
- HTFS2 predicts 35.4 % of the data within ± 30 %, and 19.8 % within ± 15 %. 95 % of the data is predicted within the range -78 % to +258 %
- HTFS3 predicts 20.8 % of the data within ± 30 %, and 13.6 % within ± 15 %. 95 % of the data is predicted within the range -13 % to +1288 %

Table 4: Pressure drop prediction accuracy of the five models, serrated fins

	Within ± 30 %	Within ± 15 %	95 % of data
PFR	64.6 %	40.2 %	-46 % to +84 %
Nir	38.7 %	21.1 %	-43 % to +114 %
HTFS1	27.8 %	16.6 %	-22 % to +1003 %
HTFS2	35.4 %	19.8 %	-78 % to +258 %
HTFS3	20.8 %	13.6 %	-13 % to +1288 %

The correlations with the best prediction accuracy for pressure drop are Nir and PFR, for solid and serrated fins, respectively. The plots in figures 29 and 30 show the pressure drop prediction accuracy of Nir and PFR. The red line in the plot represents $Eu_{Pred} = Eu_{Exp}$, and the dashed lines show the ± 30 % range. For plots for all prediction accuracies, see figures 44 through 63 in appendix A.

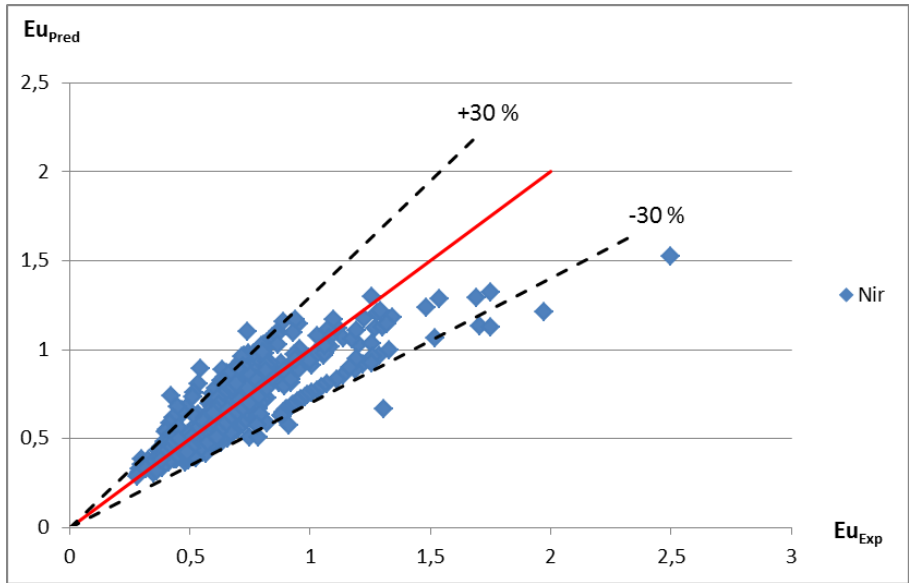


Figure 29: Pressure drop prediction accuracy of Nir, solid fins

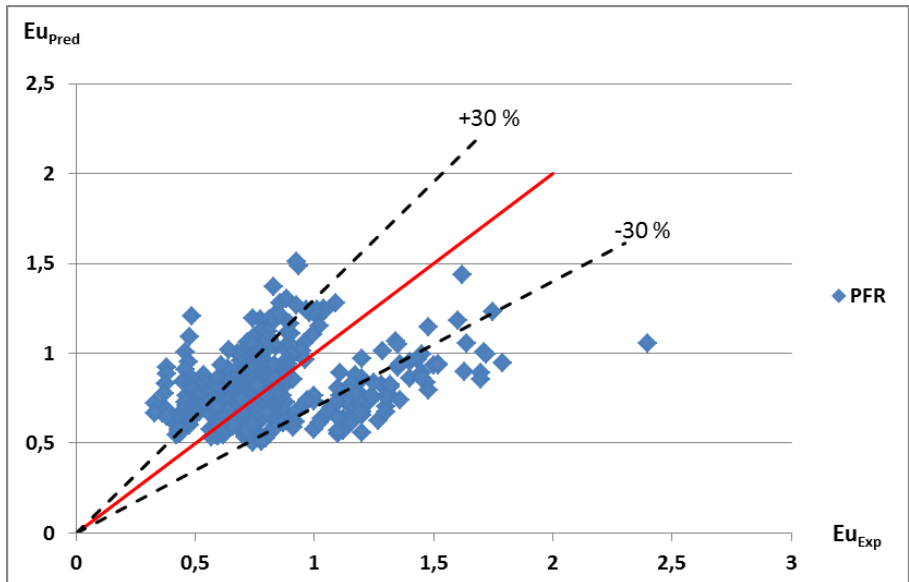


Figure 30: Pressure drop prediction accuracy of PFR, serrated fins

4.4 Geometry dependency

Evaluating the dependency of the correlated values on key geometric parameters is a way of identifying possibilities of model improvements. Introducing corrections for the effect of the parameters on the calculated values into the models can shift the predicted $NuPr^{-1/3}$ and Eu towards the experimental values.

The first step in this analysis is to determine the dependency of the measured values on the Reynold's number. Using power regression, so that the relationships $NuPr_{exp}^{-1/3} = aRe^b$ and $Eu_{exp} = aRe^b$ are determined for each of the geometries considered, the experimental values for $NuPr^{-1/3}$ and Eu are interpolated to correspond to a Reynolds number of 10000. $NuPr^{-1/3}$ and Eu are then calculated with the prediction models for all the geometries, for $Re = 10000$. With the Reynolds number locked at 10000 for the measured and calculated values, the dependency of the ratios $NuPr_{Pred}^{-1/3}/NuPr_{Exp}^{-1/3}$ and Eu_{Pred}/Eu_{Exp} on the geometric parameters P_T/P_L , P_T , h_f/p_f , A_r and W is evaluated, once again by power regression, so that

$$\frac{NuPr_{Pred}^{-1/3}}{NuPr_{Exp}^{-1/3}} = aX^b \quad (99)$$

$$\frac{Eu_{Pred}}{Eu_{Exp}} = aX^b \quad (100)$$

where X is the geometric parameter. The chosen parameters represent different influences on the $NuPr^{-1/3}$ and Eu values: P_T/P_L and P_T represent the bundle layout, h_f/p_f represents the fin dimensions and A_r and W are heat transfer and flow area parameters, respectively.

The five models - PFR, Nir, HTFS1, HTFS2 and HTFS3 - are all evaluated with regard to the five geometric parameters. Overall, few of the parameters show a definitive influence on the heat transfer and pressure drop ratios. Nir's flow area parameter W proves to correlate Eu_{Pred}/Eu_{Exp} for solid fins quite well for PFR, HTFS1, HTFS2 and HTFS3. See figures 31, 32, 33 and 34. The influence on heat transfer for solid fins is less clear. The heat transfer and pressure drop ratios for serrated fins are not correlated well by any parameter. See figures 64 through 163 in appendix B.

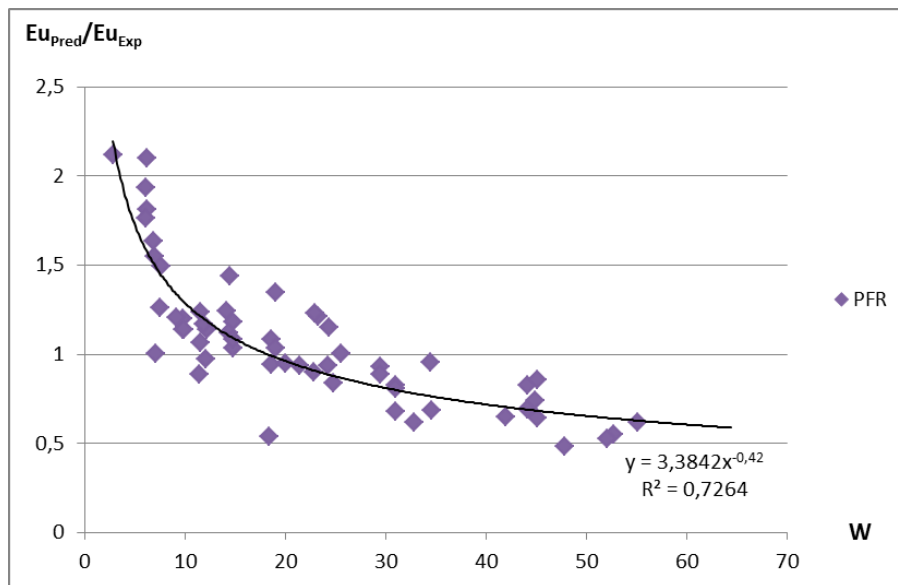


Figure 31: Predicted pressure drop dependency on W for PFR, solid fins

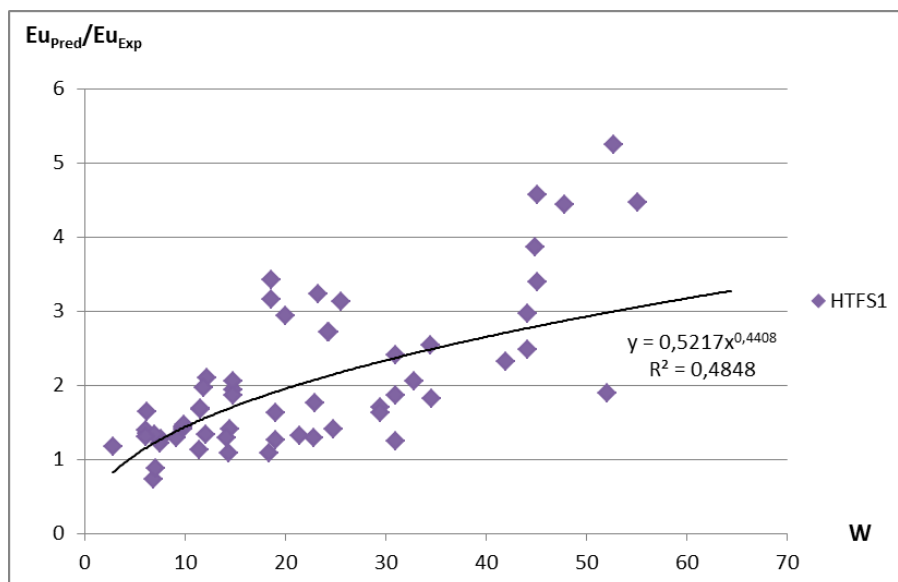


Figure 32: Predicted pressure drop dependency on W for HTFS1, solid fins

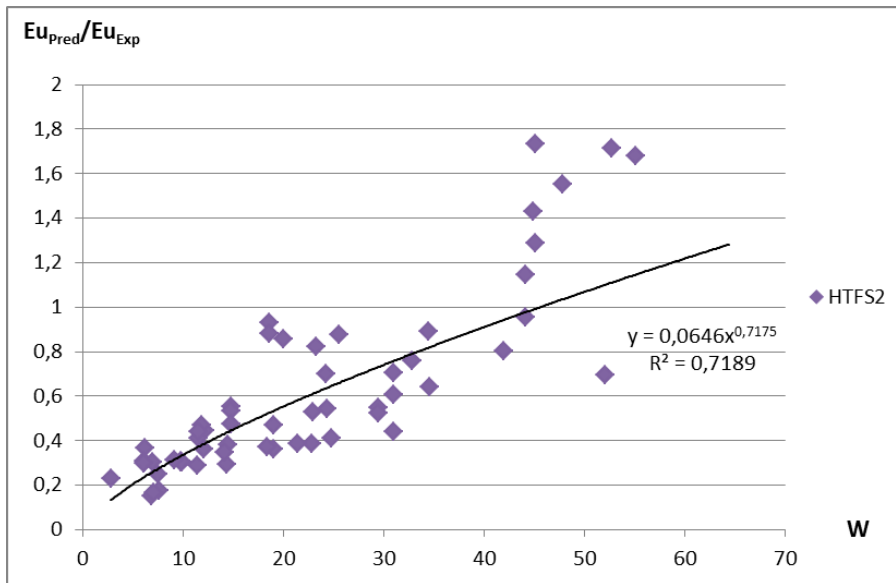


Figure 33: Predicted pressure drop dependency on W for HTFS2, solid fins

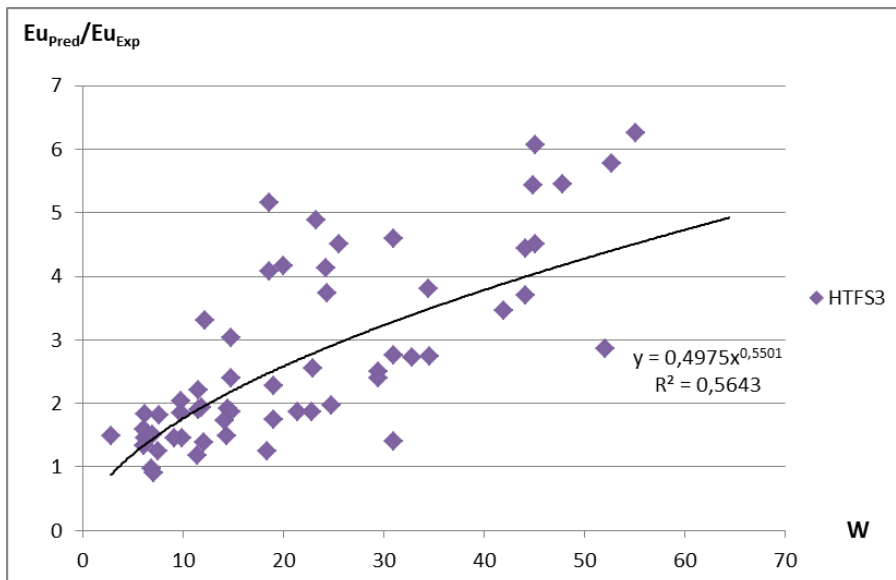


Figure 34: Predicted pressure drop dependency on W for HTFS3, solid fins

4.5 Model improvements and modified model performance

From the geometric dependency analysis, the predicted values can be modified to better match the experimental values as such:

$$\frac{NuPr_{Pred}^{-1/3}}{aX^b} = NuPr_{Exp}^{-1/3} \quad (101)$$

$$\frac{Eu_{Pred}}{aX^b} = Eu_{Exp} \quad (102)$$

Taking the geometric parameters that show the clearest influence on the heat transfer/pressure drop ratios (i.e. the regressions with the highest R^2 - see figures 64 through 163 in appendix B) and introducing these into the respective correlations produces modified calculated values that match the measured values either better or worse. As mentioned, W makes for the best choice of correction for solid fins for all correlations except the Nir pressure drop correlation. For serrated fins, the geometric parameters chosen for correction vary between the correlations.

4.5.1 Heat transfer

The modified heat transfer correlations for solid fins are:

$$NuPr_{PFR, mod.}^{-1/3} = \frac{NuPr_{PFR}^{-1/3}}{0.7349W^{0.1001}}$$

$$NuPr_{Nir, mod.}^{-1/3} = \frac{NuPr_{Nir}^{-1/3}}{0.5863W^{0.1658}}$$

$$NuPr_{HTFS1, mod.}^{-1/3} = \frac{NuPr_{HTFS1}^{-1/3}}{0.6693W^{-0.037}}$$

$$NuPr_{HTFS2, mod.}^{-1/3} = \frac{NuPr_{HTFS2}^{-1/3}}{0.6179W^{0.1776}}$$

$$NuPr_{HTFS3, mod.}^{-1/3} = \frac{NuPr_{HTFS3}^{-1/3}}{0.7167W^{0.1295}}$$

The heat transfer prediction accuracy of the modified models, for solid fins, is as follows:

- Modified PFR predicts 66.7 % of the data within ± 20 %, and 33.5 % within ± 10 %. 95 % of the data is predicted within the range -38 % to +38 %
- Modified Nir predicts 76.2 % of the data within ± 20 %, and 47.4 % within ± 10 %. 95 % of the data is predicted within the range -42 % to +30 %

- Modified HTFS1 predicts 55.2 % of the data within ± 20 %, and 26.2 % within ± 10 %. 95 % of the data is predicted within the range -41 % to +53 %
- Modified HTFS2 predicts 79.8 % of the data within ± 20 %, and 42.4 % within ± 10 %. 95 % of the data is predicted within the range -36 % to +35 %
- Modified HTFS3 predicts 76.7 % of the data within ± 20 %, and 33.2 % within ± 10 %. 95 % of the data is predicted within the range -36 % to +34 %

Table 5: Heat transfer prediction accuracy of the five modified models, solid fins

	Within ± 20 %	Within ± 10 %	95 % of data
PFR, mod.	66.7 %	33.5 %	-38 % to +38 %
Nir, mod.	76.2 %	47.4 %	-42 % to +30 %
HTFS1, mod.	55.2 %	26.2 %	-41 % to +53 %
HTFS2, mod.	79.8 %	42.4 %	-36 % to +35 %
HTFS3, mod.	76.7 %	33.2 %	-36 % to +34 %

The modified heat transfer correlations for serrated fins are:

$$NuPr_{PFR, mod.}^{-1/3} = \frac{NuPr_{PFR}^{-1/3}}{1.3337A_r^{-0.155}}$$

$$NuPr_{Nir, mod.}^{-1/3} = \frac{NuPr_{Nir}^{-1/3}}{1.2882\left(\frac{h_f}{p_f}\right)^{0.1046}}$$

$$NuPr_{HTFS1, mod.}^{-1/3} = \frac{NuPr_{HTFS1}^{-1/3}}{0.5972W^{-0.436}}$$

$$NuPr_{HTFS2, mod.}^{-1/3} = \frac{NuPr_{HTFS2}^{-1/3}}{1.1054A_r^{-0.117}}$$

$$NuPr_{HTFS3, mod.}^{-1/3} = \frac{NuPr_{HTFS3}^{-1/3}}{1.0483A_r^{-0.119}}$$

The heat transfer prediction accuracy of the modified correlations, for serrated fins, is as follows:

- Modified PFR predicts 40.6 % of the data within ± 20 %, and 20.6 % within ± 10 %. 95 % of the data is predicted within the range -17 % to +69 %
- Modified Nir predicts 1.7 % of the data within ± 20 %, and 0 % within ± 10 %. 95 % of the data is predicted within the range -73 % to -25 %
- Modified HTFS1 predicts 0 % of the data within ± 20 %, and 0 % within ± 10 %. 95 % of the data is predicted within the range +107 % to +490 %

- Modified HTFS2 predicts 72.9 % of the data within ± 20 %, and 48.6 % within ± 10 %. 95 % of the data is predicted within the range -33 % to +34 %
- Modified HTFS3 predicts 74.1 % of the data within ± 20 %, and 51.4 % within ± 10 %. 95 % of the data is predicted within the range -33 % to +35 %

Table 6: Heat transfer prediction accuracy of the five modified models, serrated fins

	Within ± 20 %	Within ± 10 %	95 % of data
PFR, mod.	40.6 %	20.6 %	-17 % to + 69 %
Nir, mod.	1.7 %	0 %	-73 % to -25 %
HTFS1, mod.	0 %	0 %	+107 % to +490 %
HTFS2, mod.	72.9 %	48.6 %	-33 % to +34 %
HTFS3, mod.	74.1 %	51.4 %	-33 % to +35 %

Out of the modified correlations, Nir, HTFS2 and HTFS3 are the most accurate for solid fins. HTFS2 and HTFS3 give very similar results, and the most accurate results for serrated fins. Nir/HTFS2 and HTFS3 have the best heat transfer prediction accuracy for solid fins and serrated fins, respectively. See figures 35 and 36. The accuracy is improved by the modification for all the correlations for solid fins, while for serrated fins the modified results from PFR, Nir and HTFS1 are less accurate.

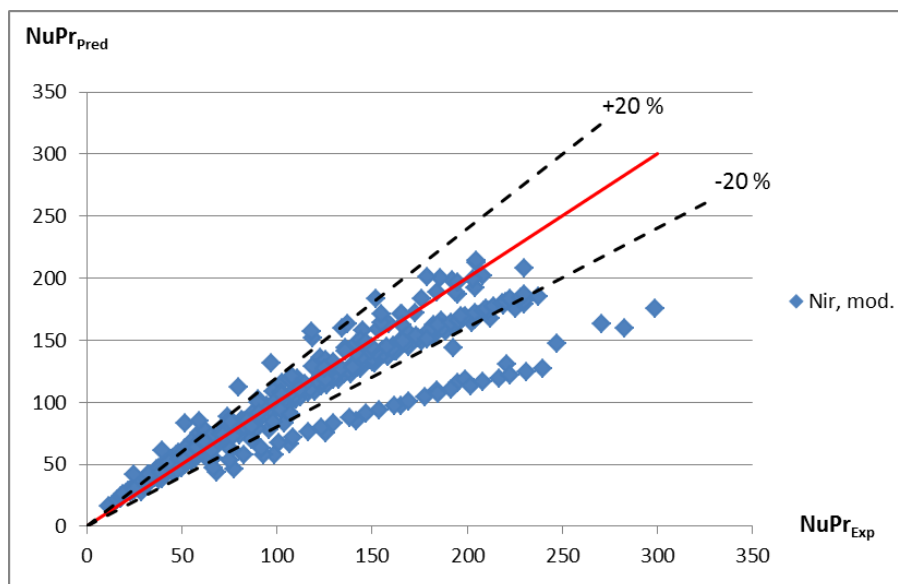


Figure 35: Heat transfer prediction accuracy of modified Nir, solid fins

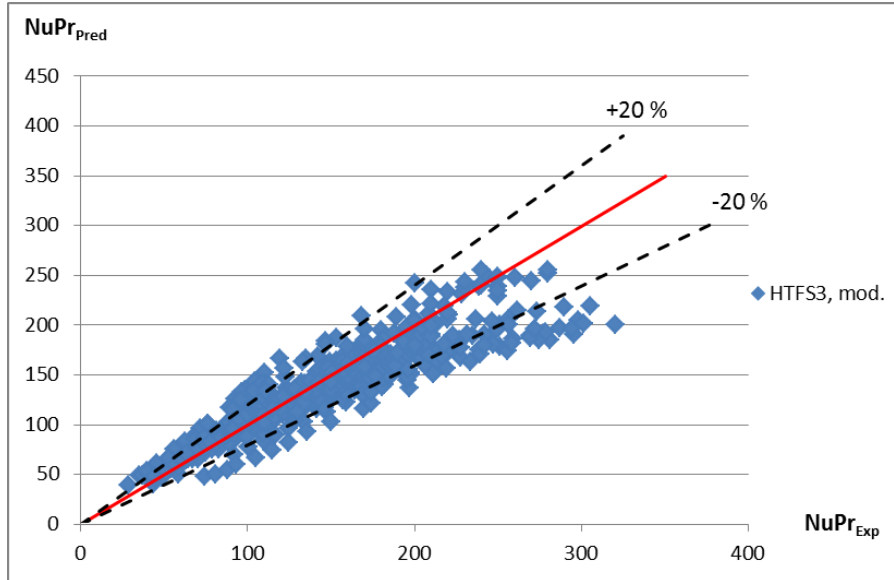


Figure 36: Heat transfer prediction accuracy of modified HTFS3, serrated fins

4.5.2 Pressure drop

The modified pressure drop correlations for solid fins are:

$$Eu_{PFR, mod.}^{-1/3} = \frac{Eu_{PFR}^{-1/3}}{3.3842W^{-0.42}}$$

$$Eu_{Nir, mod.}^{-1/3} = \frac{Eu_{Nir}^{-1/3}}{0.8531\left(\frac{h_f}{p_f}\right)^{0.1487}}$$

$$Eu_{HTFS1, mod.}^{-1/3} = \frac{Eu_{HTFS1}^{-1/3}}{0.5217W^{0.4408}}$$

$$Eu_{HTFS2, mod.}^{-1/3} = \frac{Eu_{HTFS2}^{-1/3}}{0.0646W^{0.7175}}$$

$$Eu_{HTFS3, mod.}^{-1/3} = \frac{Eu_{HTFS3}^{-1/3}}{0.4975W^{0.5501}}$$

The pressure drop prediction accuracy of the modified models, for solid fins, is as follows:

- Modified PFR predicts 92.3 % of the data within ± 30 %, and 67.0 % within ± 15 %. 95 % of the data is predicted within the range -29 % to +37 %
- Modified Nir predicts 89.6 % of the data within ± 30 %, and 71.2 % within ± 15 %. 95 % of the data is predicted within the range -29 % to +37 %

- Modified HTFS1 predicts 60.4 % of the data within ± 30 %, and 30.3 % within ± 15 %. 95 % of the data is predicted within the range -40 % to +81 %
- Modified HTFS2 predicts 59.8 % of the data within ± 30 %, and 34.9 % within ± 15 %. 95 % of the data is predicted within the range -41 % to +74 %
- Modified HTFS3 predicts 50.8 % of the data within ± 30 %, and 28.4 % within ± 15 %. 95 % of the data is predicted within the range -40 % to +103 %

Table 7: Pressure drop prediction accuracy of the five modified models, solid fins

	Within ± 30 %	Within ± 15 %	95 % of data
PFR, mod.	92.3 %	67.0 %	-29 % to +37 %
Nir, mod.	89.6 %	71.2 %	-29 % to +37 %
HTFS1, mod.	60.4 %	30.3 %	-40 % to +81 %
HTFS2, mod.	59.8 %	34.9 %	-41 % to +74 %
HTFS3, mod.	50.8 %	28.4 %	-40 % to +103 %

The modified pressure drop correlations for serrated fins are:

$$Eu_{PFR, mod.}^{-1/3} = \frac{Eu_{PFR}^{-1/3}}{1.995 \left(\frac{h_f}{p_f}\right)^{-0.271}}$$

$$Eu_{Nir, mod.}^{-1/3} = \frac{Eu_{Nir}^{-1/3}}{0.311 \left(\frac{h_f}{p_f}\right)^{-0.375}}$$

$$Eu_{HTFS1, mod.}^{-1/3} = \frac{Eu_{HTFS1}^{-1/3}}{1.5025W^{0.9013}}$$

$$Eu_{HTFS2, mod.}^{-1/3} = \frac{Eu_{HTFS2}^{-1/3}}{0.0056P_T^{1.2087}}$$

$$Eu_{HTFS3, mod.}^{-1/3} = \frac{Eu_{HTFS3}^{-1/3}}{4.6791 \left(\frac{P_T}{P_L}\right)^{-1.152}}$$

The pressure drop prediction accuracy of the modified models, for serrated fins, is as follows:

- Modified PFR predicts 0 % of the data within ± 30 %, and 0 % within ± 15 %. 95 % of the data is predicted within the range -99.8 % to -81 %
- Modified Nir predicts 0 % of the data within ± 30 %, and 0 % within ± 15 %. 95 % of the data is predicted within the range +124 % to +917 %

- Modified HTFS1 predicts 0 % of the data within ± 30 %, and 0 % within ± 15 %. 95 % of the data is predicted within the range -98.5 % to -61 %
- Modified HTFS2 predicts 42.5 % of the data within ± 30 %, and 25.5 % within ± 15 %. 95 % of the data is predicted within the range -77 % to +235 %
- Modified HTFS3 predicts 40.2 % of the data within ± 30 %, and 26.4 % within ± 15 %. 95 % of the data is predicted within the range -70 % to +250 %

Table 8: Pressure drop prediction accuracy of the five modified models, serrated fins

	Within ± 30 %	Within ± 15 %	95 % of data
PFR, mod.	0 %	0 %	-99.8 % to -81 %
Nir, mod.	0 %	0 %	+124 % to +917 %
HTFS1, mod.	0 %	0 %	-98.5 % to -61 %
HTFS2, mod.	42.5 %	25.5 %	-77 % to +235 %
HTFS3, mod.	40.2 %	26.4 %	-70 % to +250 %

The pressure drop accuracy for solid fins is improved for all correlations, with the most accurate correlation being a toss-up between the modified PFR and Nir. See figures 37 and 38. For serrated fins, on the other hand, all the modified correlations except HTFS2 and HTFS3 give substantially less accurate results. For all prediction accuracies, see figures 164 through 183 in appendix C.

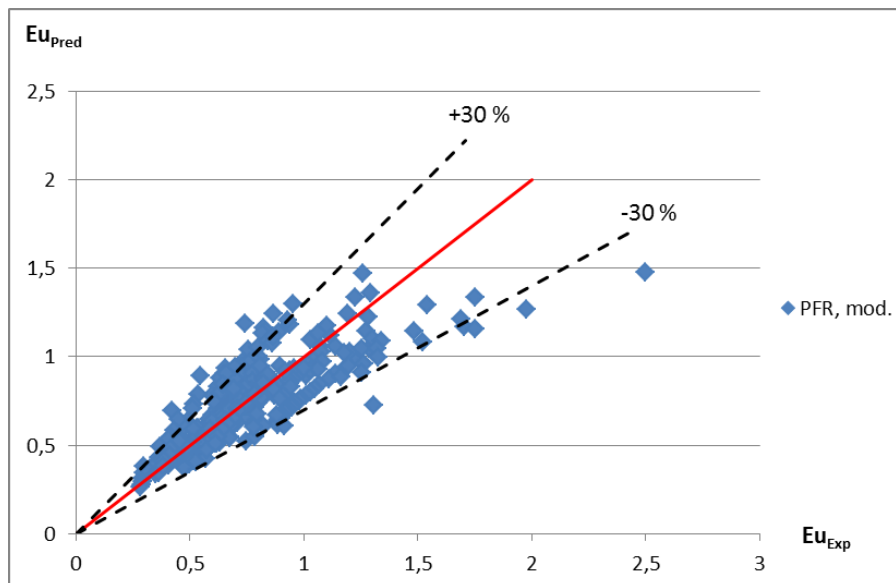


Figure 37: Pressure drop prediction accuracy of modified PFR, solid fins

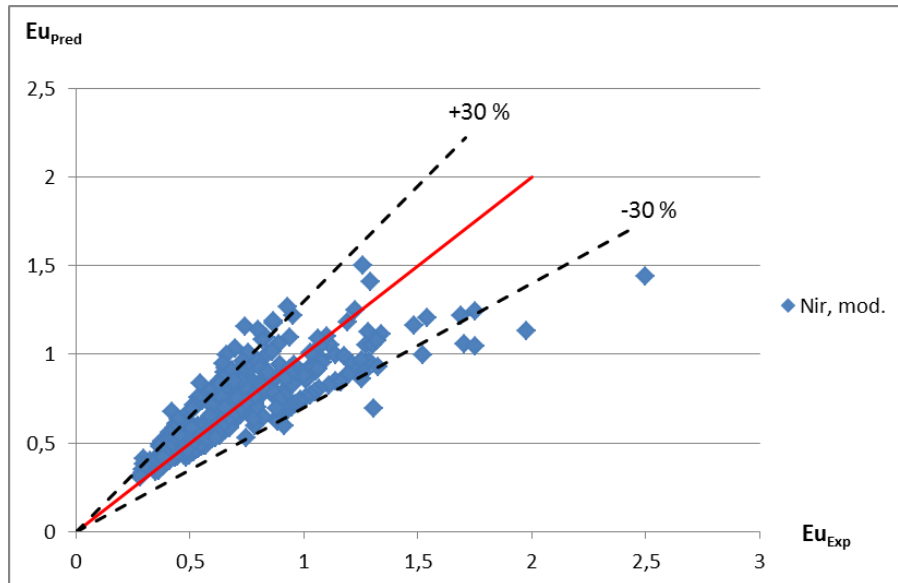


Figure 38: Pressure drop prediction accuracy of modified Nir, solid fins

4.6 Discussion

The statistic analysis of the calculated values shows that no single model gives the most accurate results for both heat transfer and pressure drop, and for both solid and serrated fins. Surprisingly, the oldest and simplest model - PFR - performs relatively well for all cases. HTFS1 performs poorly all around. HTFS1, HTFS2 and HTFS3 do not have specific correlations for serrated fins, and the calculated values for both heat transfer and pressure drop from these models for the serrated geometries are not very accurate. Nir, while having correlations specifically developed for serrated finned tubes, also gives poor results for these cases. The models' correlations are based on sets of experimental data with one range of flow and temperature conditions. This may render them invalid for some of the tested data sets, and could explain the poor performance of some of the models for some cases.

The attempt to improve the models by introducing geometric parameters succeeds in some cases, and fails in others. All the modified heat transfer and pressure drop correlations produce better results for solid fin tubes, while for serrated fins only HTFS2 and HTFS3 give more accurate results. The other modified models produce much poorer results than the original versions. This worsening of prediction accuracy may occur because the corrections introduced stem from the geometric dependencies that do not show a clear influence on the heat transfer/pressure drop ratios. The regression used for correction of PFR Eu for serrated fins, for instance, has an R^2 of only 0.1264 (see figure 75 in appendix B). Also, the introduced geometric corrections are evaluated for a Reynolds number of 10000, while the new values are calculated for different Reynolds numbers, ranging from 1714 to 48830 for serrated fins. For some

geometries, there are no tests done for $Re < 10000$, which means that their values are in effect extrapolated instead of interpolated to correspond to $Re = 10000$ for the geometry dependency analysis.

In summation the most accurate heat transfer correlations for solid fins are modified Nir:

$$NuPr_{Nir, mod.}^{-1/3} = 1.7056 Re_d^{0.6} W^{-0.4318} R_b^{-0.4} \left(\frac{D}{d}\right)^{-0.4} K_{z,h} \quad (103)$$

and modified HTFS2:

$$NuPr_{HTFS2, mod.}^{-1/3} = 0.356 Re_f^{0.04} Re_{max}^{0.632} A_r^{-0.15} W^{-0.1776} \quad (104)$$

For serrated fins, the most accurate heat transfer correlation is modified HTFS3:

$$NuPr_{HTFS3, mod.}^{-1/3} = 0.1956 Re_f^{0.04} Re_{max}^{0.632} A_r^{-0.031} \quad (105)$$

The most accurate pressure drop correlations for solid fins are modified PFR:

$$Eu_{PFR, mod.} = 4.0187 Re_h^{-0.3} \left(\frac{P_L}{d_h}\right)^{-0.42} W^{0.42} \quad (106)$$

(for $\frac{P_L}{d_h} \leq 4$) and modified Nir:

$$Eu_{Nir, mod.} = 2.485 Re_d^{-0.25} W^{0.45} \left(\frac{D}{d}\right)^{-0.25} \left(\frac{h_f}{p_f}\right)^{-0.1487} K_{z,p} \quad (107)$$

For serrated fins, the most accurate pressure drop correlation is the original PFR:

$$Eu_{PFR} = 19.04 Re_h^{-0.3} \left(\frac{P_L}{d_h}\right)^{-0.42} \quad (108)$$

(for $\frac{P_L}{d_h} \leq 4$).

5 Experimental setup

5.1 Rig design

The test rig used for the measurement of heat transfer and pressure drop in the test tube bundles is designed by PhD candidate Anna Holfeld. Its design is based on an earlier test rig used by Næss (2007). The test rig is an open-circuit wind tunnel, operated with heated air and cooled by a water-glycol circuit. See figure 39.

The rig consists of a heating battery, a diffuser, a settling chamber, a contraction section and the test section which is connected to a cooling circuit. Two fans suck in air from the outside and pass it through the heating battery. Here, the air is heated up to 120-130°C. The air passes through an orifice where the flow rate is measured, before it goes into the diffuser and is slowed down. In the settling chamber the level of turbulence is reduced by screens and a honeycomb. The contraction section speeds up the air flow again and passes it to the test section. In the test section, the flow crosses a finned tube bundle. A 30 % water-glycol mixture runs through the tubes, taking up heat from the air flow. Temperature and pressure sensors measure the temperature difference and pressure drop in the air flow over the bundle. A plate heat exchanger cools the heated water-glycol coming out from the tube bundle by use of city water.

The dimensions and performance of the various parts of the rig are as follows:

Fans: The two fans are installed in the laboratory basement and operate in series. The fan downstream the heat exchanger controls the air pressure in the test section. This provides constant pressure independent of the air flow rate.

Heating battery: The heating battery has a capacity of 400 kW. A tentative maximum outlet temperature of 200°C is proposed.

Diffuser: The diffuser is designed according to Mehta and Bradshaw (1979). It reduces the gas velocity by enlarging the flow area and changes the shape of the flow area from circular to squared.

Settling chamber: The settling chamber, including a screen and a honeycomb, was also designed according to Mehta and Bradshaw (1979).

Contraction section: The contraction section is designed according to Bell and Mehta (1998) and has two parts. The first part reduces the width of the flow area from 1100 mm to 500 mm - the constant width of the test section. The second part reduces the height from 1100 mm to a height equal to the height of the test section - which can vary according to the bundle tested.

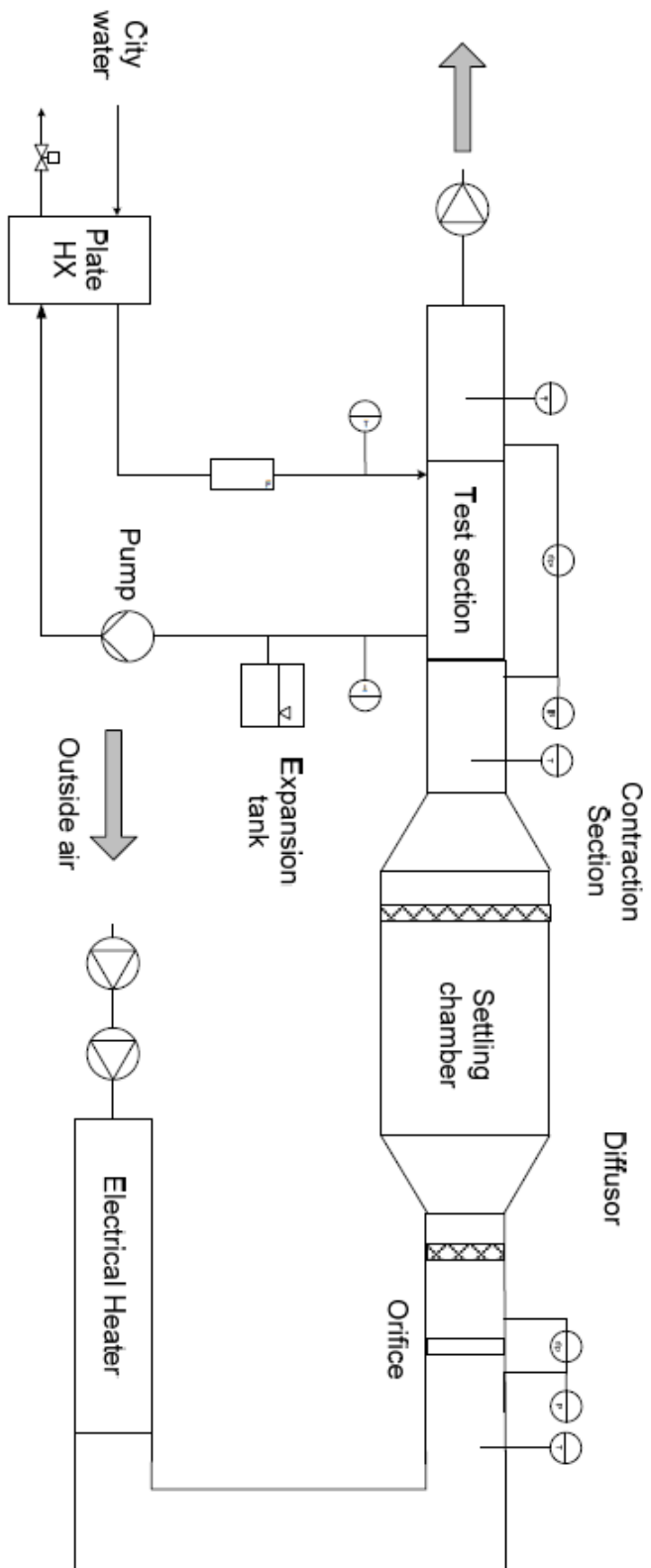


Figure 39: Test rig flow diagram (Holfeld 2012)

Cooling circuit: In order to prevent corrosion, the cooling circuit is run with a mixture of water (70 %) and glycol (30 %). It consists of a plate heat exchanger with a capacity of 150 kW taking up heat from the water-glycol mixture and dumping it to city water, a pump and an expansion tank maintaining constant pressure.

Instrumentation: The instrumentation for the test rig consists of pressure and temperature sensors, flow meters and a logging system. The LabView program is used for monitoring and steering the rig. There are four temperature sensors and four pressure sensors (two differential pressure cells and two absolute pressure transmitters) placed at different locations across the rig. The air flow rate is measured with an orifice, while the flow in the cooling cycle is measured with an electromagnetic flow meter.

5.2 Test geometry

The tested tube bundle consists of 8 tube rows in the longitudinal direction and 4 rows in the transversal direction. The fins are helically wound I-foot type serrated fins. The test geometry will from here on be referred to as geometry 1.

Tube and fin dimensions

- Outer tube diameter $d = 31.75$ mm
- Fin diameter $D = 67.75$ mm
- Total fin height $h_f = 18$ mm
- Segment height $h_s = 11$ mm
- Segment width $w_s = 4.5$ mm
- Fin thickness $t_f = 1$ mm
- Fin frequency $n_f = 276$ fins/m

Bundle dimensions

- Transversal tube pitch $P_T = 69.75$ mm
- Longitudinal tube pitch $P_L = 60.4$ mm
- Number of tube rows in flow direction $N_r = 8$

5.3 Data reduction

When calculating heat transfer in a heat exchanger, the starting point is the equation for transferred heat

$$Q = \frac{1}{2}((\dot{m}c_p)_h(T_{h,i} - T_{h,o}) + (\dot{m}c_p)_c(T_{c,o} - T_{c,i})) \quad (109)$$

where \dot{m} is the mass flow rate, c_p is the specific heat and T is the temperature of the fluids. h denotes the hot fluid - here the air, and c denotes the cold fluid - here the water-glycol. i and o denote the inlet and outlet flows, respectively (Holfeld, 2012).

The transferred heat can be expressed using the logarithmic mean temperature difference, the LMTD:

$$Q = UA_{ht}LMTD \quad (110)$$

where U is the overall heat transfer coefficient, A_{ht} is the total heat transfer area, and $LMTD$ is the logarithmic mean temperature difference between the hot and cold fluids. For a countercurrent heat exchanger

$$LMTD = \frac{(T_{h,i} - T_{c,o}) - (T_{h,o} - T_{c,i})}{\ln\left(\frac{T_{h,i} - T_{c,o}}{T_{h,o} - T_{c,i}}\right)} \quad (111)$$

For a crossflow heat exchanger, the logarithmic mean temperature difference is expressed as the $LMTD$ for a countercurrent heat exchanger multiplied with a correction factor:

$$LMTD_{cross} = \Gamma LMTD_{counter} \quad (112)$$

The correction factor Γ is a function of two parameters, the LMTD effectiveness P and the LMTD capacitance ratio R :

$$P = \frac{T_{c,o} - T_{c,i}}{T_{h,i} - T_{c,i}} \quad (113)$$

$$R = \frac{T_{h,i} - T_{h,o}}{T_{c,o} - T_{c,i}} \quad (114)$$

(Incropera et al., 2007). Investigations have shown that the error in using the $LMTD_{counter}$ in crossflow heat exchanger calculations, without the correction factor, is small (Næss, 2007). Therefore, the countercurrent LMTD will be used for the test bundle.

The ratio $\frac{1}{UA_{ht}}$ represents the overall resistance to heat transfer and is expressed as

$$\frac{1}{UA_{ht}} = \frac{1}{\alpha_i A_i} + \frac{\ln(\frac{d_o}{d_i})}{k_t A_{tube}} + \frac{1}{\alpha_g (\eta_f A_{fins} + A_{t,0})} \quad (115)$$

where α_i is the tube side heat transfer coefficient, A_i is the inner tube surface, d_o is the outer tube diameter, d_i is the inner tube diameter, k_t is the thermal conductivity of the tube material α_g is the gas side heat transfer coefficient and η_f is the fin efficiency. Knowing α_i , α_g can be evaluated as such

$$\alpha_g = \left(\frac{1}{U} - \left[\frac{A_{ht}}{\alpha_i A_i} + \frac{A_{ht} \ln(\frac{d_o}{d_i})}{k_t A_{tube}} \right] \right)^{-1} \frac{A_{ht}}{\eta_f A_{fins} + A_{t,0}} \quad (116)$$

The theoretical fin efficiency of I-foot serrated fins can be approximated according to Hashizume et al. (2002) as

$$\eta_{s,th} = \eta_{l,th} - a(\eta_{l,th} - \eta_{p,th}) \quad (117)$$

Here, $\eta_{l,th}$ is the theoretical efficiency of the serrated part of the fin, i.e. the rectangular extended surfaces, given by

$$\eta_{l,th} = \frac{\tanh(mh)}{mh} \quad (118)$$

where $h = h_s + t_f/2$ is the effective fin height of a rectangular fin with height h_s and the parameter m is given by

$$m = \sqrt{\frac{2\alpha_g}{k_f t_f}} \quad (119)$$

$\eta_{p,th}$ is the theoretical efficiency of the solid ("plain") part of the fin, estimated according to Schmidt (1966) as

$$\eta_{p,th} = \frac{\tanh(mh_e)}{mh_e} \quad (120)$$

where h_e is an equivalent fin height given by

$$h_e = h_f \left(1 + 0.35 \ln\left(\frac{D}{d}\right) \right) \quad (121)$$

The parameter a in equation 117 is given by

$$a = \left(\cos\left[\left(\frac{\pi}{2}\right)\left(\frac{h_s}{h_f}\right)\right] \right)^n \quad (122)$$

where the exponent n is a parameter given by

$$n = 1.6 - 0.094\left(mh\frac{D}{d}\right) \quad (123)$$

The heat transfer distribution across the fin surface is not uniform (Krückels & Kottke, 1970). Because of this, the actual fin efficiency η_f differs from the theoretical by a correction factor χ so that

$$\eta_f = \chi\eta_{th} \quad (124)$$

Weierman (1976) proposed a correction factor for serrated fins based on experimental data, of the form

$$\chi = 0.9 + 0.1\eta_{th} \quad (125)$$

More recently, Hashizume et al. (2002) proposed a correction factor for I-foot serrated fins, again based on experimental data, that is valid for the range of geometric parameters and Reynolds numbers pertaining to this data. The correction factor is:

$$\chi = 1 - \left(0.016\left(\frac{h_s}{w_s}\right) + 0.14\left(\frac{D}{d}\right)^{2.7}[1 - 0.097 \ln(Re_d)]\right)(mh_f) \quad (126)$$

Both of these correction factors will be applied to calculate Nu from the measured heat transfer.

Since the fin efficiency is a function of the gas side heat transfer coefficient α_g , the process of calculating α_g is iterative. The tube side heat transfer coefficient can be evaluated using Gnielinski's equation (2002)

$$Nu = \frac{\frac{c_f}{2}(Re_i - 1000)Pr_i}{1 + 12.7\sqrt{\frac{c_f}{2}}(Pr_i^{2/3} - 1)} \left(1 + \left(\frac{d_i}{L}\right)^{2/3}\right) = \frac{\alpha_i d_i}{k_i} \quad (127)$$

where k_i is the thermal conductivity of the tube side fluid, L is the characteristic length scale and $\frac{c_f}{2}$ is the friction coefficient, evaluated from Kays et al. (1984):

$$\frac{c_f}{2} = (4.639 - 2.236 \ln(Re_i))^{-2} \quad (128)$$

When it comes to pressure drop, the pressure loss coefficient (Euler number) is obtained from the measured pressure difference, temperature and flow rate:

$$Eu = \frac{2\rho\Delta p}{N_r m'^2} \quad (129)$$

where Δp is the measured pressure difference over the bundle, ρ is the density of the air, N_r is the number of tube rows in the longitudinal direction, and m'^2 is the mass flux in the minimum flow area (Næss, 2007).

6 Test results and analysis

6.1 Pressure drop

The results of the pressure drop test are presented in the following table, alongside values calculated with the prediction models:

Table 9: Measured and predicted Eu for geometry 1 at different Reynolds numbers

Re	Measured Eu	PFR Eu	Nir Eu	HTFS1 Eu	HTFS2 Eu	HTFS3 Eu
3417	3,8506	1,1986	2,1414	10,7026	0,7828	6,4637
3886	3,4536	1,1532	2,0735	10,2971	0,7532	6,2188
4044	3,2542	1,1395	2,0530	10,1747	0,7442	6,1449
5282	2,5367	1,0517	1,9204	9,3913	0,6869	5,6717
6661	2,1093	0,9810	1,8122	8,7600	0,6407	5,2905
8117	1,8777	0,9245	1,7248	8,2555	0,6038	4,9858
9596	1,7095	0,8793	1,6541	7,8513	0,5743	4,7417
11089	1,6003	0,8419	1,5954	7,5179	0,5499	4,5403
12575	1,5217	0,8108	1,5460	7,2396	0,5295	4,3723
14089	1,4656	0,7836	1,5027	6,9968	0,5118	4,2256
15550	1,4158	0,7607	1,4661	6,7928	0,4968	4,1024
16965	1,3743	0,7411	1,4345	6,6176	0,4840	3,9966
17248	1,3470	0,7374	1,4286	6,5848	0,4816	3,9768
19348	1,2910	0,7125	1,3881	6,3618	0,4653	3,8421
19720	1,3209	0,7084	1,3815	6,3255	0,4627	3,8202
20914	1,3110	0,6960	1,3614	6,2149	0,4546	3,7534
21098	1,2978	0,6942	1,3584	6,1986	0,4534	3,7436
21361	1,2538	0,6916	1,3542	6,1756	0,4517	3,7297
21361	1,2538	0,6916	1,3542	6,1756	0,4517	3,7297
23363	1,2256	0,6733	1,3242	6,0118	0,4397	3,6308
23363	1,2256	0,6733	1,3242	6,0118	0,4397	3,6308
25304	1,1961	0,6573	1,2980	5,8696	0,4293	3,5449
27698	1,1199	0,6398	1,2690	5,7126	0,4178	3,4500
28056	1,1181	0,6373	1,2650	5,6906	0,4162	3,4368
29312	1,1429	0,6290	1,2512	5,6163	0,4108	3,3919
32036	1,0797	0,6124	1,2237	5,4686	0,4000	3,3027
33863	1,0711	0,6023	1,2069	5,3784	0,3934	3,2482
35814	1,0535	0,5923	1,1901	5,2887	0,3868	3,1941
37720	1,0434	0,5831	1,1747	5,2071	0,3809	3,1447
39510	1,0308	0,5751	1,1612	5,1352	0,3756	3,1013
41032	1,0227	0,5686	1,1503	5,0773	0,3714	3,0663

6.1.1 Comparison with measured values for similar geometry

To get a sense of the validity of the measurements, the pressure drop values were compared to experimental values for Eu for a similar geometry in the database. It was found that Sintef geometry 10 - investigated by Næss (2010) - has some similar geometric dimensions, though it does have shorter fins, and thus a smaller heat transfer area. See appendix E for the specifications on this geometry. The comparison shows that the curve for Re dependency for geometry 1 is steeper than for Sintef 10. Geometry 1 has some measurements for lower Re that Sintef 10 doesn't, and for these low Re the curve is especially steep. See figure 40.

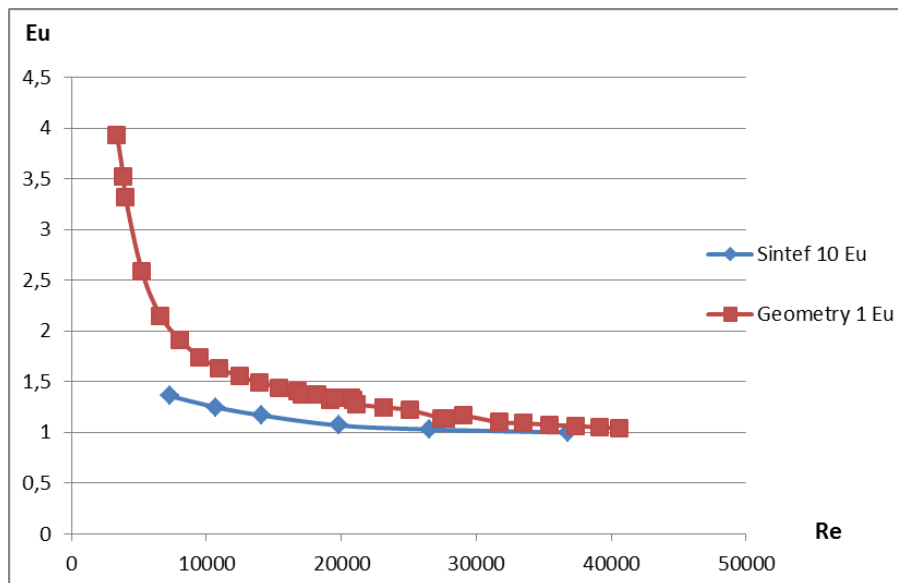


Figure 40: Measured values of Eu for geometry 1 and Sintef 10 plotted against Reynolds number

6.1.2 Comparison with predicted values

Eu was calculated for geometry 1, for the test Re numbers, using the five prediction models tested in section 4. A comparison between the experimental and predicted Eu values shows that out of the five models, Nir's values come closest to the measured. Again, the curve for Re dependency for measured Eu is much steeper for low Re than the curve for Nir's values, while it is very similar for higher Re and converges in the same way for the highest Re . HTFS1 and HTFS3 severely overpredict the pressure drop and their values do not converge for the highest Re . HTFS2 and PFR underpredict, and their curves look like the one for Nir.

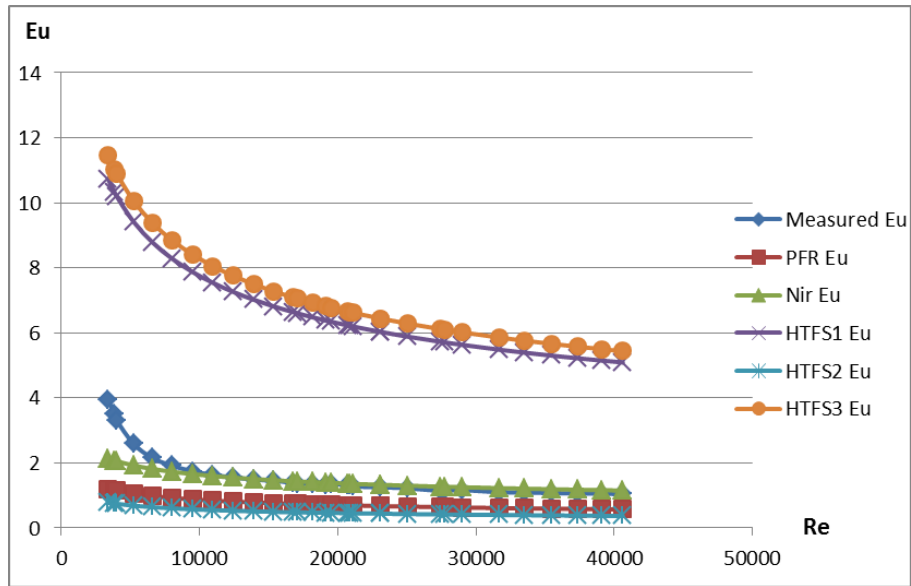


Figure 41: Measured and predicted Eu for geometry 1 plotted against Reynolds number

6.2 Heat transfer

The results of the heat transfer test are presented in the following table, alongside values calculated with the prediction models:

Table 10: Measured and predicted $NuPr^{-1/3}$ for geometry 1 at different Reynolds numbers

Re	Measured $NuPr$, Weierman	Measured $NuPr$, Hashizume	PFR	Nir $NuPr$	HTFS1 $NuPr$	HTFS2 $NuPr$	HTFS3 $NuPr$
6373	72,8350	89,3122	55,7136	46,5080	22,7382	53,8091	50,2489
8387	85,4378	102,5037	67,5207	54,8376	26,7738	64,7131	60,4315
10677	100,9096	118,5529	79,9518	63,3848	30,9095	76,1111	71,0753
13493	118,4002	135,4409	94,1909	72,9452	35,5301	89,0802	83,1864
16906	137,7669	152,6423	110,2929	83,5111	40,6307	103,6522	96,7942
19208	149,1369	161,7771	120,6054	90,1608	43,8379	112,9392	105,4668
19237	150,0095	162,7116	120,7304	90,2409	43,8766	113,0516	105,5717
19427	156,3654	169,6107	121,5663	90,7762	44,1346	113,8029	106,2733
24223	182,4080	189,7545	141,8689	103,6248	50,3260	131,9910	123,2581
26807	195,4291	198,9781	152,2989	110,1215	53,4541	141,2933	131,9449
30506	212,4394	210,0460	166,7204	119,0011	57,7270	154,1139	143,9173
34280	229,4928	220,6007	180,9045	127,6280	61,8757	166,6803	155,6522

The experimental $NuPr^{-1/3}$ values were here calculated from the temperature differences using two different correlations for fin efficiency, namely that of Weierman (1978) and that of Hashizume et al. (2002). The difference between these two lies in the correction factor applied to the theoretical fin efficiency. See section 5.3.

6.2.1 Comparison with measured values for similar geometry

Like for pressure drop, the experimental heat transfer values for geometry 1 were compared to the values for Sintef 10. See figure 42. The curve for Re dependency for Sintef 10 is very similar to the curve for the geometry 1 value based on Hashizume.

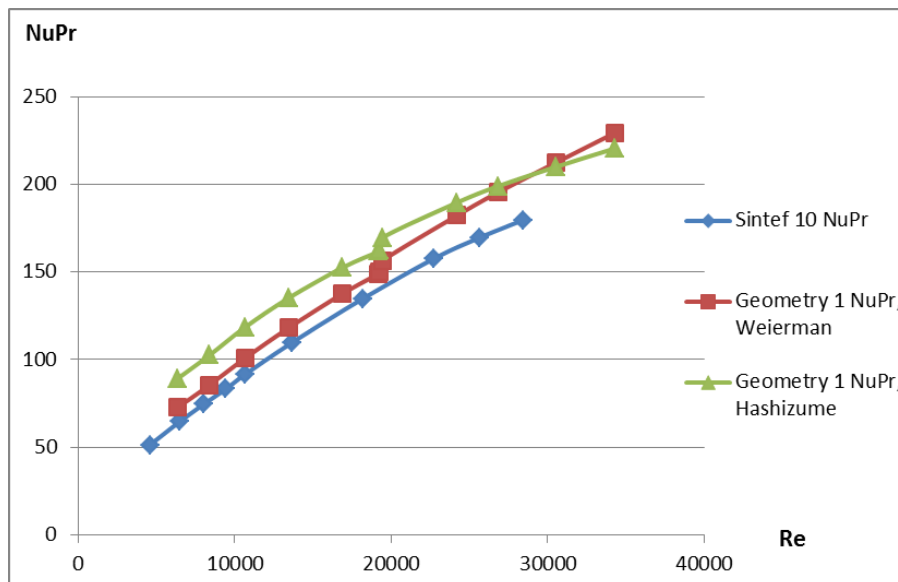


Figure 42: Measured values of $NuPr^{-1/3}$ for geometry 1 and Sintef 10 plotted against Reynolds number

6.2.2 Comparison with predicted values

The comparison between the experimental $NuPr^{-1/3}$ values and the same values calculated with the prediction models shows that all of the models underpredict $NuPr^{-1/3}$. The values calculated with PFR is in the best agreement with the experimental values.

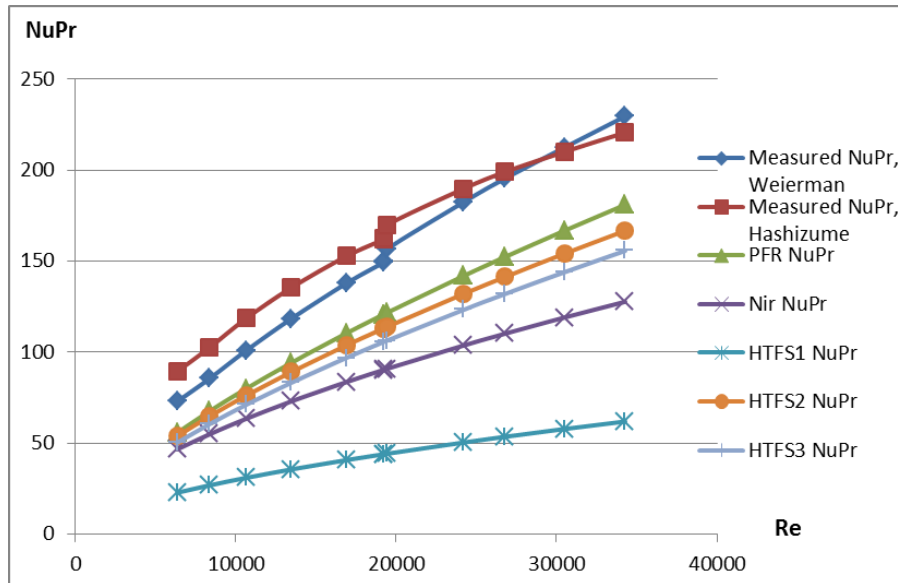


Figure 43: Measured and predicted $NuPr^{-1/3}$ for geometry 1 plotted against Reynolds number

6.3 Discussion

Since this was the first test series done with this rig and tube bundle, some errors are to be expected. Possible points of error include:

1. Low differential pressure over the bundle for the lowest Reynolds numbers. The dp here was in the range of $\sim 50-150$ Pa, which corresponds to $\sim 1-2$ % of the range of the manometer. In these tests, the uncertainty for Eu is very high, around 40 %. See appendix D. This could explain the high measured Eu for low Re compared to the predicted values. Taking 40 % off the experimental values for the three first measurements brings Eu much closer to the Nir values.
2. Too high measured heat transfer to the water-glycol. The heat balance shows up to 5 % too high heat transfer to the water-glycol compared to the measured heat transfer from the gas side. This could be the reason why the measured values for $NuPr^{-1/3}$ are higher than all the predicted values.

7 Conclusion

Model application and improvement

The application of the five prediction models with the geometry and flow parameters from the database shows that there is a large scatter in the calculated values, especially for the HTFS correlations. Out of the five, PFR - the simplest model of all - seems to be the most versatile model, giving fairly good results for both heat transfer and pressure drop, for solid and serrated fins. Nir performs well for solid fins, but fails for serrated fins, in spite of having specific correlations for serrated fin tubes. The HTFS models generally do not perform well. HTFS2 and HTFS3 have fairly good prediction accuracy for heat transfer for solid fins, and ok accuracy for heat transfer for serrated fins. HTFS1 fails for all cases. HTFS1 and HTFS3 tend to greatly overpredict pressure drop values.

Modifying the prediction models by introducing corrections in the form of geometric parameters brings about improved prediction accuracy for most of the correlations. Ultimately, the most accurate correlations are: modified Nir and modified HTFS2 for heat transfer, solid fins; modified HTFS3 for heat transfer, serrated fins; modified PFR and modified Nir for pressure drop, solid fins and original PFR for pressure drop, serrated fins.

Pressure drop and heat transfer test results for geometry 1

The testing done on the I-foot serrated fin tube bundle shows pressure drop in the range of $3.8506 \geq Eu \geq 1.0227$ for Reynolds numbers between 3417 and 41032. The uncertainty for Eu is high, especially for the lowest Re , meaning that the measured values of Eu are possibly overestimated. The heat transfer test gives values in the range of $72.83 \leq NuPr^{-1/3} \leq 229.49$ for Reynolds numbers between 6373 and 34280. Comparison with measured values for a similar test geometry from the database shows that the heat transfer and pressure drop measurements are within a plausible range. The prediction models are applied to geometry 1, and give predicted values for Eu and $NuPr^{-1/3}$ that to a large extent follow the trends seen for the database application. $NuPr^{-1/3}$ is underpredicted by all models, and HTFS1 and HTFS3 greatly overpredict Eu .

Suggestions for further work

There are several things that could be done to assist the prediction of heat transfer and pressure drop in finned tube bundles. First of all, the existing data in the finned tube database should undergo a quality assurance, and complementary data on temperature and fin efficiency should be added. The database should also be expanded, with more new measurements for different geometries and

Reynolds numbers. Complementary experiments on special cases, such as geometries with zero fin gap could be helpful for building new and more accurate correlations. A new mechanistic model, based on CFD flow models and the data in the database, could then be developed.

References

- Bell, J. H. & Mehta, R. D** : Contraction Design for Small Low Speed Wind Tunnels. *JIAA TR - 84*. Joint Institute for Aeronautics and Acoustics, 1998.
- Brauer, H** : Wärme-und strömungstechnische Untersuchungen an quer angeströmten Rippenrohrbündeln. Teil 1: Versuchsanlagen und Meßergebnisse bei höheren Drucken. *Chemie Ingenieur Technik*, 33, 327-335, 1961.
- Briggs, D. E. & Young, E. H.** : Convection Heat Transfer and Pressure Drop of Air Flowing Across Triangular Pitch Banks of Finned Tubes. *Chem. Eng. Prog. Symposium*, series no. 41, vol. 59, 1963.
- Chu, C. M. & Ralston, T.** : HTFS2: Improved Models for Heat Transfer and Pressure Drop Applied to Staggered Arrangements of Tubes with Plain Helical Fins. HTFS/NEL, 1998.
- Gnielinski, V.** : Forced Convection in Ducts. Chapter 2.5.2 in Hewitt, G. et al: *Heat Exchanger Design Handbook*, Begell House, 2002.
- Grimison, E. D.** : Correlation and Utilization of New Data on Flow Resistance and Heat Transfer for Crossflow of Gases over Tube Banks. *Trans. ASME*, vol. 54, 1937.
- Hashizume, K.; Morikawa, R.; Koyama, T. & Matsue, T.** : Fin Efficiency of Serrated Fins. *Heat Transfer Engineering*, vol. 23, pp. 6-14, 2002.
- Henry, J. A. R.** : Effect of Fin Frequency and Tube Pitch on Bundle Pressure Loss. HTFS/NEL, 1994.
- Henry, J. A. R.** : The HTFS Finned Tube Bundle Data Bank. HTFS/NEL, 1993.
- Holfeld, A.** : Test rig design and experimental set up. NTNU, 2012.
- Incropera, F. P.; Dewitt, D. P.; Bergman, T. L. & Lavine, A. S.** : *Fundamentals of Heat and Mass Transfer*, Wiley & Sons, 2007.
- Kaspersen, T.** : *Varmeovergang og trykktap på gassiden i en avgassdampkjele*. MSc thesis, Norges tekniske høgskole, 1995.
- Kays, W. M. & London, A. L.** : *Compact Heat Exchangers*. National Press, 1955.
- Kays, W. M.; Crawford, M. E. & Weigand, B.** : *Convective Heat and Mass Transfer*, 3rd edition, McGraw-Hill Book Company, 1984.
- Krückels, W. & Kottke, V.** : Untersuchung über die Verteilung des Wärmeübergangs an Rippen und Rippenrohr-Modellen. *Chemie-Ing.-Techn.*, vol. 42, pp. 355-362, 1970.
- Kunttysh, V. B. & Iokhvedov, F. M.** : Heat Transfer. *Soviet Research*, vol. 3, pp. 50-61, 1971.

- McIlwain, S. R.** : *Improved Prediction for Finned Tube Bundle Heat Exchangers in Crossflow*. PhD thesis, University of Strathclyde, 2003.
- Mehta, R. D. & Bradshaw, P.** : Design Rules for Small Low Speed Wind Tunnels. *Aeronautical Journal*, vol. 83, pp. 443-449, 1979.
- Moffat, R. J.** : Describing the Uncertainties in Experimental Results. *Experimental Thermal and Fluid Science*, vol. 1, pp. 3-17, 1988.
- Neal, S. B. H. C. & Hitchcock, J. A.** : Study of the Heat Transfer Process in Banks of Finned Tube in Cross Flow, Using a Large Scale Model Technique. *Proceeding of the Third International Heat Transfer Conference*, vol. 3, pp. 290-298, 1966.
- Nir, A.** : Heat Transfer and Friction Factor Correlations for Crossflow over Staggered Finned Tube Banks. *Heat Transfer Engineering*, vol. 12, pp. 43-58, 1991.
- Næss, E.** : *An Experimental Study of Heat Transfer and Pressure Drop in Serrated-fin Tube Bundles and Investigation of Particulate Fouling in Waste Heat Recovery Heat Exchangers*. Dr.ing. thesis, Norwegian University of Science and Technology, 2007.
- PFR Engineering Systems, Inc.** : Heat Transfer and Pressure Drop Characteristics of Dry Tower Extended Surfaces. Battelle Memorial Institute, 1976.
- Ralston, T.; Byskov, R. K.; Farrant, P. E. & Chu, C. M.** : HTFS Models for Heat Transfer and Pressure Drop Applied to Staggered Arrangements of Tubes with Plain Helical Fins. HTFS/NEL, 1997.
- Real World Physics Problems website** : <http://www.real-world-physics-problems.com/heat-exchanger.html>
- Schmidt, T. E.** : Verbesserte Methoden zur Bestimmung des Wärmeaustausches an berippten Flächen. *Kältetechnik-Klimatisierung*, vol. 18, pp. 135-138, 1966.
- Weierman, C.; Taborek, J. & Marner, W. J.** : Comparison of the Performance of In-line and Staggered Banks of Tubes with Segmented Fins. AICHE Symposium Series, vol. 74, pp. 39-46, 1978.

List of Figures

1	Crossflow finned tube bundle heat exchanger (Source: Real World Physics Problems website)	17
2	a. Individual annular fins; b. Helically wound fins (according to PFR, 1976)	18
3	Types of round fins: a. Plain/solid fin; b. I-foot serrated fin; c. L-foot serrated fin (according to PFR, 1976)	18
4	Attachment methods for serrated fins: a. I-foot fins; b. L-foot fins	19
5	Tube and fin parameters: a. Tube and fin diameters; b. Fin thickness and spacing; c. Segment height and width	19
6	Bundle arrangements: a. Inline bundle; b. Staggered bundle (according to PFR, 1976)	21
7	Staggered layout parameters	21
8	Bypass flow model (according to Henry, 1994)	22
9	Flow area between two adjacent tubes	22
10	Flow pattern over a finned tube (Neal & Hitchcock, 1966)	25
11	Tube layout in staggered tube banks: a. $X_t/D = 1, R_b = 1, R_d = 2$; b. $X_t/D > 1, R_b > 1, R_d = 2$; c. $X_t/D = 0.5, R_b < 1$ (Nir, 1991)	29
12	Test section (Henry, 1994)	32
13	Range of pitches (Henry, 1994)	32
14	Effect of transverse pitch on pressure drop (Henry, 1994)	33
15	Velocities in bypass flow model (Henry, 1994)	34
16	Pressure drop, PFR (McIlwain, 2003)	39
17	Pressure drop, HTFS1 (McIlwain, 2003)	39
18	Pressure drop, HTFS2 (McIlwain, 2003)	40
19	Velocity contours (McIlwain, 2003)	41
20	Geometric parameters (McIlwain, 2003)	41
21	Experimental and predicted values for $NuPr^{-1/3}$ plotted against Reynolds number, solid fins	46
22	Experimental and predicted values for $NuPr^{-1/3}$ plotted against Reynolds number, serrated fins	46
23	Heat transfer prediction accuracy of HTFS3, solid fins	48

24	Heat transfer prediction accuracy of PFR, serrated fins	49
25	Experimental and predicted values (all models) for Eu plotted against Reynolds number, solid fins	49
26	Experimental and predicted values (PFR, Nir and HTFS2) for Eu plotted against Reynolds number, solid fins	50
27	Experimental and predicted values (all models) for Eu plotted against Reynolds number, serrated fins	50
28	Experimental and predicted values (PFR, Nir and HTFS2) for Eu plotted against Reynolds number, serrated fins	51
29	Pressure drop prediction accuracy of Nir, solid fins	53
30	Pressure drop prediction accuracy of PFR, serrated fins	53
31	Predicted pressure drop dependency on W for PFR, solid fins . . .	55
32	Predicted pressure drop dependency on W for HTFS1, solid fins . .	55
33	Predicted pressure drop dependency on W for HTFS2, solid fins . .	56
34	Predicted pressure drop dependency on W for HTFS3, solid fins . .	56
35	Heat transfer prediction accuracy of modified Nir, solid fins	59
36	Heat transfer prediction accuracy of modified HTFS3, serrated fins	60
37	Pressure drop prediction accuracy of modified PFR, solid fins . . .	62
38	Pressure drop prediction accuracy of modified Nir, solid fins	63
39	Test rig flow diagram (Holfeld 2012)	66
40	Measured values of Eu for geometry 1 and Sintef 10 plotted against Reynolds number	73
41	Measured and predicted Eu for geometry 1 plotted against Reynolds number	74
42	Measured values of $NuPr^{-1/3}$ for geometry 1 and Sintef 10 plotted against Reynolds number	75
43	Measured and predicted $NuPr^{-1/3}$ for geometry 1 plotted against Reynolds number	76
44	Heat transfer prediction accuracy of PFR, solid fins	89
45	Pressure drop prediction accuracy of PFR, solid fins	89
46	Heat transfer prediction accuracy of PFR, serrated fins	90
47	Pressure drop prediction accuracy of PFR, serrated fins	90
48	Heat transfer prediction accuracy of Nir, solid fins	91

49	Pressure drop prediction accuracy of Nir, solid fins	91
50	Heat transfer prediction accuracy of Nir, serrated fins	92
51	Pressure drop prediction accuracy of Nir, serrated fins	92
52	Heat transfer prediction accuracy of HTFS1, solid fins	93
53	Pressure drop prediction accuracy of HTFS1, solid fins	93
54	Heat transfer prediction accuracy of HTFS1, serrated fins	94
55	Pressure drop prediction accuracy of HTFS1, serrated fins	94
56	Heat transfer prediction accuracy of HTFS2, solid fins	95
57	Pressure drop prediction accuracy of HTFS2, solid fins	95
58	Heat transfer prediction accuracy of HTFS2, serrated fins	96
59	Pressure drop prediction accuracy of HTFS2, serrated fins	96
60	Heat transfer prediction accuracy of HTFS3, solid fins	97
61	Pressure drop prediction accuracy of HTFS3, solid fins	97
62	Heat transfer prediction accuracy of HTFS3, serrated fins	98
63	Pressure drop prediction accuracy of HTFS3, serrated fins	98
64	Predicted heat transfer dependency on $\frac{P_T}{P_L}$ for PFR, solid fins	99
65	Predicted pressure drop dependency on $\frac{P_T}{P_L}$ for PFR, solid fins	99
66	Predicted heat transfer dependency on $\frac{P_T}{P_L}$ for PFR, serrated fins	100
67	Predicted pressure drop dependency on $\frac{P_T}{P_L}$ for PFR, serrated fins	100
68	Predicted heat transfer dependency on P_T for PFR, solid fins	101
69	Predicted pressure drop dependency on P_T for PFR, solid fins	101
70	Predicted heat transfer dependency on P_T for PFR, serrated fins	102
71	Predicted pressure drop dependency on P_T for PFR, serrated fins	102
72	Predicted heat transfer dependency on $\frac{h_f}{p_f}$ for PFR, solid fins	103
73	Predicted pressure drop dependency on $\frac{h_f}{p_f}$ for PFR, solid fins	103
74	Predicted heat transfer dependency on $\frac{h_f}{p_f}$ for PFR, serrated fins	104
75	Predicted pressure drop dependency on $\frac{h_f}{p_f}$ for PFR, serrated fins	104
76	Predicted heat transfer dependency on A_r for PFR, solid fins	105

77	Predicted pressure drop dependency on A_r for PFR, solid fins . . .	105
78	Predicted heat transfer dependency on A_r for PFR, serrated fins . .	106
79	Predicted pressure drop dependency on A_r for PFR, serrated fins .	106
80	Predicted heat transfer dependency on W for PFR, solid fins	107
81	Predicted pressure drop dependency on W for PFR, solid fins . . .	107
82	Predicted heat transfer dependency on W for PFR, serrated fins . .	108
83	Predicted pressure drop dependency on W for PFR, serrated fins .	108
84	Predicted heat transfer dependency on $\frac{P_T}{P_L}$ for Nir, solid fins	109
85	Predicted pressure drop dependency on $\frac{P_T}{P_L}$ for Nir, solid fins	109
86	Predicted heat transfer dependency on $\frac{P_T}{P_L}$ for Nir, serrated fins . . .	110
87	Predicted pressure drop dependency on $\frac{P_T}{P_L}$ for Nir, serrated fins . .	110
88	Predicted heat transfer dependency on P_T for Nir, solid fins	111
89	Predicted pressure drop dependency on P_T for Nir, solid fins	111
90	Predicted heat transfer dependency on P_T for Nir, serrated fins . . .	112
91	Predicted pressure drop dependency on P_T for Nir, serrated fins . .	112
92	Predicted heat transfer dependency on $\frac{h_f}{p_f}$ for Nir, solid fins	113
93	Predicted pressure drop dependency on $\frac{h_f}{p_f}$ for Nir, solid fins	113
94	Predicted heat transfer dependency on $\frac{h_f}{p_f}$ for Nir, serrated fins . . .	114
95	Predicted pressure drop dependency on $\frac{h_f}{p_f}$ for Nir, serrated fins . .	114
96	Predicted heat transfer dependency on A_r for Nir, solid fins	115
97	Predicted pressure drop dependency on A_r for Nir, solid fins	115
98	Predicted heat transfer dependency on A_r for Nir, serrated fins . . .	116
99	Predicted pressure drop dependency on A_r for Nir, serrated fins . .	116
100	Predicted heat transfer dependency on W for Nir, solid fins	117
101	Predicted pressure drop dependency on W for Nir, solid fins	117
102	Predicted heat transfer dependency on W for Nir, serrated fins . . .	118
103	Predicted pressure drop dependency on W for Nir, serrated fins . .	118
104	Predicted heat transfer dependency on $\frac{P_T}{P_L}$ for HTFS1, solid fins . .	119

105	Predicted pressure drop dependency on $\frac{P_T}{P_L}$ for HTFS1, solid fins . .	119
106	Predicted heat transfer dependency on $\frac{P_T}{P_L}$ for HTFS1, serrated fins .	120
107	Predicted pressure drop dependency on $\frac{P_T}{P_L}$ for HTFS1, serrated fins	120
108	Predicted heat transfer dependency on P_T for HTFS1, solid fins . .	121
109	Predicted pressure drop dependency on P_T for HTFS1, solid fins . .	121
110	Predicted heat transfer dependency on P_T for HTFS1, serrated fins	122
111	Predicted pressure drop dependency on P_T for HTFS1, serrated fins	122
112	Predicted heat transfer dependency on $\frac{h_f}{p_f}$ for HTFS1, solid fins . . .	123
113	Predicted pressure drop dependency on $\frac{h_f}{p_f}$ for HTFS1, solid fins . .	123
114	Predicted heat transfer dependency on $\frac{h_f}{p_f}$ for HTFS1, serrated fins .	124
115	Predicted pressure drop dependency on $\frac{h_f}{p_f}$ for HTFS1, serrated fins	124
116	Predicted heat transfer dependency on A_r for HTFS1, solid fins . .	125
117	Predicted pressure drop dependency on A_r for HTFS1, solid fins . .	125
118	Predicted heat transfer dependency on A_r for HTFS1, serrated fins	126
119	Predicted pressure drop dependency on A_r for HTFS1, serrated fins	126
120	Predicted heat transfer dependency on W for HTFS1, solid fins . . .	127
121	Predicted pressure drop dependency on W for HTFS1, solid fins . .	127
122	Predicted heat transfer dependency on W for HTFS1, serrated fins .	128
123	Predicted pressure drop dependency on W for HTFS1, serrated fins	128
124	Predicted heat transfer dependency on $\frac{P_T}{P_L}$ for HTFS2, solid fins . .	129
125	Predicted pressure drop dependency on $\frac{P_T}{P_L}$ for HTFS2, solid fins . .	129
126	Predicted heat transfer dependency on $\frac{P_T}{P_L}$ for HTFS2, serrated fins .	130
127	Predicted pressure drop dependency on $\frac{P_T}{P_L}$ for HTFS2, serrated fins	130
128	Predicted heat transfer dependency on P_T for HTFS2, solid fins . .	131
129	Predicted pressure drop dependency on P_T for HTFS2, solid fins . .	131
130	Predicted heat transfer dependency on P_T for HTFS2, serrated fins	132
131	Predicted pressure drop dependency on P_T for HTFS2, serrated fins	132

132	Predicted heat transfer dependency on $\frac{h_f}{p_f}$ for HTFS2, solid fins . . .	133
133	Predicted pressure drop dependency on $\frac{h_f}{p_f}$ for HTFS2, solid fins . .	133
134	Predicted heat transfer dependency on $\frac{h_f}{p_f}$ for HTFS2, serrated fins .	134
135	Predicted pressure drop dependency on $\frac{h_f}{p_f}$ for HTFS2, serrated fins	134
136	Predicted heat transfer dependency on A_r for HTFS2, solid fins . .	135
137	Predicted pressure drop dependency on A_r for HTFS2, solid fins . .	135
138	Predicted heat transfer dependency on A_r for HTFS2, serrated fins	136
139	Predicted pressure drop dependency on A_r for HTFS2, serrated fins	136
140	Predicted heat transfer dependency on W for HTFS2, solid fins . . .	137
141	Predicted pressure drop dependency on W for HTFS2, solid fins . .	137
142	Predicted heat transfer dependency on W for HTFS2, serrated fins .	138
143	Predicted pressure drop dependency on W for HTFS2, serrated fins	138
144	Predicted heat transfer dependency on $\frac{P_T}{P_L}$ for HTFS3, solid fins . .	139
145	Predicted pressure drop dependency on $\frac{P_T}{P_L}$ for HTFS3, solid fins . .	139
146	Predicted heat transfer dependency on $\frac{P_T}{P_L}$ for HTFS3, serrated fins .	140
147	Predicted pressure drop dependency on $\frac{P_T}{P_L}$ for HTFS3, serrated fins	140
148	Predicted heat transfer dependency on P_T for HTFS3, solid fins . .	141
149	Predicted pressure drop dependency on P_T for HTFS3, solid fins . .	141
150	Predicted heat transfer dependency on P_T for HTFS3, serrated fins	142
151	Predicted pressure drop dependency on P_T for HTFS3, serrated fins	142
152	Predicted heat transfer dependency on $\frac{h_f}{p_f}$ for HTFS3, solid fins . . .	143
153	Predicted pressure drop dependency on $\frac{h_f}{p_f}$ for HTFS3, solid fins . .	143
154	Predicted heat transfer dependency on $\frac{h_f}{p_f}$ for HTFS3, serrated fins .	144
155	Predicted pressure drop dependency on $\frac{h_f}{p_f}$ for HTFS3, serrated fins	144
156	Predicted heat transfer dependency on A_r for HTFS3, solid fins . .	145
157	Predicted pressure drop dependency on A_r for HTFS3, solid fins . .	145

158	Predicted heat transfer dependency on A_r for HTFS3, serrated fins	146
159	Predicted pressure drop dependency on A_r for HTFS3, serrated fins	146
160	Predicted heat transfer dependency on W for HTFS3, solid fins . . .	147
161	Predicted pressure drop dependency on W for HTFS3, solid fins . .	147
162	Predicted heat transfer dependency on W for HTFS3, serrated fins .	148
163	Predicted pressure drop dependency on W for HTFS3, serrated fins	148
164	Heat transfer prediction accuracy of modified PFR, solid fins	149
165	Pressure drop prediction accuracy of modified PFR, solid fins . . .	149
166	Heat transfer prediction accuracy of modified PFR, serrated fins . .	150
167	Pressure drop prediction accuracy of modified PFR, serrated fins .	150
168	Heat transfer prediction accuracy of modified Nir, solid fins	151
169	Pressure drop prediction accuracy of modified Nir, solid fins	151
170	Heat transfer prediction accuracy of modified Nir, serrated fins . .	152
171	Pressure drop prediction accuracy of modified Nir, serrated fins . .	152
172	Heat transfer prediction accuracy of modified HTFS1, solid fins . .	153
173	Pressure drop prediction accuracy of modified HTFS1, solid fins . .	153
174	Heat transfer prediction accuracy of modified HTFS1, serrated fins	154
175	Pressure drop prediction accuracy of modified HTFS1, serrated fins	154
176	Heat transfer prediction accuracy of modified HTFS2, solid fins . .	155
177	Pressure drop prediction accuracy of modified HTFS2, solid fins . .	155
178	Heat transfer prediction accuracy of modified HTFS2, serrated fins	156
179	Pressure drop prediction accuracy of modified HTFS2, serrated fins	156
180	Heat transfer prediction accuracy of modified HTFS3, solid fins . .	157
181	Pressure drop prediction accuracy of modified HTFS3, solid fins . .	157
182	Heat transfer prediction accuracy of modified HTFS3, serrated fins	158
183	Pressure drop prediction accuracy of modified HTFS3, serrated fins	158

List of Tables

1	Heat transfer prediction accuracy of the five models, solid fins . . .	47
2	Heat transfer prediction accuracy of the five models, serrated fins .	48
3	Pressure drop prediction accuracy of the five models, solid fins . .	51
4	Pressure drop prediction accuracy of the five models, serrated fins	52
5	Heat transfer prediction accuracy of the five modified models, solid fins	58
6	Heat transfer prediction accuracy of the five modified models, serrated fins	59
7	Pressure drop prediction accuracy of the five modified models, solid fins	61
8	Pressure drop prediction accuracy of the five modified models, serrated fins	62
9	Measured and predicted Eu for geometry 1 at different Reynolds numbers	72
10	Measured and predicted $NuPr^{-1/3}$ for geometry 1 at different Reynolds numbers	74
11	Experimental uncertainties in pressure drop test	159
12	Experimental uncertainties in heat transfer test, gas side	160
13	Experimental uncertainties in heat transfer test, cooling side	161
14	Experimental uncertainty in heat transfer test for heat transfer coefficient	162

A Model performance

A.1 PFR

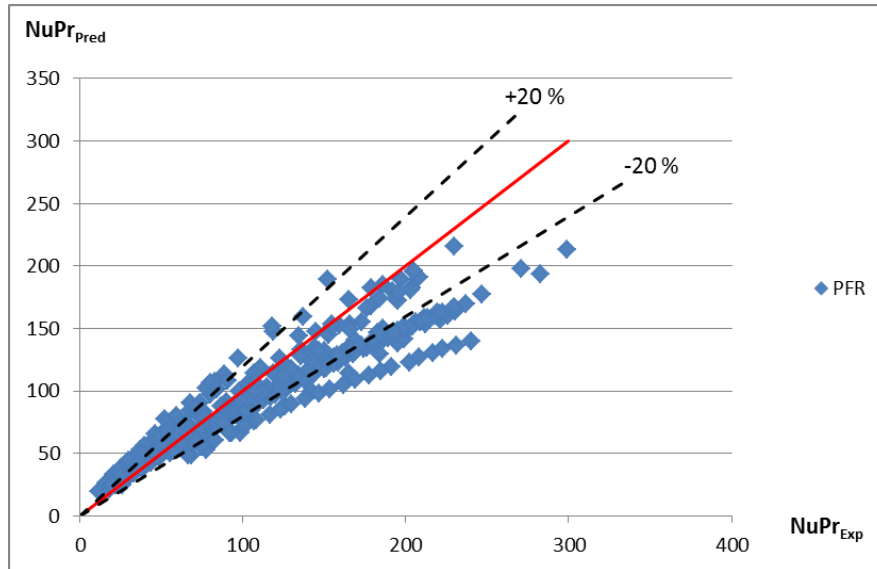


Figure 44: Heat transfer prediction accuracy of PFR, solid fins

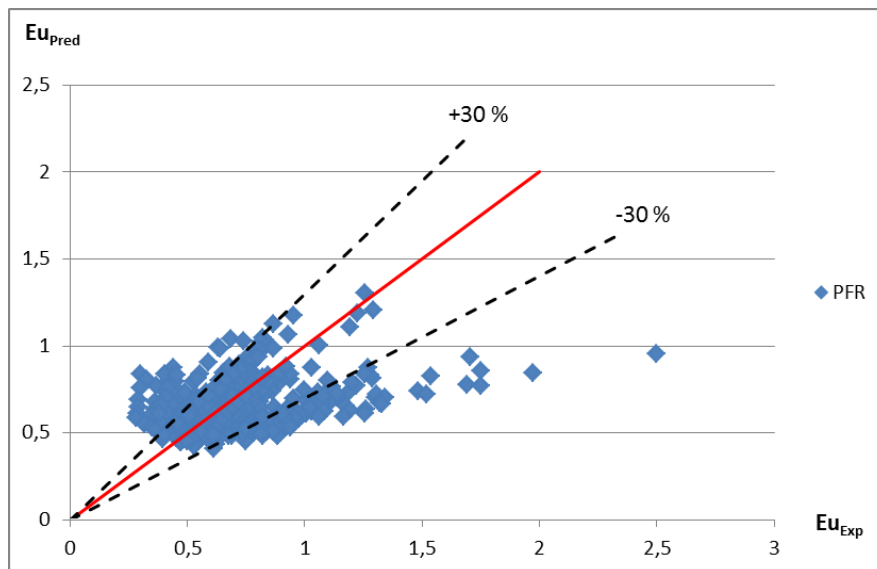


Figure 45: Pressure drop prediction accuracy of PFR, solid fins

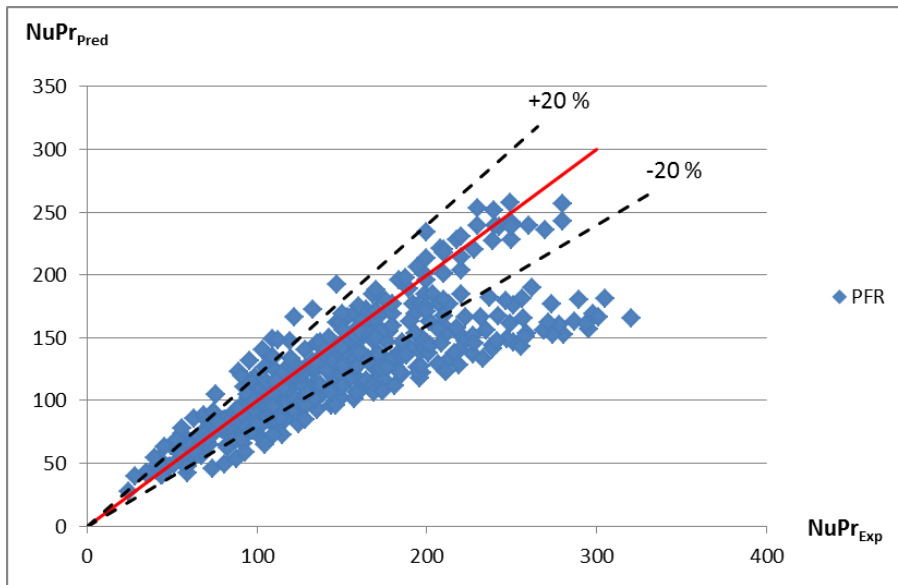


Figure 46: Heat transfer prediction accuracy of PFR, serrated fins

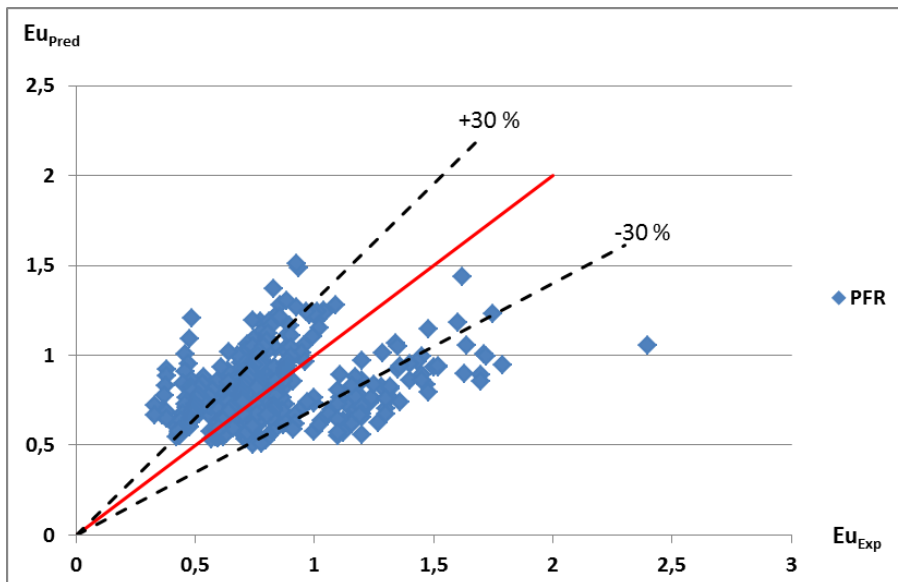


Figure 47: Pressure drop prediction accuracy of PFR, serrated fins

A.2 Nir

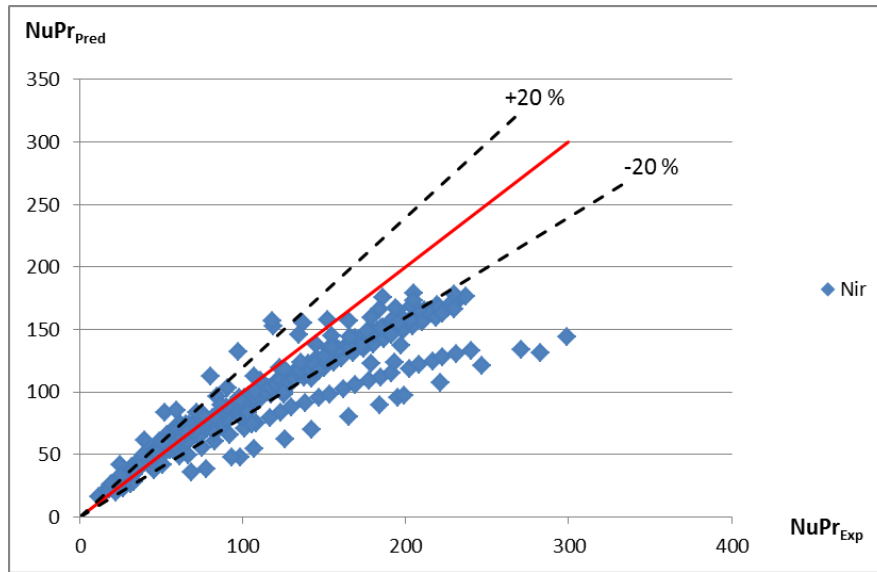


Figure 48: Heat transfer prediction accuracy of Nir, solid fins

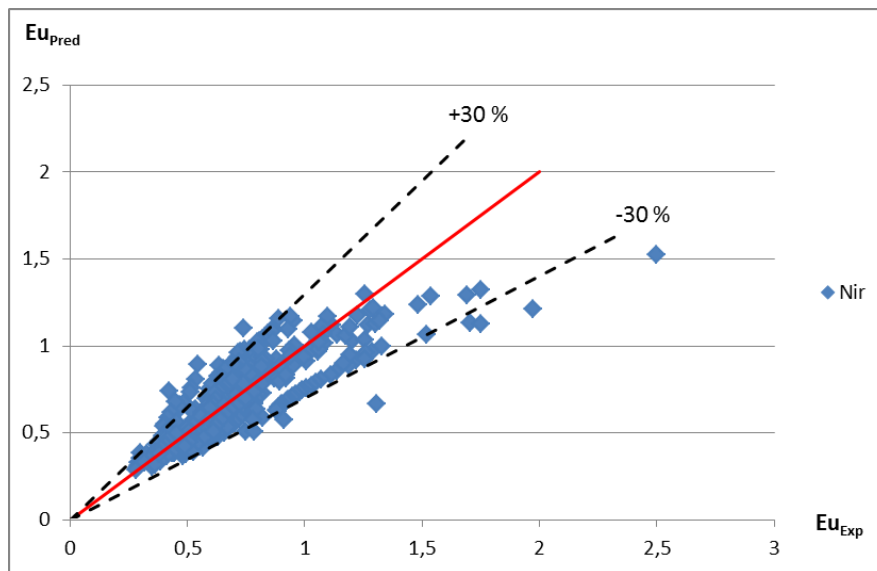


Figure 49: Pressure drop prediction accuracy of Nir, solid fins

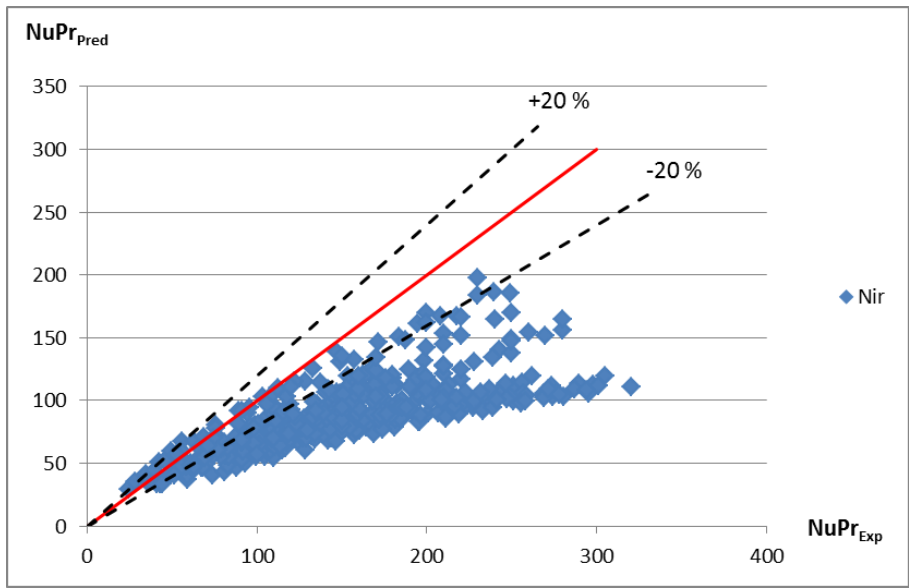


Figure 50: Heat transfer prediction accuracy of Nir, serrated fins

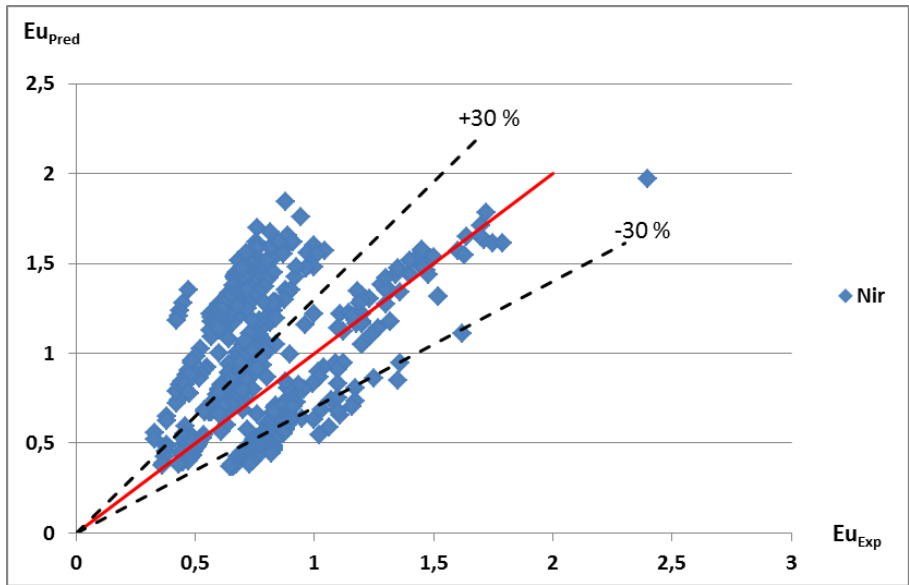


Figure 51: Pressure drop prediction accuracy of Nir, serrated fins

A.3 HTFS1

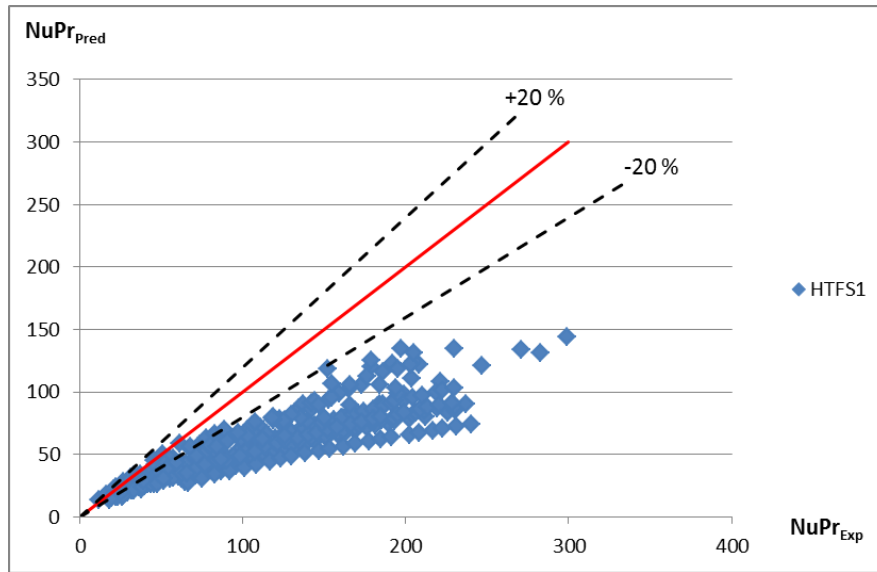


Figure 52: Heat transfer prediction accuracy of HTFS1, solid fins

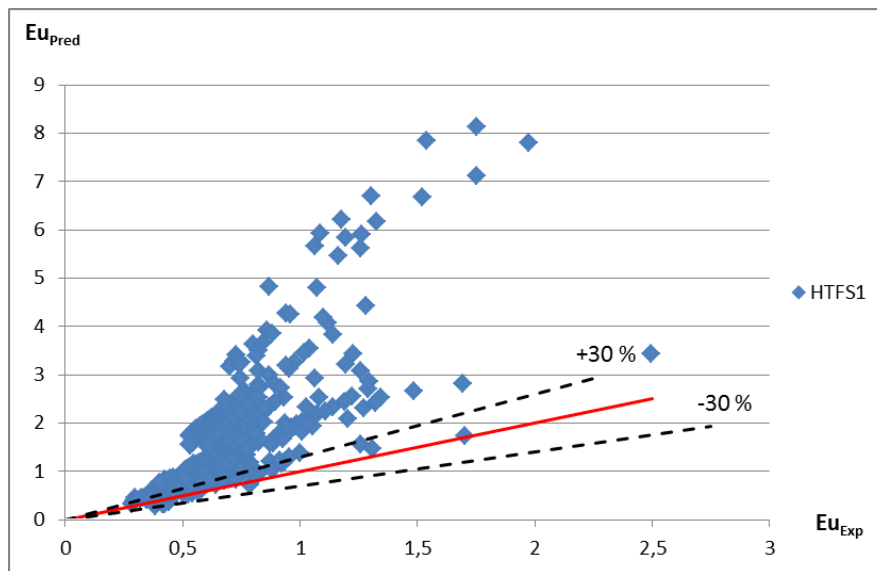


Figure 53: Pressure drop prediction accuracy of HTFS1, solid fins

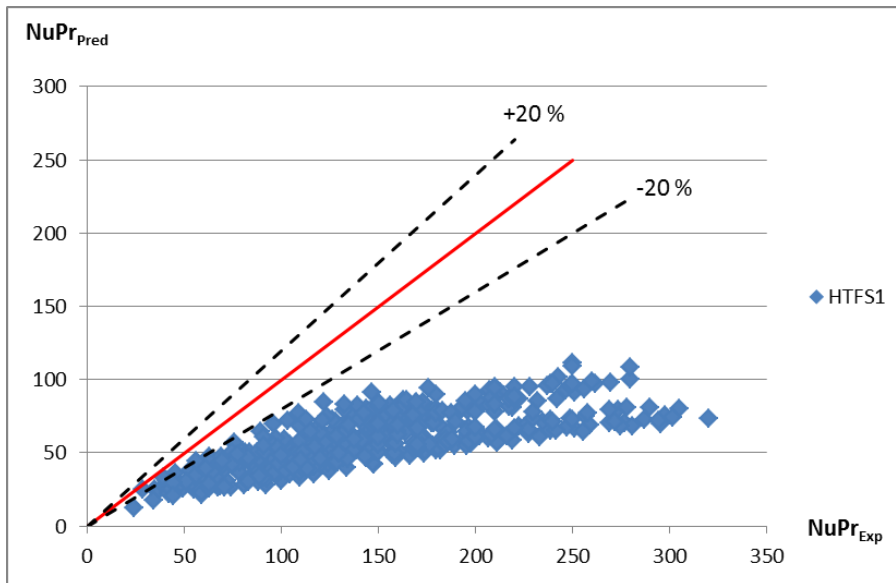


Figure 54: Heat transfer prediction accuracy of HTFS1, serrated fins

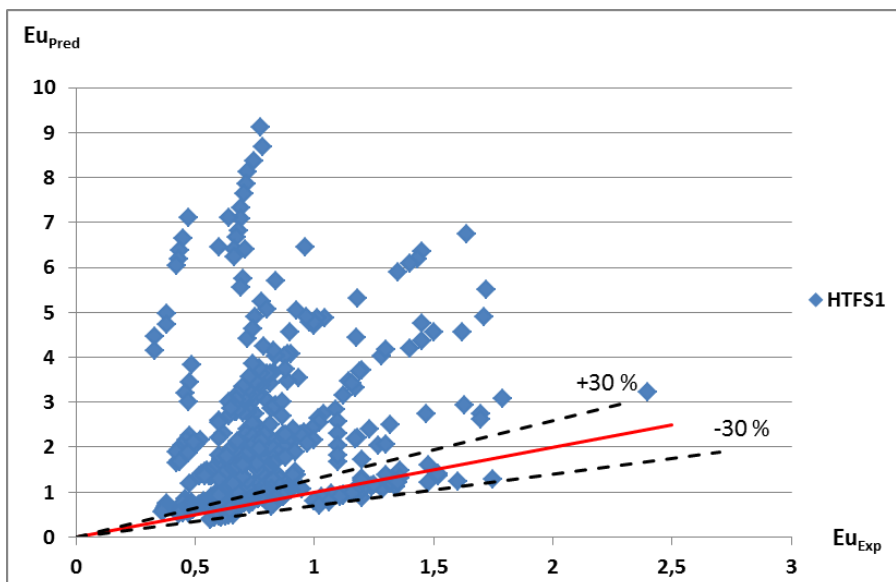


Figure 55: Pressure drop prediction accuracy of HTFS1, serrated fins

A.4 HTFS2

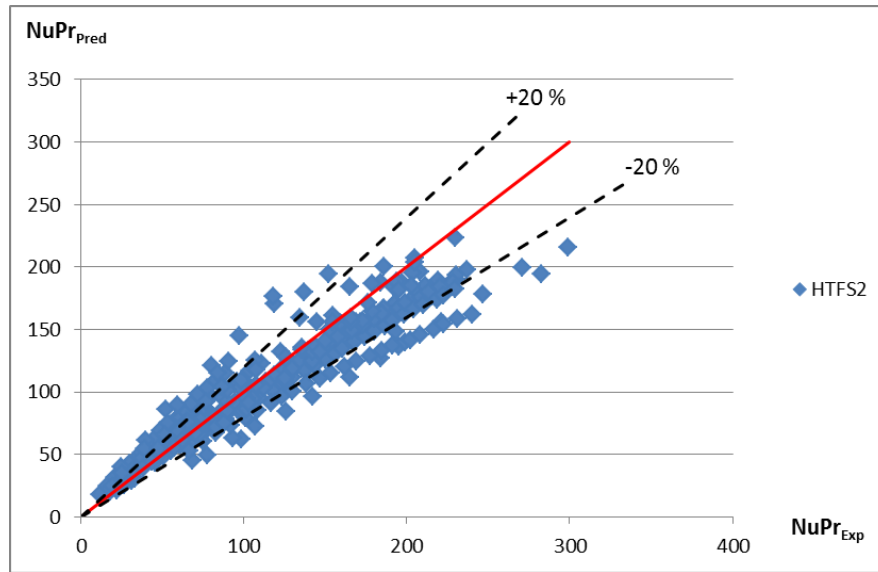


Figure 56: Heat transfer prediction accuracy of HTFS2, solid fins

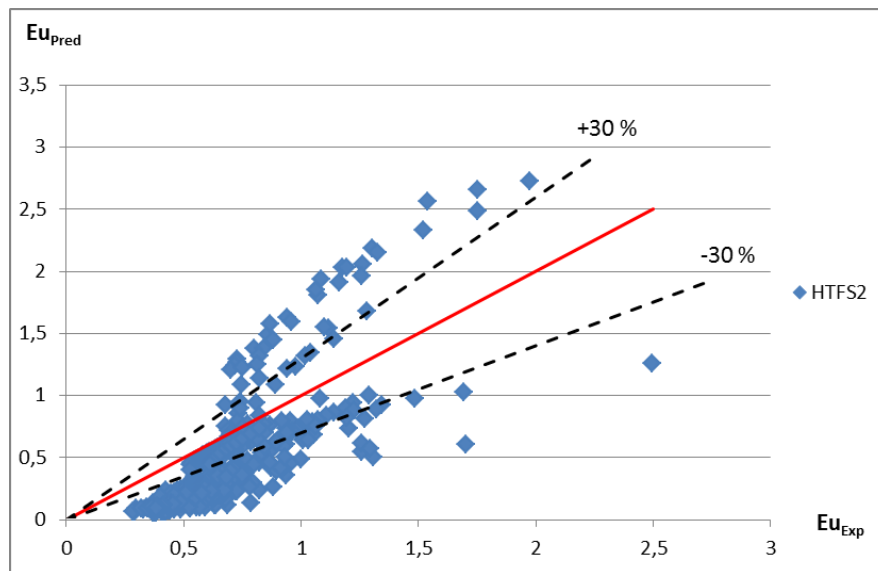


Figure 57: Pressure drop prediction accuracy of HTFS2, solid fins

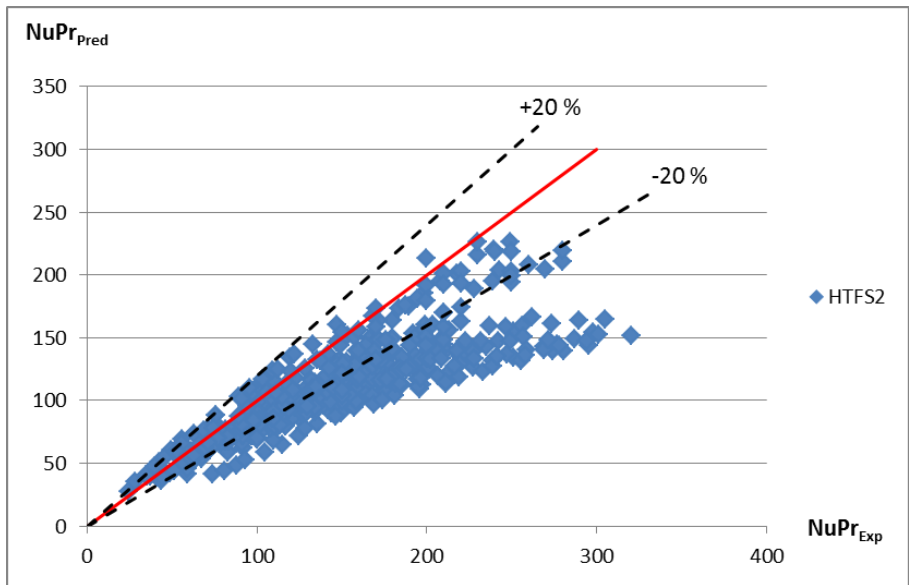


Figure 58: Heat transfer prediction accuracy of HTFS2, serrated fins

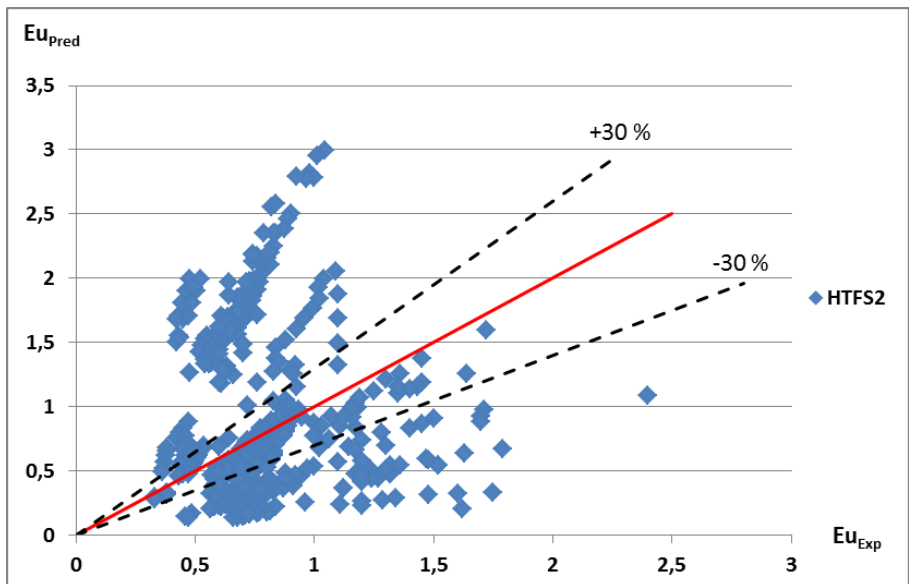


Figure 59: Pressure drop prediction accuracy of HTFS2, serrated fins

A.5 HTFS3

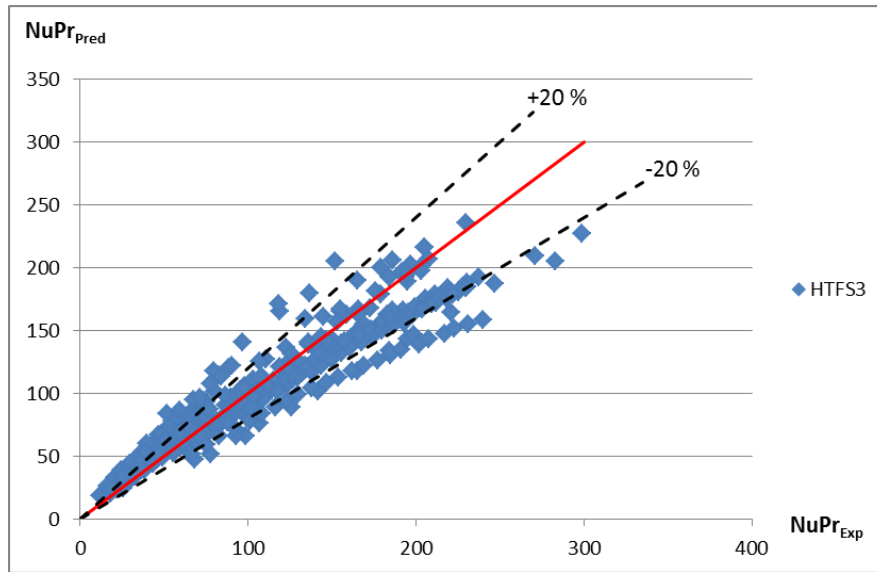


Figure 60: Heat transfer prediction accuracy of HTFS3, solid fins

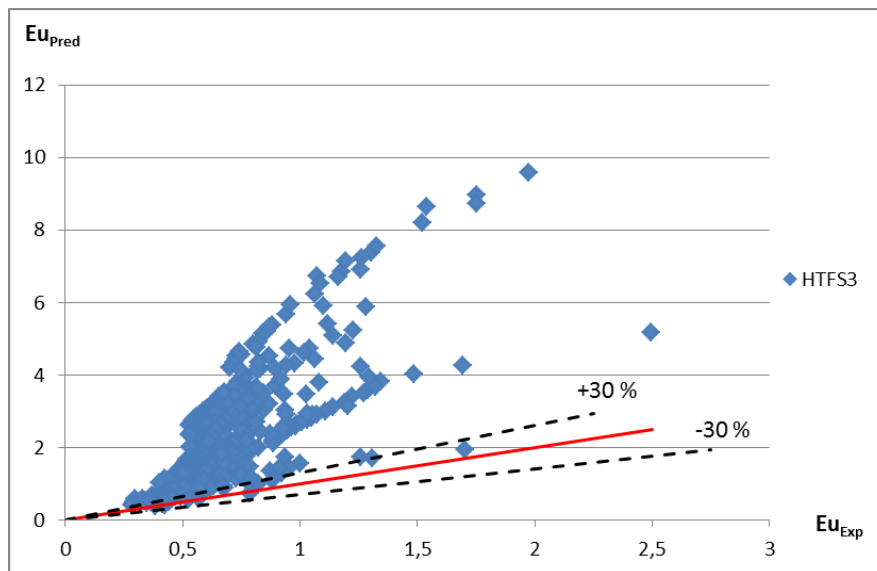


Figure 61: Pressure drop prediction accuracy of HTFS3, solid fins

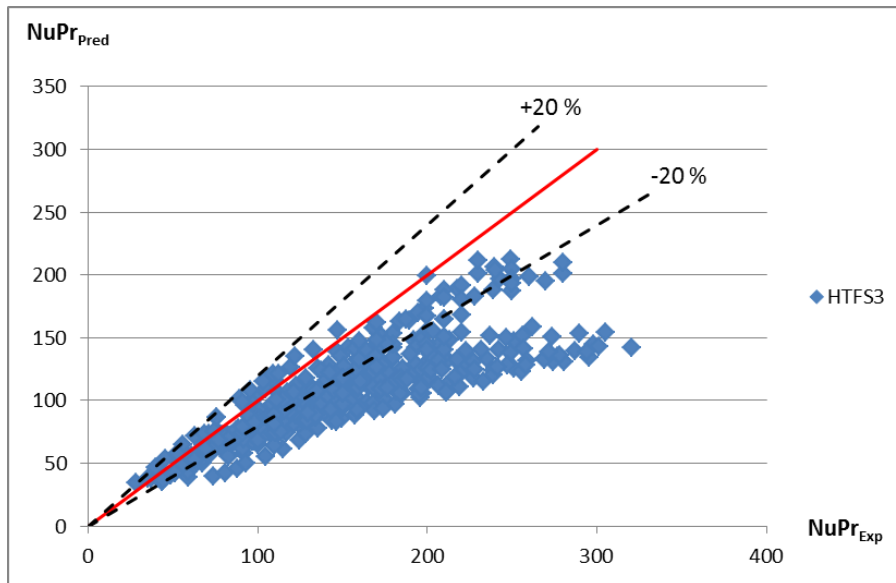


Figure 62: Heat transfer prediction accuracy of HTFS3, serrated fins

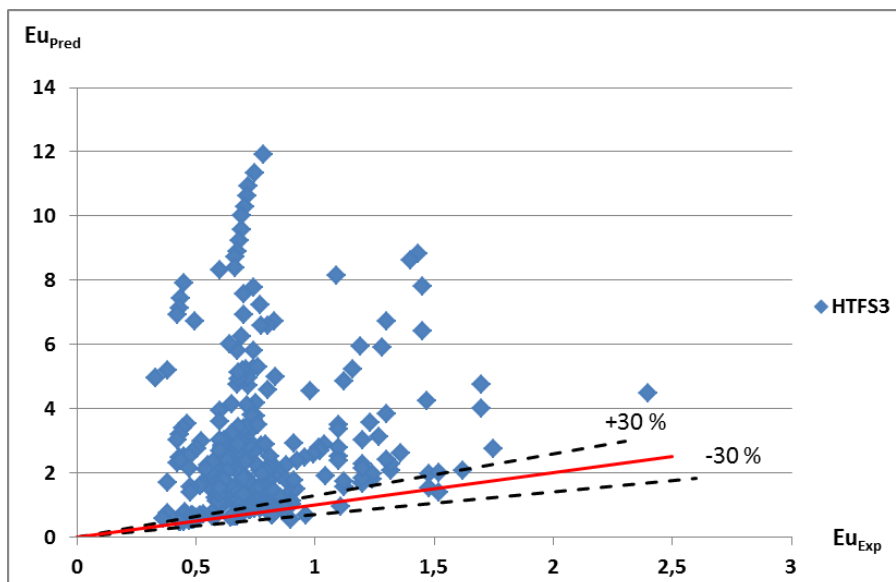


Figure 63: Pressure drop prediction accuracy of HTFS3, serrated fins

B Geometry dependency

B.1 PFR

Dependency on $\frac{P_T}{P_L}$

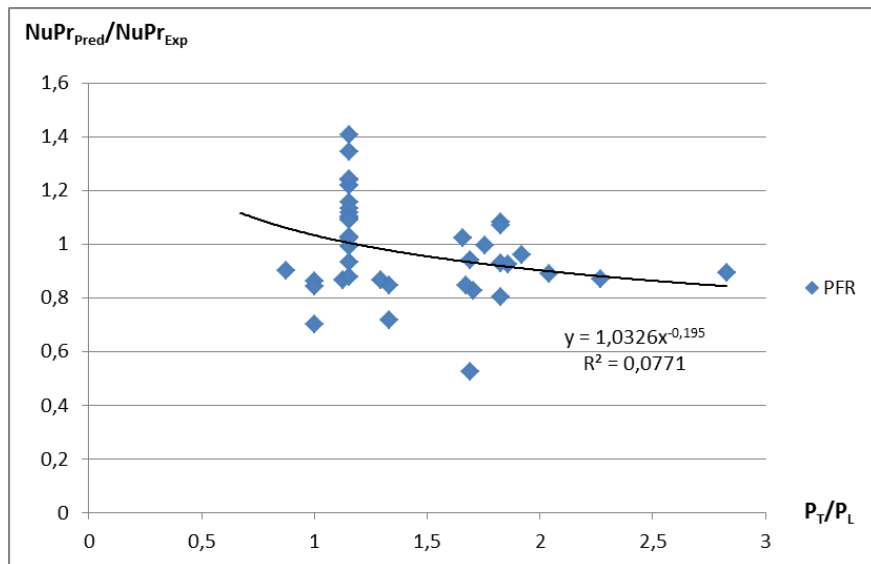


Figure 64: Predicted heat transfer dependency on $\frac{P_T}{P_L}$ for PFR, solid fins

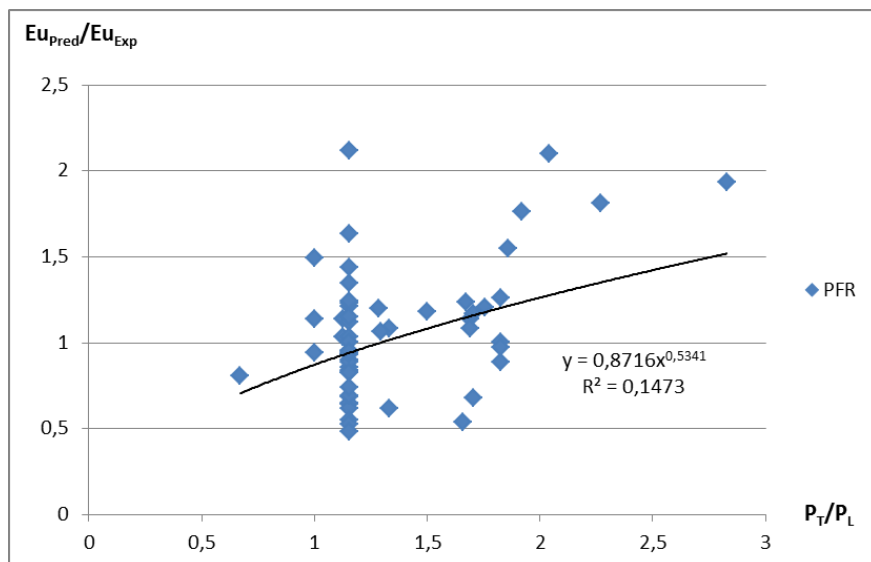


Figure 65: Predicted pressure drop dependency on $\frac{P_T}{P_L}$ for PFR, solid fins

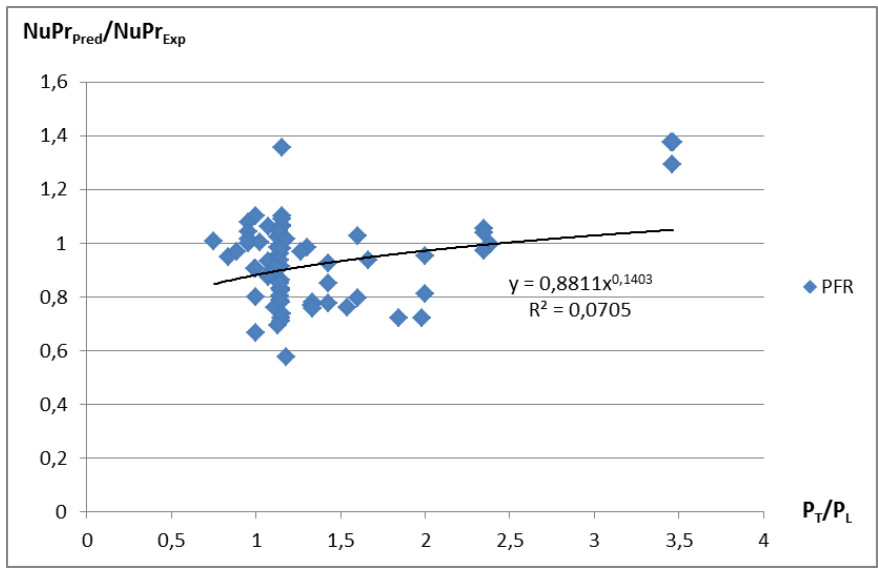


Figure 66: Predicted heat transfer dependency on $\frac{P_T}{P_L}$ for PFR, serrated fins

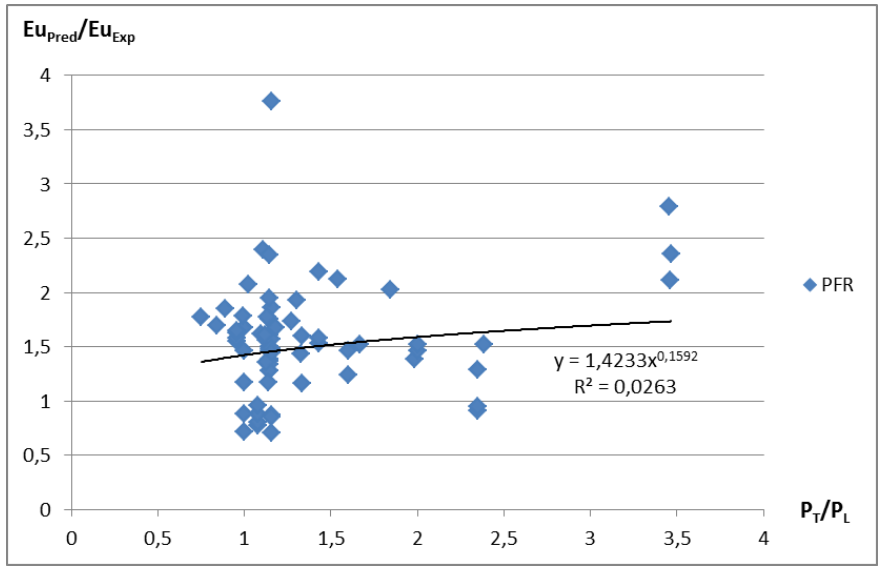


Figure 67: Predicted pressure drop dependency on $\frac{P_T}{P_L}$ for PFR, serrated fins

Dependency on P_T

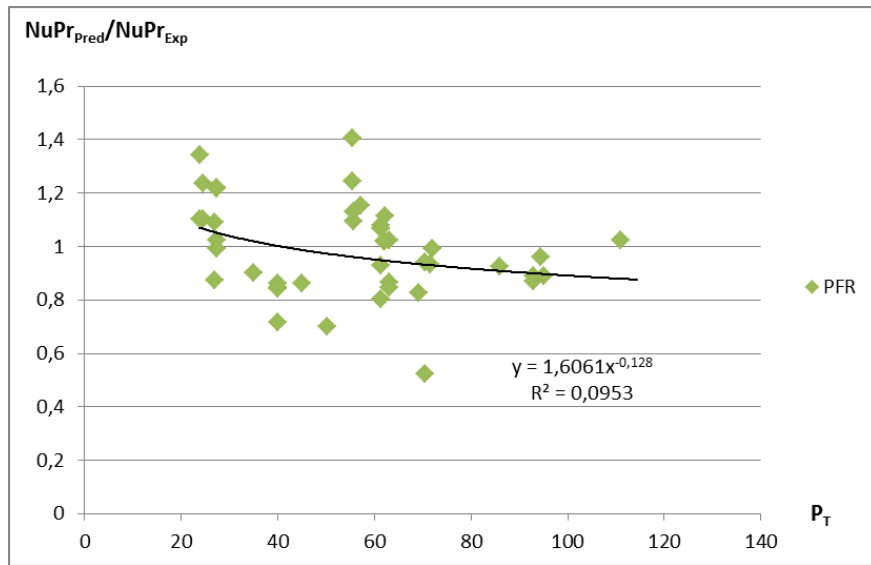


Figure 68: Predicted heat transfer dependency on P_T for PFR, solid fins

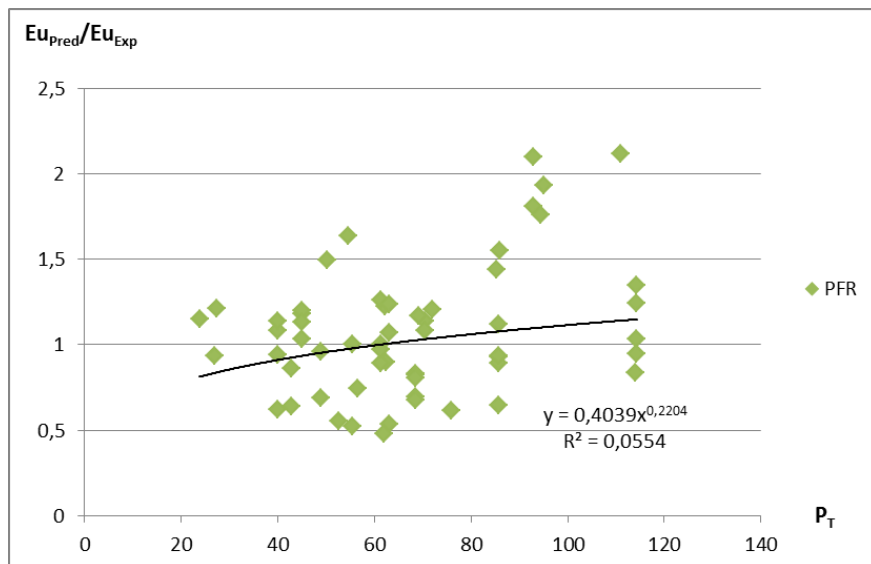


Figure 69: Predicted pressure drop dependency on P_T for PFR, solid fins

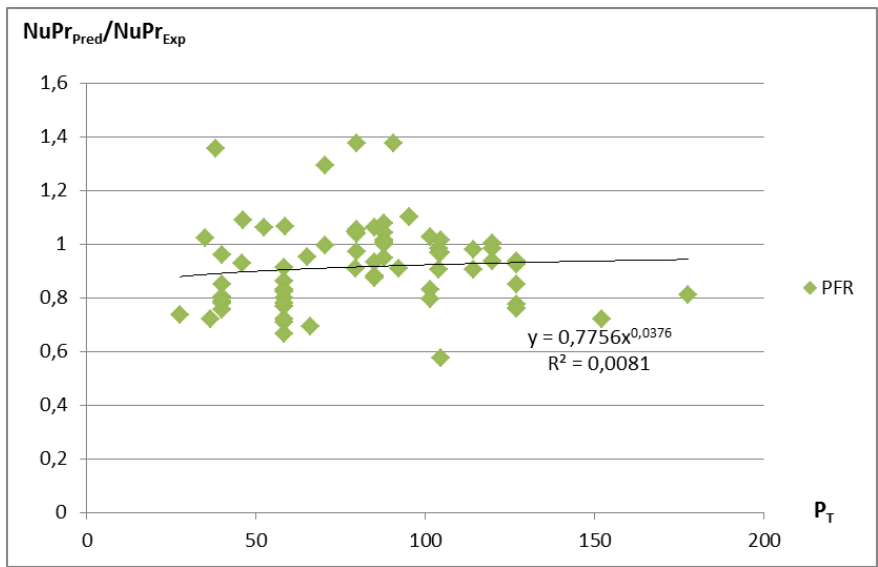


Figure 70: Predicted heat transfer dependency on P_T for PFR, serrated fins

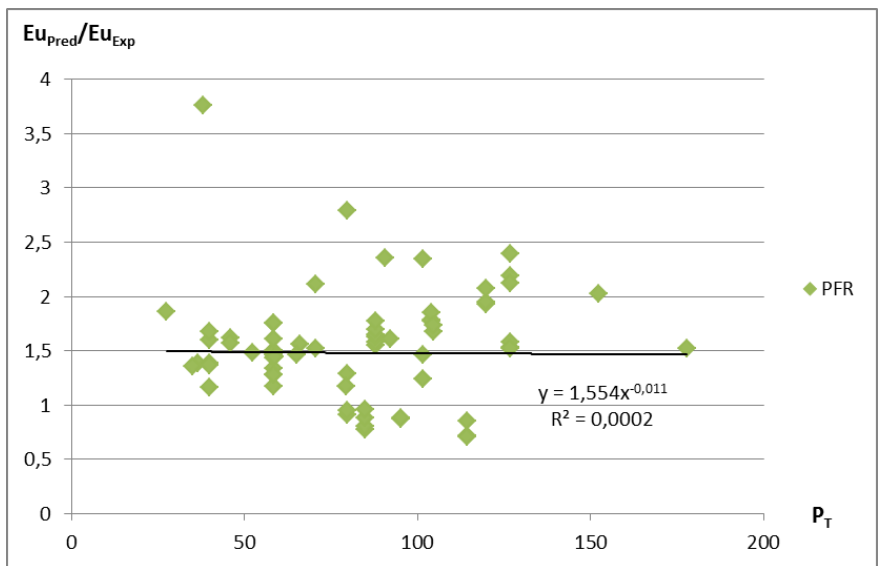


Figure 71: Predicted pressure drop dependency on P_T for PFR, serrated fins

Dependency on $\frac{h_f}{p_f}$

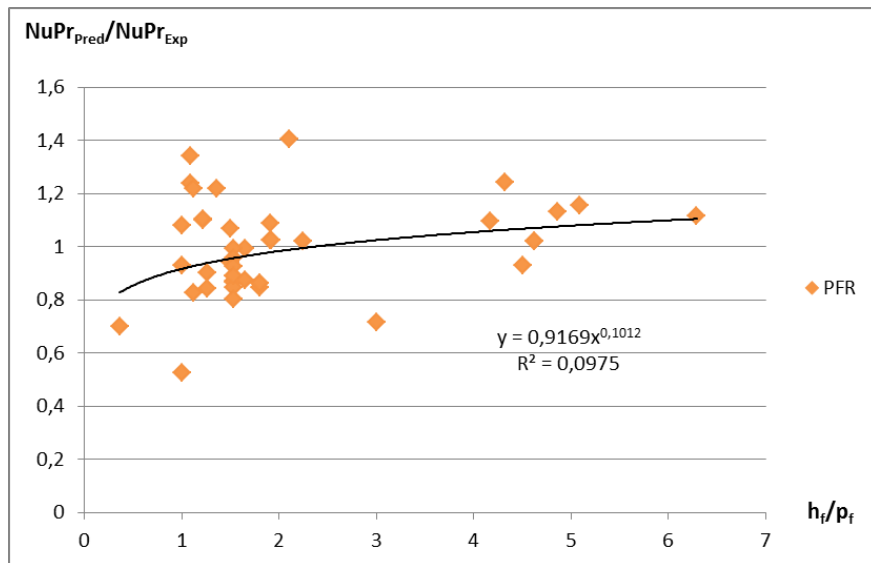


Figure 72: Predicted heat transfer dependency on $\frac{h_f}{p_f}$ for PFR, solid fins

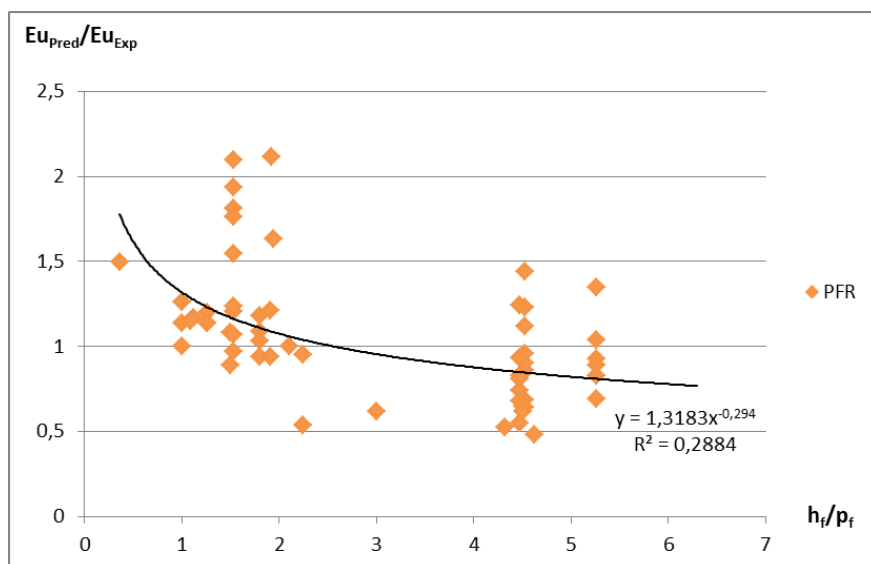


Figure 73: Predicted pressure drop dependency on $\frac{h_f}{p_f}$ for PFR, solid fins

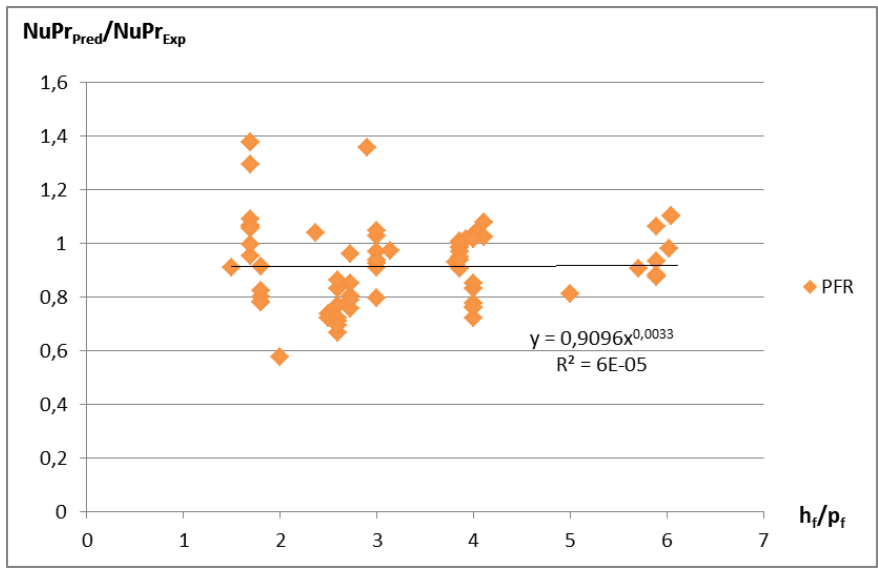


Figure 74: Predicted heat transfer dependency on $\frac{h_f}{p_f}$ for PFR, serrated fins

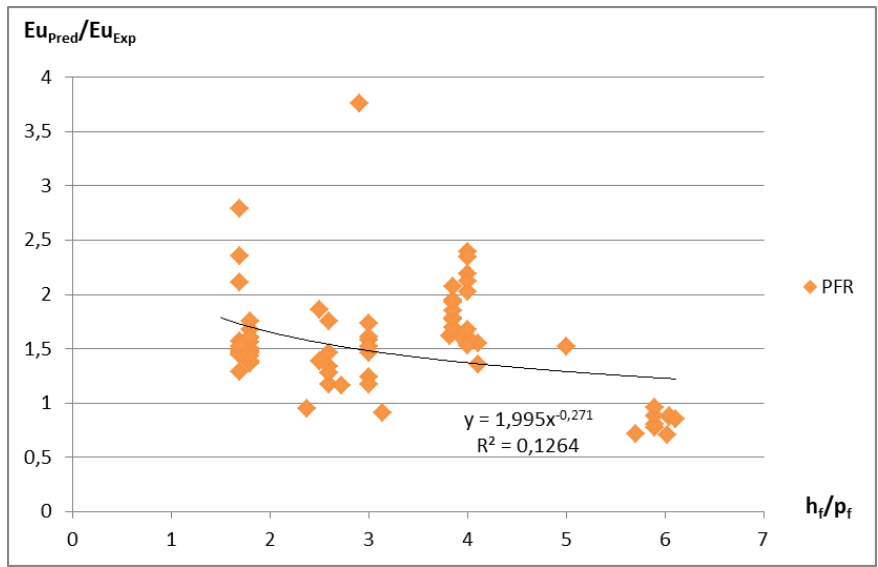


Figure 75: Predicted pressure drop dependency on $\frac{h_f}{p_f}$ for PFR, serrated fins

Dependency on A_r

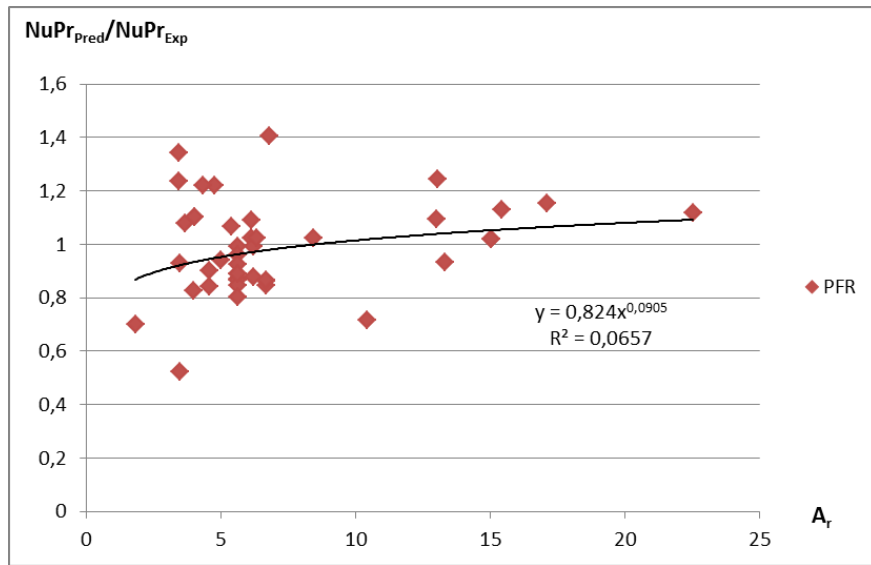


Figure 76: Predicted heat transfer dependency on A_r for PFR, solid fins

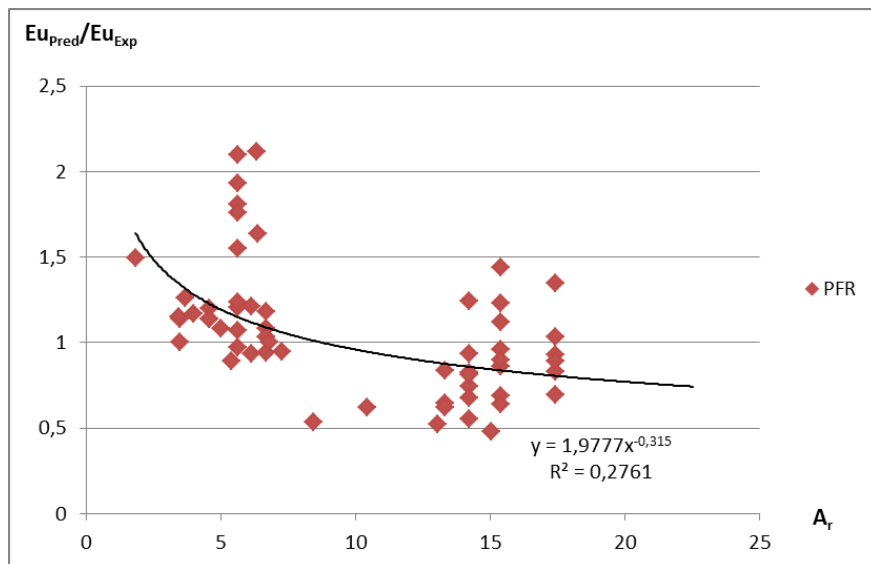


Figure 77: Predicted pressure drop dependency on A_r for PFR, solid fins

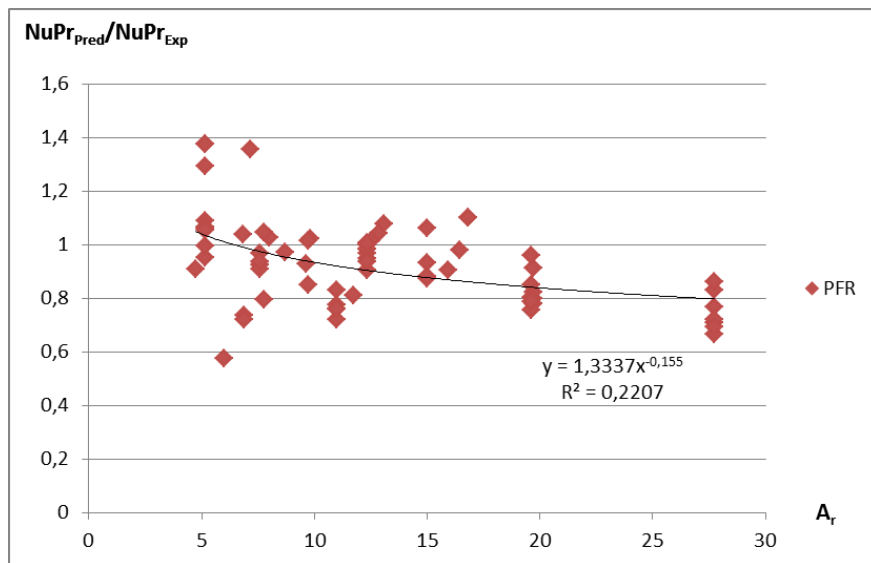


Figure 78: Predicted heat transfer dependency on A_r for PFR, serrated fins

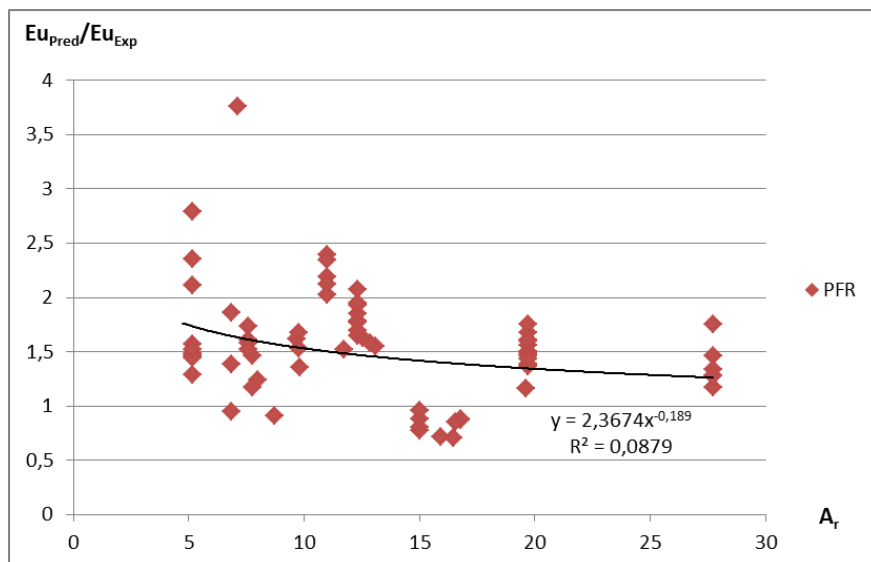


Figure 79: Predicted pressure drop dependency on A_r for PFR, serrated fins

Dependency on W

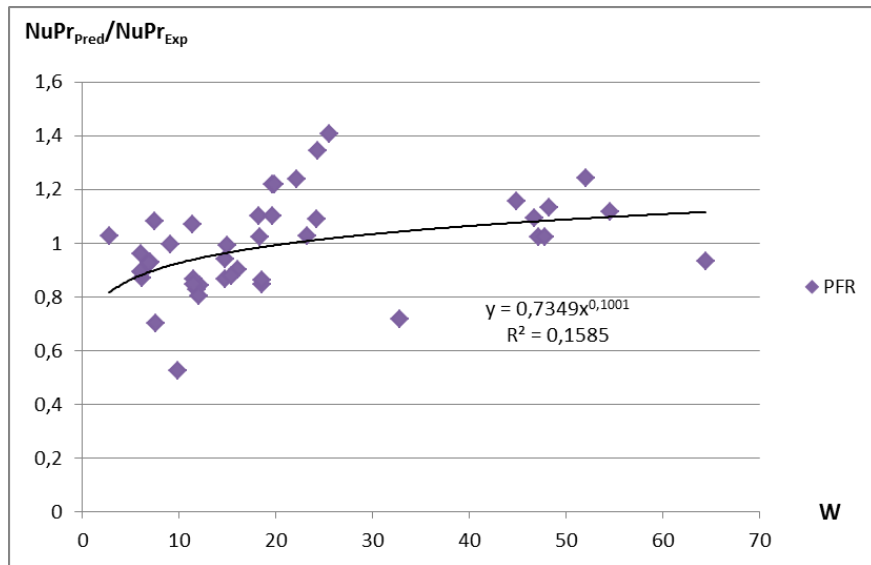


Figure 80: Predicted heat transfer dependency on W for PFR, solid fins

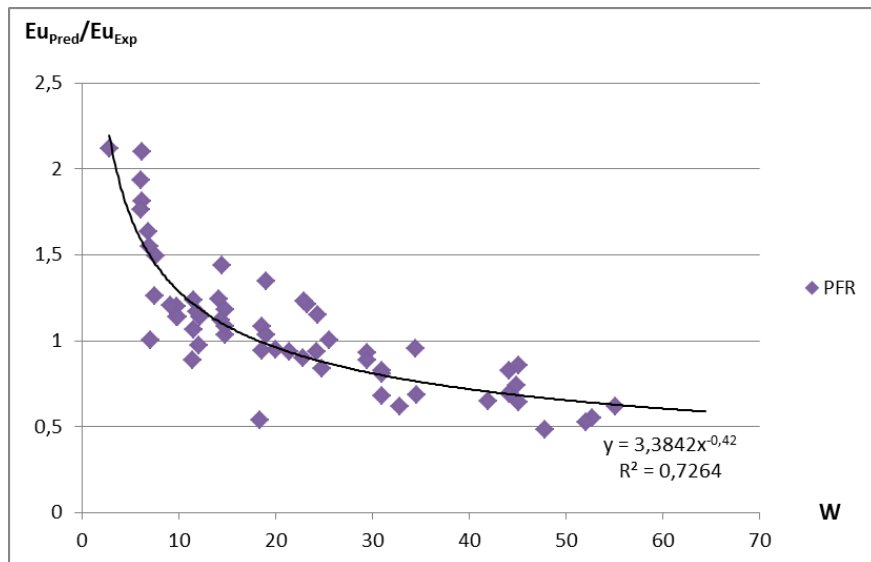


Figure 81: Predicted pressure drop dependency on W for PFR, solid fins

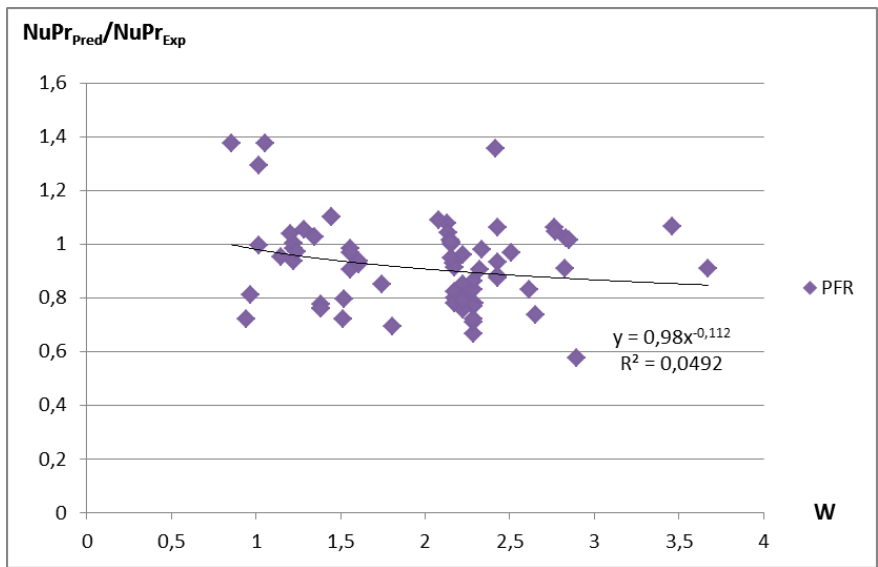


Figure 82: Predicted heat transfer dependency on W for PFR, serrated fins

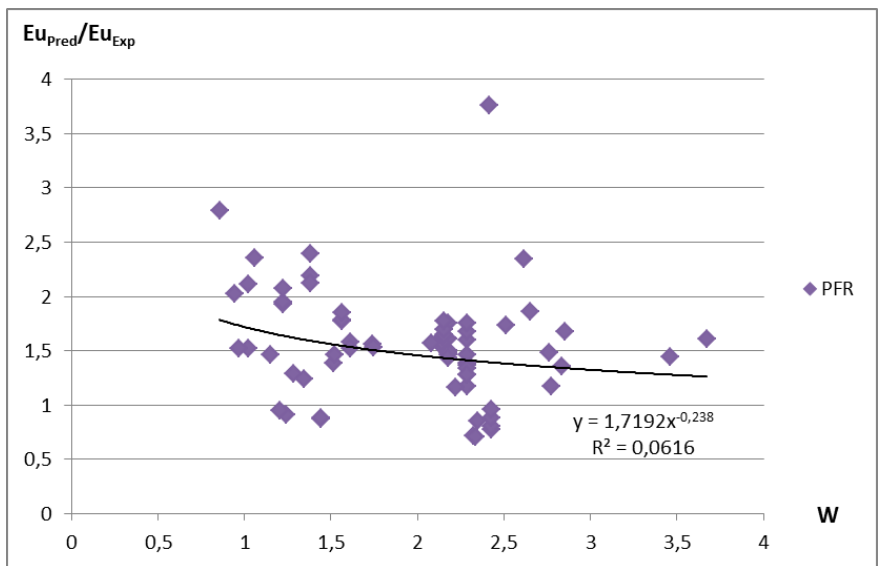


Figure 83: Predicted pressure drop dependency on W for PFR, serrated fins

B.2 Nir

Dependency on $\frac{P_T}{P_L}$

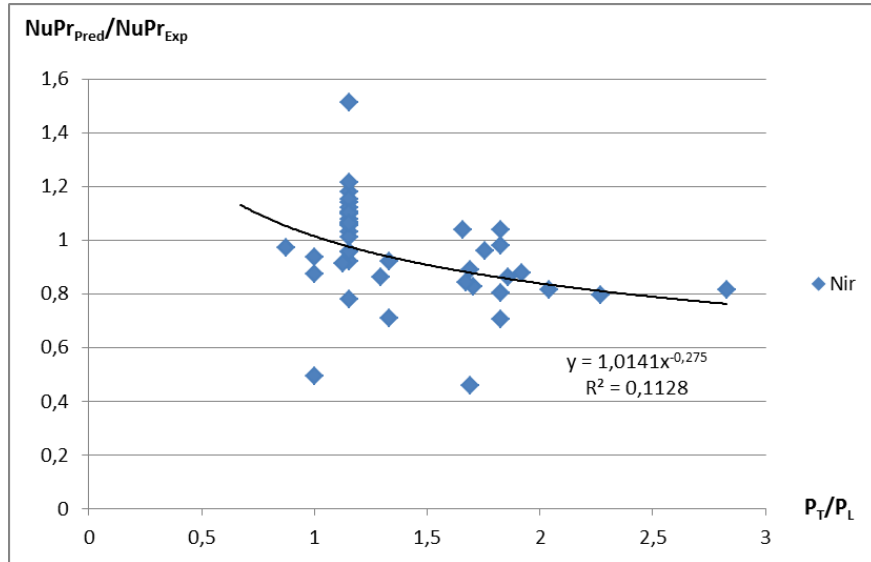


Figure 84: Predicted heat transfer dependency on $\frac{P_T}{P_L}$ for Nir, solid fins

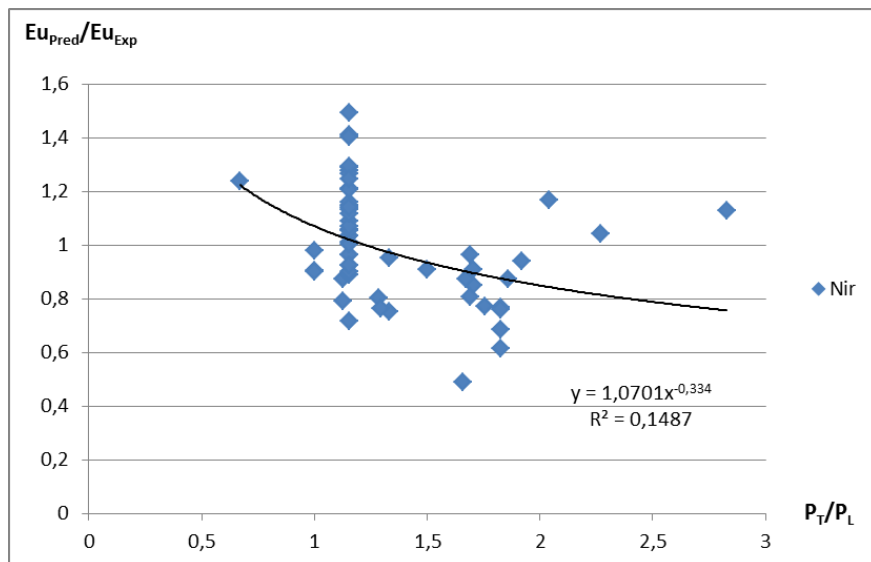


Figure 85: Predicted pressure drop dependency on $\frac{P_T}{P_L}$ for Nir, solid fins

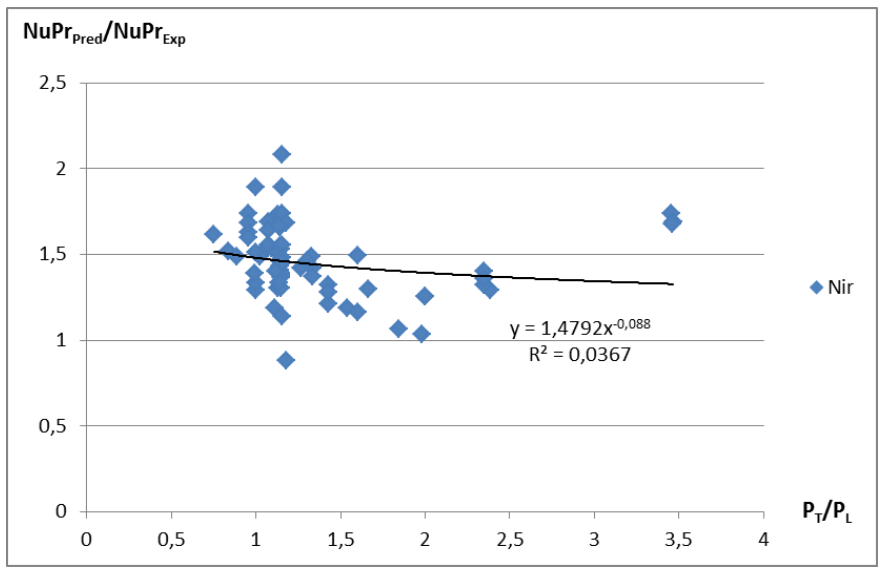


Figure 86: Predicted heat transfer dependency on $\frac{P_T}{P_L}$ for Nir, serrated fins

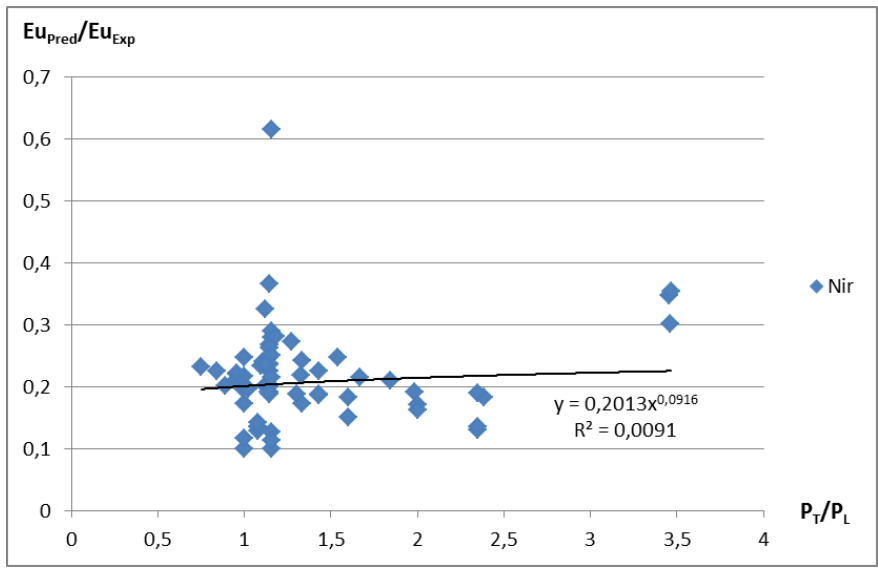


Figure 87: Predicted pressure drop dependency on $\frac{P_T}{P_L}$ for Nir, serrated fins

Dependency on P_T

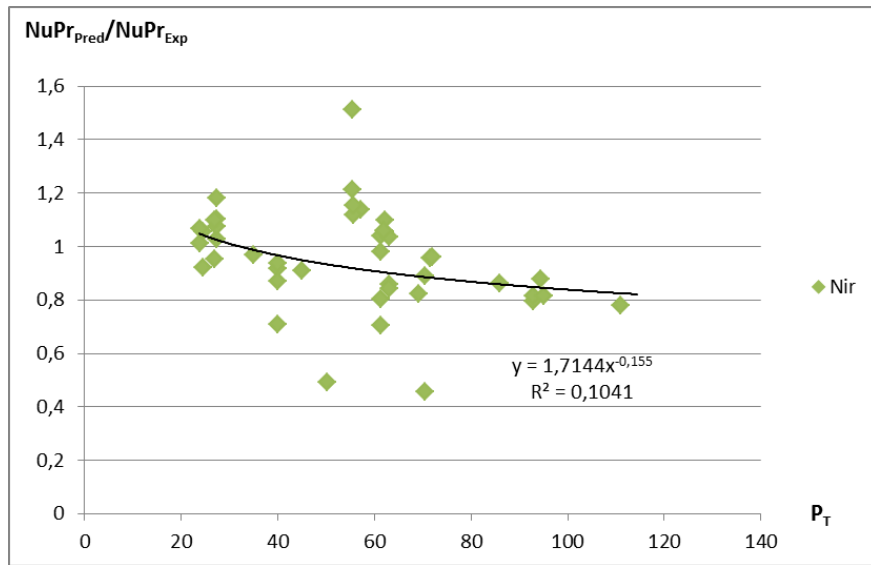


Figure 88: Predicted heat transfer dependency on P_T for Nir, solid fins

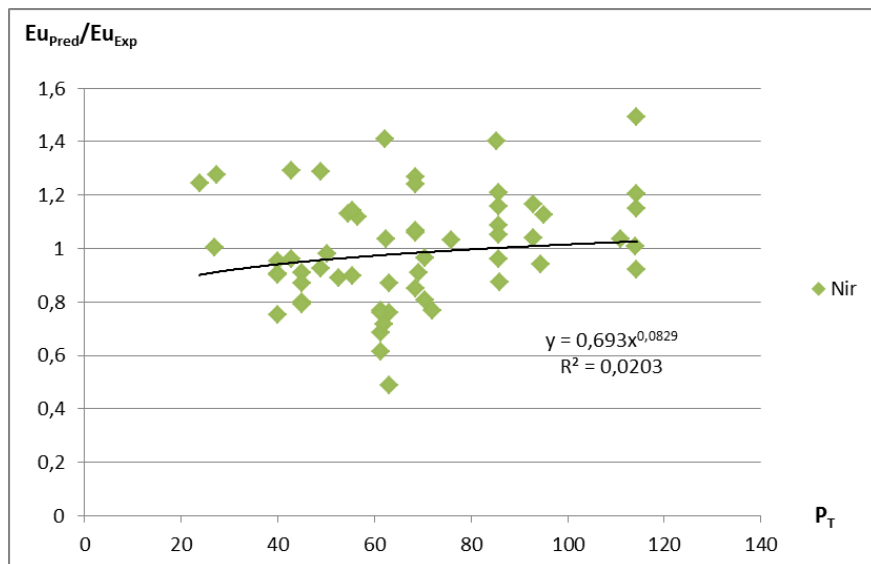


Figure 89: Predicted pressure drop dependency on P_T for Nir, solid fins

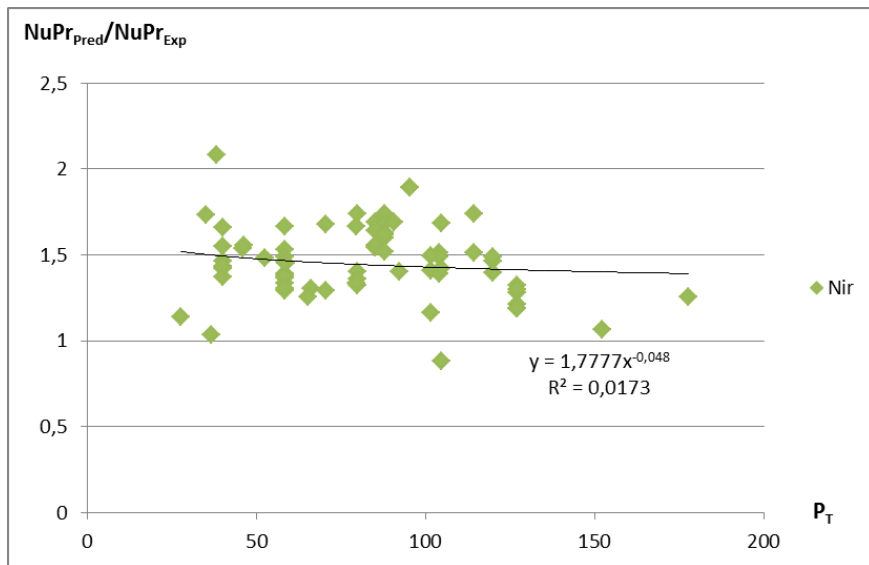


Figure 90: Predicted heat transfer dependency on P_T for Nir, serrated fins

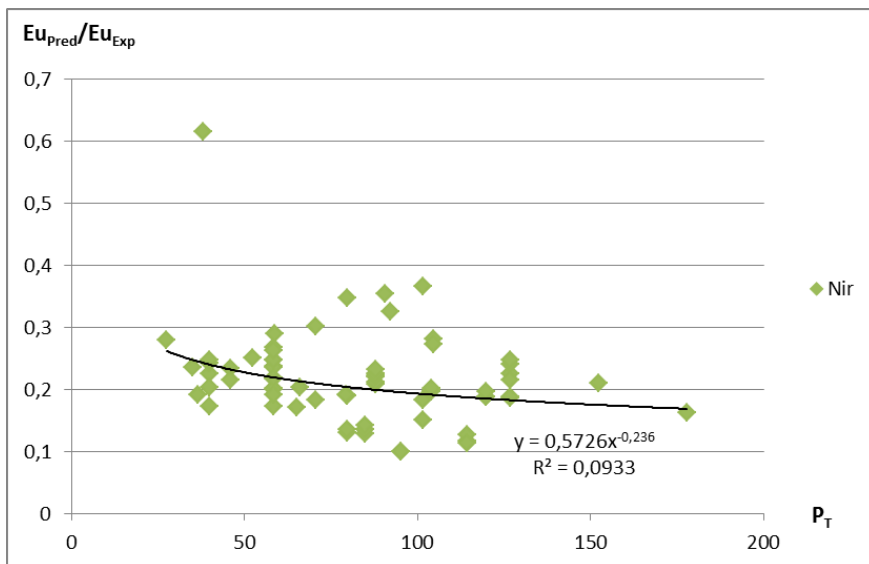


Figure 91: Predicted pressure drop dependency on P_T for Nir, serrated fins

Dependency on $\frac{h_f}{p_f}$

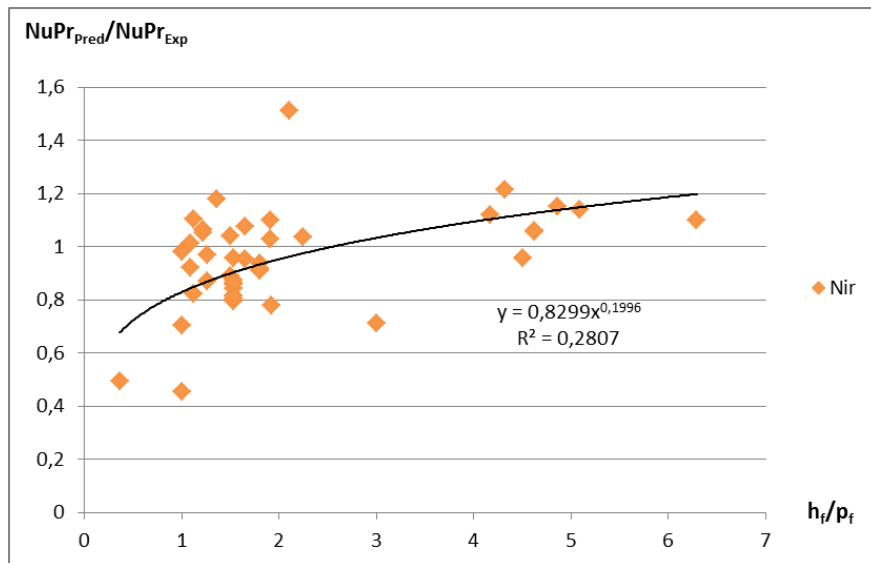


Figure 92: Predicted heat transfer dependency on $\frac{h_f}{p_f}$ for Nir, solid fins

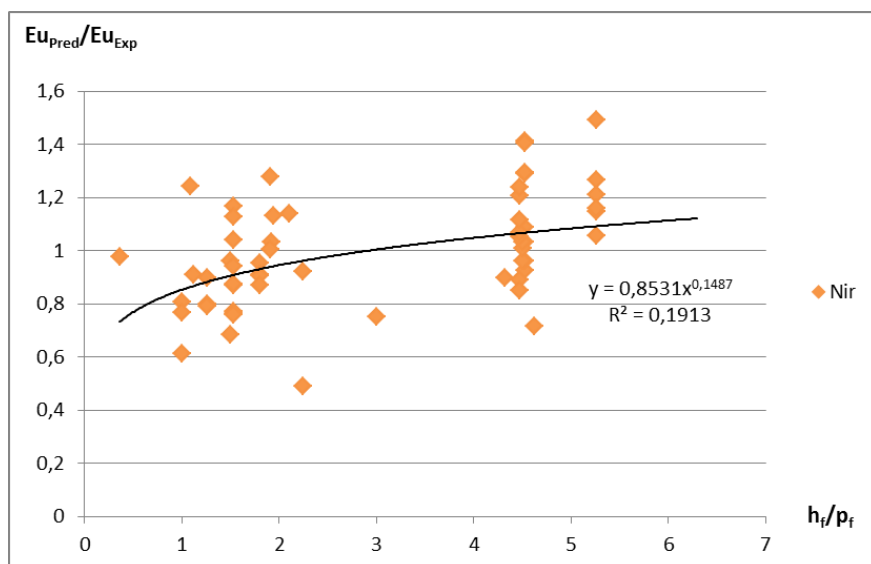


Figure 93: Predicted pressure drop dependency on $\frac{h_f}{p_f}$ for Nir, solid fins

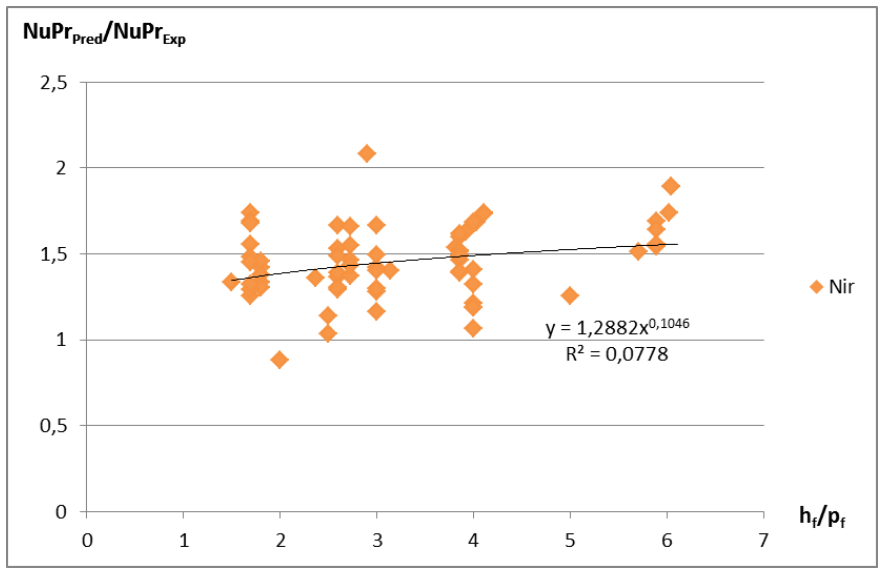


Figure 94: Predicted heat transfer dependency on $\frac{h_f}{p_f}$ for Nir, serrated fins

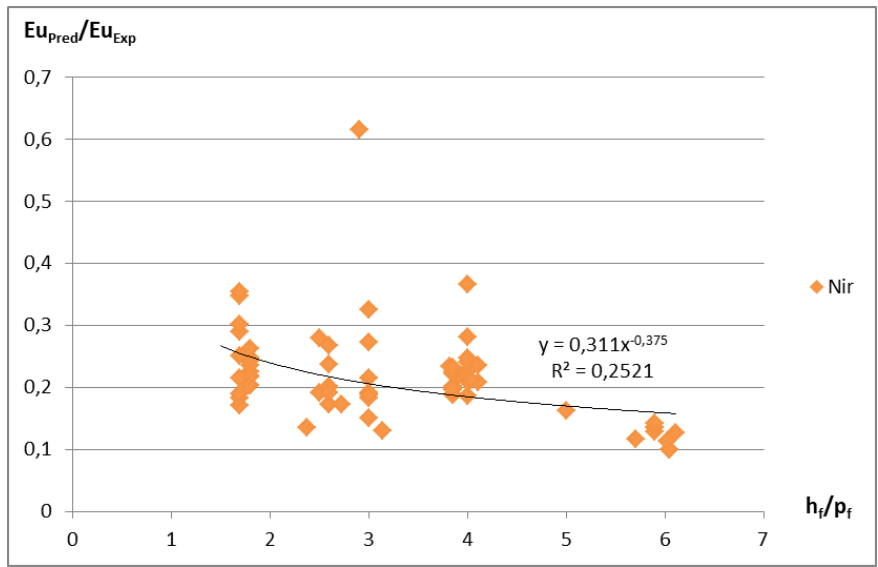


Figure 95: Predicted pressure drop dependency on $\frac{h_f}{p_f}$ for Nir, serrated fins

Dependency on A_r

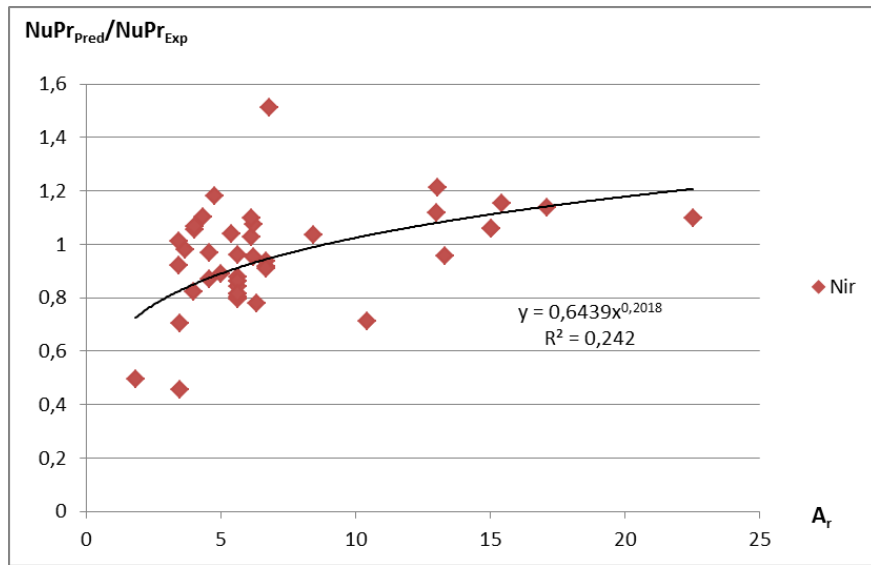


Figure 96: Predicted heat transfer dependency on A_r for Nir, solid fins

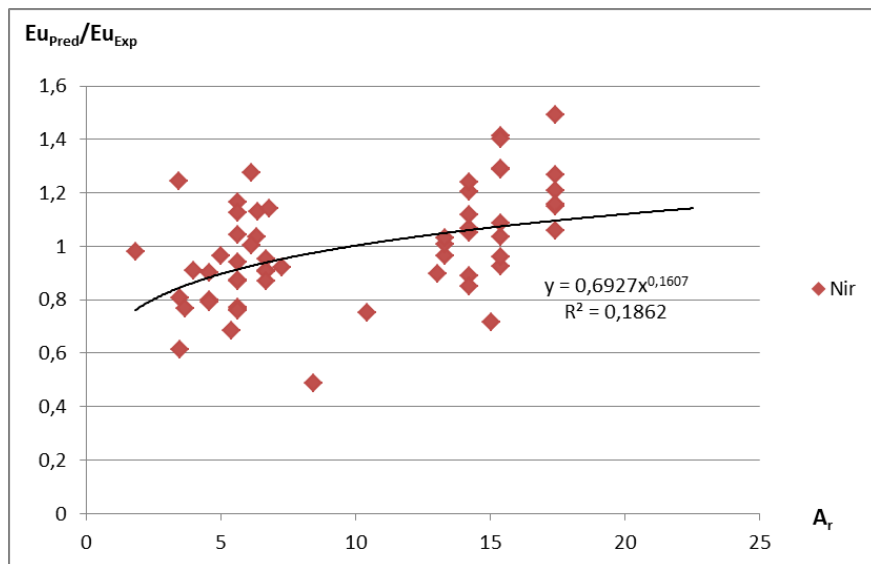


Figure 97: Predicted pressure drop dependency on A_r for Nir, solid fins

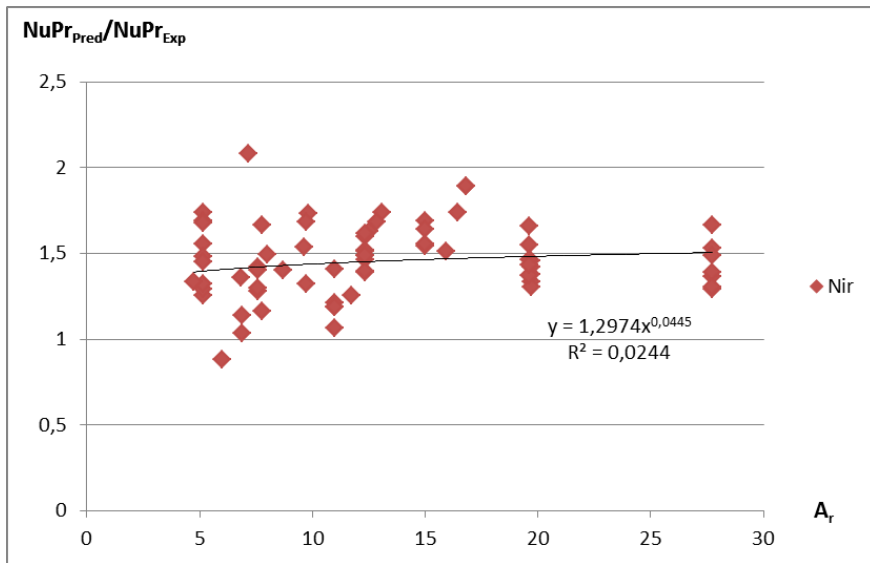


Figure 98: Predicted heat transfer dependency on A_r for Nir, serrated fins

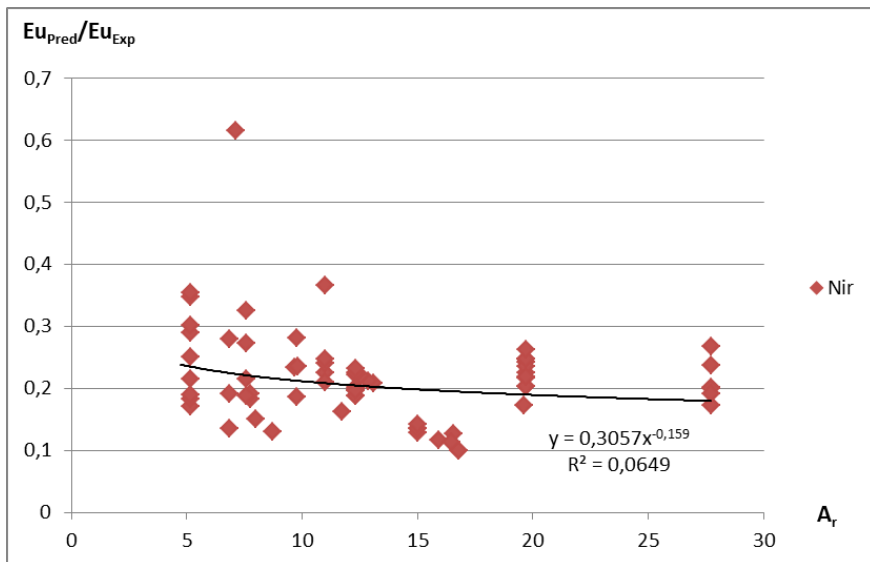


Figure 99: Predicted pressure drop dependency on A_r for Nir, serrated fins

Dependency on W

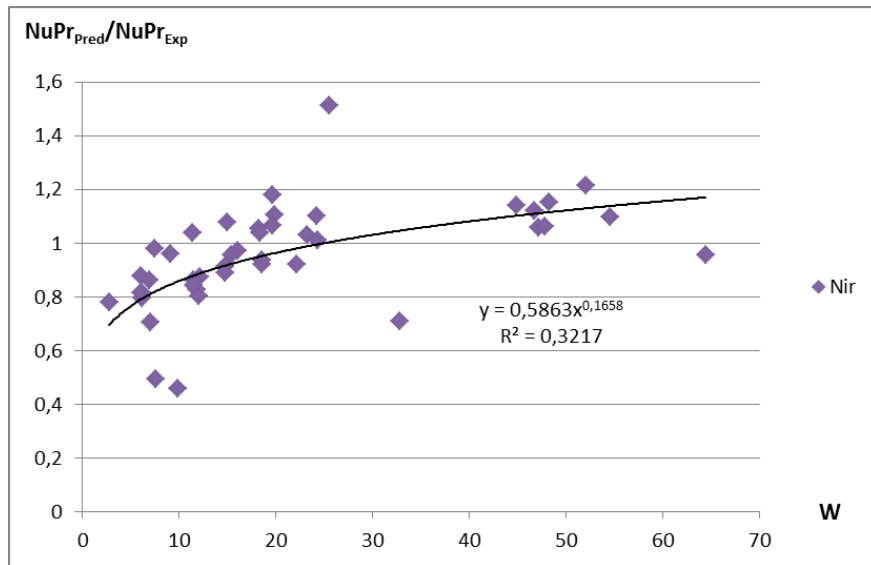


Figure 100: Predicted heat transfer dependency on W for Nir, solid fins

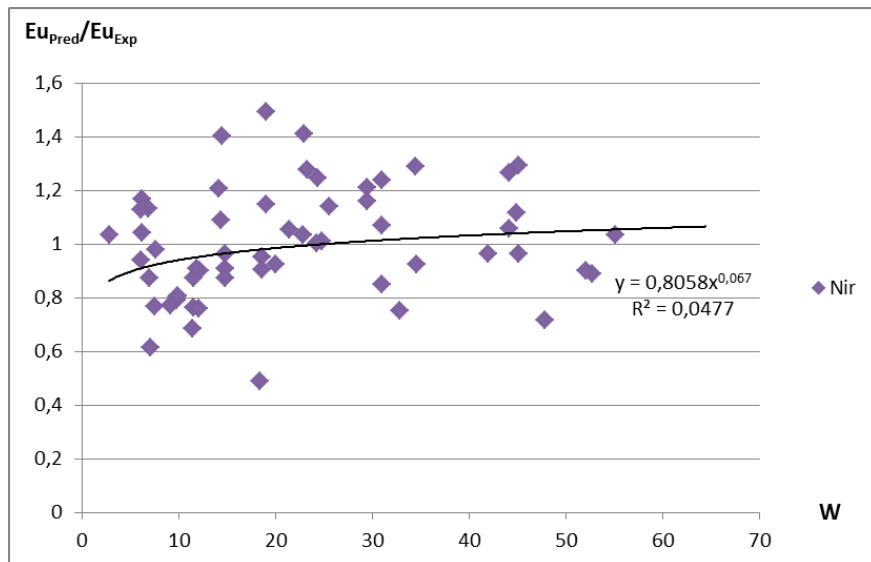


Figure 101: Predicted pressure drop dependency on W for Nir, solid fins

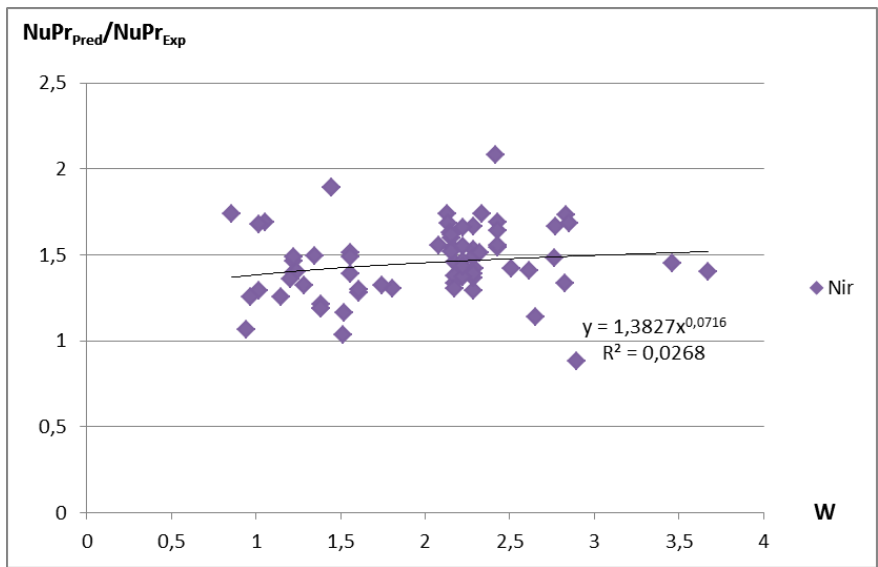


Figure 102: Predicted heat transfer dependency on W for Nir, serrated fins

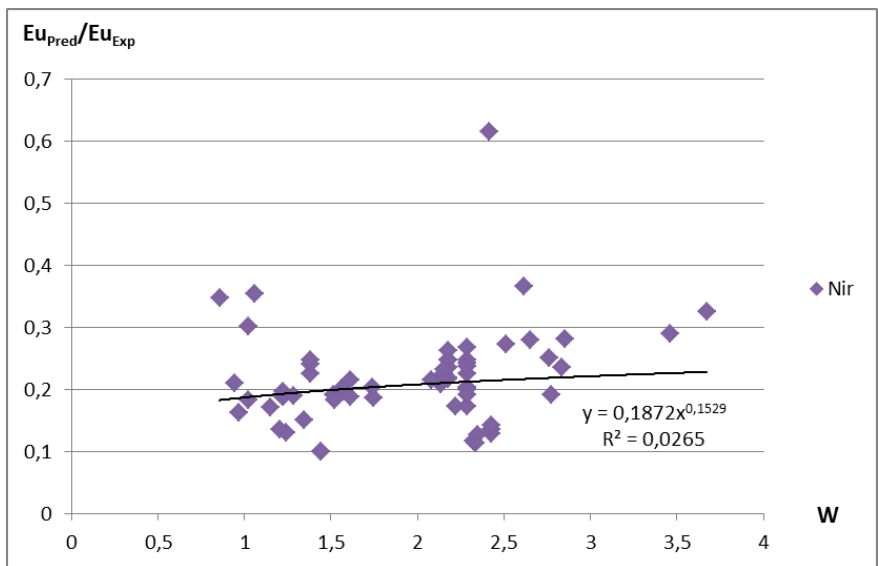


Figure 103: Predicted pressure drop dependency on W for Nir, serrated fins

B.3 HTFS1

Dependency on $\frac{P_T}{P_L}$

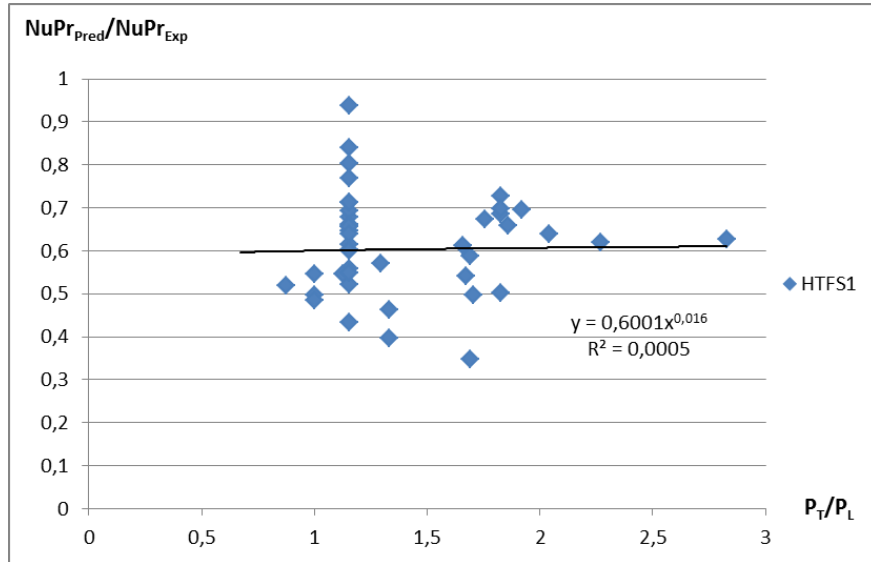


Figure 104: Predicted heat transfer dependency on $\frac{P_T}{P_L}$ for HTFS1, solid fins

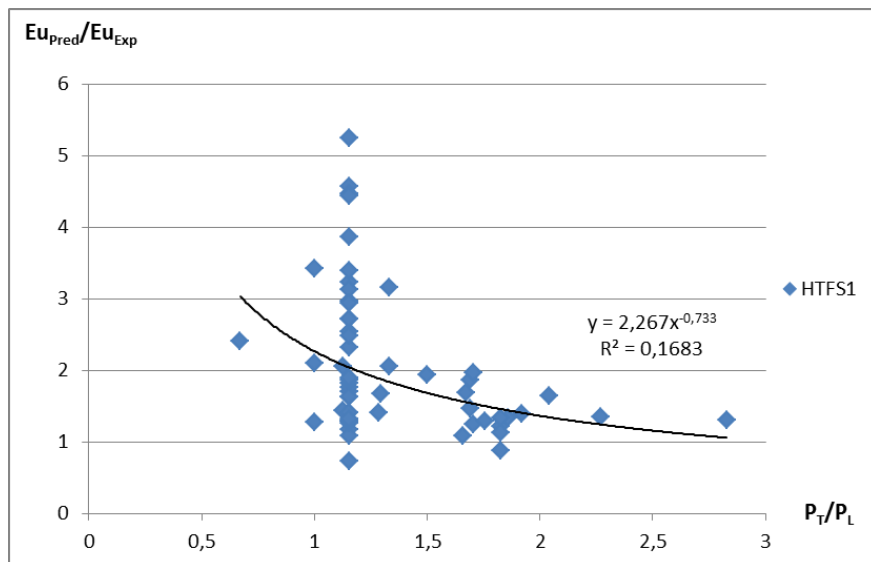


Figure 105: Predicted pressure drop dependency on $\frac{P_T}{P_L}$ for HTFS1, solid fins

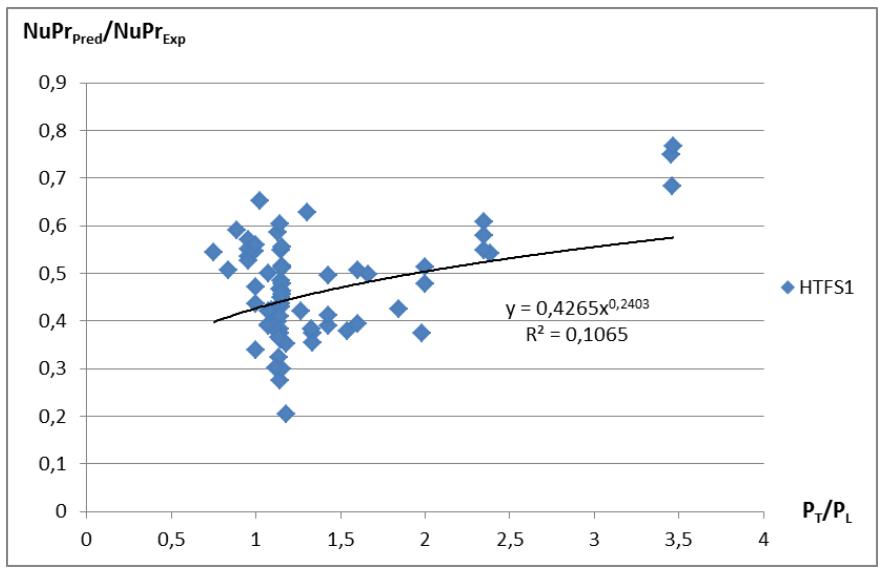


Figure 106: Predicted heat transfer dependency on $\frac{P_T}{P_L}$ for HTFS1, serrated fins

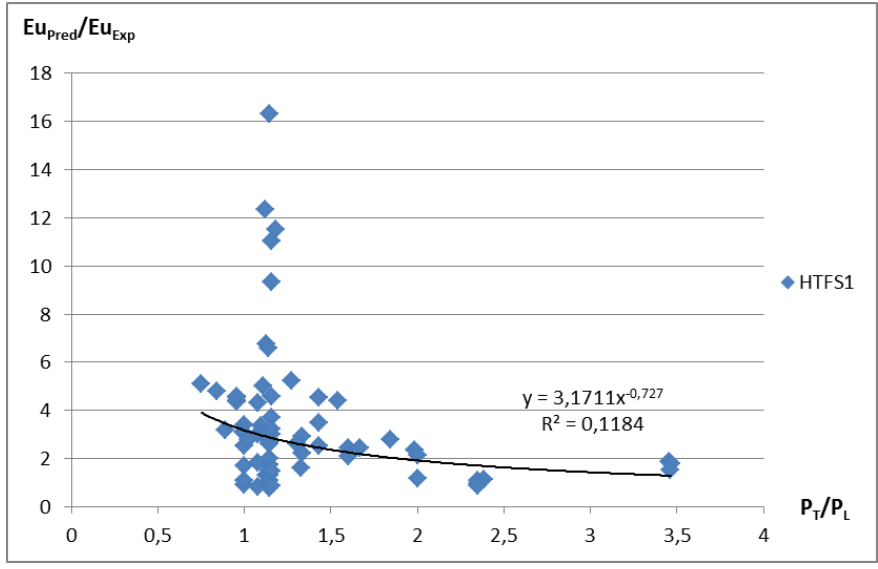


Figure 107: Predicted pressure drop dependency on $\frac{P_T}{P_L}$ for HTFS1, serrated fins

Dependency on P_T

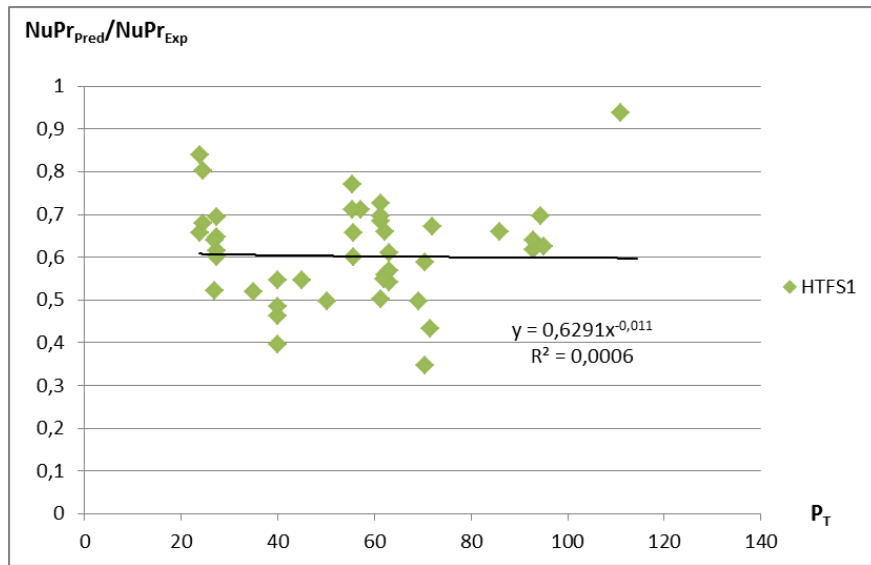


Figure 108: Predicted heat transfer dependency on P_T for HTFS1, solid fins

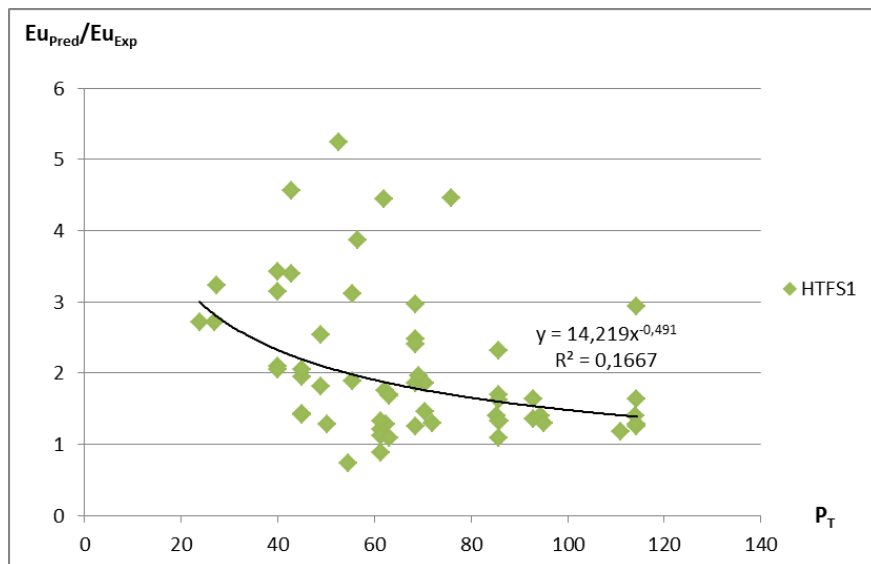


Figure 109: Predicted pressure drop dependency on P_T for HTFS1, solid fins

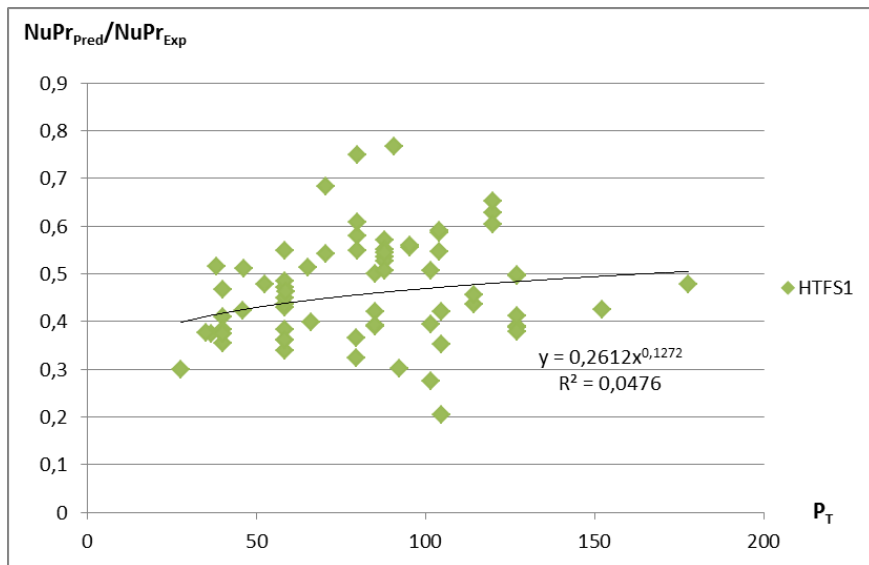


Figure 110: Predicted heat transfer dependency on P_T for HTFS1, serrated fins

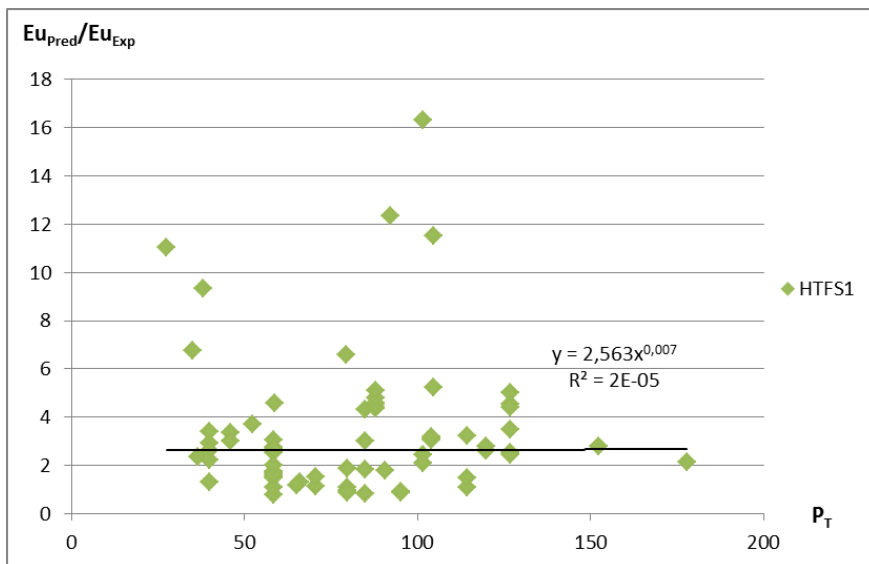


Figure 111: Predicted pressure drop dependency on P_T for HTFS1, serrated fins

Dependency on $\frac{h_f}{p_f}$

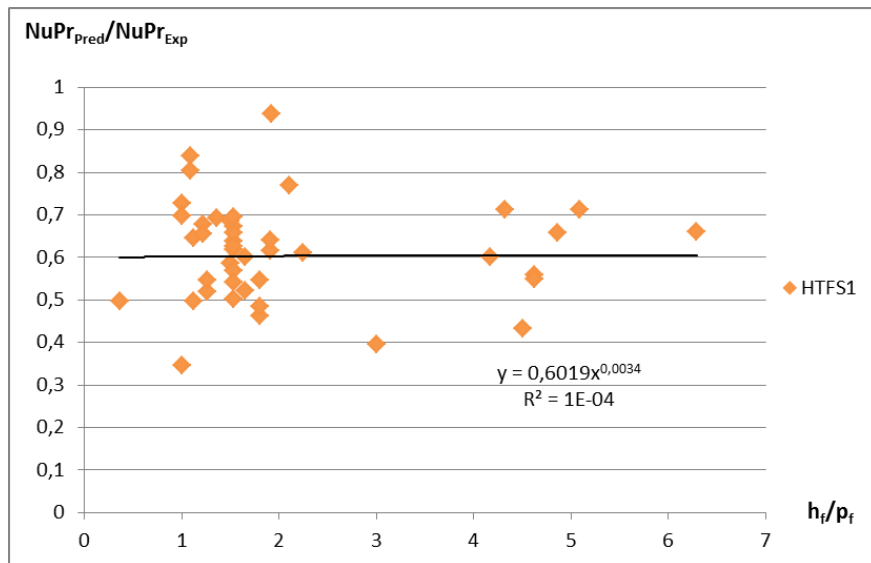


Figure 112: Predicted heat transfer dependency on $\frac{h_f}{p_f}$ for HTFS1, solid fins

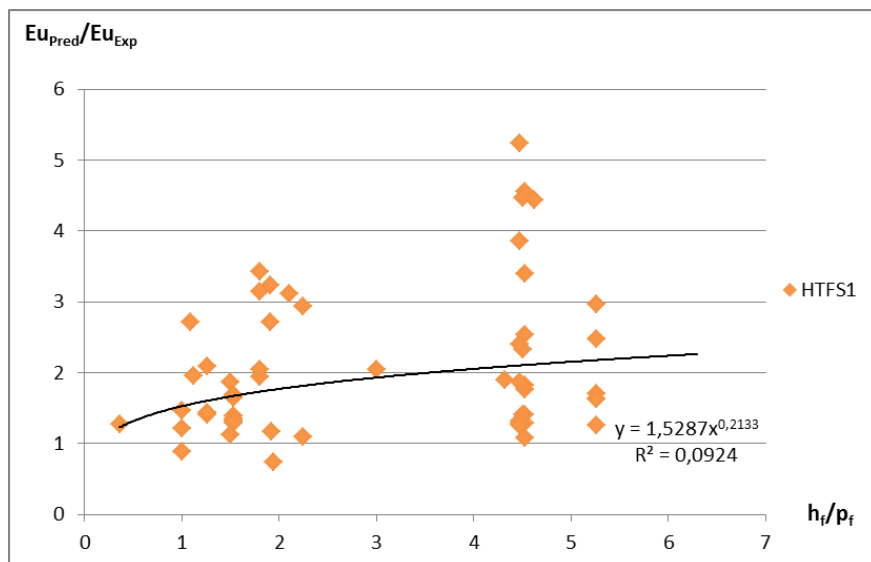


Figure 113: Predicted pressure drop dependency on $\frac{h_f}{p_f}$ for HTFS1, solid fins

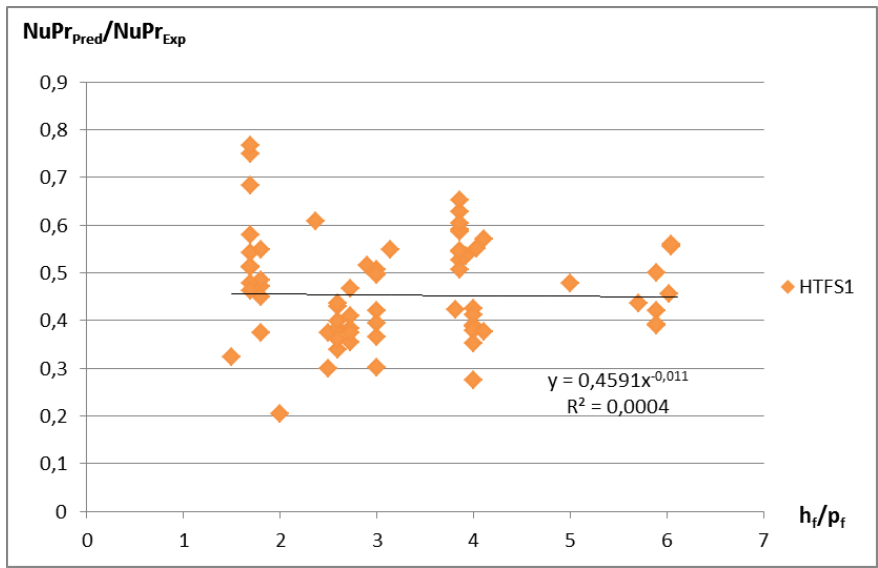


Figure 114: Predicted heat transfer dependency on $\frac{h_f}{p_f}$ for HTFS1, serrated fins

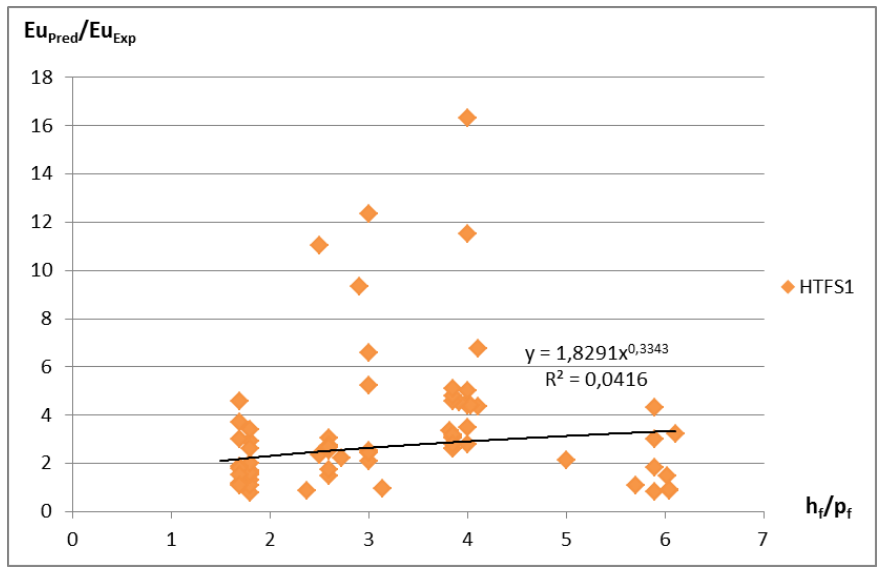


Figure 115: Predicted pressure drop dependency on $\frac{h_f}{p_f}$ for HTFS1, serrated fins

Dependency on A_r

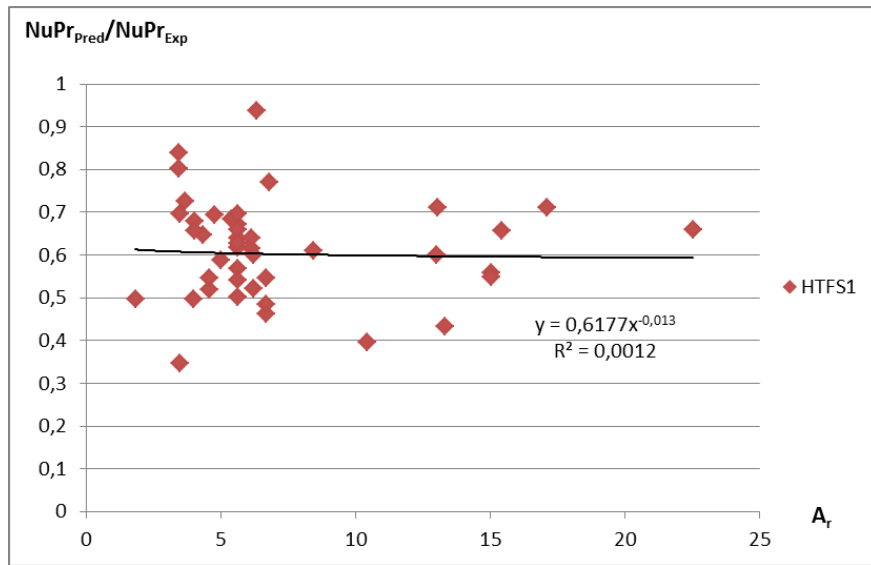


Figure 116: Predicted heat transfer dependency on A_r for HTFS1, solid fins

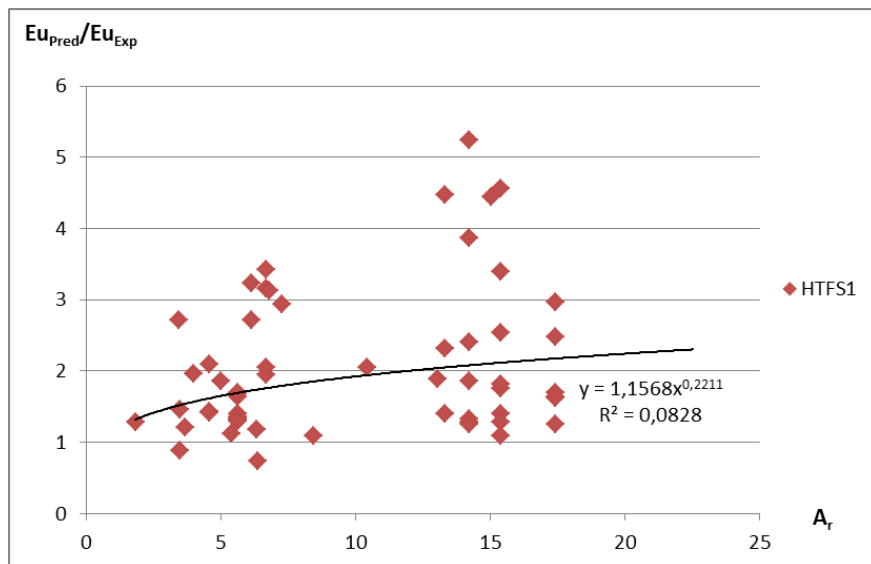


Figure 117: Predicted pressure drop dependency on A_r for HTFS1, solid fins

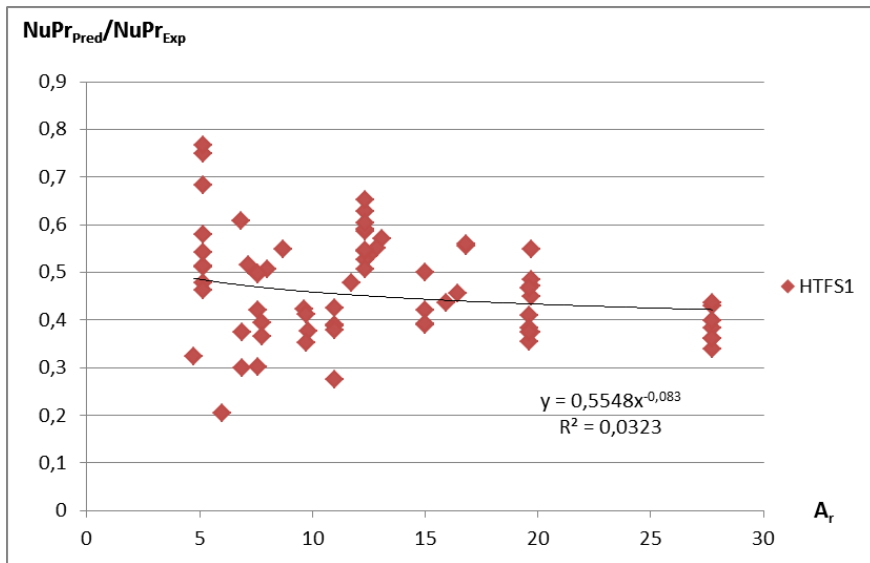


Figure 118: Predicted heat transfer dependency on Ar for HTFS1, serrated fins

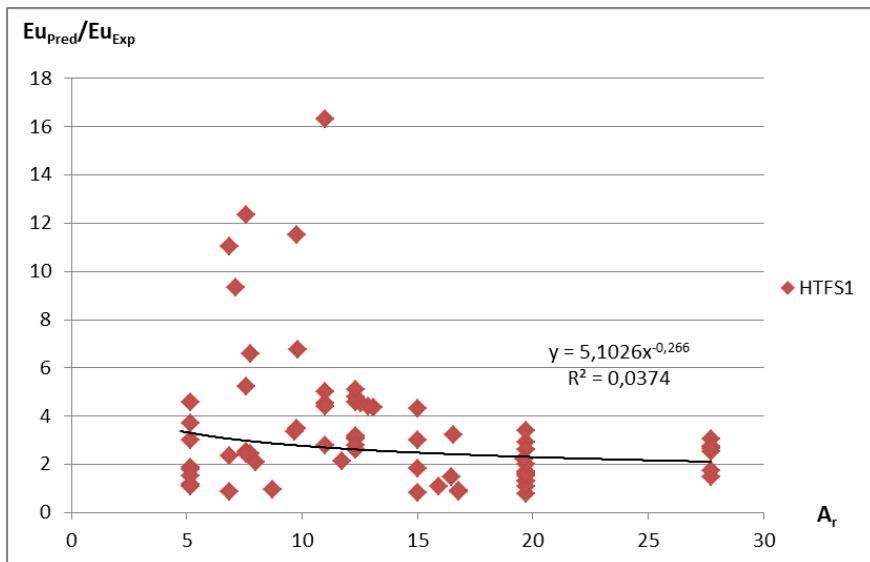


Figure 119: Predicted pressure drop dependency on Ar for HTFS1, serrated fins

Dependency on W

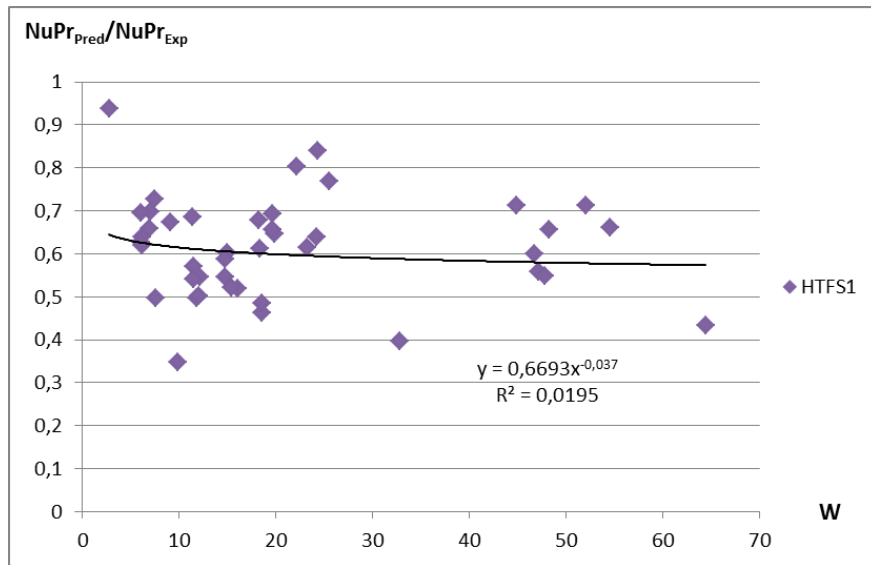


Figure 120: Predicted heat transfer dependency on W for HTFS1, solid fins

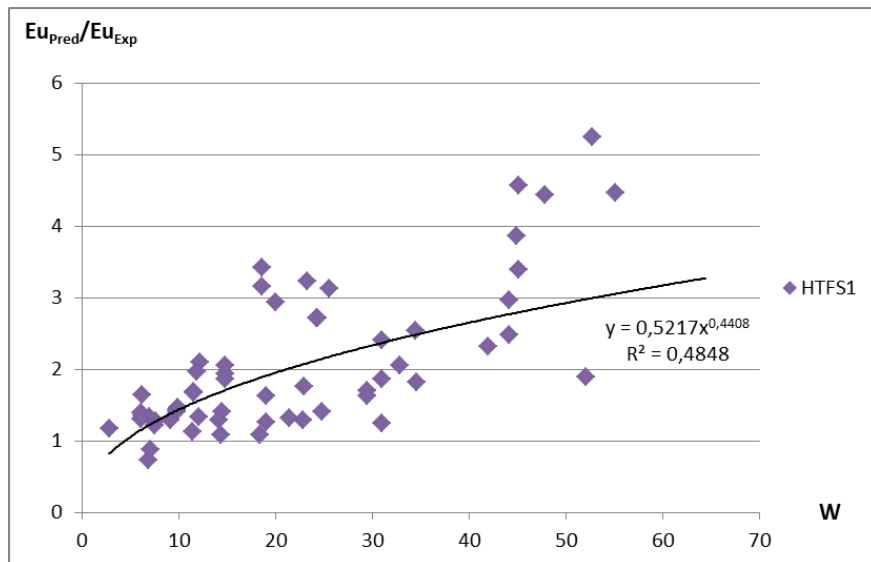


Figure 121: Predicted pressure drop dependency on W for HTFS1, solid fins

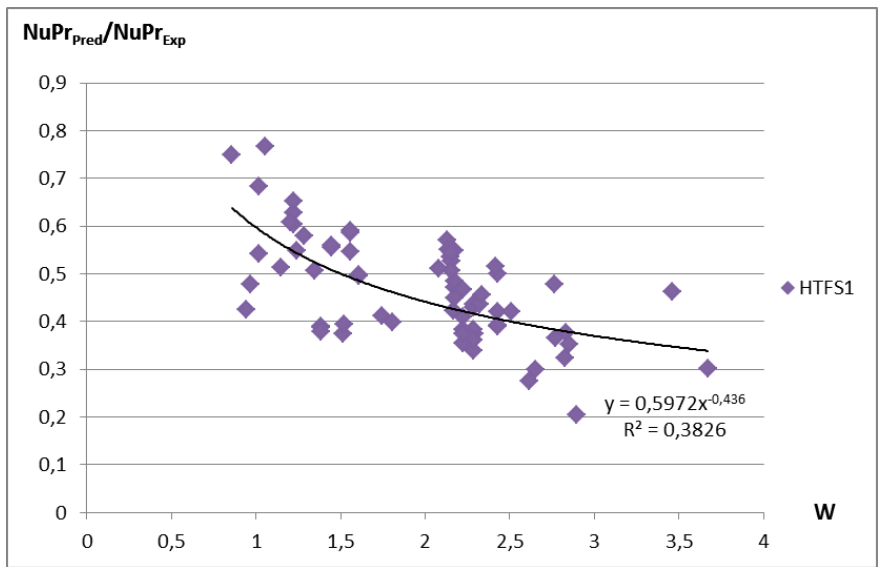


Figure 122: Predicted heat transfer dependency on W for HTFS1, serrated fins

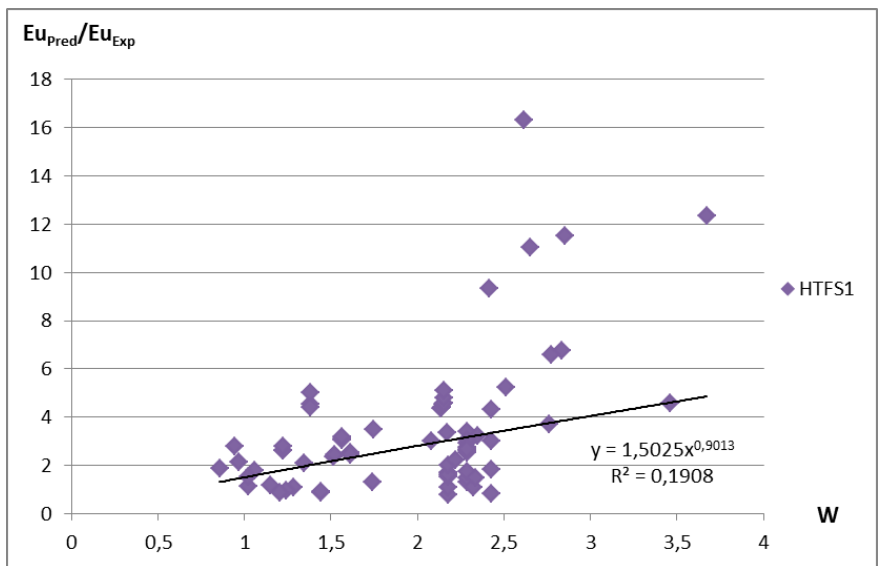


Figure 123: Predicted pressure drop dependency on W for HTFS1, serrated fins

B.4 HTFS2

Dependency on $\frac{P_T}{P_L}$

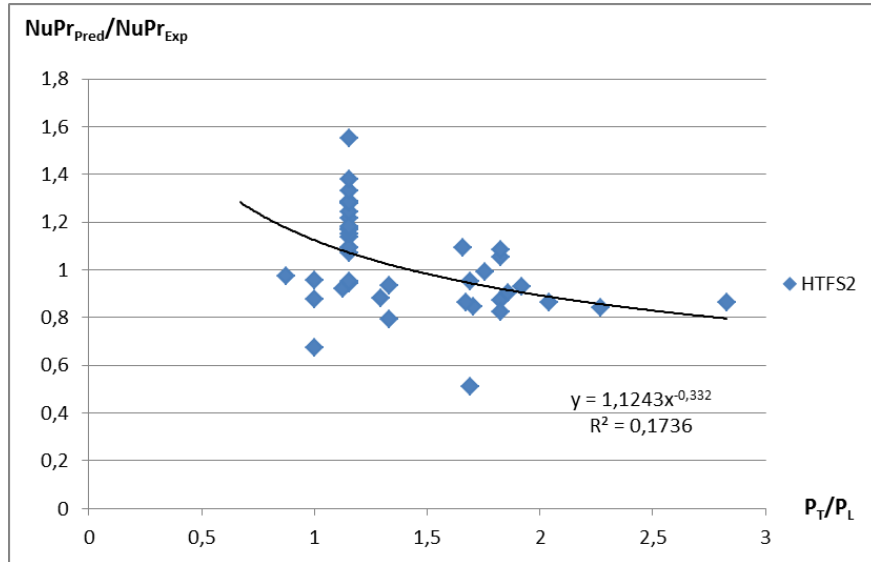


Figure 124: Predicted heat transfer dependency on $\frac{P_T}{P_L}$ for HTFS2, solid fins

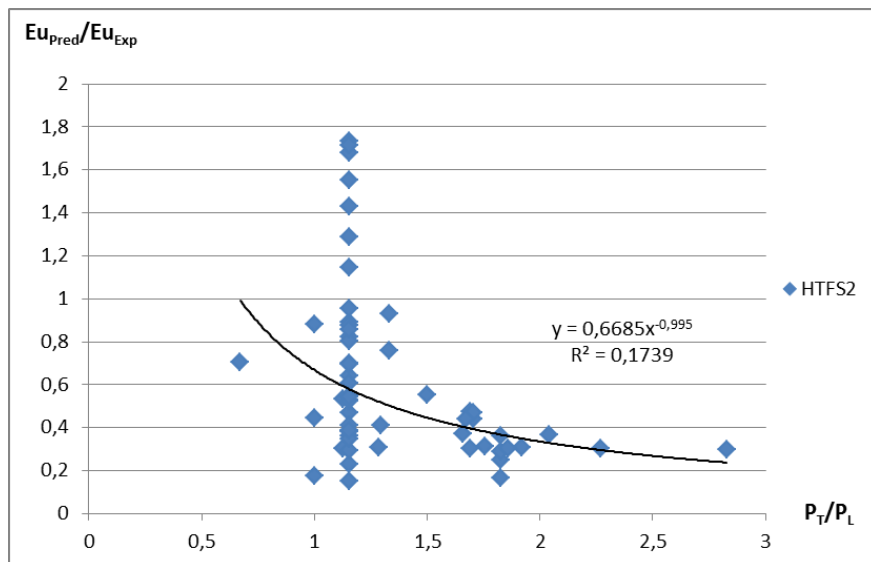


Figure 125: Predicted pressure drop dependency on $\frac{P_T}{P_L}$ for HTFS2, solid fins

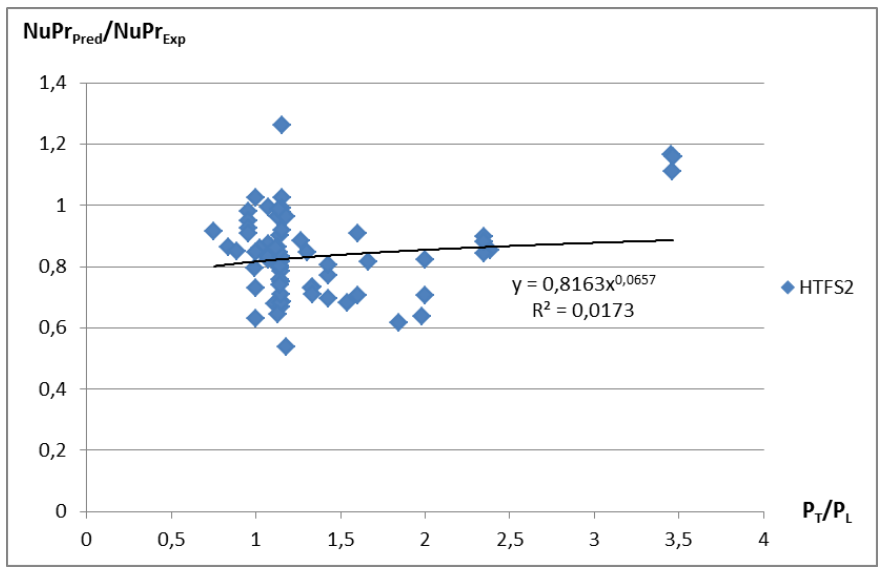


Figure 126: Predicted heat transfer dependency on $\frac{P_T}{P_L}$ for HTFS2, serrated fins

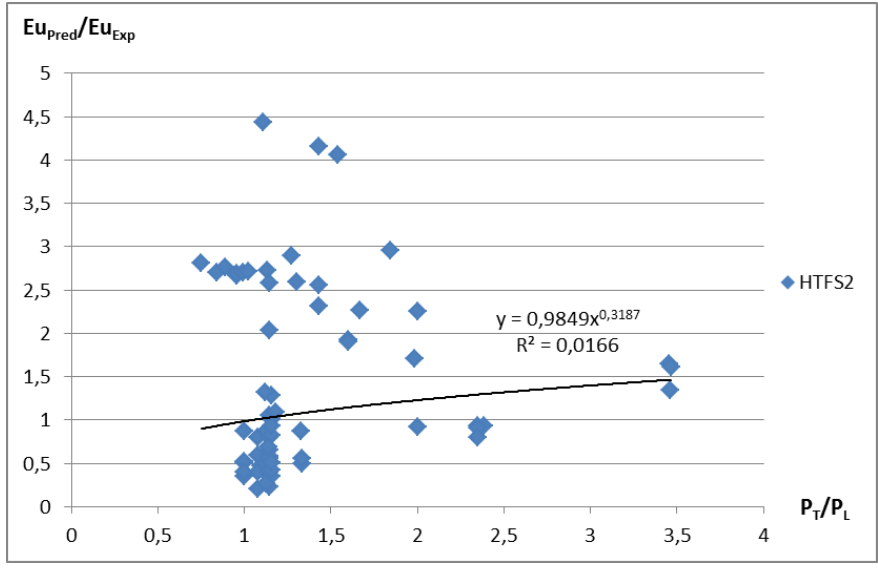


Figure 127: Predicted pressure drop dependency on $\frac{P_T}{P_L}$ for HTFS2, serrated fins

Dependency on P_T

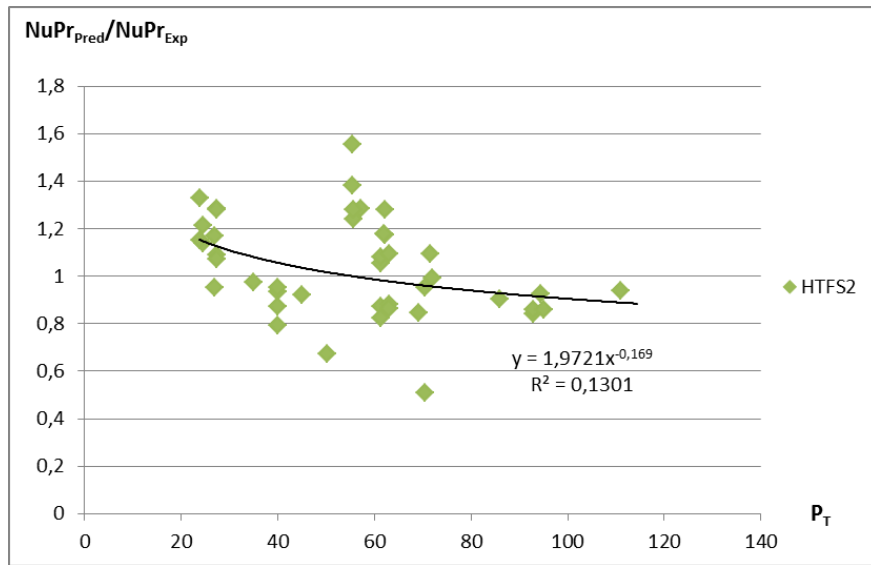


Figure 128: Predicted heat transfer dependency on P_T for HTFS2, solid fins

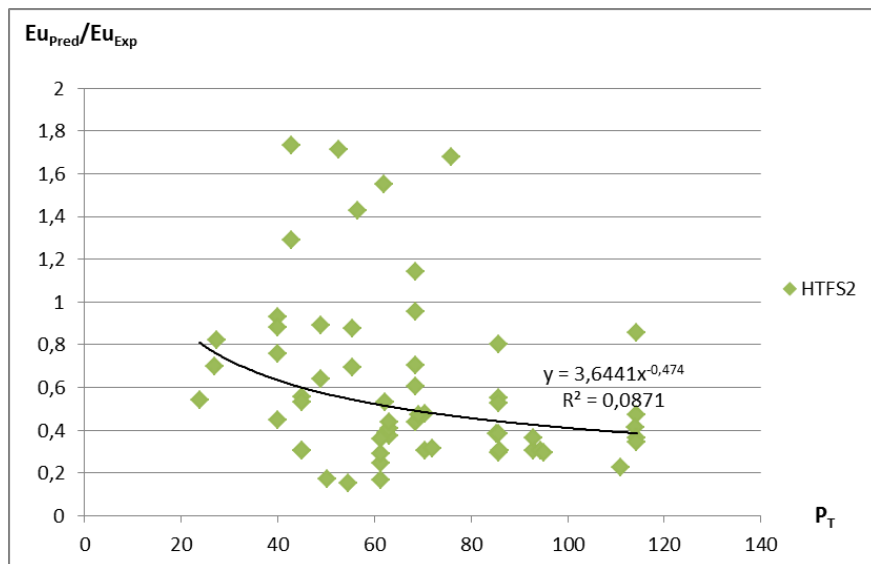


Figure 129: Predicted pressure drop dependency on P_T for HTFS2, solid fins

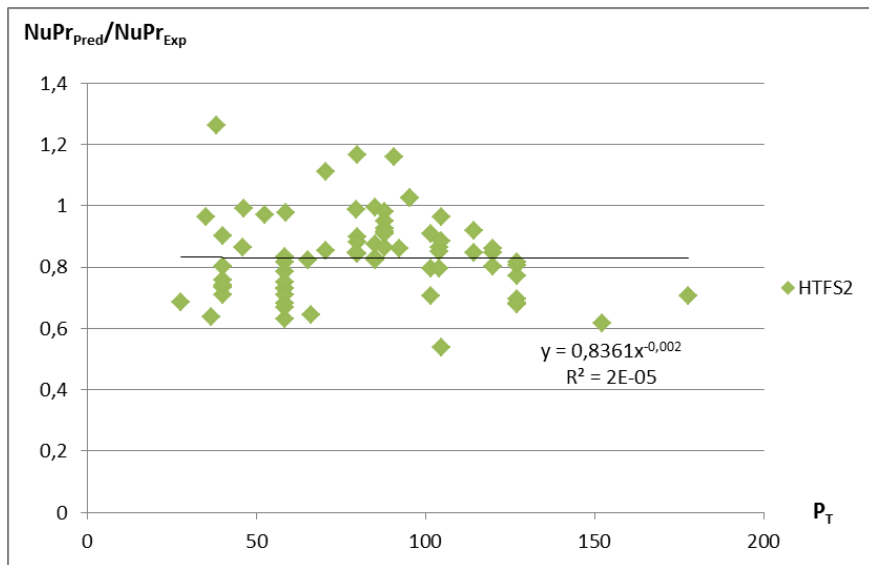


Figure 130: Predicted heat transfer dependency on P_T for HTFS2, serrated fins

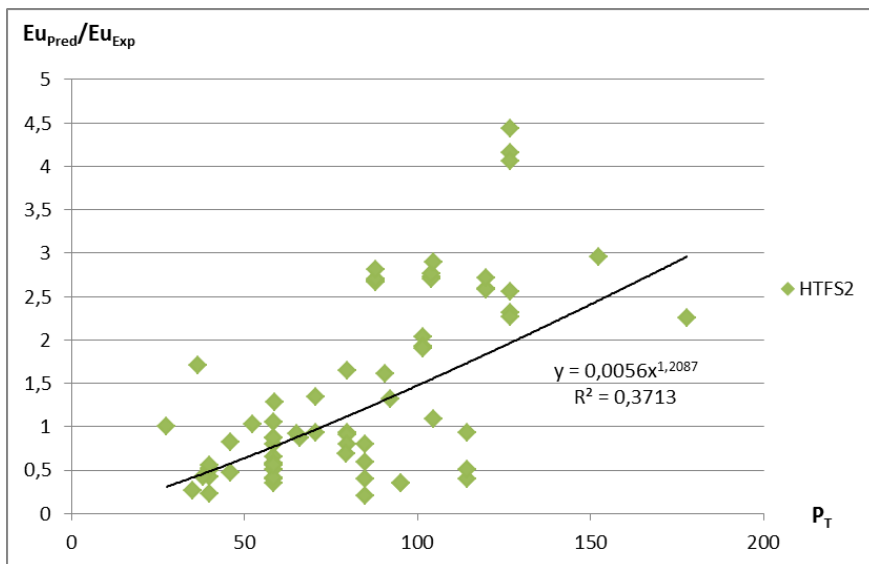


Figure 131: Predicted pressure drop dependency on P_T for HTFS2, serrated fins

Dependency on $\frac{h_f}{p_f}$

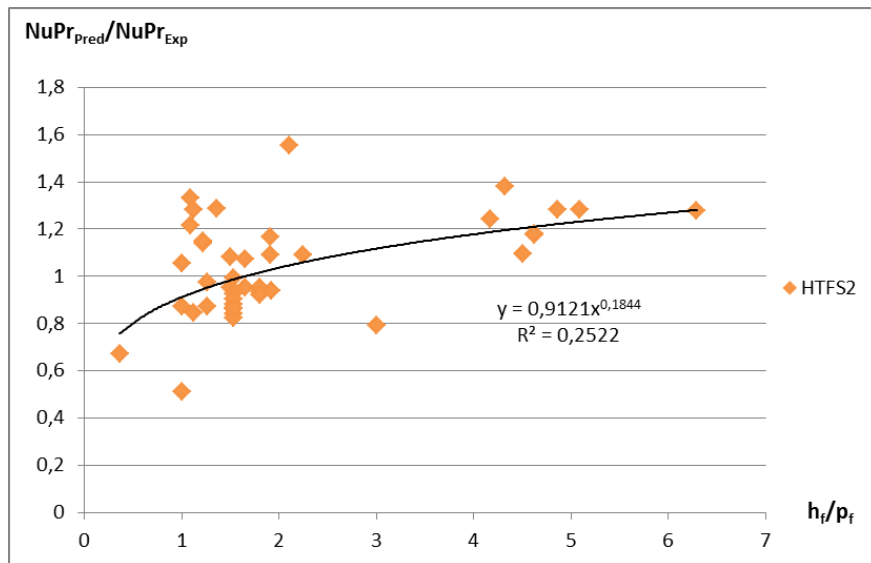


Figure 132: Predicted heat transfer dependency on $\frac{h_f}{p_f}$ for HTFS2, solid fins

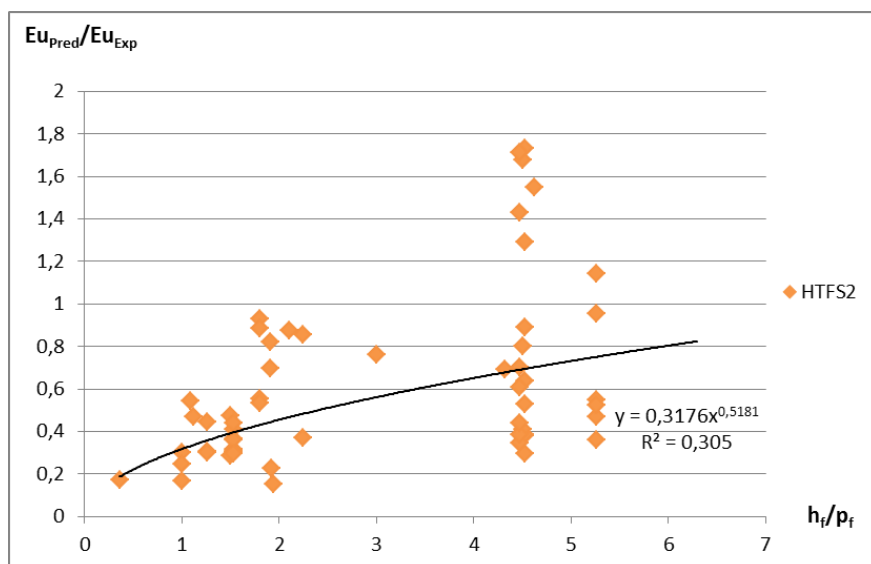


Figure 133: Predicted pressure drop dependency on $\frac{h_f}{p_f}$ for HTFS2, solid fins

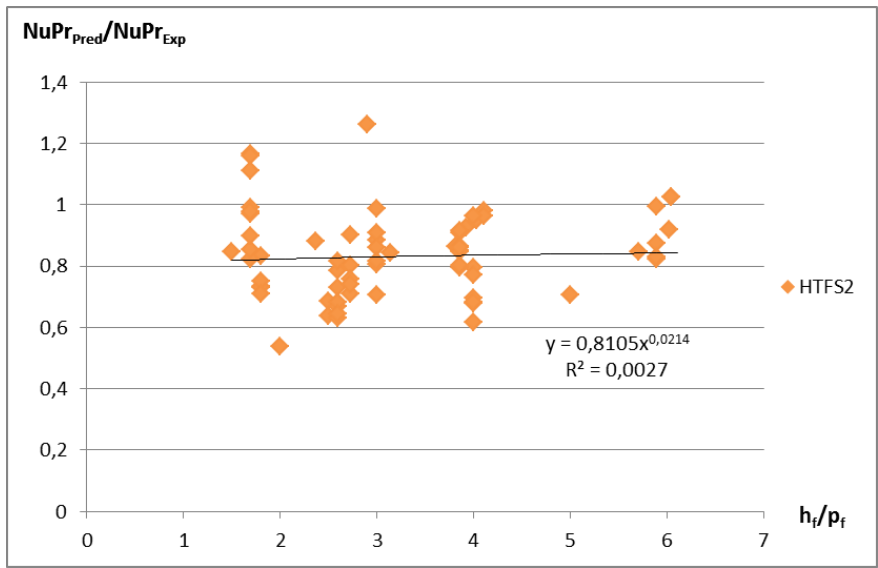


Figure 134: Predicted heat transfer dependency on $\frac{h_f}{p_f}$ for HTFS2, serrated fins

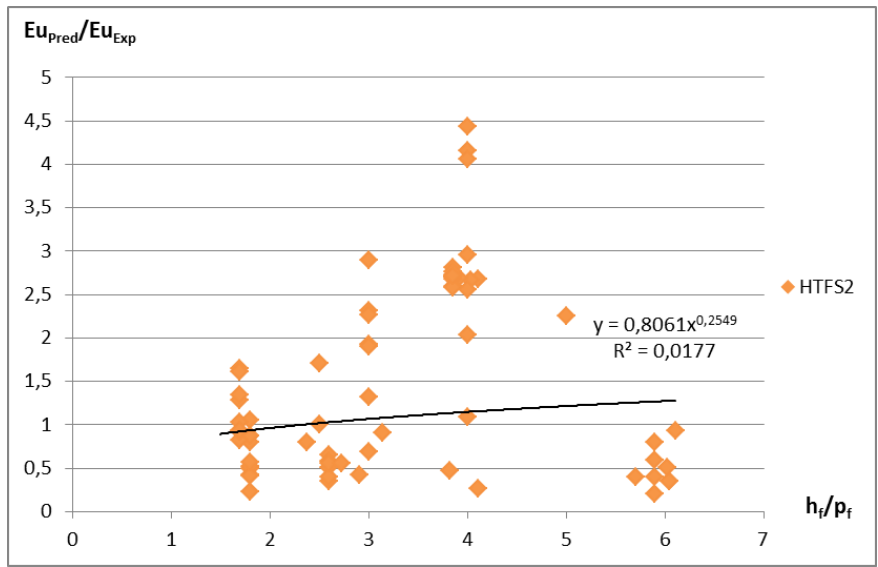


Figure 135: Predicted pressure drop dependency on $\frac{h_f}{p_f}$ for HTFS2, serrated fins

Dependency on A_r

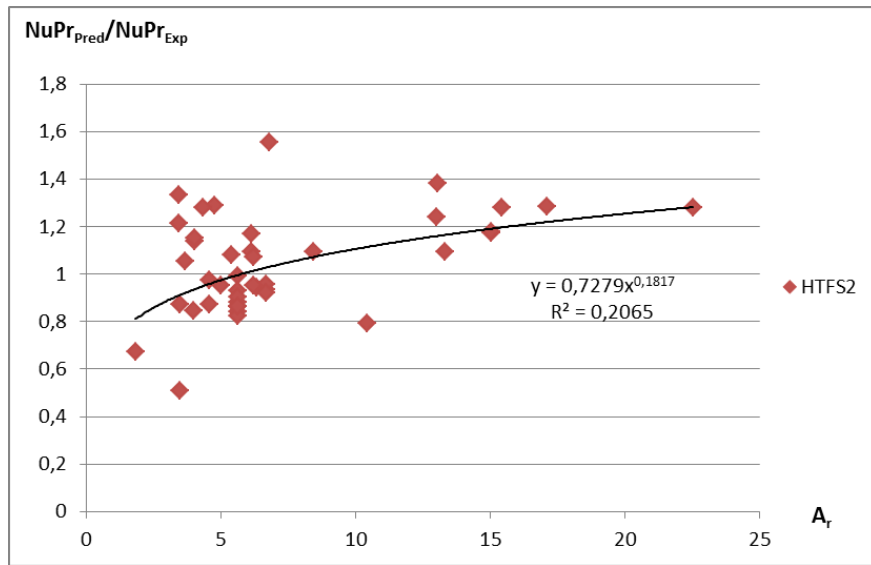


Figure 136: Predicted heat transfer dependency on A_r for HTFS2, solid fins

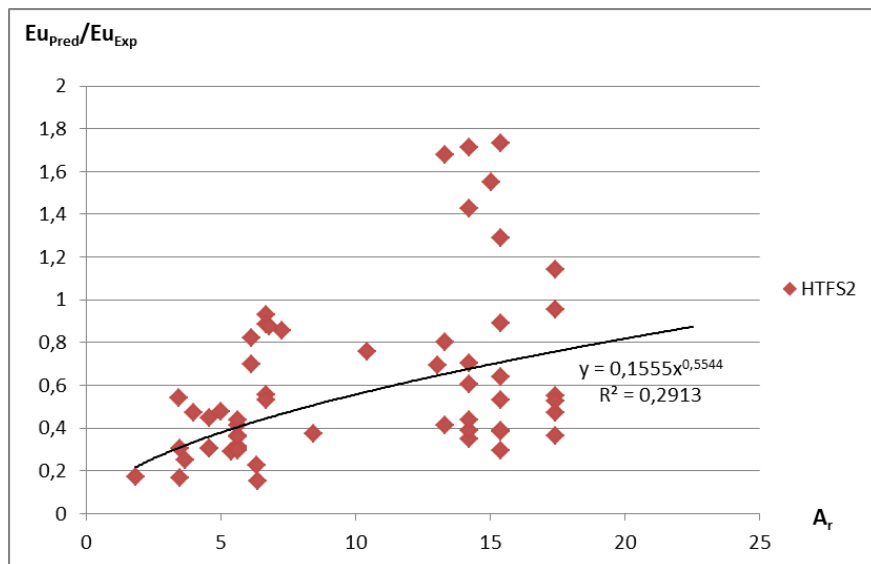


Figure 137: Predicted pressure drop dependency on A_r for HTFS2, solid fins

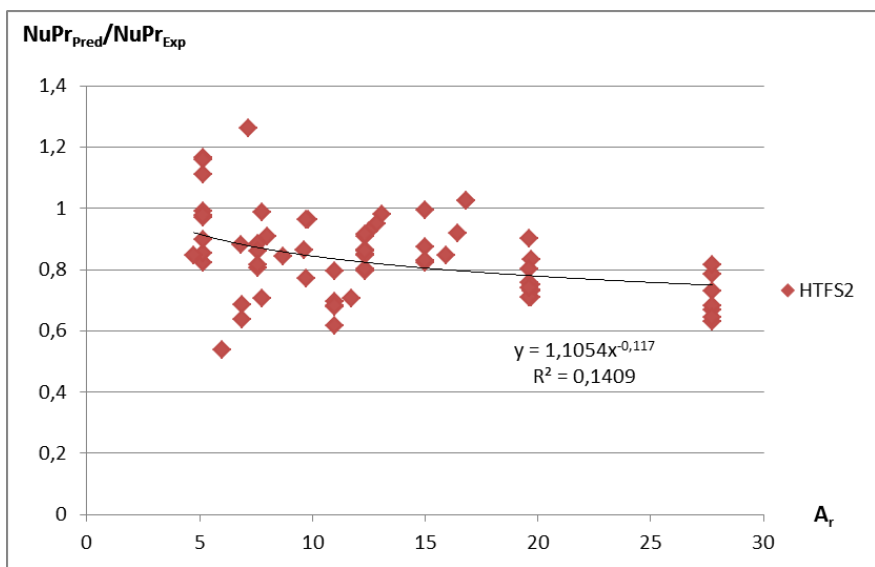


Figure 138: Predicted heat transfer dependency on A_r for HTFS2, serrated fins

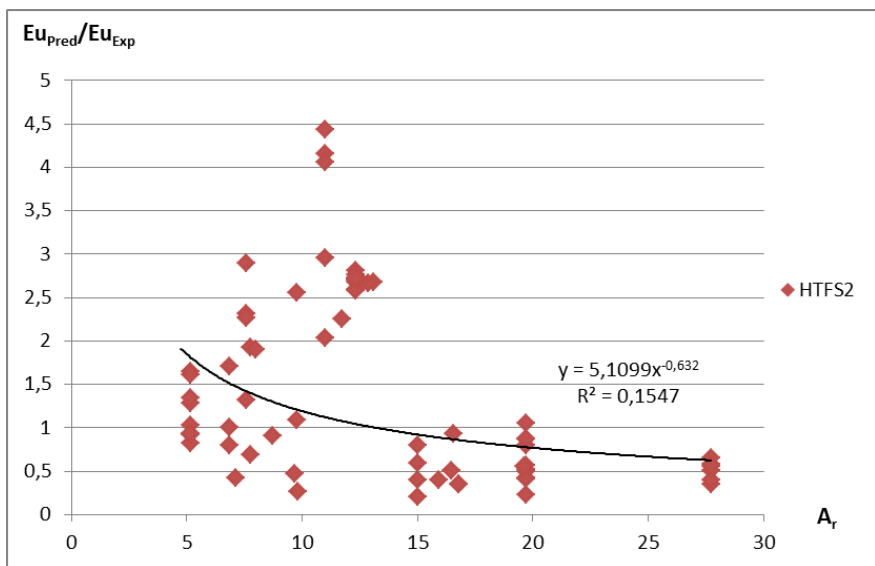


Figure 139: Predicted pressure drop dependency on A_r for HTFS2, serrated fins

Dependency on W

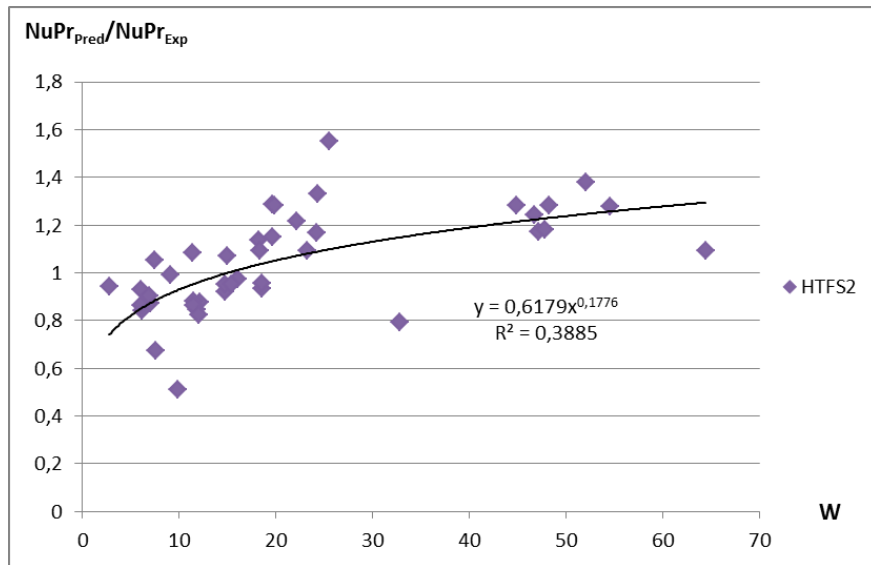


Figure 140: Predicted heat transfer dependency on W for HTFS2, solid fins

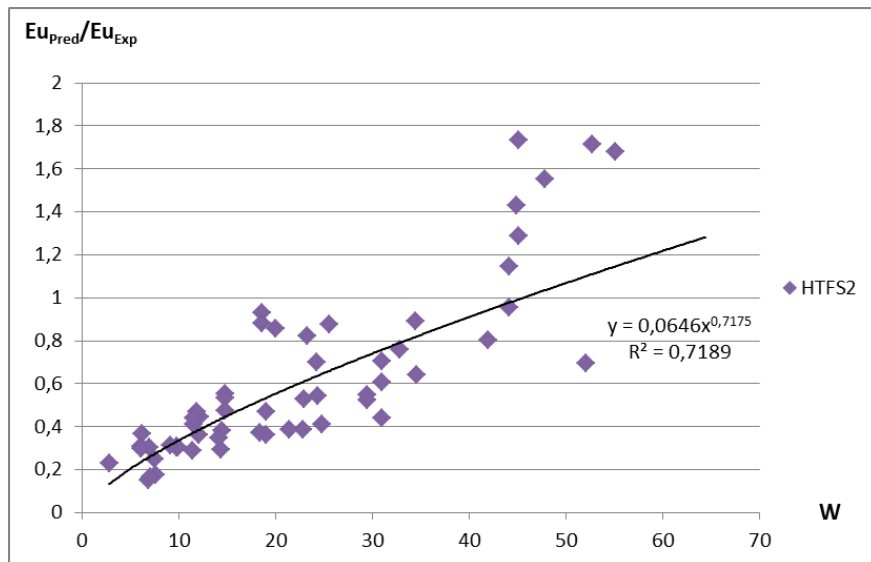


Figure 141: Predicted pressure drop dependency on W for HTFS2, solid fins

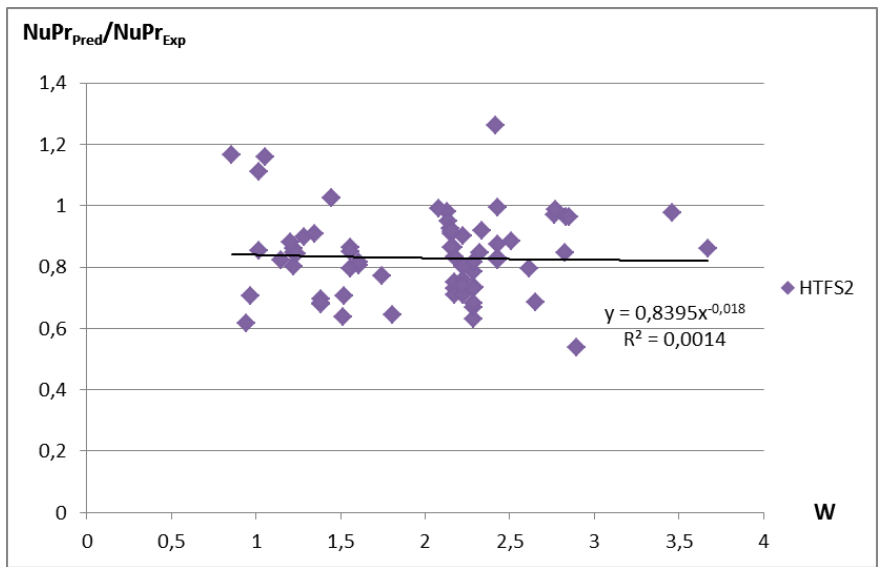


Figure 142: Predicted heat transfer dependency on W for HTFS2, serrated fins

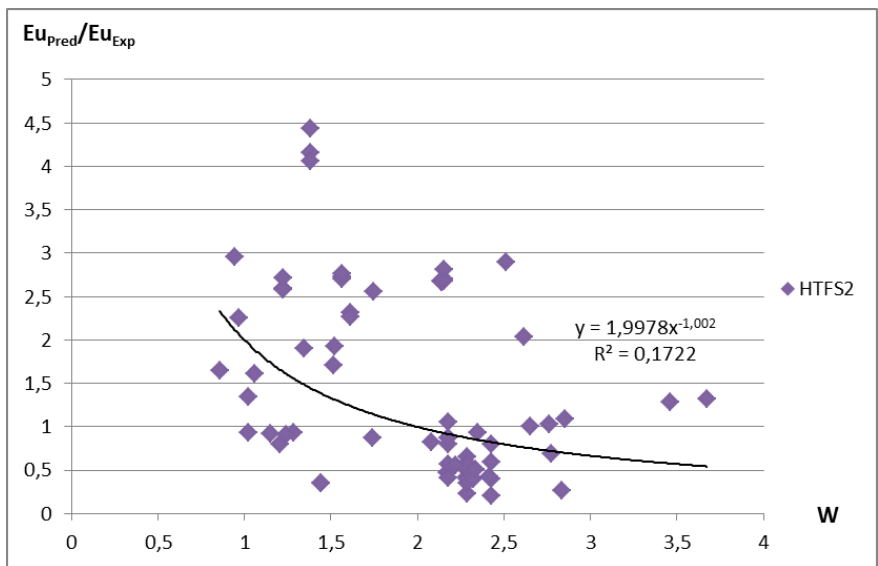


Figure 143: Predicted pressure drop dependency on W for HTFS2, serrated fins

B.5 HTFS3

Dependency on $\frac{P_T}{P_L}$

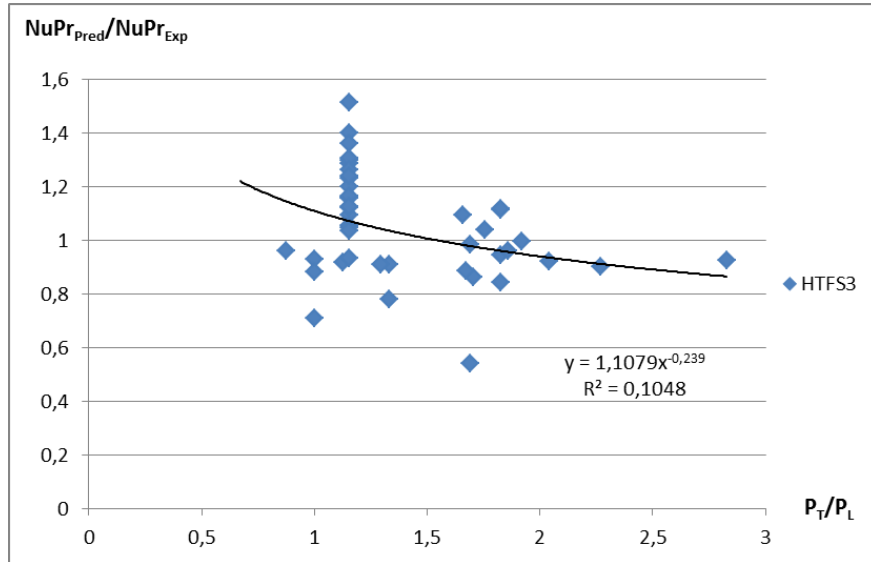


Figure 144: Predicted heat transfer dependency on $\frac{P_T}{P_L}$ for HTFS3, solid fins

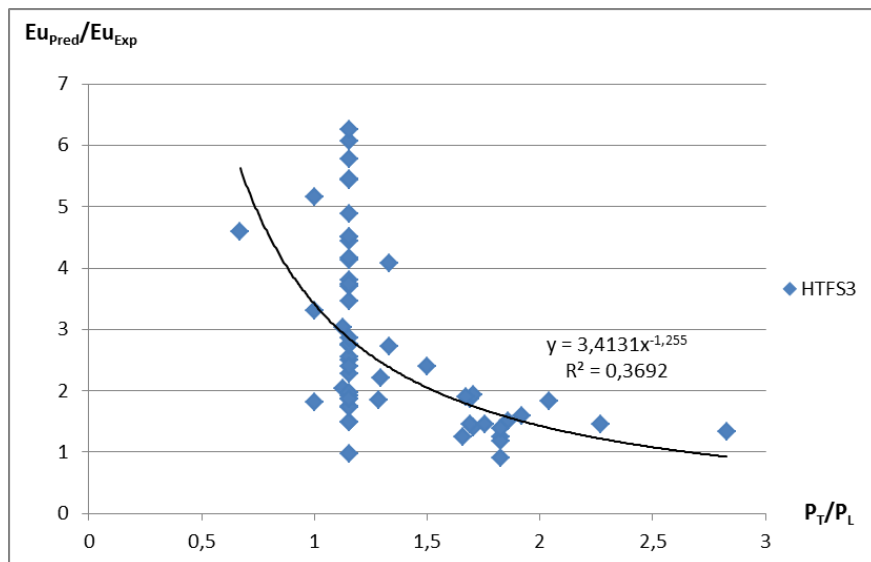


Figure 145: Predicted pressure drop dependency on $\frac{P_T}{P_L}$ for HTFS3, solid fins

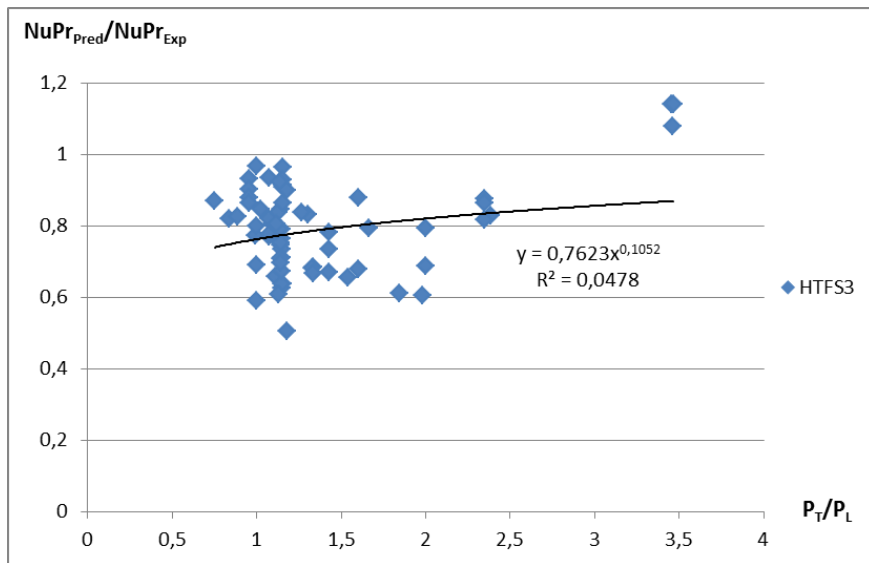


Figure 146: Predicted heat transfer dependency on $\frac{P_T}{P_L}$ for HTFS3, serrated fins

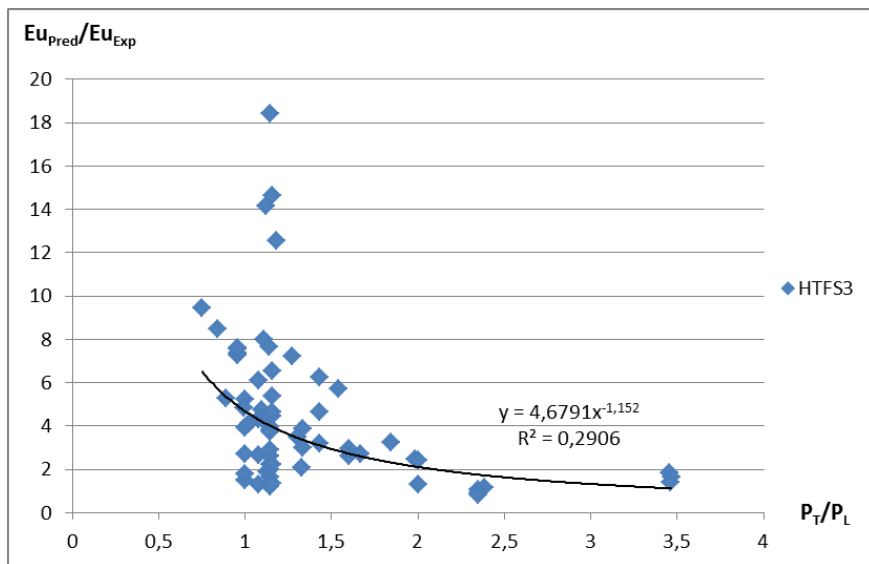


Figure 147: Predicted pressure drop dependency on $\frac{P_T}{P_L}$ for HTFS3, serrated fins

Dependency on P_T

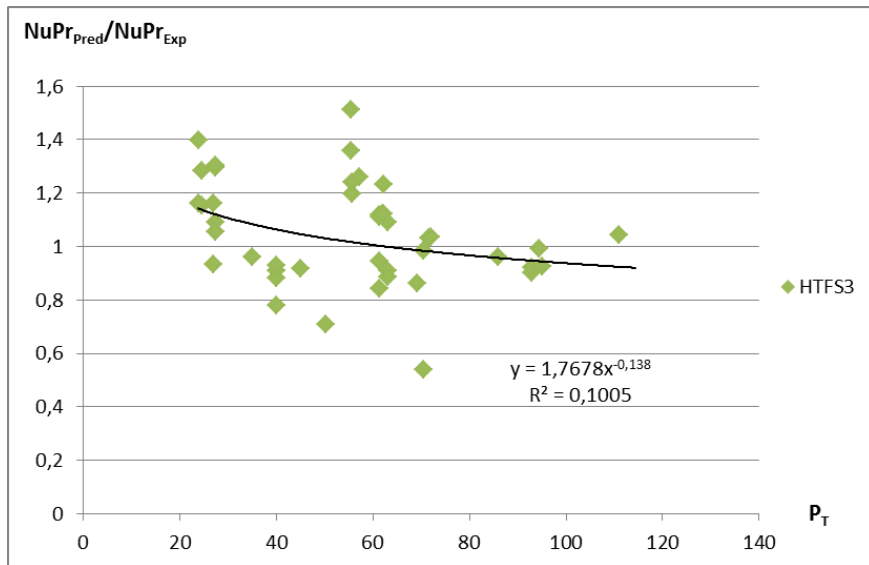


Figure 148: Predicted heat transfer dependency on P_T for HTFS3, solid fins

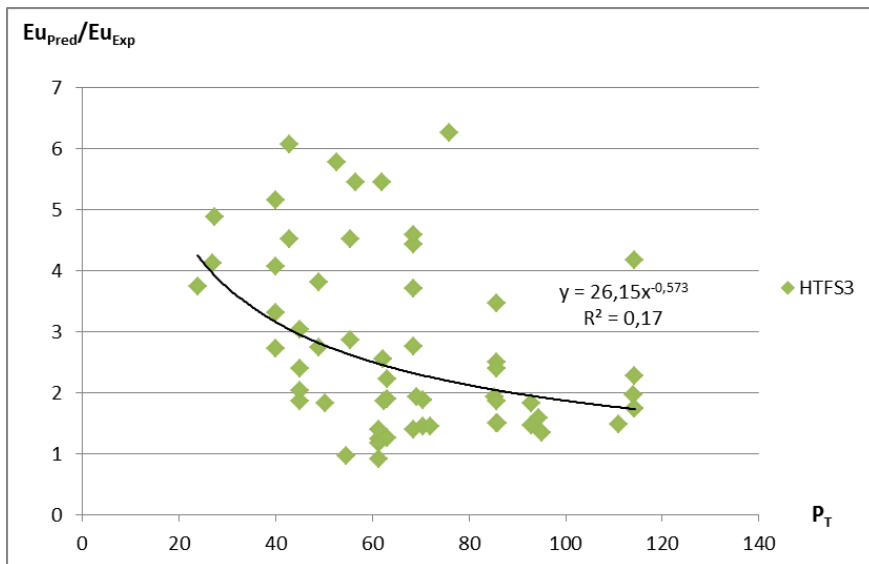


Figure 149: Predicted pressure drop dependency on P_T for HTFS3, solid fins

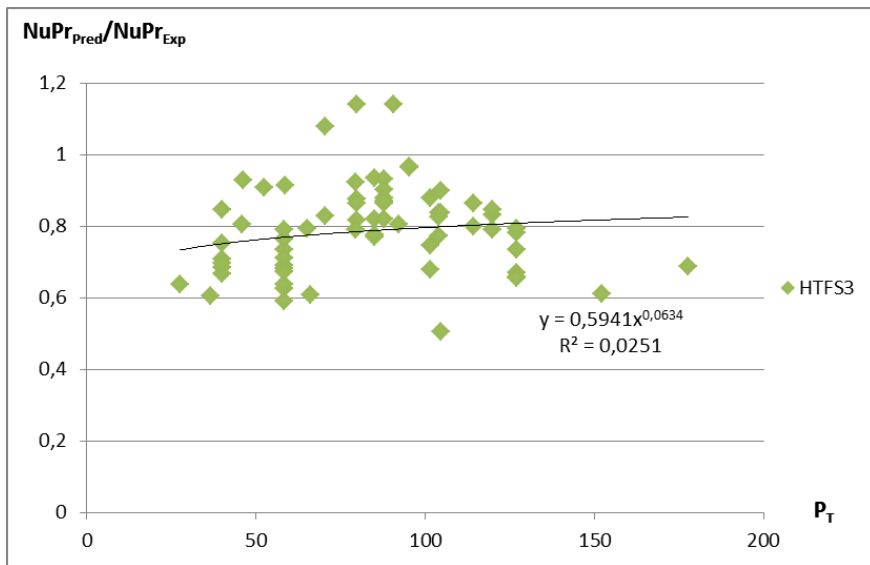


Figure 150: Predicted heat transfer dependency on P_T for HTFS3, serrated fins

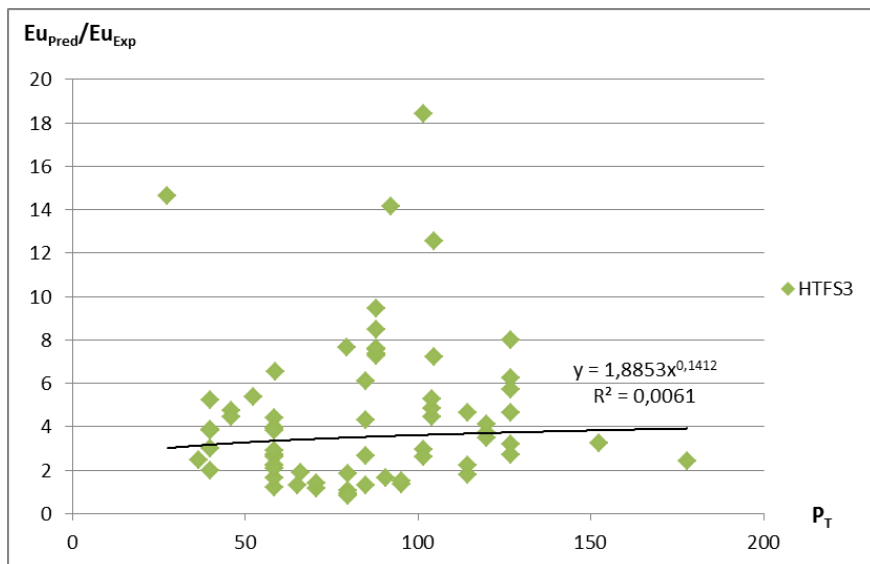


Figure 151: Predicted pressure drop dependency on P_T for HTFS3, serrated fins

Dependency on $\frac{h_f}{p_f}$

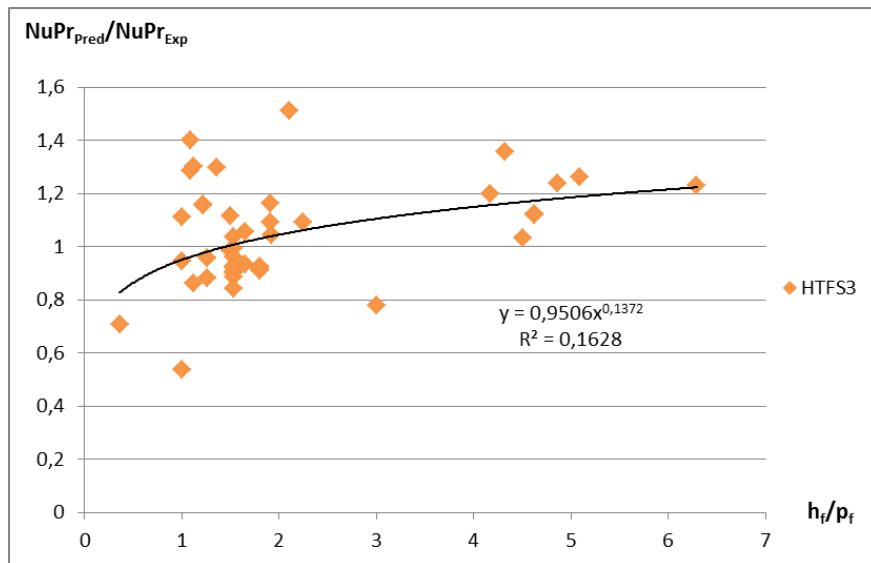


Figure 152: Predicted heat transfer dependency on $\frac{h_f}{p_f}$ for HTFS3, solid fins

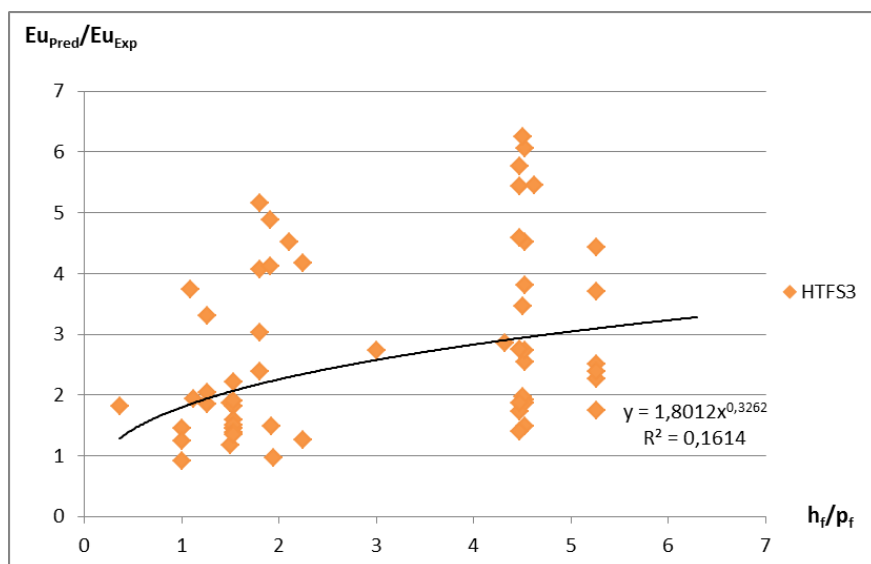


Figure 153: Predicted pressure drop dependency on $\frac{h_f}{p_f}$ for HTFS3, solid fins

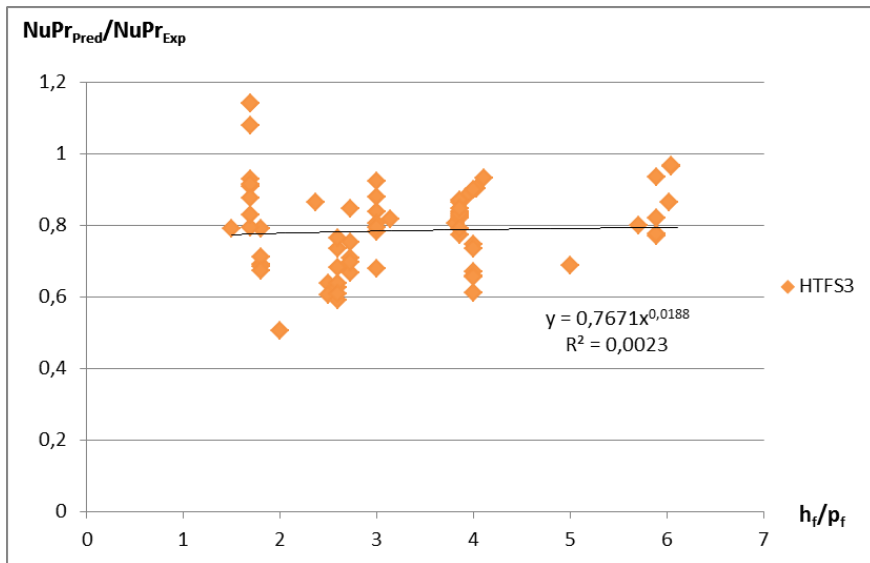


Figure 154: Predicted heat transfer dependency on $\frac{h_f}{p_f}$ for HTFS3, serrated fins

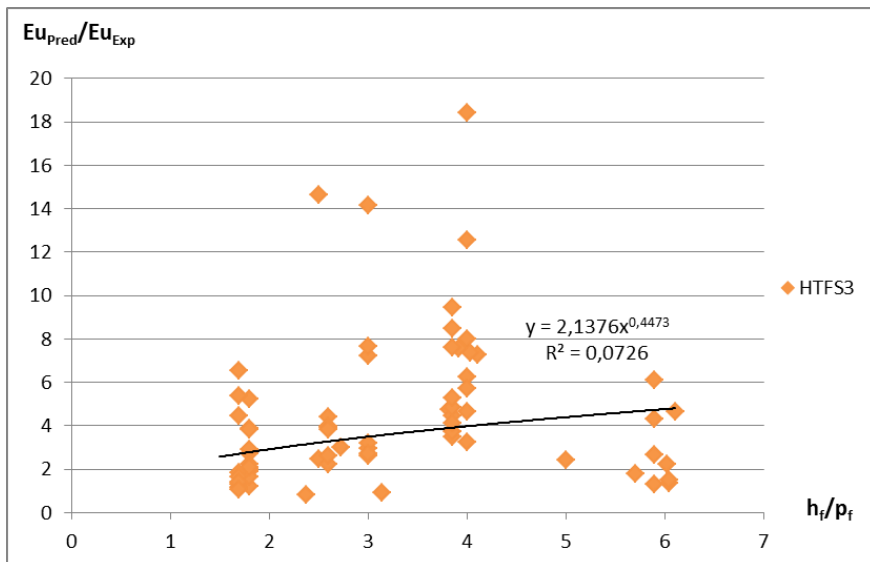


Figure 155: Predicted pressure drop dependency on $\frac{h_f}{p_f}$ for HTFS3, serrated fins

Dependency on A_r

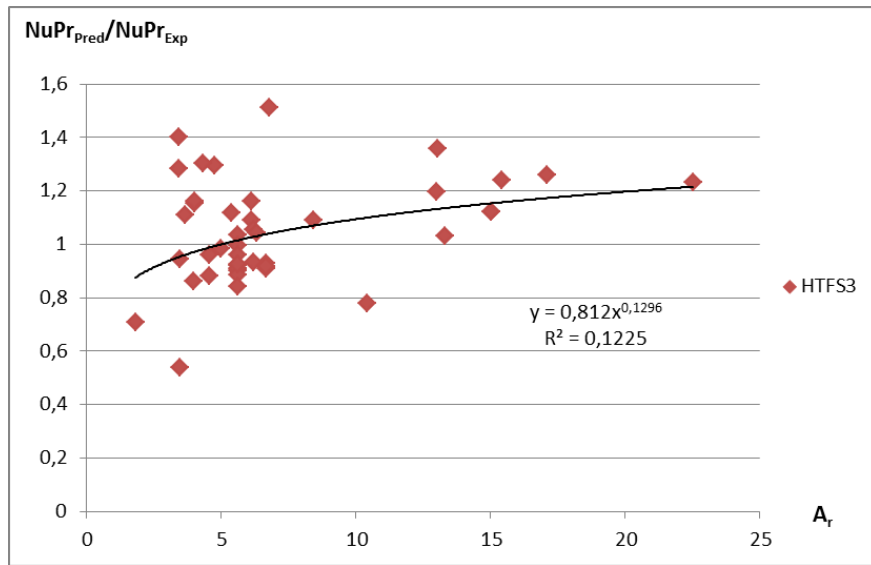


Figure 156: Predicted heat transfer dependency on A_r for HTFS3, solid fins

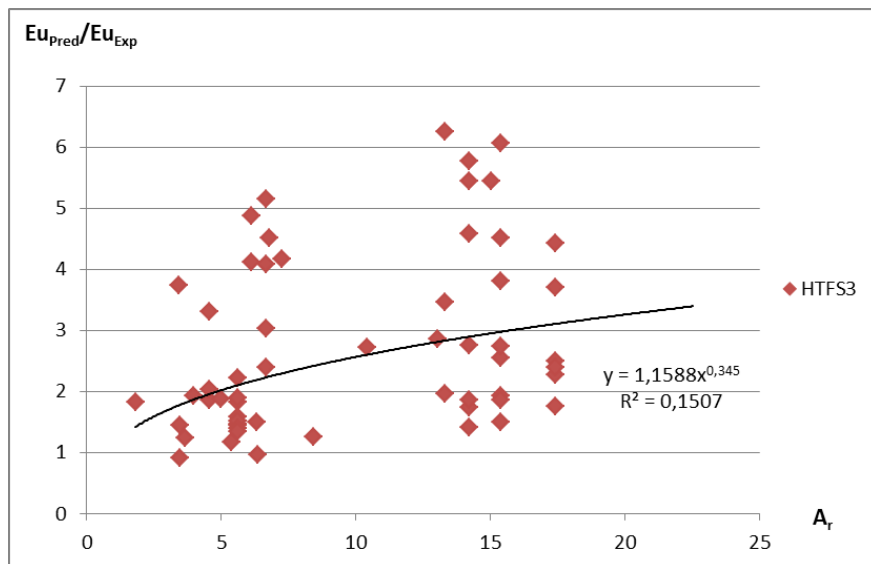


Figure 157: Predicted pressure drop dependency on A_r for HTFS3, solid fins

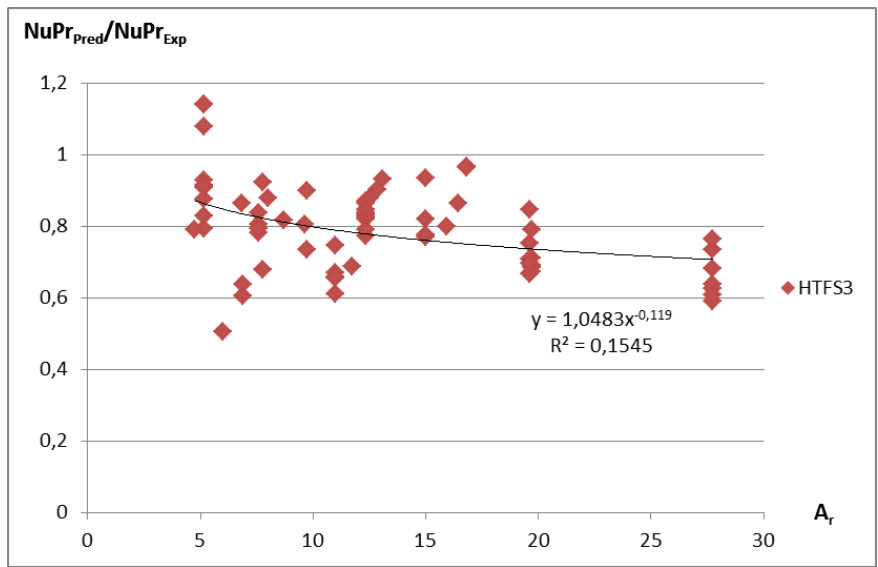


Figure 158: Predicted heat transfer dependency on A_r for HTFS3, serrated fins

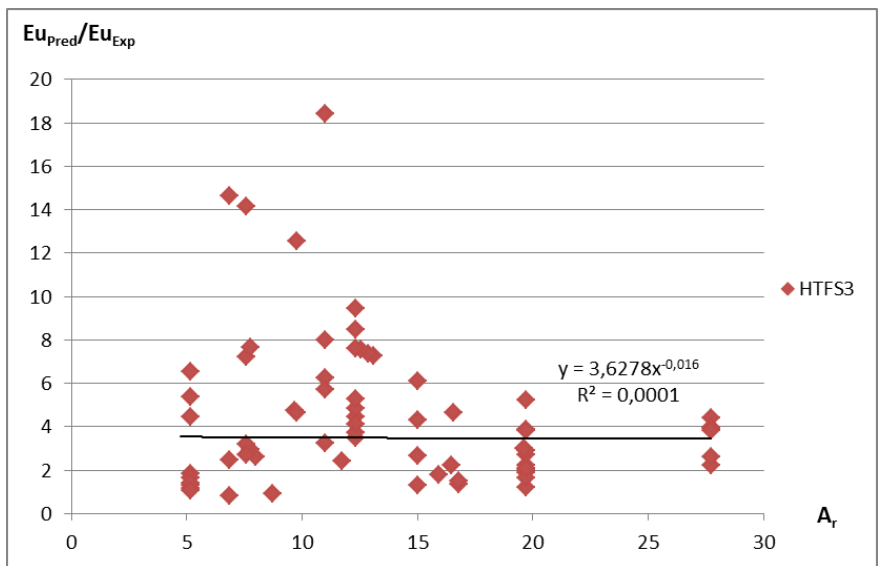


Figure 159: Predicted pressure drop dependency on A_r for HTFS3, serrated fins

Dependency on W

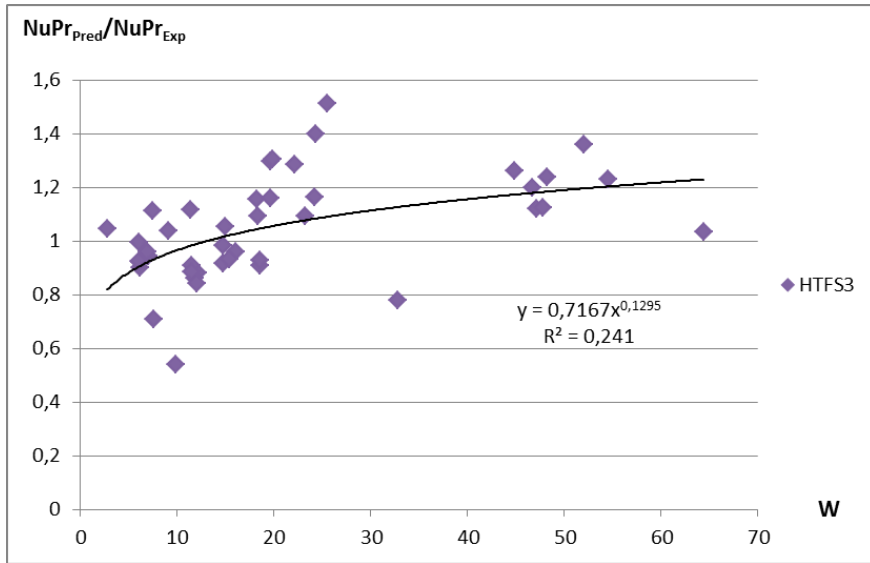


Figure 160: Predicted heat transfer dependency on W for HTFS3, solid fins

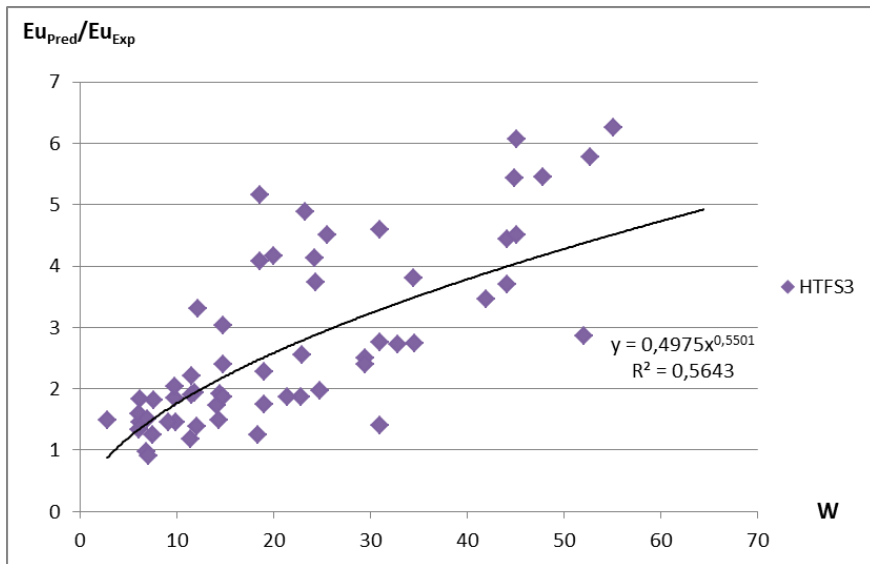


Figure 161: Predicted pressure drop dependency on W for HTFS3, solid fins

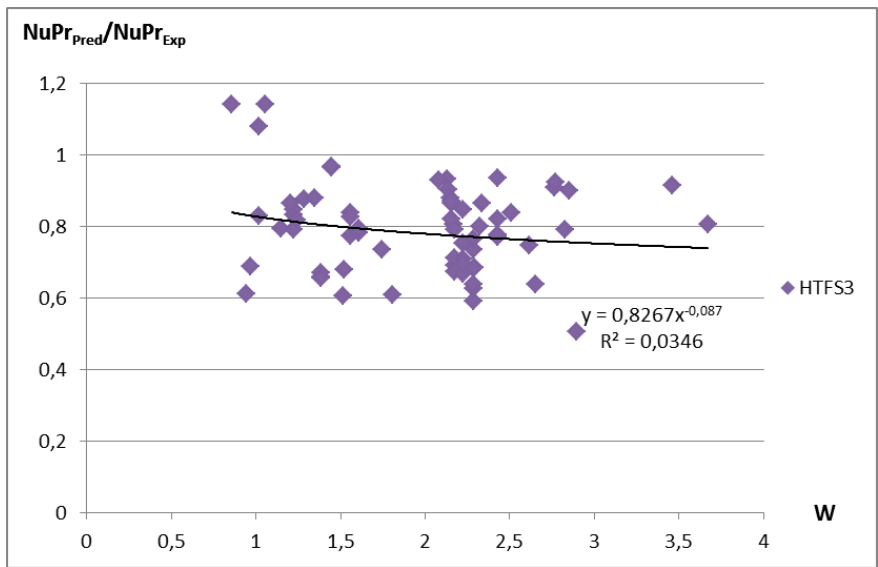


Figure 162: Predicted heat transfer dependency on W for HTFS3, serrated fins

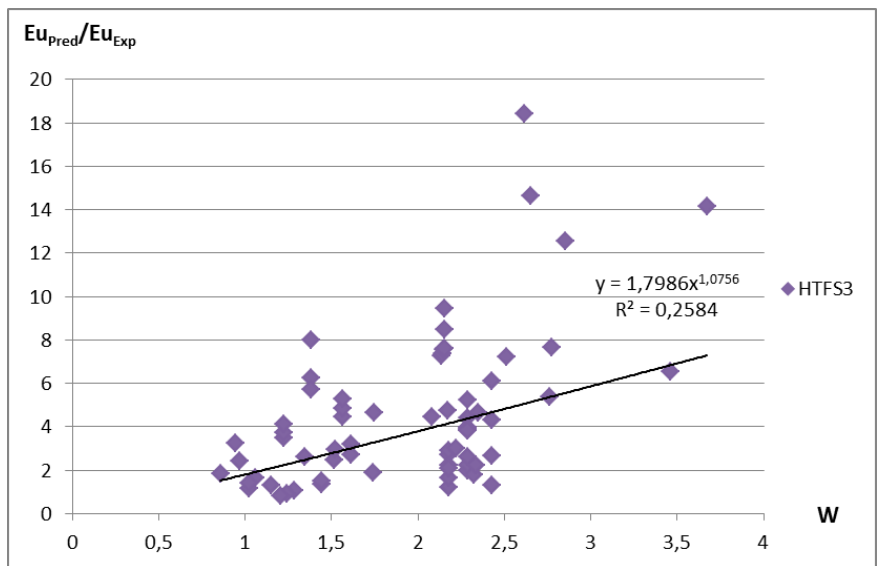


Figure 163: Predicted pressure drop dependency on W for HTFS3, serrated fins

C Modified model performance

C.1 PFR

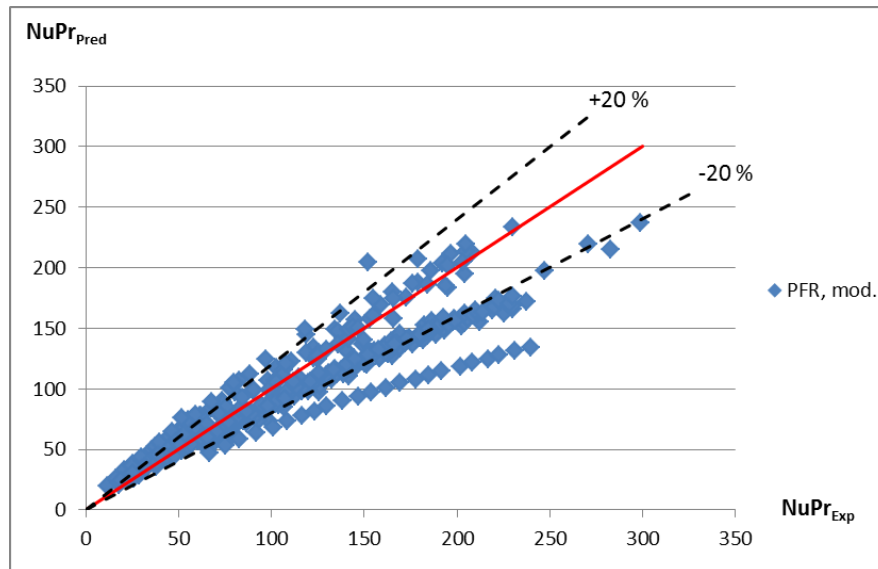


Figure 164: Heat transfer prediction accuracy of modified PFR, solid fins

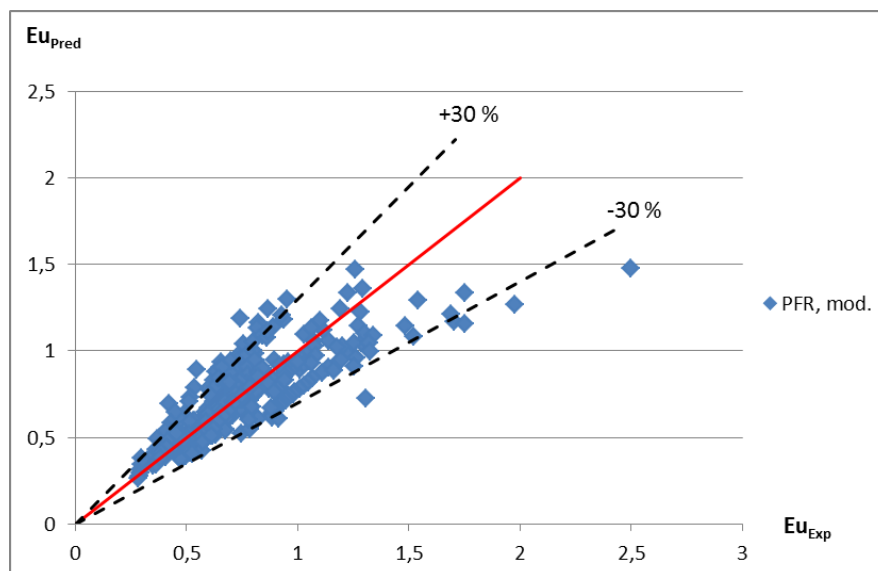


Figure 165: Pressure drop prediction accuracy of modified PFR, solid fins

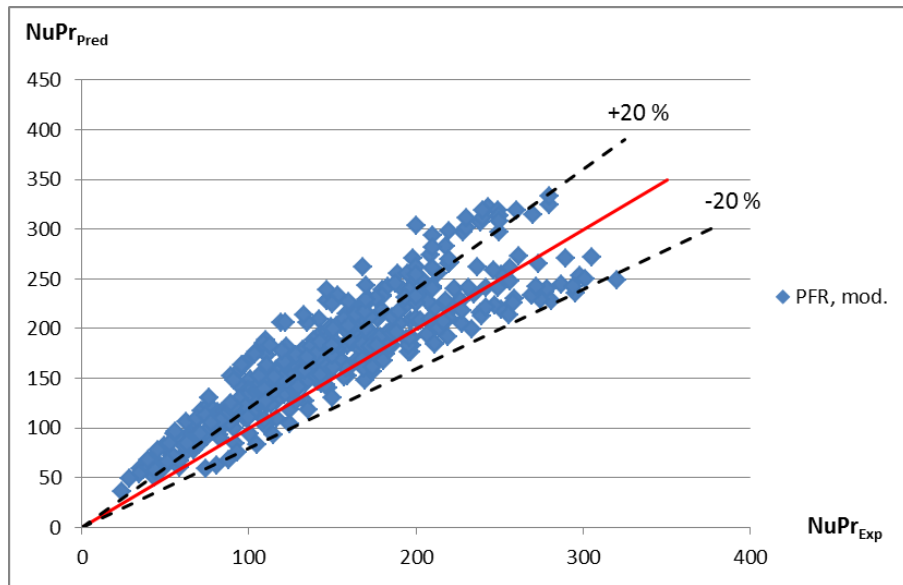


Figure 166: Heat transfer prediction accuracy of modified PFR, serrated fins

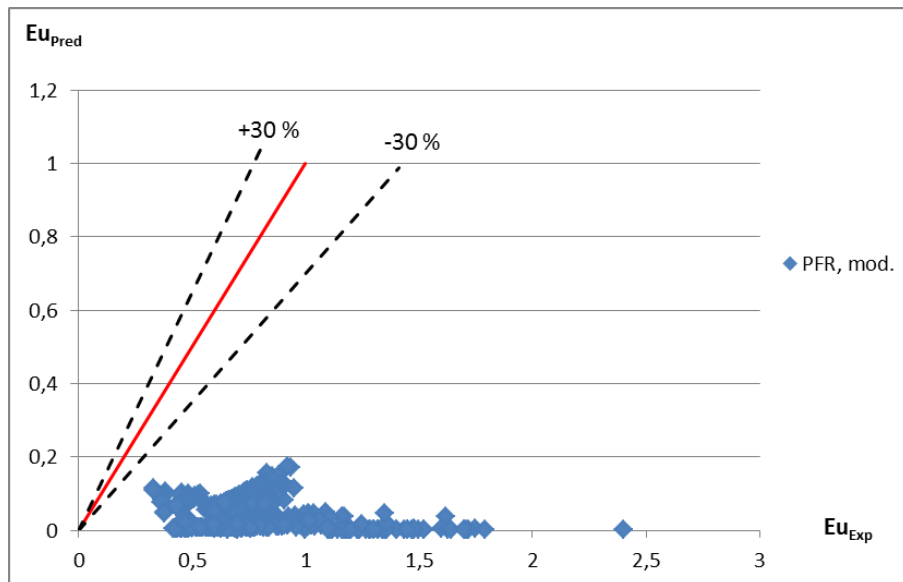


Figure 167: Pressure drop prediction accuracy of modified PFR, serrated fins

C.2 Nir

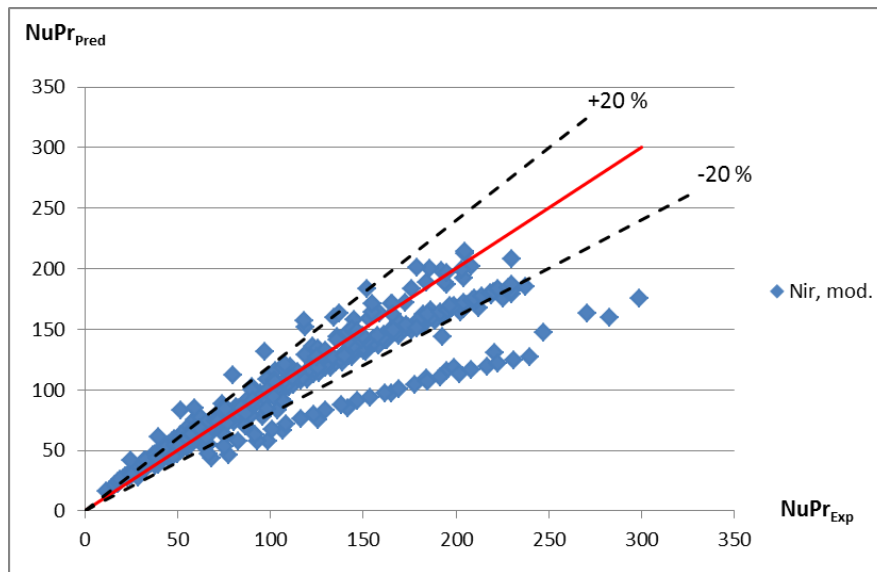


Figure 168: Heat transfer prediction accuracy of modified Nir, solid fins

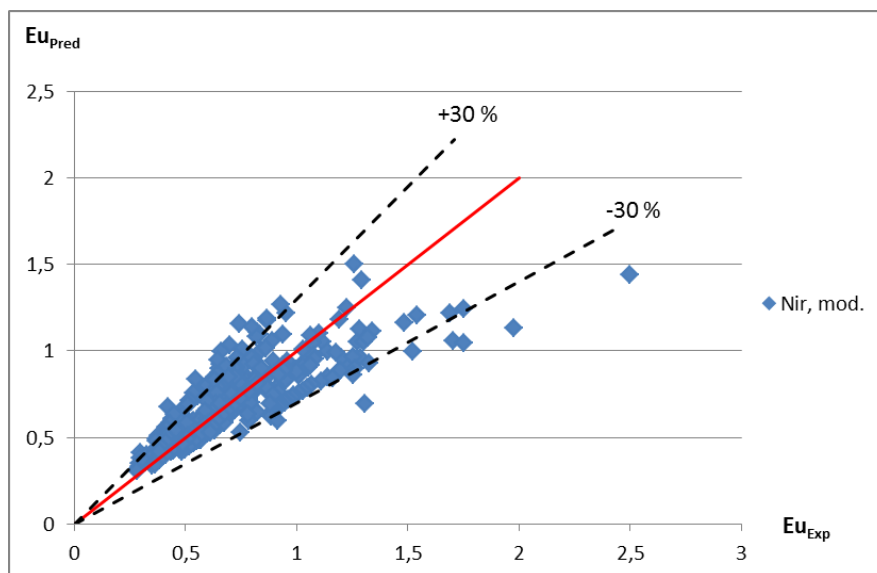


Figure 169: Pressure drop prediction accuracy of modified Nir, solid fins

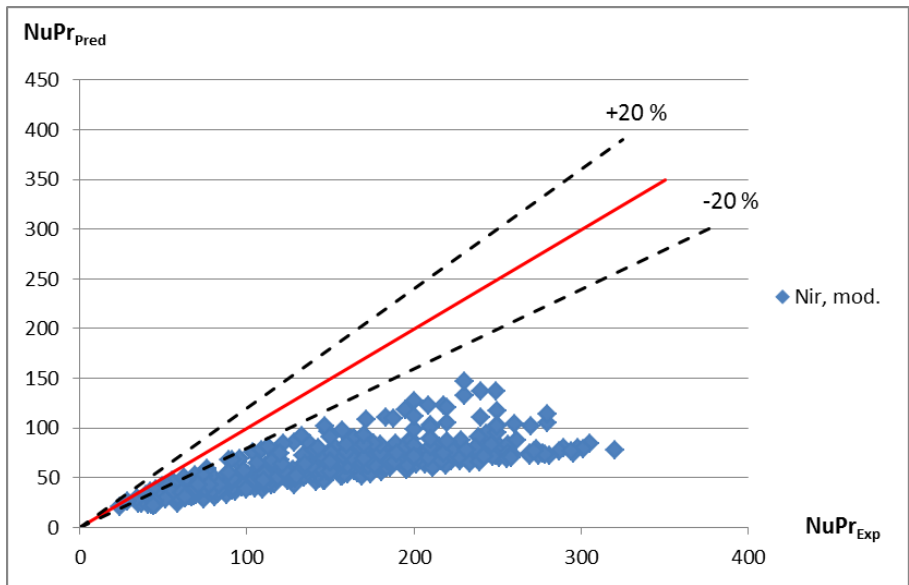


Figure 170: Heat transfer prediction accuracy of modified Nir, serrated fins

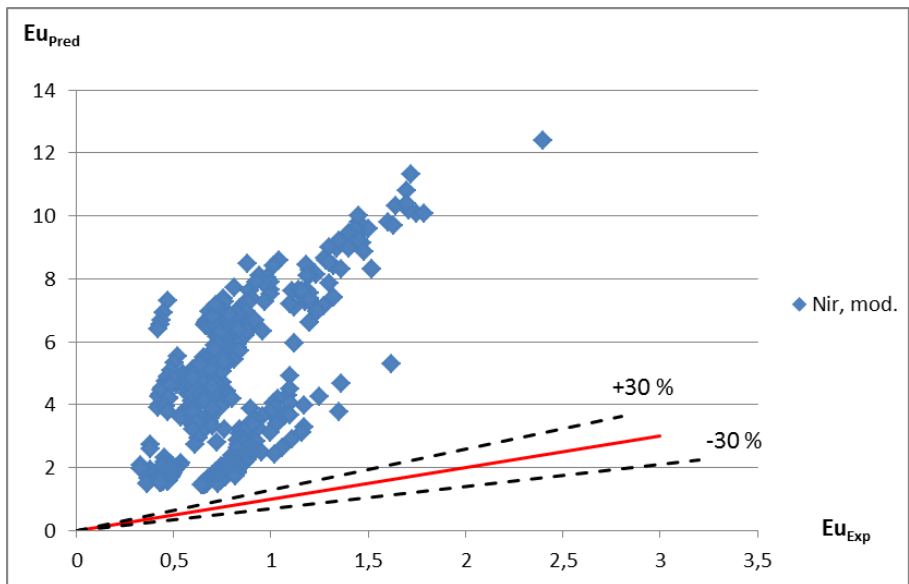


Figure 171: Pressure drop prediction accuracy of modified Nir, serrated fins

C.3 HTFS1

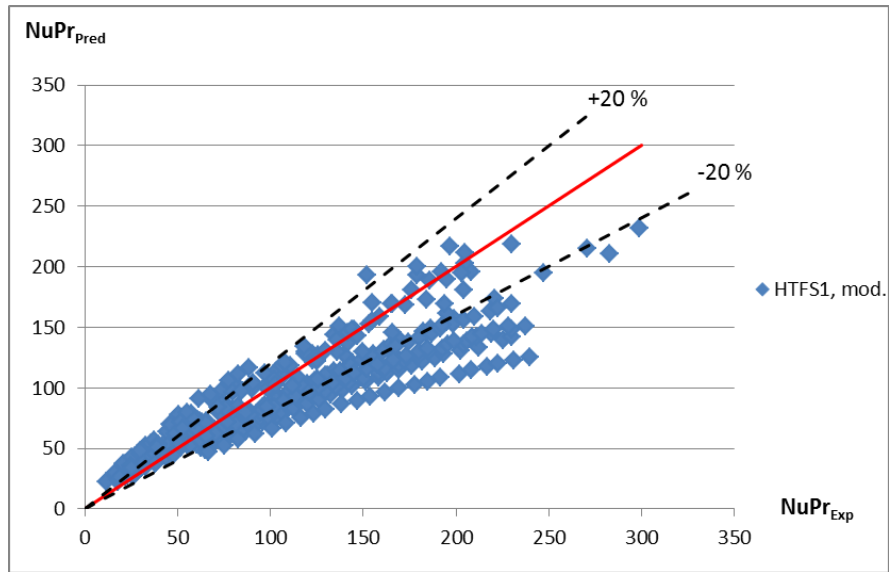


Figure 172: Heat transfer prediction accuracy of modified HTFS1, solid fins

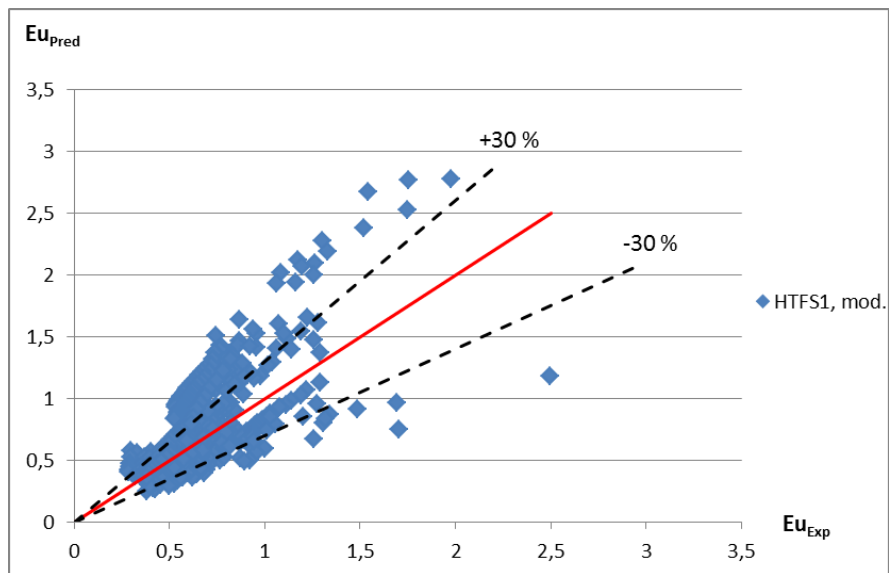


Figure 173: Pressure drop prediction accuracy of modified HTFS1, solid fins

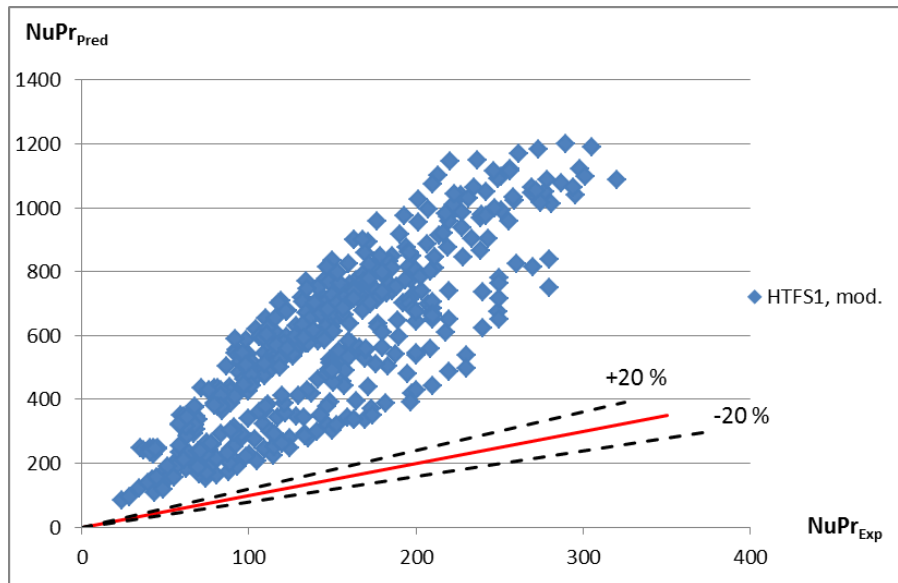


Figure 174: Heat transfer prediction accuracy of modified HTFS1, serrated fins

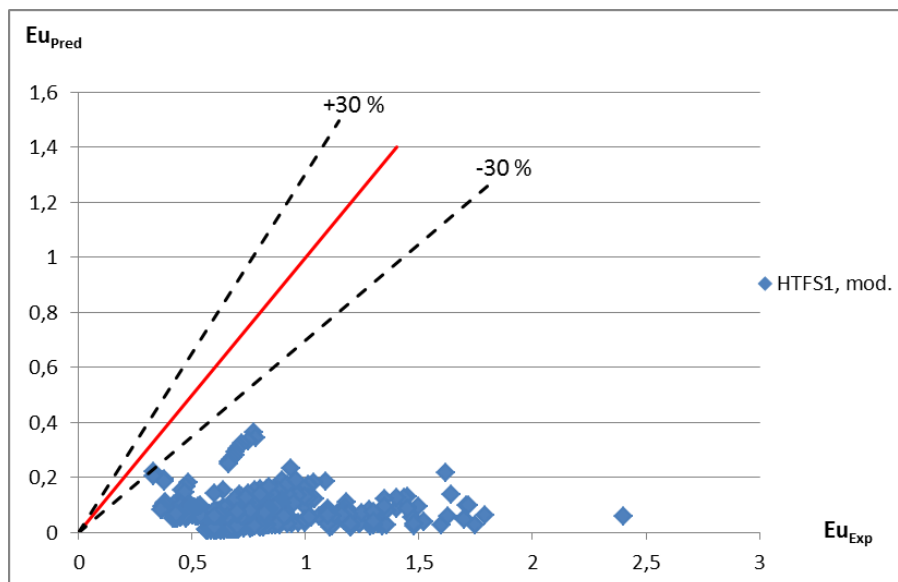


Figure 175: Pressure drop prediction accuracy of modified HTFS1, serrated fins

C.4 HTFS2

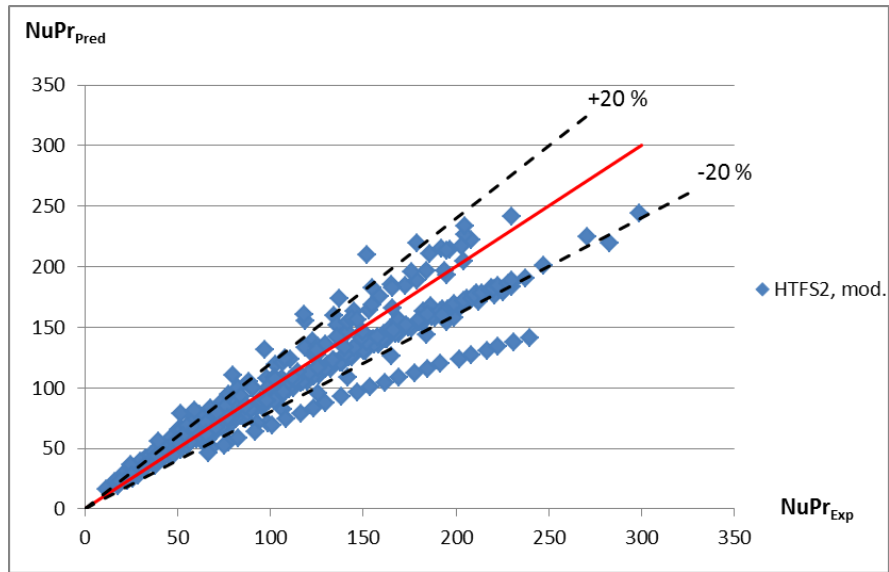


Figure 176: Heat transfer prediction accuracy of modified HTFS2, solid fins

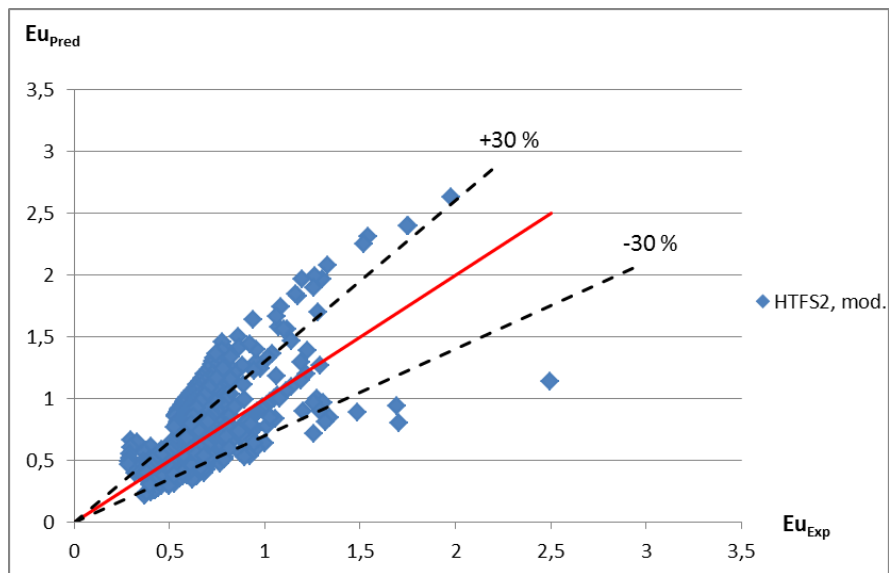


Figure 177: Pressure drop prediction accuracy of modified HTFS2, solid fins

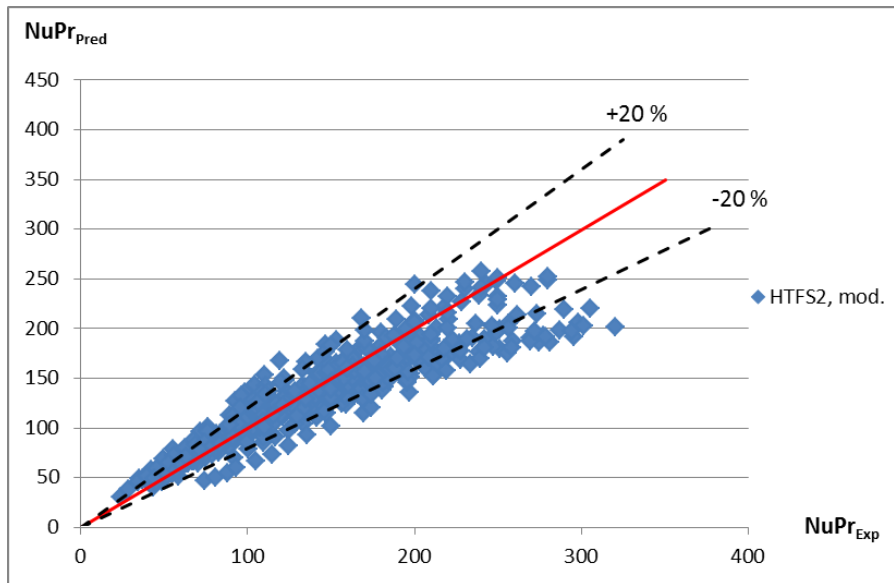


Figure 178: Heat transfer prediction accuracy of modified HTFS2, serrated fins

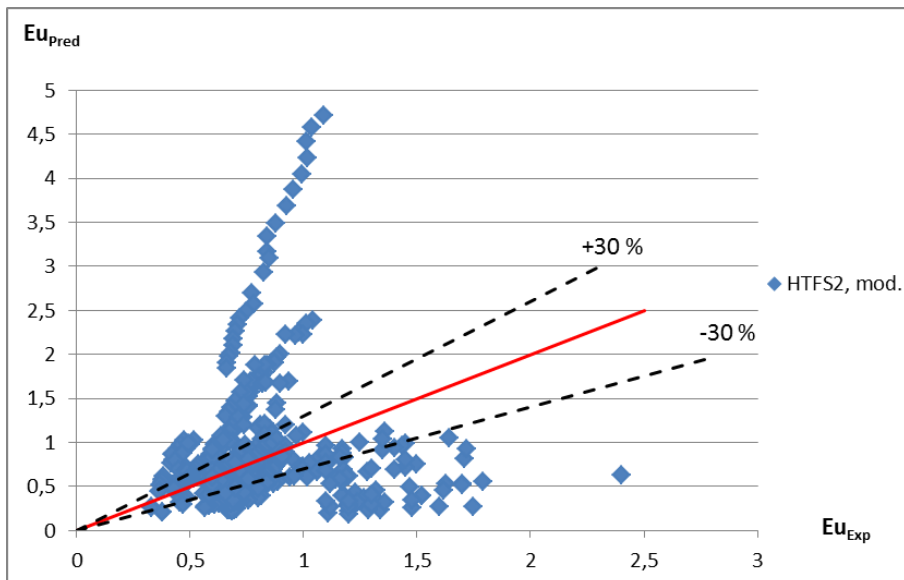


Figure 179: Pressure drop prediction accuracy of modified HTFS2, serrated fins

C.5 HTFS3

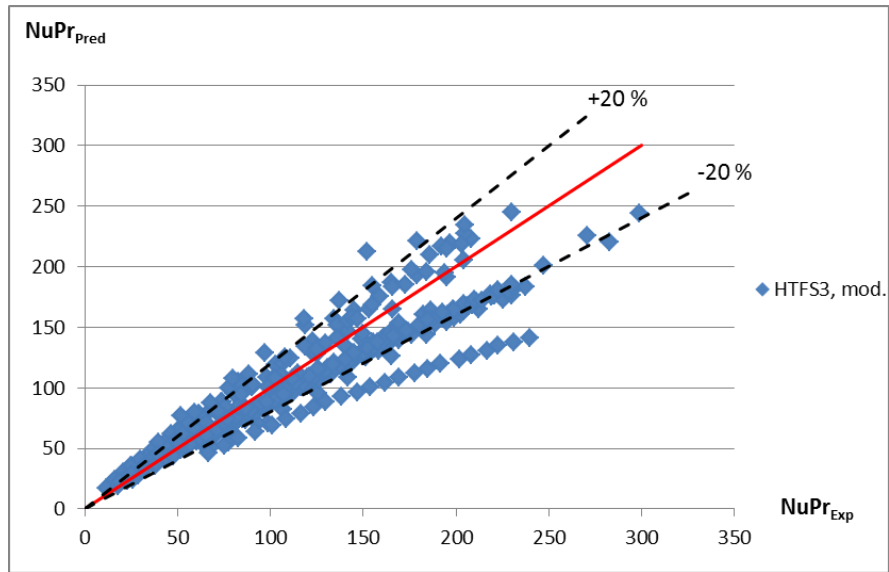


Figure 180: Heat transfer prediction accuracy of modified HTFS3, solid fins

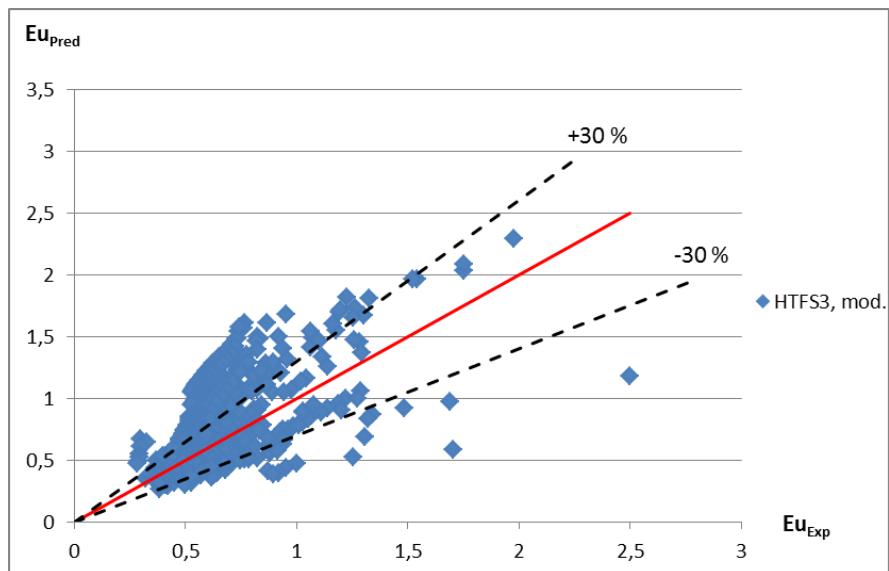


Figure 181: Pressure drop prediction accuracy of modified HTFS3, solid fins

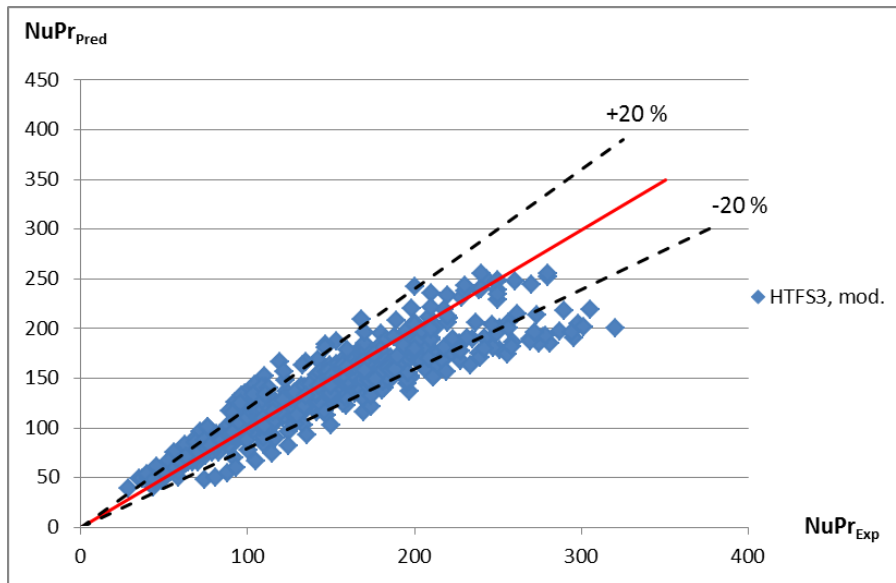


Figure 182: Heat transfer prediction accuracy of modified HTFS3, serrated fins

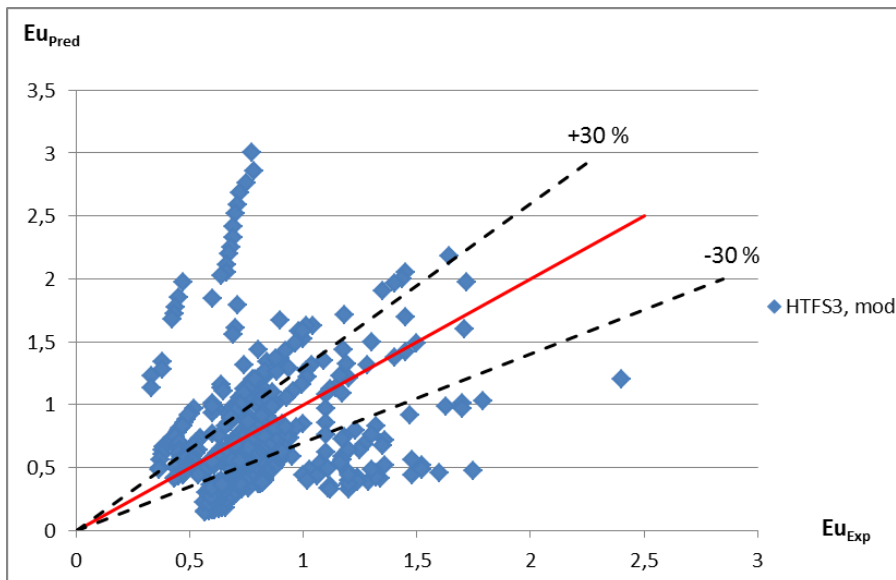


Figure 183: Pressure drop prediction accuracy of modified HTFS3, serrated fins

D Experimental uncertainty

The uncertainty analysis for the pressure drop and heat transfer testing was carried out by Anna Holfeld. It is based on Moffat's (1988) method and Næss' (2007) procedure for experimental uncertainty in tube bundle testing. The uncertainties associated with the testing are summed up as follows:

D.1 Pressure drop test

Table 11: Experimental uncertainties in pressure drop test

Variable	Symbol	Relative uncertainty
Measured data, gas side		
Orifice		
Differential pressure	dp_or	0.019-0.555
Absolute pressure	p_or	0.004-0.009
Temperature	T_air_or	0.010-0.115
Test section		
Differential pressure	dp_ts	0.117-0.486
Absolute pressure	p_ts	0.002-0.003
Temperature	T_air_in	0.010-0.096
Differential pressure	T_air_out	0.010-0.103
Fluid properties, gas side		
Orifice		
Density	roh_air_or	0.005-0.012
Dynamic viscosity	my_air_or	0.0007-0.007
Test section		
Average temperature	t_air_m	0.007-0.071
Density	roh_air_ts	0.004-0.007
Conductivity	lambda_air_ts	0.0005-0.005
Dynamic viscosity	my_air_ts	0.0005-0.005
Mass flow, gas side		
Orifice diameter	d_or	0.001
Pipe diameter	D	0.004
Expansion coeff.	epsilon	0.00001-0.0005
Discharge coeff.	discharge	0.005-0.008
Mass flow	mf_air	0.006-0.011
Pressure drop, gas side		
Euler nr.	Eu	0.020-0.486
Reynolds nr.	Re_d_o	0.006-0.012

D.2 Heat transfer test

Table 12: Experimental uncertainties in heat transfer test, gas side

Variable	Symbol	Relative uncertainty
Measured data, gas side		
Orifice		
Differential pressure	dp_or	0.020-0.201
Absolute pressure	p_or	0.008-0.013
Temperature	T_air_or	0.0034-0.0035
Test section		
Differential pressure	dp_ts	0.015-0.265
Absolute pressure	p_ts	0.0035-0.0043
Temperature	T_air_in	0.0035-0.0039
Differential pressure	T_air_out	0.005-0.013
Fluid properties, gas side		
Orifice		
Density	roh_air_or	0.009-0.013
Dynamic viscosity	my_air_or	0.00079-0.00081
Test section		
Average temperature	t_air_m	0.003-0.004
Density	roh_air_ts	0.005-0.006
Heat capacity	cp_air_ts	0.00003-0
Conductivity	lambda_air_ts	0.000026-0.000032
Dynamic viscosity	my_air_ts	0.0005-0.0007
Mass flow, gas side		
Orifice diameter	d_or	0.001
Pipe diameter	D	0.004
Expansion coeff.	epsilon	0.00008-0.0007
Discharge coeff.	discharge	0.005-0.008
Mass flow	mf_air	0.009-0.013
Pressure drop, gas side		
Euler nr.	Eu	0.031-0.266
Reynolds nr.	Re_d_o	0.009-0.013
Transferred heat, gas side		
Heat duty	Q_air	0.011-0.016
Heat transfer, gas side		
Temperature	LMTD	0.006-0.026
Heat transfer coeff.	U_Q_air	0.014-0.028
Heat transfer coeff.	U_Q_gl	0.041-0.110
Heat transfer coeff.	U_Q_m	0.022-0.061
Prandtl nr.	Pr_air	0.0008-0.001
Reynolds nr.	Re_d_o	0.009-0.013

Table 13: Experimental uncertainties in heat transfer test, cooling side

Variable	Symbol	Relative uncertainty
Measured data, cooling side		
Volume flow	Vf_gl	0.020-0.023
Inlet temperature	T_gl_in	0.010-0.015
Temperature	T_gl_1	0.010-0.015
Temperature	T_gl_2	0.010-0.016
Temperature	T_gl_3	0.009-0.014
Temperature	T_gl_4	0.009-0.014
Temperature	T_gl_5	0.009-0.014
Temperature	T_gl_6	0.009-0.013
Temperature	T_gl_7	0.008-0.013
Outlet temperature	T_gl_out	0.008-0.012
Fluid properties, cooling side		
Average temperature	t_gl_m	0.006-0.010
Conductivity	lambda_gl_ts	0.0003-0.0005
Density	roh_gl_ts	0.00010-0.00013
Heat capacity	cp_gl_ts	0.0001-0.0002
Kinematic viscosity	ny_gl_ts	0.005-0.007
Mass flow, cooling side		
Mass flow	mf_gl	0.020-0.023
Transferred heat, cooling side		
Heat duty	Q_gl	0.041-0.106
Heat transfer, cooling side		
Prandtl nr.	Pr_gl	0.005-0.007
Reynolds nr.	Re_i	0.020-0.024
Friction factor	cf/2	0.0055-0.0065
Nusselt nr.	Nu_i	0.022-0.026
Heat transfer coeff.	alpha_i	0.022-0.026

Table 14: Experimental uncertainty in heat transfer test for heat transfer coefficient

Variable	Symbol	Relative uncertainty
Heat transfer coefficient, Weierman		
Eff. fin hight	l	0.0
Parameter	m_ser	0.024-0.047
Fin efficiency	ny_f_th_ser	0.005-0.061
Fin efficiency	ny_f_ser_W	0.005-0.058
Heat transfer coeff.	alpha_air_ser	0.048-0.094
Nusselt nr.	Nu_air	0.048-0.094
NuPr ^(-1/3)		0.048-0.094
Heat transfer coefficient, Hashizume		
Parameter	m	0.025-0.046
Fin efficiency	ny_f_l_th	0.0003-0.036
Correct. factor	h_e=h_f*phi	0.0
Fin efficiency	ny_f_p_Sch	0.00002-0.102
Correct. factor	n	0.004-0.007
Correct. factor	ny_ser	0.004-0.006
Correct. factor	psi_ser	0.013-0.021
Fin efficiency	ny_f_s_a	0.011-0.037
Fin efficiency	ny_f_ser_H	0.018-0.043
Heat transfer coeff.	alpha_air_ser	0.05-0.093
Nusselt nr.	Nu_air	0.05-0.093
NuPr ^(-1/3)		0.05-0.093

E Sintef 10 geometry

The Sintef 10 tube bundle consists of 8 tube rows in the longitudinal direction and 4 rows in the transversal direction. The fins are helically wound L-foot type serrated fins.

Tube and fin dimensions

- Outer tube diameter $d = 25.4$ mm
- Fin diameter $D = 49.99$ mm
- Total fin height $h_f = 11.385$ mm
- Segment width $w_s = 3.97$ mm
- Fin thickness $t_f = 0.91$ mm
- Fin frequency $n_f = 275.59$ fins/m

Bundle dimensions

- Transversal tube pitch $P_T = 79.8$ mm
- Longitudinal tube pitch $P_L = 34$ mm
- Number of tube rows in flow direction $N_r = 8$